NEGATIVE ION PHOTOELECTRON SPECTROSCOPY OF ALKYL PEROXIDES, ALKOXIDES, AND GROUP VIII TRANSITION METAL OXIDES

By

TANYA MICHELLE RAMOND

A. B., Bryn Mawr College, 1994

M. S., University of Colorado, 1996

A thesis submitted to the

Faculty of the Graduate School of the

University of Colorado in partial fulfillment

of the requirements for the degree of

Doctor of Philosophy

Department of Physics

2001

This thesis entitled:
Negative Ion Photoelectron Spectroscopy of Alkyl Peroxides, Alkoxides, and Group VIII Transition Metal Oxides
written by Tanya Michelle Ramond
has been approved for the Department of Physics

_____

Prof. W. Carl Lineberger

_____

Prof. G. Barney Ellison

_____

Prof. Chris Greene

_____

Prof. Stephen Leone

_____

Prof. Henry Kapteyn

Date_____

The final copy of this thesis has been examined by the signatories, and we find that both the content and the form meet acceptable presentation standards of scholarly work in the above mentioned discipline.

Ramond, Tanya Michelle (PhD., Physics)

Negative Ion Photoelectron Spectroscopy of Alkyl Peroxides, Alkoxides, and Group VIII Transition Metal Oxides

Thesis directed by Professor W. Carl Lineberger

I employed negative ion photoelectron spectroscopy to investigate the structure and energetics of three groups of anions and their corresponding neutrals: alkyl peroxides ROO^-, (R = H, D, CH_3, CD_3, and CH_3CH_2); alkoxides RO^- (R=CH_3, CD_3, CH_3CH_2, CD_3CD_2, $(CH_3)_2CH$, and $(CH_3)_3C$); and Group VIII transition metal oxides XO^- and OXO^- (X = Ni, Pd, Pt). The peroxides and the alkoxides are of great interest to those who study atmospheric or combustion chemistry, while the metal oxides play an important role in catalysis reactions. However, each of these groups of molecules displays interesting behavior that is itself a motivation for their investigation.

The spectra of HOO^- and DOO^- are relatively straightforward to analyze and understand and provide a good basis from which to compare the larger alkyl peroxides. The ROO^- spectra exhibit the normal Franck-Condon behavior leading to clear assignments of the expected vibrational progressions in both the ground and first excited state of the neutral species. Although the molecules increase in size from HOO to CH_3CH_2OO, many of the spectral characteristics such as electron affinity (*EA*) and prominence of the O-O stretch vibration do not appreciably change. The *EA* of HOO is revised, which becomes important as part of a newly revised thermochemistry of HOO and HOOH.

The RO^- species exhibit an additional layer of complexity. Both the CH_3O^- and $(CH_3)_3CO^-$ molecules possess relatively high C_{3v} symmetry about the CO axis as well as a doubly degenerate ground electronic state of the neutral RO molecule. Both of these elements are expected to produce a Jahn-Teller effect, where in order to break the molecular symmetry and electronic state degeneracy, the Born-Oppenheimer approximation breaks down and nuclear and electronic wavefunctions become coupled. The extent to which Jahn-Teller effects affect the RO molecule photoelectron spectra is discussed.

Although the transition metal monoxides are diatomics and thus perhaps presumed to be uncomplicated molecules, they are the most difficult to understand in this thesis and the most difficult to obtain in the laboratory. The d orbitals of the metals are closely spaced together, leading to congested spectra and mixing of the properties of orbitals that complicates analysis and *ab initio* calculations. Furthermore, the high nuclear charge of the atoms involved leads to non-negligible spin-orbit and other relativistic effects. Perhaps for these reasons there is relatively little information in the literature on these molecules. However, despite the complexities involved, comparison of all three metal molecules has allowed for a consistent interpretation of the spectra. Assignments are made including electron affinities, spin-orbit excited states of both anion and neutral XO molecules, other excited electronic states of anion and neutral, and vibrational frequencies and bond length changes. Analysis of the OXO molecules yields electron affinities, vibrational frequencies, and anion to neutral geometry changes.

Acknowledgements

There are many people I want to thank for acting as a positive force in my trek through graduate school. To begin with, I thank my advisor, Dr. Carl Lineberger. He took me into his lab having had no lab experience and only one (high school!) chemistry class under my belt and gave me the chance to learn. He has great physical insight and I hope to carry away a small amount of that when I leave. I have also had the good fortune to work with Dr. Barney Ellison. Barney has been a persistent ambassador of organic chemistry to my resistant physics-oriented mind and through his lively and convincing manner of presentation may have succeeded in getting some of it to stick!

I thank Dr. Rebecca Schwartz and Prof. Gustavo Davico, who taught me much of what I know, and especially to Gus who has kept in touch and remained supportive even after joining the ranks of busy university professors. I have enjoyed working with and learning from Profs. Kent Ervin and Mitchio Okumura. I have benefited from the camaraderie of both Lineberger and Ellison group members including Krista Beck, Todd Sanford, Sang Yun Han, Mark Taylor, Bert Callicoatt, Felician Muntean, Andrei Sanov, Xu Zhang, Mark Nimlos, Evan Jochnowitz, Django Andrews, and especially Stephen Blanksby who showed me how explosive chemicals can actually yield beautiful data. Many of these people are depicted below in the wonderful drawing by a great visiting fellow, Prof. Zdenek Herman. None of the experiments could have been possible without the superb expertise of members of the

JILA machine and electronics shops, most notably Hans Green and James Fung-A-Fat. I am thankful for the "Peace Room presence" of Nada Djuric and Duska Popovic, who have been great friends and colleagues.

I began friendships with the members of my physics graduate class through countless late-night homework sessions, TA grading assignments, and post-exam revelry. I am happy to have stayed in touch throughout the various stages of grad school, especially with Erin Gill, Maija Besky, Jamie Williams, Adrienne Allen, and Yoriko Morita. Several people have been particularly encouraging for helping get me through those turbulent comps years: Profs. Anna Hasenfratz, Jinx Cooper, and John Taylor, and Mike Dubson. I cannot forget Dr. Katy Garmany who provided a sympathetic ear and unconditional support. I also have fond memories of working with Profs. Peter Conti and Bob Blum and I hope they finally realize I didn't leave astrophysics because of anything they did! I feel lucky to have earned the friendship of Kelsey Johnson over my grad school years. I admire her intelligence and drive, and enjoyed sharing many talks, hikes, and ultimate games. I hope to stay close friends with her and her husband, Remy Indebetouw, and wish them the best of luck as they leave Boulder and start their post-doc careers.

I cannot forget the unqualified love and support from the members of my family: Pierre and Lillian, Lisa and Jennifer, as well as all my grandparents, aunts, uncles, and cousins. I come from a very scientifically and academically accomplished family, and they have provided much empathy along the path to a Ph.D. in physics. Finally, I thank my sweetie, Jim Piccolini, for overcoming a (probably warranted!) suspicion of scientists and loving and believing in me.

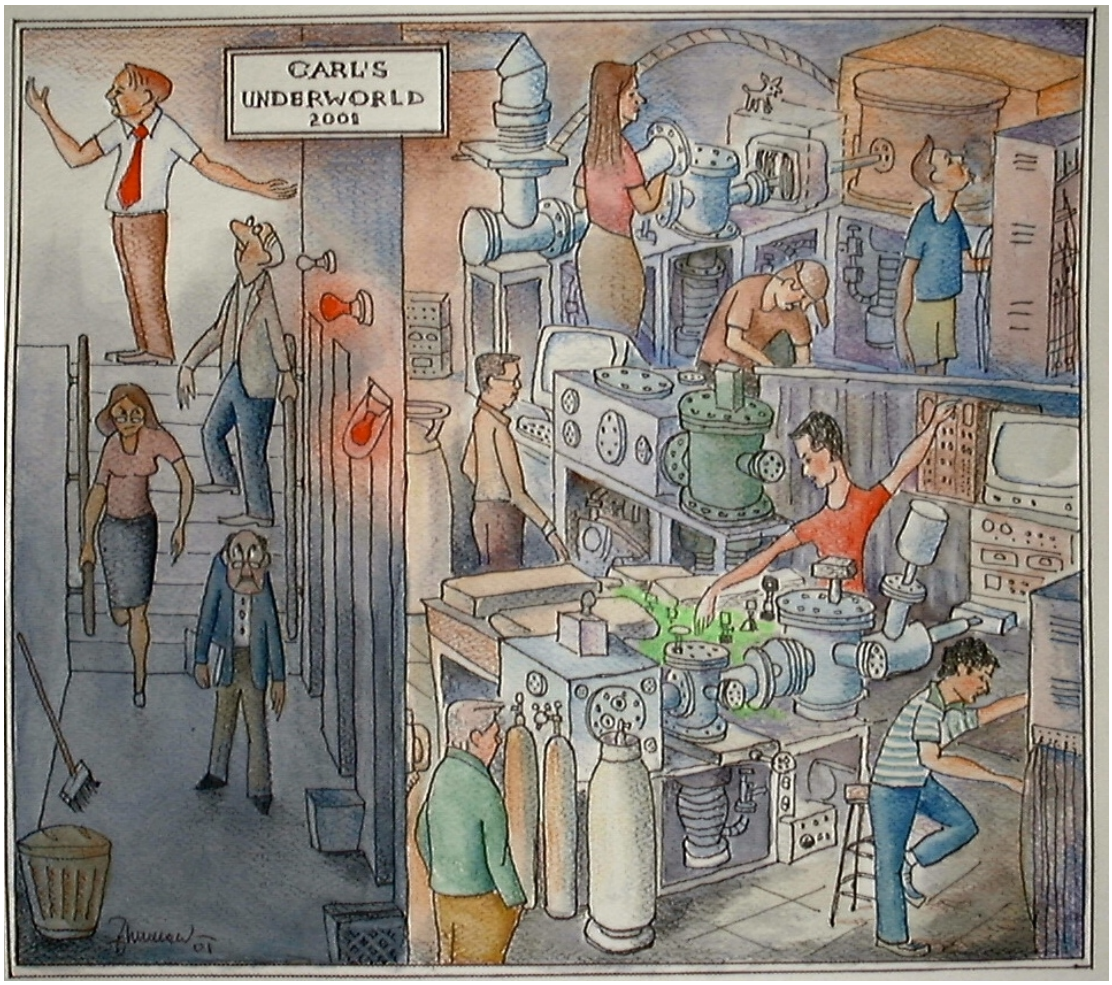
CARL'S
UNDERWORLD
2001

Contents

Tables

Table

Figures

Figure

Chapter 1

Introduction

This thesis offers an examination of the structure and energetics of three groups of molecules through negative ion photoelectron spectroscopy: alkyl peroxyls (ROO), alkoxy radicals (RO), and metal oxides (XO, OXO). All have in common an organic (R) or inorganic (X) substituent bonded to either one or two oxygen atoms. Oxygen has obvious importance to our everyday lives and is abundant in our atmosphere; however, an important property is that oxygen is the second most electronegative element of the periodic table and thus bonds readily. It is useful to start with a physical picture of the orbital structure of both the oxygen atom and the bonding pattern in the dioxygen molecule. A basic overview is given here although for more details, the reader should consult Ref. (*1*).

Oxygen atom has a ground state configuration of $1s^2\ 2s^2\ 2p^4$. The orbitals of the valence configuration are displayed in a schematic way in Figure 1.1, with the p_x orbital pointing up, the p_y orbital coming out of the page, and the p_z orbital pointing to the right. The way the figure is drawn, both the p_y and p_z electrons are unpaired, although there is no preferred direction and the lone pair may go to any of the three lobes. The ground state of the oxygen atom possesses two electrons with spins parallel, forming a ^3P state. Anything bonding to the oxygen may bond with either the p_z or p_y electron, both configurations being energetically equivalent. For example, the oxygen bonds to a methyl CH_3 group to form the methoxy radical CH_3O, as shown in Figure 1.2. Here a σ-type bond is formed along the z axis

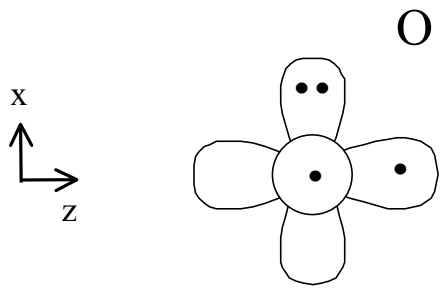

Figure 1.1. Valence $2p^4$ configuration of O.

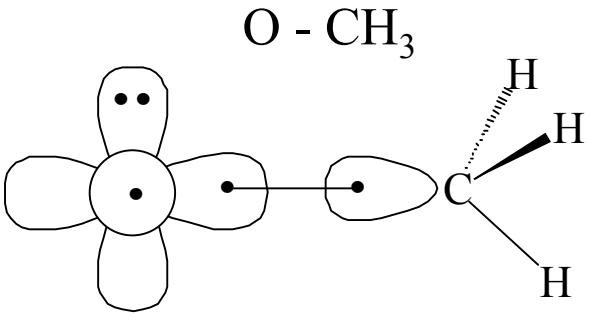

Figure 1.2. Valence picture of O-CH_3.

(represented by the solid line) between the p_z oxygen lobe and the p_z carbon lobe and one unpaired electron is left in the p_y orbital.

The homonuclear diatomic O_2 molecule offers a fairly straightforward picture of bonding, with a ground state molecular orbital diagram shown in Figure 1.3. Each oxygen molecule has 8 electrons, for a total 16 electrons in O_2, which are depicted in the diagram. The s orbitals combine to give bonding σ and antibonding σ^* orbitals symmetric about the z axis, depending on if the individual s wavefunctions are added or subtracted, respectively. The three orthogonal p orbitals may be combined in three ways to make a bond. The first way the overlap of p_z bonds forms the σ and σ^* orbitals depicted in Figure 1.4. The dashed lines indicate the spatial region where the atomic orbitals overlap to make the molecular orbitals. The second way is displayed in Figure 1.5. In this case, the p_x orbitals overlap broadside to form both π_x and π_x^* orbitals. This bond is energetically equivalent to forming the π_y and π_y^* orbitals from the broadside overlap of the p_y orbitals, as shown in Figure 1.6.

The ground state configuration of O_2 is $(1s\sigma)^2\ (1s\sigma^*)^2\ (2s\sigma)^2\ (2s\sigma^*)^2\ (3p\sigma)^2\ (1p\pi_x)^2\ (1p\pi_y)^2\ (1p\pi_x^*)^1\ (1p\pi_y^*)^1$ (see Fig. 1.3) which is commonly written as $(1\sigma_g^+)^2\,(1\sigma_u^+)^2\,(2\sigma_g^+)^2\,(2\sigma_u^+)^2\,(3\sigma_g^+)^2\,(1\pi_u)^4\,(1\pi_g)^2\ {}^3\Sigma_g^-$. This triplet $(1p\pi_x^*)^1\,(1p\pi_y^*)^1$ configuration is energetically favored over a singlet $(1p\pi_x^*)^2\ {}^1\Delta_g$ or ${}^1\Sigma_g^+$ because Hund's rules predict that a configuration with higher multiplicity will be lower in energy. The O_2 ground state is represented schematically in Figure 1.7. The two degenerate unpaired electrons are staggered, one in a π_x^* and one in a π_y^* orbital, the double dots symbolizing closed-shell orbitals. From this point it is not difficult to picture the structure of HOO. The hydrogen will bond with one of the unpaired

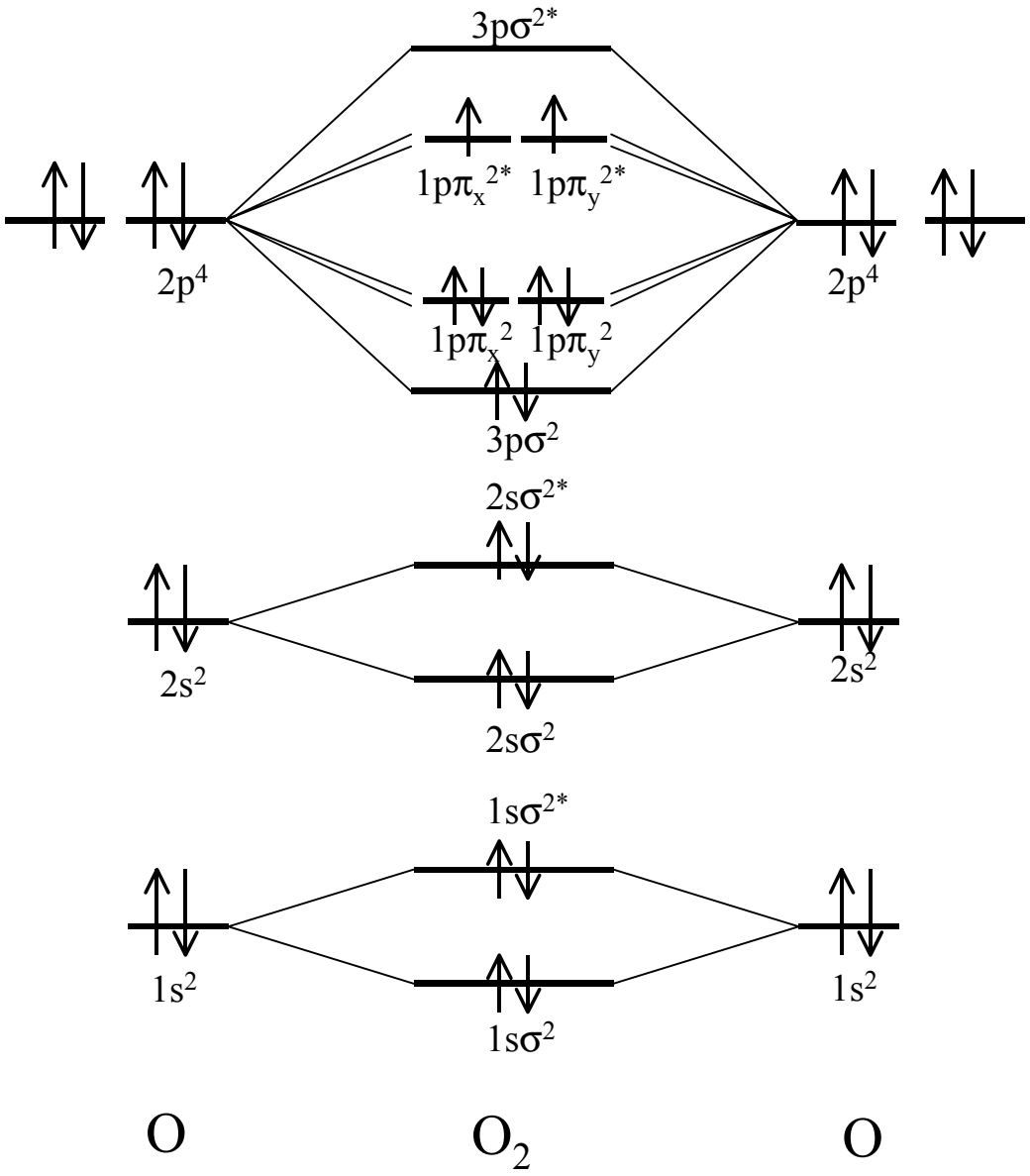

Figure 1.3. Molecular orbital diagram of $(1s\sigma)^2$ $(1s\sigma^*)^2$ $(2s\sigma)^2$ $(2s\sigma^*)^2$ $(3p\sigma)^2$ $(1p\pi_x)^2$ $(1p\pi_y)^2$ $(1p\pi_x^*)^1$ $(1p\pi_y^*)^1$ O_2 composed from $1s^2$ $2s^2$ $2p^4$ O.

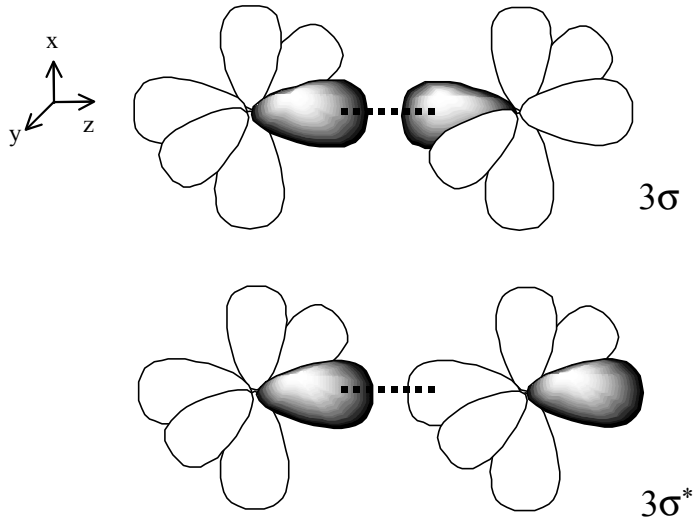

Figure 1.4. Schematic picture of formation of bonding 3σ and antibonding 3σ* orbitals from the p_z atomic orbitals of oxygen. Dashed lines indicate region where atomic orbitals overlap to form molecular orbitals.

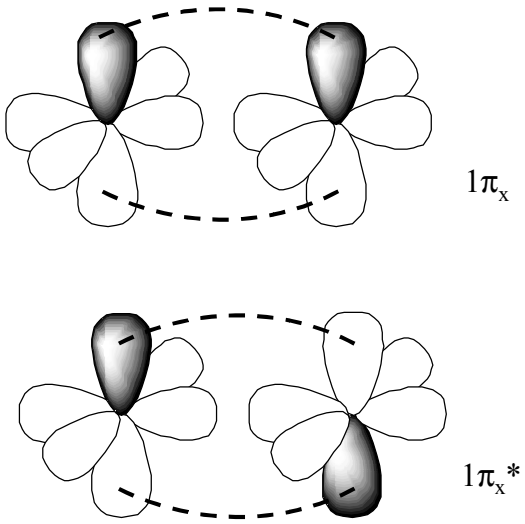

Figure 1.5. Schematic picture of formation of bonding $1\pi_x$ and antibonding $1\pi_x$* orbitals from the p_x atomic orbitals of oxygen. Dashed lines indicate regions where atomic orbitals overlap to form molecular orbitals.

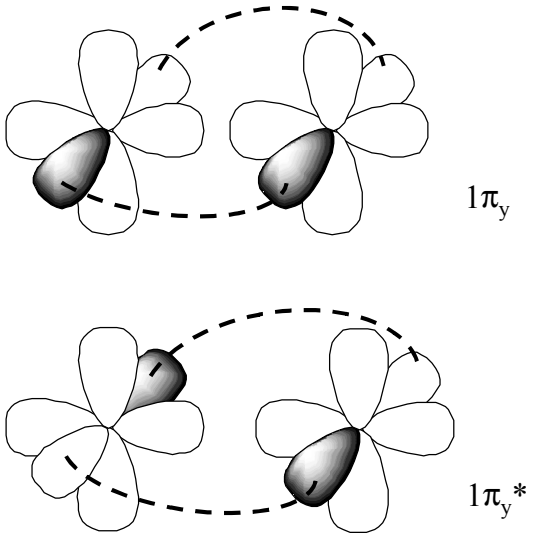

Figure 1.6. Schematic picture of formation of bonding $1\pi_y$ and antibonding $1\pi_y^*$ orbitals from the p_y atomic orbitals of oxygen. Dashed lines indicate regions where atomic orbitals overlap to form molecular orbitals.

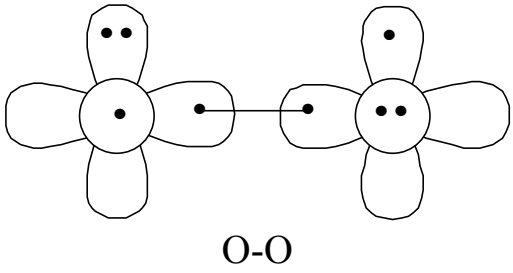

Figure 1.7. Valence orbital schematic of dioxygen O_2. The single dots represent unpaired electrons and the double dots indicate a filled lobe. The solid line indicates a bond.

electrons, as shown in Figure 1.8, with rearrangement of the orbital positions to minimize interactions between electrons. This will be further addressed in Chapter 3. The experimental method used to probe such molecular structure in this thesis will now be discussed.

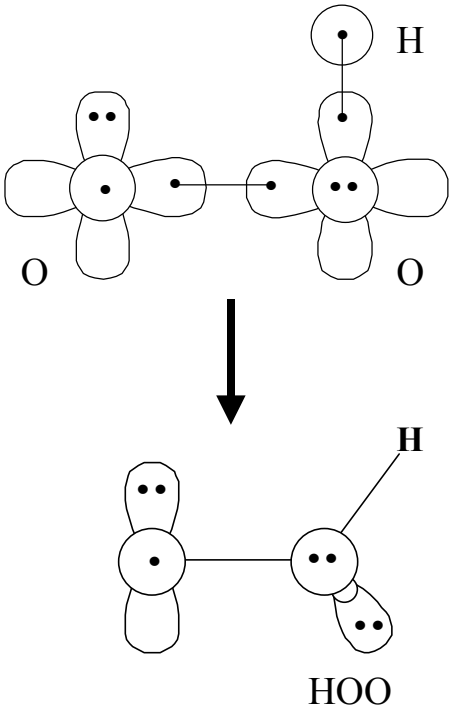

Figure 1.8. Valence orbital schematic of HOO. The single dots represent unpaired electrons and the double dots indicate a filled lobe. The solid line indicates a bond.

1.1 Negative ion photoelectron spectroscopy overview

Negative ion photoelectron spectroscopy (PES) is a valuable tool to examine the fundamental structure of molecules (*2*). A schematic of the experiment is presented in Figure 1.9. Negative ions are synthesized in a flowing afterglow source, shaped into a beam with a series of ion lenses, and then are mass-selected with a Wien mass filter. The continuous ion beam intersects the beam of a fixed frequency 3.4 eV cw laser, which ejects the photoelectron and leaves a neutral molecule and a photoelectron with non-zero kinetic energy (eKE). The experiment may be summarized as follows:

$$AB^- + h\nu \rightarrow AB + e^-(eKE) \qquad (1.1)$$

This process is depicted schematically in Figure 1.9. It is a direct photodetachment process in a frozen nucleus approximation which may be thought of as proceeding via an intermediate $(AB^-)^*$ state whose lifetime is significantly less than a vibrational period. In this case, the nuclear geometry of the anion is effectively directly superimposed onto that of the neutral, neglecting any intermediate state contribution. This is the Franck-Condon approximation. The photon imparts enough energy to expel the extra electron from the anion and the molecule transitions into a bound internal state of the neutral molecule. The energy imparted to the system, hν, must be conserved. The energy that is not used to make the transition from anion to neutral, the electron binding energy (eBE), leaves the system in the form of the kinetic energy

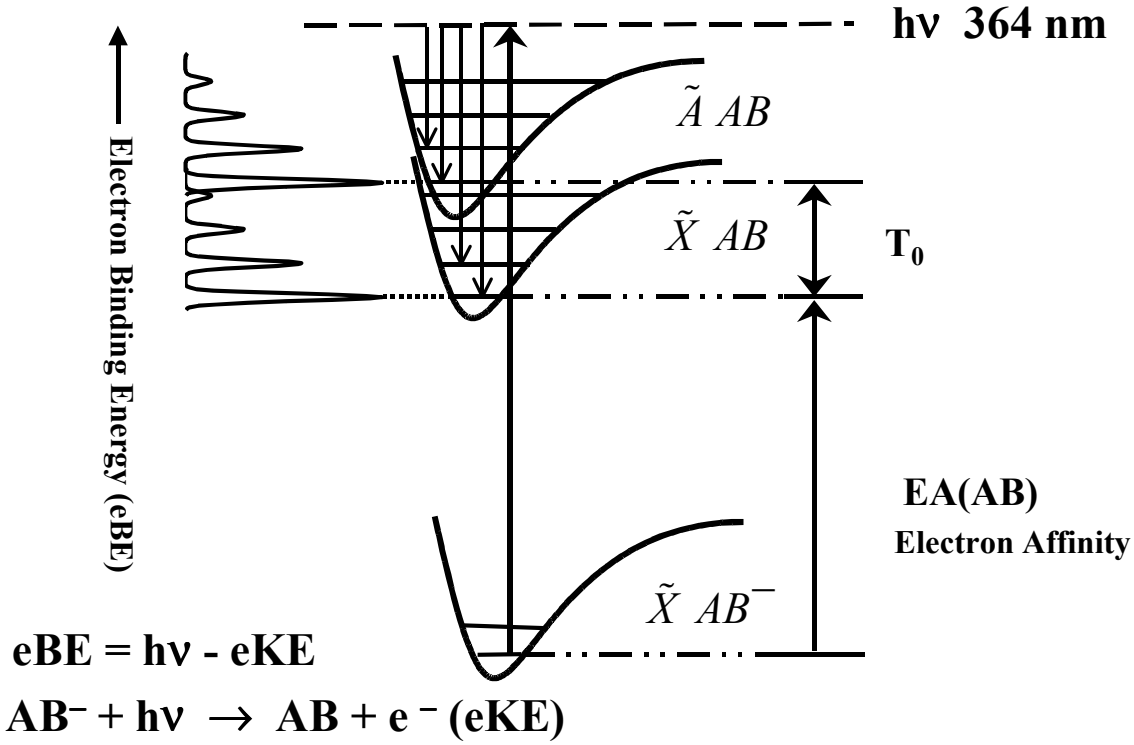

Figure 1.9. Schematic picture of negative ion photoelectron spectroscopy. Negative ions intercept 364 nm photons, leaving the molecule in a bound state of the neutral molecule. The excess energy leaves in the form of the kinetic energy of the detached electron and a spectrum of photoelectron peaks versus electron kinetic energy (eKE) is recorded.

of the photoelectron; for every discrete transition $AB^- \rightarrow AB$ there is an electron with a discrete amount of electron kinetic energy (eKE) expelled. The observable for this experiment is the electron kinetic energy of the photoelectrons. They pass into a hemispherical kinetic energy analyzer and then onto a position sensitive detector. In this way a spectrum of photoelectron peaks versus eKE is collected. The energy axis may also be expressed in terms of electron binding energy, where eBE = hν – eKE.

A wealth of information may be extracted from the spectra, including vibrational frequencies and anharmonicities of both anion and neutral species, geometrical parameters (see following section), and the electron affinity (*EA*). The *EA* is defined as the transition between the vibrationless ground states of the anion and the neutral, denoted 0_0^0. The *EA* is both a key spectroscopic value and of vital importance for use in thermochemical cycles in order to determine bond dissociation energies (Chapters 3 and 4) (*3*).

There are many advantages to negative ion PES. One is that frequently the 3.4 eV photon energy is great enough to observe transitions into excited states of the neutral molecule, which is represented in Figure 1.9 by two potential wells in the neutral state. In the case of the RO and ROO organic molecules examined in this thesis, the separation between the anion highest occupied molecular orbital (HOMO) and HOMO-1 orbitals, for example, is large enough that accessing only ground and first excited states is possible with the 3.4 eV photon energy. For the metal oxide anions, the energy levels are much closer together, which permits several low-lying electronic states to be observed.

In optical spectroscopy, a direct transition from a singlet to triplet electronic state is dipole forbidden. However, the PES technique is valuable in that splittings between singlet and triplet electronic states may be measured directly: the spin selection rule is $\Delta S = \pm ½$ so that a transition made from a doublet anion state can access both S=3 and S=1 neutral states.

Another advantage to PES is the ability to glean information from short-lived radical species and anions. Radical molecules would not endure long enough to serve as samples for most spectroscopic techniques as they react so readily. Furthermore, there is much less information in the literature in general about molecular anions compared to neutrals, and negative ion PES offers a way to observe anion structure directly. The anion source region of the PES can be cooled, which shifts the population distribution in the vibrational levels of the anion ground state. Upon cooling the sample, a peak originating from a vibrationally excited anion state (hot band) will decrease in intensity with respect to one coming from the ground state. Therefore, comparisons of spectra taken with cooled and non-cooled anions permits identification of hot bands (and thus anion vibrational frequencies), which also allows an unambiguous electron affinity assignment.

Another important tool for assignment of spectral features is the ability to measure angular distributions of photoelectrons. In this PES configuration, a half-wave plate is inserted into the laser beam path that allows rotation of the laser polarization. Comparing the intensities of peaks recorded at different laser polarization angles yields insight into the symmetry of the detached photoelectron. Electrons detached from two different orbitals will yield transitions into different

electronic states of the neutral. In most cases these two orbitals will possess different symmetries that will translate into observation that the photoelectron peaks of different electronic states yield contrasting angular distributions (*4*).

In addition to our experiments (*5*-*8*), there are several other laboratories that use negative ion photoelectron spectroscopy. For example, the experiments headed by both Kit Bowen (*9*) and Doreen Leopold (*10*) are modeled after this apparatus. In these labs, a visible 488 nm laser line is used. This provides more laser intensity than our 364 nm (3.4 eV) uv line and therefore avoids the need for a laser intensity build-up cavity (Chapter 2). However, there is less laser photon energy available, which decreases the energy range of observable spectral features. Also, the laser polarization is fixed, preventing the measurement of photoelectron angular distributions. Bowen uses a Branscomb hot-cathode discharge source (*11*), which can provide a large amount of ions although with higher vibrational temperatures than can be obtained with a flowing afterglow microwave discharge source (Chapter 2). Leopold uses a magnetic sector mass analyzer instead of a Wien filter, which provides mass resolution around 10 times better than what is available here ($m/\Delta m \approx 40$).

If significantly greater photon energies than around 3.4 eV are desired, pulsed lasers are a necessity, and the experimental architecture changes fundamentally. The first anion photoelectron spectrum obtained using a pulsed experiment was reported in 1986 by Mark Johnson and co-workers (*12*). Cluster ions were formed using electron impact ionization of a pulsed supersonic jet that passed through a time-of-flight (TOF) mass spectrometer and intersected a 532 nm Nd: YAG laser. The

detached photoelectrons were then analyzed in a field-free TOF apparatus. The experiment of Daniel Neumark (*13,14*) employs a similar setup. Ion sources used have included both a pulsed molecular beam supersonic expansion crossed with a beam of electrons as well as a pulsed electrical discharge (*15*). Both methods are effective means of producing a vibrationally cooled beam of anions. A TOF mass spectrometer is used with a mass resolution of $m/\Delta m$ = 250-300, and the resolution can reach 2000 with the incorporation of a reflectron stage (*14*). A field-free TOF electron energy analyzer is used. The energy resolution therefore degrades as $(eKE)^{3/2}$ from 5-10 meV resolution (similar to what is used here) at low electron kinetic energies. This setup also allows angular distribution measurements through rotation of the laser polarization angle.

Other laboratories use a pulsed source/laser setup. Both Wang (*16*) and Jarrold (*17*) use a pulsed molecular beam laser ablation source with a time of flight mass spectrometer and a 3.49 eV Nd: YAG laser. Like Neumark, Jarrold uses a field-free TOF electron energy analyzer that permits angular distribution studies. Wang, however, uses a magnetic bottle TOF, which uses a magnetic field to direct all the photoelectrons toward the detector. This is efficient because it collects a full 2π solid angle of photoelectrons, although it sacrifices all photoelectron angular information. Continetti has a similar apparatus to Neumark (*18,19*). However, in this case angular distribution information is obtained not by rotating the laser polarization angle but using a time and position sensitive detector.

Pulsed photoelectron spectroscopy has been successfully employed in the study of molecular clusters such as $Cu_n(CN)_m^-$ (*20*), $(C_6F_6)_n^-$ and $(Au\text{-}C_6F_6)^-$ (*21*),

and In_n^- and Tl_n^- (*22*) produced using laser vaporization sources. These were studies of relatively small clusters, where n and m ≤ 20. Development of a pulsed arc cluster ion source (PACIS) (*23,24*) has allowed production of clusters of several hundreds of anions, neutrals, or positive ions. The PACIS source has been incorporated into the negative ion photoelectron spectroscopy of Sb_n^- and Bi_n^- clusters (*25*) and Pb_n^- (*26*).

1.2 Franck-Condon analysis

Understanding the factors that determine the relative intensities of photoelectron peaks reveals further information about molecular structure. The intensity of a photoelectron transition is expressed (*27*) as the square of the transition moment integral, M,

$$M = \langle \Psi' | \hat{\mu} | \Psi \rangle \qquad (1.2)$$

where $\hat{\mu}$ is the dipole moment operator and Ψ is the total wavefunction of the molecule. At this point, the Born-Oppenheimer approximation allows simplification of Eq. 1.2. This principle acknowledges the different timescales for nuclear and electron motion in a molecule. Because the nuclei are orders of magnitude heavier than the electrons, the Born-Oppenheimer approximation can be used to treat the electrons as moving with respect to nuclei that are considered fixed in space. As a result, the molecular wavefunction can be separated into an electronic part and a vibrational part:

$$|\Psi\rangle = |\Psi_{es}\rangle|\Psi_{v}\rangle. \quad (1.3)$$

Furthermore, the electric dipole operator may be assumed to have a negligible effect on the nuclear coordinates of the molecule on the timescale of electron detachment, $\hat{\mu} \cong \hat{\mu}_e$. This allows Eq. 1.2 to be written as

$$M = \langle \Psi_{e's'} | \hat{\mu}_e | \Psi_{es} \rangle \langle \Psi_{v'} | \Psi_{v} \rangle \quad (1.4)$$

Therefore relative intensities of vibrational levels all originating and ending in the same electronic states are determined by the square of the overlap between initial and final state vibrational wavefunctions,

$$|\langle \Psi_{v'} | \Psi_{v} \rangle|^2. \quad (1.5)$$

This is known as the Franck-Condon factor. The validity of the approximation depends upon the absence of resonant anion states in the photodetachment continuum.

In Chapter 4, the photoelectron spectrum of methoxy radical is discussed. This molecule suffers from a Jahn-Teller effect that couples electronic and nuclear motion and in this case, Eq. 1.3 is not valid. However, for the remainder of the molecules in this thesis and the majority of the molecules investigated with this apparatus, the Born-Oppenheimer approximation is legitimate and the Franck-Condon factors determine the intensities of the vibrational levels observed.

To gain a qualitative sense of the mechanics of Franck-Condon overlap integrals, consider the case of an arbitrary diatomic that has only one geometrical parameter, the internuclear spacing, or r_e. Furthermore, assume that both the ground anion and neutral states may be approximated as harmonic oscillators and all anion population is in the vibrational ground state. In the case of zero bond length change between the anion and neutral molecules, the potential wells are exactly aligned, one directly above the other. The resulting photoelectron spectrum from detaching an electron from the anion looks like a single peak, as shown in Figure 1.10a. Because the wavefunctions of the harmonic oscillator are orthogonal, the only Franck-Condon factor with a non-zero integral is the 0-0 transition (1-1, 2-2, etc. are also non-zero, but they will have the same energy as the 0-0 transition in the harmonic oscillator approximation).

Now consider the case where the two potential wells are slightly offset so that the neutral bond length is, say, 0.07 Å shorter or longer than that of the anion. This may be thought of as a slight perturbation away from case a, and is reflected in the corresponding spectrum shown in Figure 1.10b. Here the 0-0 transition is still the most intense, but now there is non-zero Franck-Condon overlap with excited vibrational states of the neutral, producing a monotonically decaying peak profile.

If the two potential wells are separated farther, say by 0.12 Å, the vibrational progression becomes more extended, and the 0-0 transition is no longer the most intense (Figure 1.10c). For a relatively large Δr_e of 0.20 Å, the vibrational progression extends further (Figure 1.10d). The peak profile begins to follow a

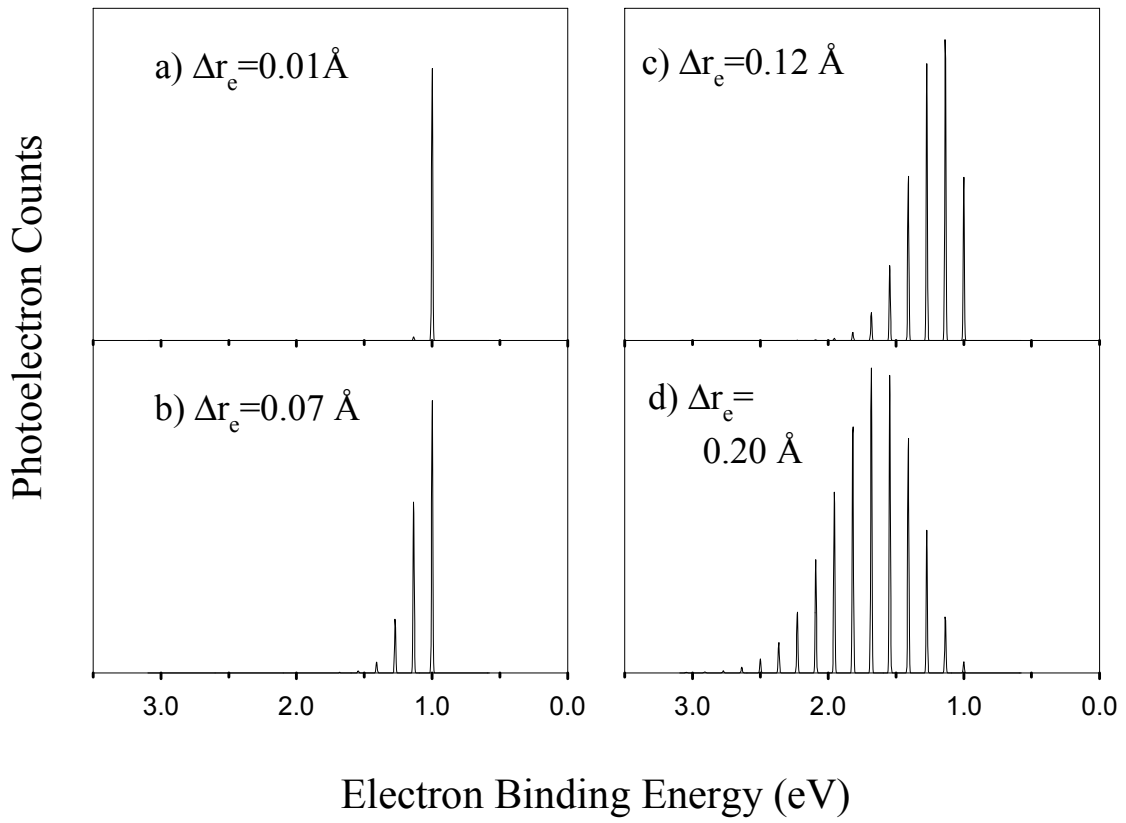

Figure 1.10. Photoelectron spectrum simulation of an arbitrary diatomic molecule and various changes to the anion bond length r_e upon electron photodetachment. a) No change in r_e yields non-zero Franck-Condon intensity only in the 0-0 transition. b) A small Δr_e yields a monotonically decaying profile of peaks. c) A large Δr_e shows an extended progression where the 0-0 peak is no longer the most intense peak. d) For large enough Δr_e, the peak profile is even more extended, takes on a gaussian envelope, and the Franck-Condon factor for the 0-0 transition is small to nondetectable.

gaussian envelope. More significantly, the overlap between the vibrational ground states of the anion and neutral is relatively small and may not be observable above the noise of the experiment.

In this way, the photoelectron spectrum offers insight into the geometrical alteration an anion suffers upon electron detachment. Each of the peak profiles shown above is observed in the various molecules in this thesis. For a polyatomic molecule, more than one geometrical parameter (bond length or bond angle) will change upon detaching an anion electron. However, if the detached electron originates in an orbital that is essentially localized to one or two atoms in the molecule, as will be seen in chapters 3 and 4, the changes in geometry may be limited to a change in a single bond length or bond angle. In the case of a diatomic molecule, a previous knowledge of the neutral bond length allows an estimation of the anion bond length based on the Δr_e needed to reproduce the intensities of the peaks in the spectrum.

1.3 Thesis overview

The remainder of this thesis is organized into four chapters. Chapter 2 offers a general overview of the negative ion photoelectron spectrometer apparatus used to obtain the data presented here, with references to sources of more specific information. In addition, a detailed section is provided regarding the new position sensitive detector and accompanying electronics and software incorporated during the summer and fall of 2000.

Chapters 3-5 present data and analysis of three different groups of molecules beginning with the most straightforward spectra to understand and ending with the most complex. Chapter 3 covers the photoelectron spectroscopy of alkyl peroxide anions ROO^-, (R = H, D, CH_3, CD_3, and CH_3CH_2). Such molecules are of great interest to those studying atmospheric chemistry and combustion as they play key roles as reaction intermediates. The spectra of HOO^- and DOO^- are relatively straightforward to analyze and understand and provide a good basis from which to compare the larger alkyl peroxides. Furthermore, with a few exceptions explained in the chapter, the ROO^- spectra exhibit the normal Franck-Condon behavior leading to clear assignments of the expected vibrational progressions in both the ground and first excited state of the neutral species. Although the molecules increase in size from HOO to CH_3CH_2OO, many of the spectral characteristics such as the electron affinity and the prominence of the O-O stretch vibration do not appreciably change. Finally, the *EA* of HOO is revised, which becomes important as part of newly revised thermochemistry of HOO and HOOH.

In Chapter 4, the photoelectron spectroscopy of alkoxide anion RO^- species (R=CH_3, CD_3, CH_3CH_2, CD_3CD_2, $(CH_3)_2CH$, and $(CH_3)_3C$) is presented. These molecules are also important in atmospheric chemistry, although they are intriguing in their own right due to their inherent spectroscopic complexities. Both the CH_3O^- and $(CH_3)_3CO^-$ molecules possess relatively high (C_{3v}) symmetry about the CO axis as well as a doubly degenerate ground electronic state of the neutral RO molecule. Both of these elements are expected to produce a Jahn-Teller effect where in order to break the molecular symmetry and state degeneracy, the Born-Oppenheimer

approximation breaks down and nuclear and electronic wavefunctions are coupled. The extent to which Jahn-Teller effects affect the RO photoelectron spectra is illustrated throughout the chapter.

Finally, Chapter 5 examines the structure of Group VIII transition metal oxides XO^- and OXO^- (X = Ni, Pd, Pt). Although the XO molecules are small diatomics, they are the most difficult to understand in this thesis and the most difficult to obtain in the laboratory. The d orbitals of the metals are closely spaced together, leading to congested spectra and mixing of the properties of orbitals, which complicates analysis and *ab initio* calculations. Furthermore, the size of the atoms involved leads to non-negligible spin-orbit and other relativistic effects. Perhaps for these reasons there is relatively little information in the literature on these molecules that are so prevalent in catalysis processes and surface science. However, despite the complexities involved, comparison of all three metal molecules has allowed for a consistent interpretation of the spectra. Assignments are made including electron affinities, spin-orbit excited states of both anion and neutral XO molecules, other excited electronic states of anion and neutral, and vibrational frequencies and bond length changes. Analysis of the OXO molecules yields electron affinities, vibrational frequencies, and anion to neutral geometry changes.

Bibliography

1. P. W. Atkins, "Physical Chemistry.", 2nd ed. W. H. Freeman and Company, San Francisco, 1978.

2. K. M. Ervin and W. C. Lineberger, *in "Advances in Gas Phase Ion Chemistry"*, Vol. 1, (N. G. Adams and L. M. Babcock, Eds.), JAI Press, Greenwich, 1992.

3. J. C. Rienstra-Kiracofe, G. S. Tschumper, H. F. Schaefer III, S. Nandi, and G. B. Ellison, *Chem. Revs.***,** (2001, in press).

4. R. L. Schwartz, G. E. Davico, T. M. Ramond, and W. C. Lineberger, *J. Phys. Chem. A* **103,** 8213-8221 (1999).

5. G. E. Davico, R. L. Schwartz, T. M. Ramond, and W. C. Lineberger, *J. Phys. Chem. A* **103,** 6167-6172 (1999).

6. G. E. Davico, R. L. Schwartz, T. M. Ramond, and W. C. Lineberger, *J. Am. Chem. Soc.* **121,** 6047-6054 (1999).

7. G. E. Davico, T. M. Ramond, and W. C. Lineberger, *J. Chem. Phys.* **113,** 8852-8853 (2000).

8. T. M. Ramond, G. E. Davico, R. L. Schwartz, and W. C. Lineberger, *J. Chem. Phys.* **112,** 1158-1169 (2000).

9. J. V. Coe, J. T. Snodgrass, C. B. Freidhoff, K. M. Mc Hugh, and K. H. Bowen, *J. Chem. Phys.* **84,** 618 (1986).

10. A. A. Bengali, S. M. Casey, C.-L. Cheng, J. P. Dick, P. T. Fenn, P. W. Villalta, and D. G. Leopold, *J. Am. Chem. Soc.* **114,** 5257-5268 (1992).

11. L. M. Branscomb and S. J. Smith, *Phys. Rev.* **98,** 1028 (1955).

12. L. A. Posey, M. J. Deluca, and M. A. Johnson, *Chem. Phys. Lett.* **131,** 170-174 (1986).

13. R. B. Metz, A. Weaver, S. E. Bradforth, T. N. Kitsopoulos, and D. M. Neumark, *J. Phys. Chem.* **94,** 1377-1388. (1990).

14. C. Xu, G. R. Burton, T. R. Taylor, and D. M. Neumark, *J. Chem. Phys.* **107,** 3428 (1997).

15. D. L. Osborn, D. J. Leahy, D. R. Cyr, and D. M. Neumark, *J. Phys. Chem.* **104,** 5026 (1996).

16. L.-S. Wang, H.-S. Cheng, and J. Fan, *J. Chem. Phys.* **102,** 9480 (1995).

17. V. D. Moravec and C. C. Jarrold, *J. Chem. Phys.* **108,** 1804 (1998).

18. V. Zengin, B. J. Persson, K. M. Strong, and R. E. Continetti, *J. Chem. Phys.* **105,** 9740 (1996).

19. K. A. Hanold, C. R. Sherwood, M. C. Garner, and R. E. Continetti, *Rev. Sci. Instrum.* **66,** 5507 (1995).

20. Y. Negishi, T. Yasuike, F. Hayakawa, M. Kizawa, S. Yabushita, and A. Nakajima, *J. Chem. Phys.* **113,** 1725-1731 (2000).

21. A. Nakajima, T. Taguwa, K. Hoshino, T. Sugioka, T. Naganuma, F. Ono, K. Watanabe, K. Nakao, Y. Konishi, R. Kishi, and K. Kaya, *Chem. Phys. Lett.* **214,** 22-26 (1993).

22. M. Gausa, G. Gantefor, H. O. Lutz, and K. H. Meiwes-Broer, *Int. J. Mass Spectrom.* **102,** 227-237 (1990).

23. H. R. Siekmann, C. Luder, J. Faehrmann, H. O. Lutz, and K. H. Meiwes-Broer, *Z. Phys. D* **20,** 417-420 (1991).

24. H. R. Siekmann, E. Holub-Krappe, B. Wrenger, C. Pettenkofer, and K. H. Meiwes-Broer, *Z. Phys. B* **90,** 201-206 (1993).

25. M. Gausa, R. Kaschner, G. Seifert, J. H. Faehrmann, H. O. Lutz, and K. H. Meiwes-Broer, *J. Chem. Phys.* **104,** 9719-9728. (1996).

26. C. Luder and K. H. Meiwes-Broer, *Chem. Phys. Lett.* **294,** 391-396 (1998).

27. D. C. Harris and M. D. Bertolucci, "Symmetry and Spectroscopy." Dover Publications, New York, 1989.

Chapter 2

Description of experimental methods

2.1 Introduction

There are three primary sections to the anion photoelectron spectrometer, as shown in Figure 2.1. The first involves creation of the anions followed by the manipulation of the anion beam and mass selection. The second is the 364 nm cw laser whose beam intersects the anion beam perpendicularly to eject an electron. The third is the electron energy analysis and detection system. Detached electrons leave the molecule in all directions, but those traveling perpendicular to the anion and laser beams are kinetic energy-selected through a hemispherical energy analyzer and subsequently focused onto a position sensitive detector. The apparatus measures photoelectron intensity as a function of electron kinetic energy to produce a photoelectron spectrum.

2.2 Ion beam

The formation of a beam of anions begins with ion synthesis. There are two primary ion sources employed in this apparatus that may be used to create them: a microwave discharge in a flowing afterglow and a cold cathode sputtering source.

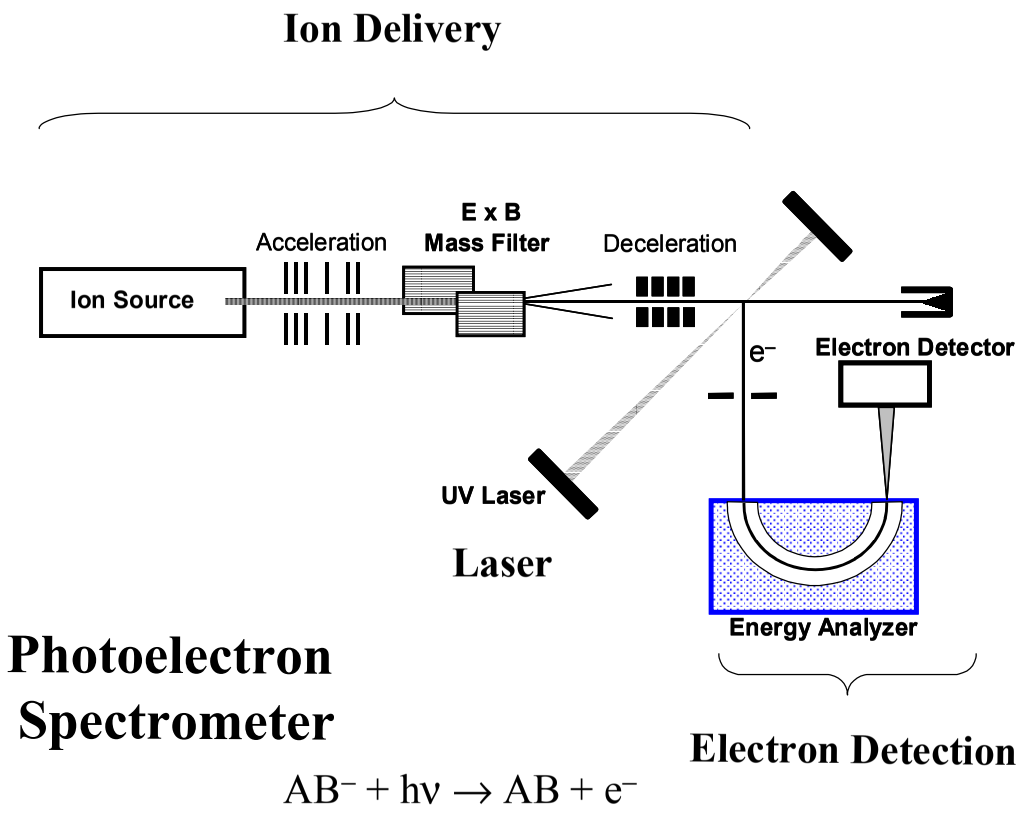

Figure 2.1. Schematic description of the main parts of the negative ion photoelectron spectrometer including anion creation and delivery, the UV laser system, and photoelectron energy analysis and detection.

2.2.1 Microwave discharge

The microwave discharge ion source was used in the creation of both the alkoxide anions and the peroxide anions, as it is generally used for creation of organic anions. A diagram of the apparatus is shown in Figure 2.2. To begin with, He buffer gas is injected through a microwave discharge as shown. The gas has been purified upon passage through a liquid nitrogen-cooled molecular sieve trap. A Tylan flow controller sets the helium flow at typically 6-7 standard liters per minute, although this number may be varied depending on the system studied. The microwave discharge takes place in a quartz cylinder around which a microwave resonant cavity fits. The cavity is powered by a 2.45 GHz microwave generator that ionizes and heats the gas into a plasma upon ignition with a Tesla coil. The cavity may be tuned with a ceramic tuning rod. The neutral plasma contains metastable He as well as He^+, He_2^+, and free electrons. A small amount of O_2 (7-10 cm^3 $minute^{-1}$) is also injected into the discharge at the same point as the He through a variable leak valve. In the microwave cavity, the O_2 collides with the free electrons to produce metastable O_2^- that then dissociates into O and O^-. The products are carried out of the discharge with the He buffer gas into the afterglow region. At this point they react with reagents that can be introduced into the system through one or two inlets at varying positions. For example, the reaction used to create the RO^- species (and equivalently, ROO^-) went as follows. Methane gas passes through a leak valve and is injected through an inlet positioned just after the discharge to form OH^-:

$$CH_4 + O^- \rightarrow CH_3 + OH^- \qquad (2.1)$$

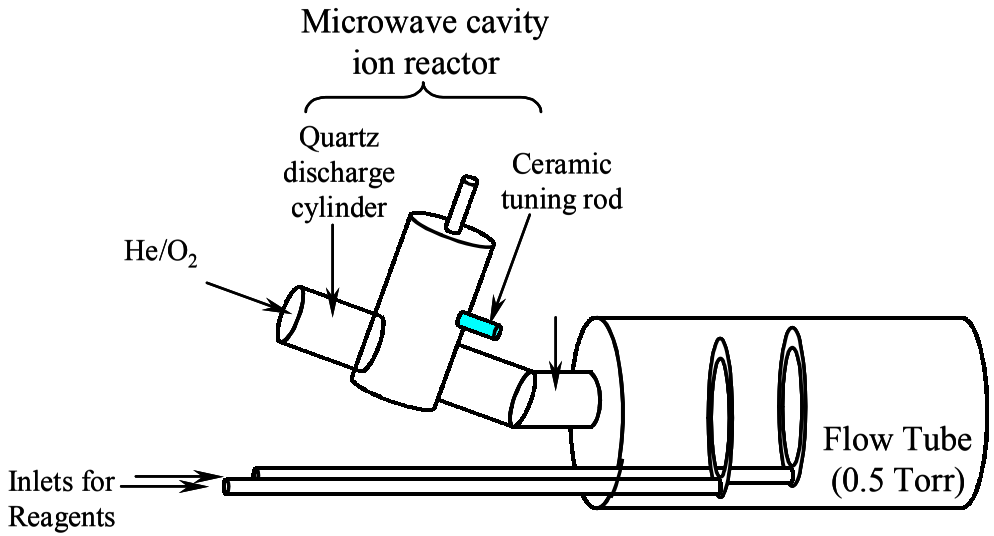

Microwave Discharge Source

Figure 2.2. The microwave discharge ion source. He and O_2 gas are injected into a 2.48 GHz microwave resonator which produces O^- and O_2^- anions. These anions can react with a variety of precursor gases introduced by inlets located further downstream to create the desired negative ion.

The second inlet is positioned further downstream. One end is attached to a test tube of liquid ROH. The vapor pressure is high enough to ensure a sufficient amount of sample present in the gas phase. The ROH gas travels into the flow tube through a needle valve and loses a proton to OH^- to form RO^-:

$$ROH + OH^- \rightarrow RO^- + HOH \qquad (2.2)$$

In order to maximize the production of the desired anion, gas flow rates, absolute and relative inlet positions, and source temperature may be varied.

2.2.2 Cold cathode DC sputter source

In order to efficiently create metal anions, a sputter source is employed. A diagram of the apparatus is shown in Figure 2.3.

The sputter cathode is held at the end of an approximately 30 cm long stainless steel rod of 1/8″ outer diameter. The cathode is located on the axis of the flow tube. The rod is surrounded by a glass cylinder of ¼″ outer diameter that serves to electrically insulate it from the flow tube. On the end inside the chamber, a metal holder is attached with set screws onto the rod. In turn, the other end of the metal holder supports the metal cathode rod. High purity (≥ 99.95 %) metal cathode rods (Goodfellow) of about 2 mm diameter and 5 cm length Ni, Pd, or Pt were used. Around the holder a glass shield is fit in order to prevent arcing between the sample

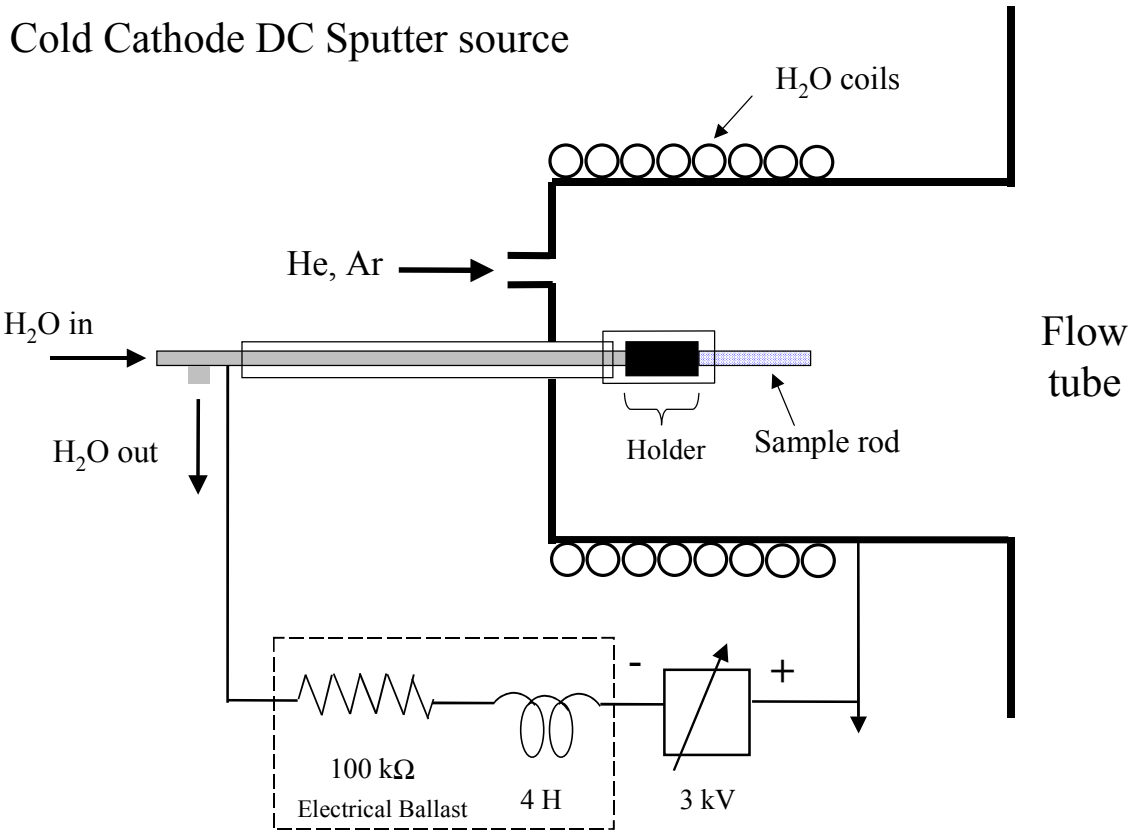

Figure 2.3. Schematic of the cold cathode DC sputter ion source. A sample metal is attached to a stainless steel water-cooled holder that is biased at a few thousand volts and is electrically isolated from the grounded flow tube. Argon gas is leaked into the system, is accelerated to the rod, and anions are sputtered off upon impact.

and the chamber walls. An open loop water cooling system is employed to reduce the temperature of the sample. The stainless steel rod is hollow and inside it fits a smaller stainless steel rod. Water flows in through the smaller rod to the tip inside the chamber, then returns between the concentric rods and exits the system as shown in the figure. In addition, the entire source region is wrapped in copper tubing through which cooling water flows. The stainless steel rod is negatively biased through a variable power supply in series with an electrical ballast consisting of a 100 kΩ resistor and a 4H inductor. The ballast is designed to add resistive elements to limit current surges in the event of arcing between the cathode and the grounded chamber walls. Typical bias voltages for the cathode are roughly -1500 V and the discharge current is about 15 mA. Helium buffer gas prepared as described above is seeded with typically 10-20 % argon and flows into the chamber near the sample. The high bias of the cathode creates a strong electric field with respect to the grounded walls of the chamber that is sufficient to ionize the neutral Ar. The Ar^+ is then accelerated by the electric field and collides with the cathode. Neutrals and charged atoms, as well as dimers, trimers, etc. of the sample metal, are sputtered off the rod. O_2 may be introduced in the same manner as described above to form metal monoxides, dioxides, etc.

Once created via microwave discharge or sputtering, the anions proceed through the flow tube as shown in Figure 2.4 and are thermalized via 10^4-10^5 collisions with the helium gas. In the flow tube, most of the He is pumped away by a Roots pump operating at 300 l/s which maintains the region at a pressure of approximately 0.5 Torr. The flow tube is surrounded by a dewar in which liquid

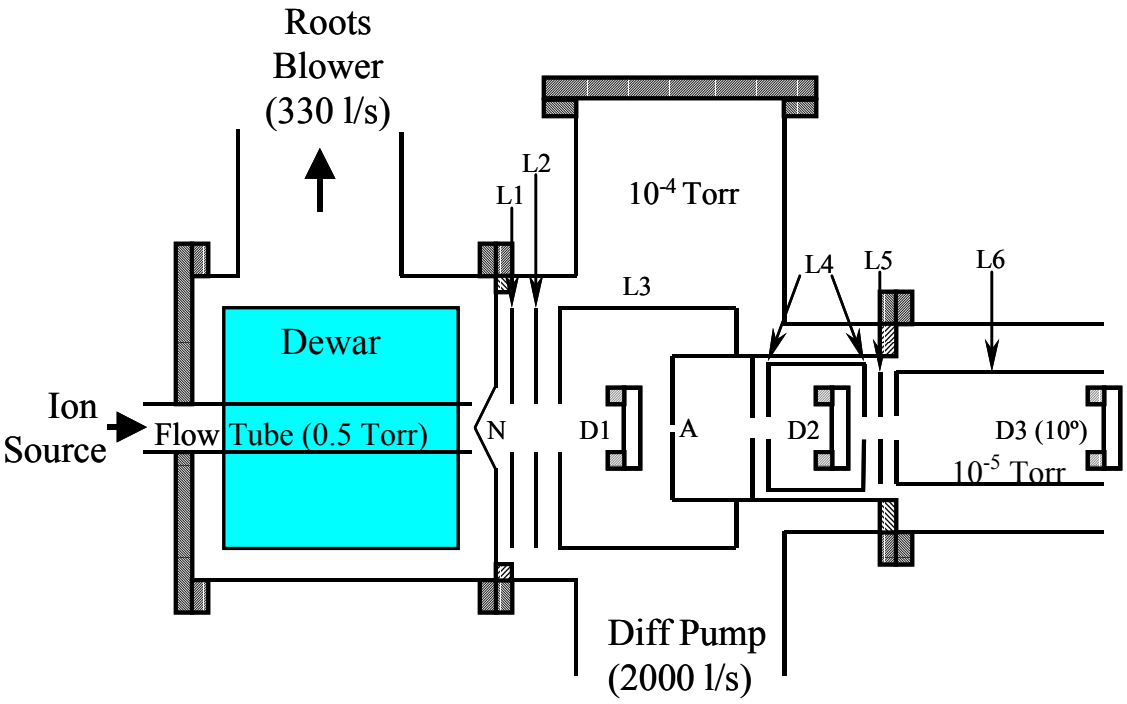

Flowing Afterglow and Ion Optics

Figure 2.4. Schematic of the flowing afterglow and the first section of ion optics before the mass analyzer. "N" stands for nosecone, "D" indicates a deflector, "A" indicates an aperture, and "L" indicates an einzel electrostatic lens. Ions created in the source region undergo collisional relaxation in the flow tube filled with helium buffer gas. The ions are gently extracted into a differentially pumped region and are shaped into a beam and accelerated with ion electrostatic optics.

nitrogen (LN_2) may be introduced. The helium buffer gas thus collides with the liquid nitrogen-cooled walls and thermalizes to LN_2 temperature and subsequently the sample is cooled through collisions with the cold helium. In the case of the microwave discharge source without the liquid nitrogen, the sample is thermalized to room temperature and with the LN_2, the sample is cooled to around 200 K. However, the sputter source creates much hotter ions than the microwave discharge and collisions with the helium thermalize the ions to higher final temperatures (< 500K).

Cooling of the flow tube is a highly valuable tool in photoelectron spectrum analysis. Comparison of a spectrum taken at different sample temperatures is a definitive way to identify peaks that depend on the temperature of the sample, i.e. hot bands. For example, the electron affinity (*EA*) is the 0_0^0 transition from anion to neutral. The same transition originating from a vibrationally excited state in the anion would appear to the lower binding energy side of the electron affinity. It is not always obvious which peak is the *EA* or if there is a hot band. If upon cooling the sample to 200 K the intensity of the lower binding energy peak diminishes with respect to the other peak, one may assign the *EA* with confidence.

The anions are gently extracted through a roughly 1 mm aperture in a nosecone at the end of the flow tube (labeled 'N' in Figure 2.4) with a small positive voltage (< +1 V). They then pass into a differentially pumped region where they are accelerated, focused into a beam, and deflected through a system of electrostatic lenses. These are indicated schematically as the letters L, D, and Q in Figures 2.4 and 2.5. The first lens is an einzel lens, denoted by an 'L'. It is a biased flat plate with a hole in the center that serves to accelerate and focus the beam. The 'D' elements are

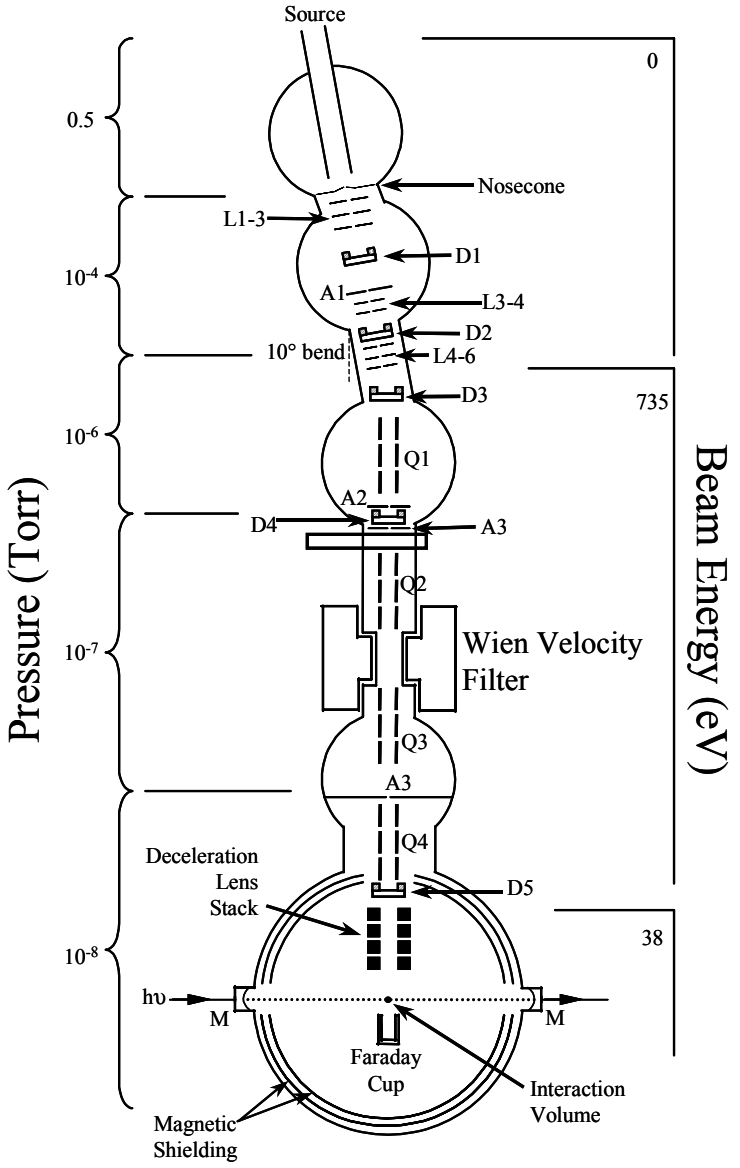

Figure 2.5. Diagram of the entire ion beam line from the source region to the Faraday cup. "D" indicates a deflector ion lens, "A" indicates an aperture, "Q" signifies a quadrupole electrostatic lens element, "L" indicates an einzel electrostatic lens, and "M" indicates interaction cavity mirrors. The ion beam is extracted from the source region, accelerated, mass selected in a Wien velocity filter, and decelerated into the region of interaction with the laser beam.

deflectors, formed by two horizontal bars and two vertical bars, which further accelerate and steer the beam. By the time they reach the last einzel lens, L6, the ions have been accelerated to 735 eV kinetic energy. A 6″ diffusion pump operating at a rate of 2000 l/s maintains the chamber at about 10^{-4} Torr at the nosecone to around 10^{-6} Torr at the opposite end. The acceleration to 735 eV is done gradually through this region so as to avoid collisional excitation in these higher pressure areas. At the third deflector, D3, there is a 10° bend in the beam direction. The anions are guided through the bend while any remaining neutrals collide with the walls and are pumped away. The ions pass into the next chamber pumped by a second diffusion pump (8″) that maintains the pressure at 10^{-6} Torr. Here, there is a quadrupole lens, Q1, which is formed by four rods positioned symmetrically about an axis through which the ion beam travels. The quadrupoles serve to further deflect and shape the beam. The beam is navigated through a plate with an aperture A2. At this point the anions that miss the aperture collide with the plate and their current is measured on an electrometer.

2.3 Mass selection

Products of the ion source region will include many more species than the one intended for photodetachment. In order to secure an ion beam of an unambiguous identity, a Wien mass filter is placed in the beam path. The filter works with perpendicular electric and magnetic fields (E and B) that produce an electric force (F_E = qE, where q is the charge) on the ions normal to the beam direction, and a magnetic

force (F_M = qvB, where v is the velocity of the anion) in the opposite direction from the electric force. The magnetic force is related to the mass of the ion, since v = $(2KE/m)^{1/2}$ where KE is the kinetic energy of the ion (735 eV) and m is the mass. When the two forces are equal for the desired mass they cancel and the selected ion species passes out of the mass filter undeflected. This happens for mass m= $2KE(B/E)^2$. All other ions not of this mass will suffer a net force up or down and thus be deflected out of the beam. If the electric force is kept constant, the magnetic force can be changed to mass-select different species. If the magnetic force is varied monotonically, a mass spectrum of ion species abundance versus ion mass can be generated in order to investigate the products created in the flow tube chemistry.

The Wien mass filter gives a mass resolution of $m/\Delta m$ approximately 40. Therefore for higher mass species one cannot resolve between M and M-1 species, for example. However, an advantage to this mass selection apparatus is that if the electric and magnetic fields are turned off, one regains the full ion beam, which can be useful for diagnostic purposes.

Once the ions of desired mass have left the Wien filter, they are guided into the interaction region, which is pumped down to 10^{-8} Torr by two ion pumps. In this region deceleration lenses slow the beam to 38 eV to maximize the interaction time with the laser. At the center of the interaction region the ion beam crosses the laser beam and then continues on to terminate in a Faraday cup. The current in the Faraday cup is read on an electrometer and is recorded in the lab book. The magnitude of the ion current depends on the species investigated and the ion source employed. Currents of one nanoamp of O^- are possible while for both the RO^- and ROO^-

systems, beams of several tens of picoamps are more typical. For sputtered systems, smaller currents of order a few picoamps are common.

2.4 Ultraviolet laser system

The near uv laser system used in the photoelectron spectroscopy apparatus consists of a fixed frequency 364 nm argon ion continuous wave (cw) laser whose output is steered through a buildup cavity where it is maintained in resonance via an electronic servo system. A diagram of the laser system is shown in Figure 2.6. A very detailed treatment is given in Ref. (*1*); however, a more conceptual overview is presented here.

There are two main parts to the laser system: the laser itself and a separate power buildup cavity where the laser intersects the ion beam. We start by discussing the laser itself. We use a Spectra Physics Argon Ion model 2045 operating at a single 364 nm near-uv line. The laser consists of four primary elements: an end mirror, an output coupler, the Ar gas, and an etalon. The back mirror has been adapted from the usual stationary mirror into a broadband UV flat reflector that is mounted on a piezoelectric transducer stage. The position of the stage can be translated along the laser cavity axis to lengthen or shorten the cavity. The 364 nm output coupler is mounted at a fixed position at the other end of the laser cavity. The two mirrors define a length L of the cavity. Only when the cavity length equals an integer number of half-wavelengths, $L = n\lambda/2$, where n is an integer, can radiation of wavelength λ_L be sustained inside the cavity; all other wavelengths will dissipate (*2,3*).

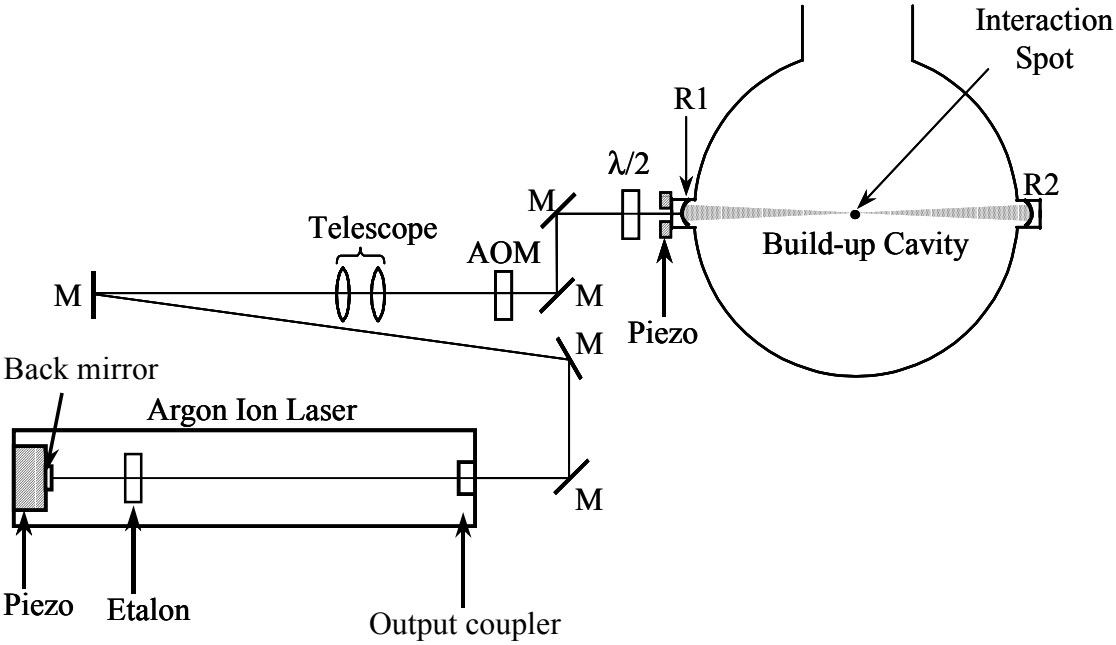

UV Laser System

Figure 2.6. Diagram of the UV laser system. In the drawing, "M" represents mirror elements, and "R" indicates highly reflecting cavity mirrors. The system consists primarily of an argon ion laser and an external intensity build-up cavity. The back mirror of the laser and the front mirror of the build up cavity are mounted on piezoelectric stages. Together with an acousto-optic modulator (AOM) and various electronics, these stages form a servoamplifier system designed to amplify the laser output intensity inside the build-up cavity.

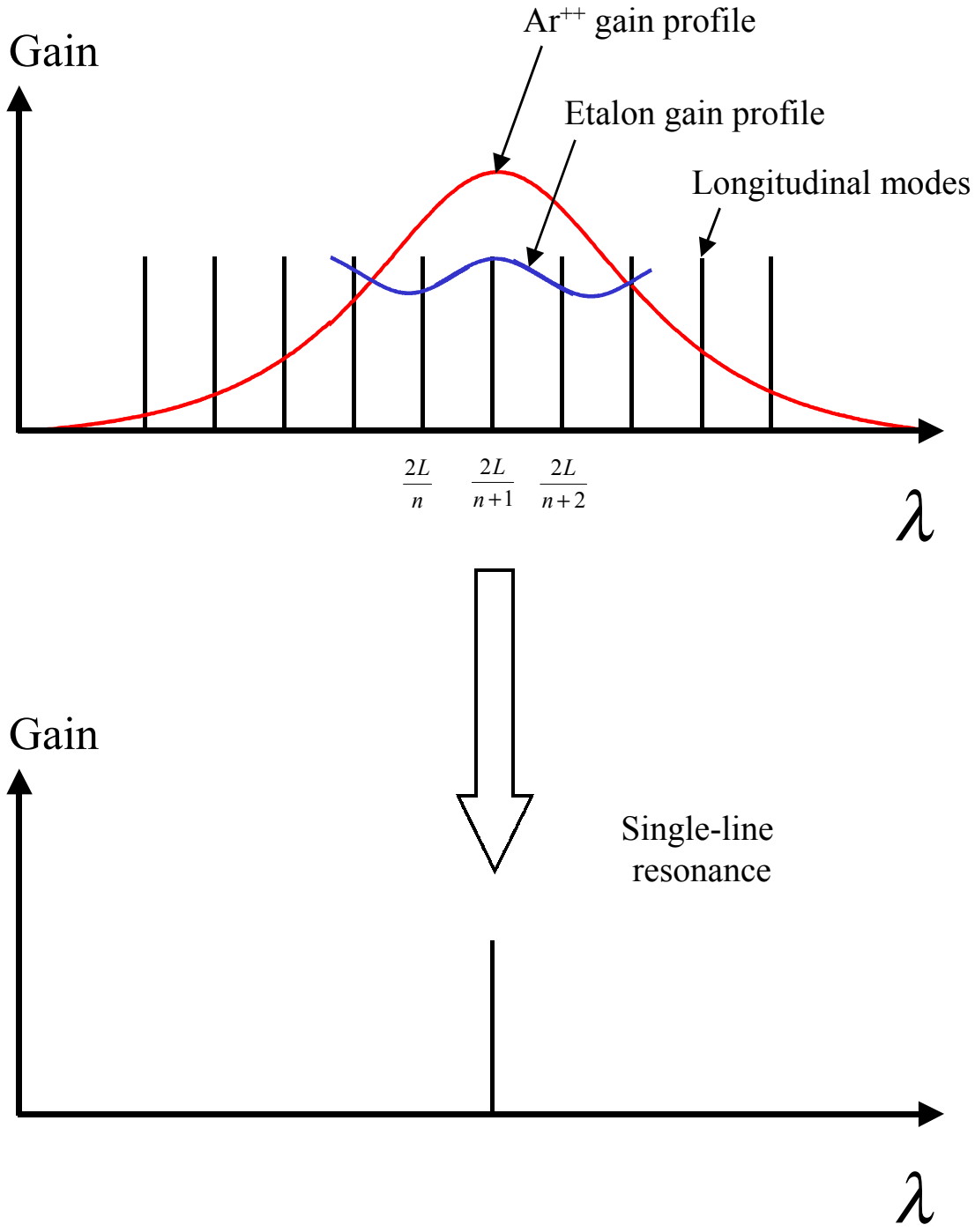

Figure 2.7. Single-mode operation of a cw laser. The Doppler-broadened gain profile of the Ar^{++} gas overlaps with the comb of allowed longitudinal modes for a laser with cavity length L. An etalon is incorporated into the laser cavity to select a single resonance line.

Equivalently, only wavelengths where $\lambda_L = 2L/n$ will resonate in the laser cavity. These resonant wavelengths, or longitudinal modes, are indicated in Figure 2.7.

The laser cavity is filled with Ar gas. An intense discharge in the laser capillary tube doubly ionizes the gas. The output coupler and back mirror optics select a single lasing transition of Ar^{++} that is doppler-broadened due to the high temperatures during operation. This results in a specific gain profile for the medium, which is superimposed upon the longitudinal modes in Figure 2.7. The region where the two overlap determines the lasing modes for the cavity. The number of resonating modes can be reduced to one using a around 1 cm thick frequency-restricting etalon placed between the two end mirrors. The gain profile of the etalon is such to be able to select a single mode to resonate, as illustrated in the figure.

The second main part of the laser system is a buildup cavity. The argon ion laser typically outputs 1 W of single frequency power at 364 nm. This alone is not enough to detach workable intensities of photoelectrons from picoamp ion beam currents and therefore prohibits working intracavity. Thus the laser beam intensity is amplified in an external buildup cavity. The idea is to match the buildup cavity length to the laser output wavelength using the same idea as for laser cavity resonance. The buildup cavity has two highly reflecting mirrors: R1 = 99.6 % and R2 = 99.8% in Figure 2.6. R1 and R2 define a cavity length L_{BC}. In order for the laser output wavelength, λ_L, to resonate and thus be amplified in the cavity, one must have $\lambda_L = 2\ L_{BC}/n$.

The length of the cavities L and L_{BC} can change slightly for various reasons: thermal fluctuations as well as acoustic noise due to the Roots pump or building

noise, etc. To respond to all these length fluctuations in order to maintain the condition $\lambda_L = 2L_{BC}/n$, an electronic servoamplifier system has been incorporated into the laser setup. There are three main elements to the servo system, which are all connected through various electronics. One element is the back mirror of the laser that can change the laser cavity length L and thus λ_L. Another is the front mirror in the buildup cavity that is mounted on piezos that change the cavity length L_{BC}. The third element is an acousto-optic modulator (AOM) placed in the beam path before the interaction region.

The AOM is an integral part of the servo system used to lock the laser radiation to the buildup cavity. It is comprised of a transducer connected to a block of quartz glass and vibrates back and forth to produce a standing wave in the medium. This wave acts as a Bragg diffraction grating for the incoming laser beam (364 nm is about 800 THz). The diffraction produces a beam that has been Doppler shifted by an amount equal to the acoustic frequency in the glass. Therefore the first order diffraction of the beam is shifted by a constant bias, between 55-85 MHz. The output first order beam is different from the input beam by this amount, and if the transducer frequency is varied by a small amount on top of the beam frequency, a small dither (around 1 MHz), or frequency jitter about the laser frequency + bias is superimposed on the beam.

The output of the AOM can therefore be thought of as {800 THz + (55-85) MHz} ± 1 MHz. This frequency modification serves two purposes. First, the 55-85 MHz constant frequency shift is employed to frequency isolate the two resonance cavities. This way, none of the beam reflected from the buildup cavity will return to

the laser cavity and produce interference since before and after the AOM the beam has different frequencies by an amount shifted out of the resonance range of the laser cavity. Second, the frequency dither (± 1 MHz) serves to vary the frequency of radiation entering the interaction chamber by a small amount about the exact resonance frequency. The reflected light off the cavity front mirror is monitored by the servoamplifier electronics. Assume the frequency is exactly on resonance. As the frequency is dithered slightly away from this resonance frequency, the system will begin to come out of resonance, resulting in an increase in light reflected by the front mirror. The electronic response will come in some combination of adjusting the cavity lengths L or L_{BC} or varying the AOM frequency accordingly so that the buildup cavity resonance is recovered. When this is done properly, all cavity lengths are maintained such that there is a permanent state of resonance in the buildup cavity. This is known as "locking" the laser. When locking is achieved, laser power is increased by a factor of 150-200.

2.5 Electron detachment and angular distributions

In the center of the laser buildup cavity, the ion and laser beams intersect. At this point, the laser beam is approximately ten times narrower (about 0.1 mm) than the ion beam (around 1 mm). Photoelectrons are detached and are ejected in all directions in the chamber. The eKE analyzer is located below the interaction region. Thus the direction of photoelectron detection is fixed in space. We cannot rotate the detector about the interaction point to monitor the angular distribution of

photoelectrons. However, we effectively do the same thing by varying the polarization of the laser interacting with the molecules. This is done with a half-waveplate (λ/2) placed in the beam path after the AOM and before the interaction region in Figure 2.6. Here 0° is defined as the electron detection direction, perpendicular to the laser beam/ion beam plane. The waveplate is calibrated using the angular distribution of O^-, whose photoelectrons are heavily peaked in the horizontal direction.

In the ion beam delivery, no effort is made to spatially orient the molecules, therefore in the case of molecules with non-zero dipole moments, they cross the interaction point with a random spatial distribution of dipole moments. The waveplate selects an orientation of the laser electric field. One may imagine, therefore, that molecules with electric dipoles oriented parallel to the laser electric field will preferentially absorb the radiation while molecules whose dipole moment is perpendicular to the polarization direction will not absorb. Thus to sample the entire angular distribution of photoelectrons one has only to rotate the laser polarization through 90°. Of course, there is a $\cos\theta$ effect since the proportion of molecules which absorb the radiation vary with $\cos\theta$, where θ is the angle between the laser polarization and the dipole moment of the molecule. However, it has been worked out (*4*) that in the dipole approximation the angular distribution of photoelectrons follows the equation

$$\frac{d\sigma}{d\Omega} = \frac{\sigma_{tot}}{4\pi}(1+\beta P_2(\cos\theta)), \qquad (2.3)$$

where $P_2(\cos\theta)$ is the second Legendre polynomial

$$P_2(\cos\theta) = \frac{1}{2}(3\cos^2\theta - 1). \qquad (2.4)$$

The β factor is the asymmetry parameter and ranges between $-1 \le \beta \le 2$. The angular distribution of a peak in the photoelectron spectrum of a molecule is directly related to the symmetry character of the orbital from which the photoelectrons originate. This is most easily demonstrated starting with the case of atomic photoelectron detachment. If a photon detaches an electron from an s-orbital, it imparts one unit of angular momentum to the system, and that photoelectron departs in the form of a p partial wave. A p partial wave has an angular distribution of $\cos^2\theta$. Such behavior for $d\sigma/d\Omega$ is achieved if β has a value of 2. If a photon detaches an electron from a p-orbital, the single quantum of angular momentum can add or subtract, yielding either s-waves or d-waves. However, if the photon energy is close to the threshold for detachment, the s-wave channel will be preferred. An s partial wave is isotropic, and requires that $\beta = 0$. As the photon energy increases, mixing between s and d partial waves occurs, and the angular distribution moves to $\sin^2\theta$, achieved when $\beta = -1$.

For molecules, the physics is not as clear-cut. In some cases, the symmetry of molecular orbitals can be reasonably approximated by atomic orbitals; however, in others (for example if the orbital is involved in bonding), the orbitals can mix together characters from two or more atomic orbital components. It is difficult to make generalizations about the angular distributions from detaching electrons in

molecular orbitals. The exception to this is that a very positive β (>1) may still be considered the signature of detaching from a σ-like orbital.

Thus measuring the asymmetry parameter can lend insight into the symmetry of the detached electron. This is particularly useful for identifying different electronic states. Frequently, transitions to the ground and excited states of the neutral require detaching different types of electrons. In these cases, peaks belonging to the different electronic states will exhibit contrasting angular distributions and are readily identified as such.

In this experiment, it is the large contrasts in β which provide us with clues for spectrum analysis. Thus we limit ourselves to only sampling β at two different polarization angles, and β is calculated through the relation

$$\beta = \frac{I_0 - I_{90}}{\frac{1}{2} I_0 + I_{90}} \tag{2.5}$$

where I_0 is the photoelectron intensity of the peak at 0° laser polarization angle and I_{90} is the intensity at 90° laser polarization. We also record spectra when the polarization angle is set to the 'magic angle', θ_{MA}, which is defined as

$$P_2(\cos\theta_{MA}) = \frac{1}{2}(3\cos^2\theta_{MA} - 1) \equiv 0. \tag{2.6}$$

This condition is fulfilled for an angle $\theta_{MA} \cong 54.7°$. At this angle, the photoelectron angular distribution is independent of laser polarization angle and is proportional to the total cross section for detachment, σ_{tot}. More importantly, recording a spectrum at either polarization extremes (0° or 90°) frequently results in electronic states with little or no electron detachment (for all electronic transitions without an isotropic angular distribution). Taking a spectrum at θ_{MA} ensures that some amount of signal is recorded from all detectable transitions.

2.6 Photoelectron detection

A diagram of the photoelectron kinetic energy analyzer is displayed in Figure 2.8. The diagram is oriented with the ion beam in the plane of the paper and the laser beam directed into the page. The detached electrons leave the interaction spot in different directions at different kinetic energies. Only those which travel through an acceptance cone of 5° half angle directly downward enter the detection apparatus. It is comprised of an input stack of electrostatic lenses (V1-3 and V_{HC}) leading to a hemispherical electron energy analyzer, then an output stack of lenses (V_{HC} and V4-6) and finally a position sensitive detector. Lenses V1 and V2 serve to accelerate the electrons by a factor of roughly 5-10. The voltage on V3 is computer-controlled. It is a function related to the electron kinetic energy being measured at the moment. This function is determined during the tungsten calibration discussed in the data analysis section. The V3 voltages are selected to be those which best focus the electrons onto the center of the hemispherical analyzer opening at a given electron kinetic energy.

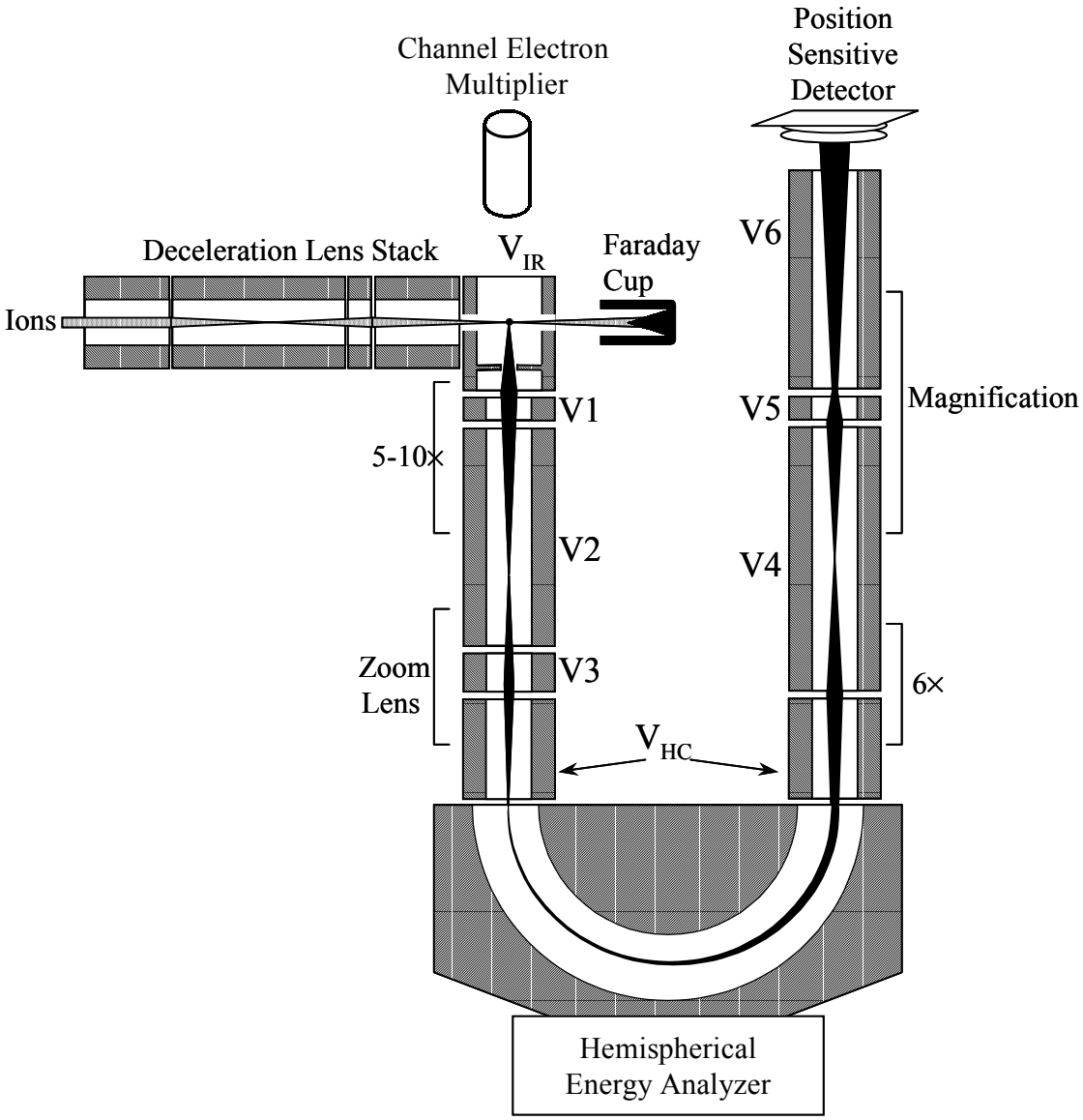

Figure 2.8. Schematic of the electron kinetic energy analyzer. The laser beam is directed into the page. The desired kinetic energies are selected using a hemispherical analyzer together with acceleration and positioning voltages (denoted "V") and the photoelectrons are measured on a position sensitive detector.

V_{HC} is the Herzog corrector voltage that is employed to compensate for fringe fields surrounding the entrance and exit to the charged hemispherical analyzer.

The hemispherical analyzer serves to select a single electron kinetic energy. It is composed of two hemispheres of OFHC copper, each with a constant voltage applied to it. The two hemisphere voltages define a central transmission energy, T_E, such that only electrons with kinetic energy equal to T_E (plus or minus some small spread in energies) will successfully travel through the analyzer. Electrons with higher or lower energies will collide with the walls of the hemisphere. Without acceleration or deceleration of electrons into the analyzer, only one electron kinetic energy, T_E, will be measured. To pass an electron of a different kinetic energy, that electron can be accelerated (or decelerated) to the transmission energy and passed through and recorded. Thus in order to scan through a range of electron kinetic energies, the input lens acceleration voltages step through values to scan through the desired spectrum energy limits. A more detailed description of hemispherical energy analyzers may be found in reference (*5*).

The kinetic energy-selected electrons pass through the analyzer with about 2 eV transmission energy. They must be accelerated to the detector for maximum detection efficiency at around 300 eV. V_{HC} and V4 accelerate the electrons by a factor of 6 with no magnification. The final voltages (V4,V5,V6) serve as a zoom lens, accelerating the electrons to 300 eV and magnifying their image by a factor of 5 to maximize use of the face of the detector. The typical energy resolution of this apparatus is 5-10 meV.

Finally, a channel electron multiplier (CEM) electron detector is positioned above the interaction spot. This is a Amptektron MD-502 ceramic CEM housed in a cylinder 3.81 cm in length and 1.905 cm diameter, with a 3.6 mm acceptance aperture. The CEM signal is passed out of the vacuum chamber, into amplifier electronics, and then directly to a digital counter for diagnostic purposes.

2.7 Position sensitive detector

During the summer of 2000, the position sensitive detector was upgraded to a higher gain device with five microchannel plates. This detector replaced the previous one with only two microchannel plates (*6*). The new detector is a Quantar Technology 3318A microchannel plate/resistive anode encoder (MCP/RAE) sensor including 10-bit digitized output (2412B). This hardware is installed inside the interaction chamber at ultra high vacuum. Outside the chamber it interfaces with a 2401 Preamp module, a 2401B Position Analyzer, and a 2412B Histogramming Memory Buffer (see Figure 2.9).

The MCP/RAE sensor is comprised of five wafer-type microchannel plates (MCPs) followed by a resistive anode. A MCP is an approximately 1mm thick plate comprised of a honeycomb of electron multiplying channels. In model 3318A, the MCPs have an 18 mm diameter active area. Since each channel is about 10 μm in diameter, this gives approximately 10^6 channels per plate. Each channel operates along the same principles as an electron multiplier (*5*). The channels are lined with a series of electrodes in alternating positions on either side of the channel. The

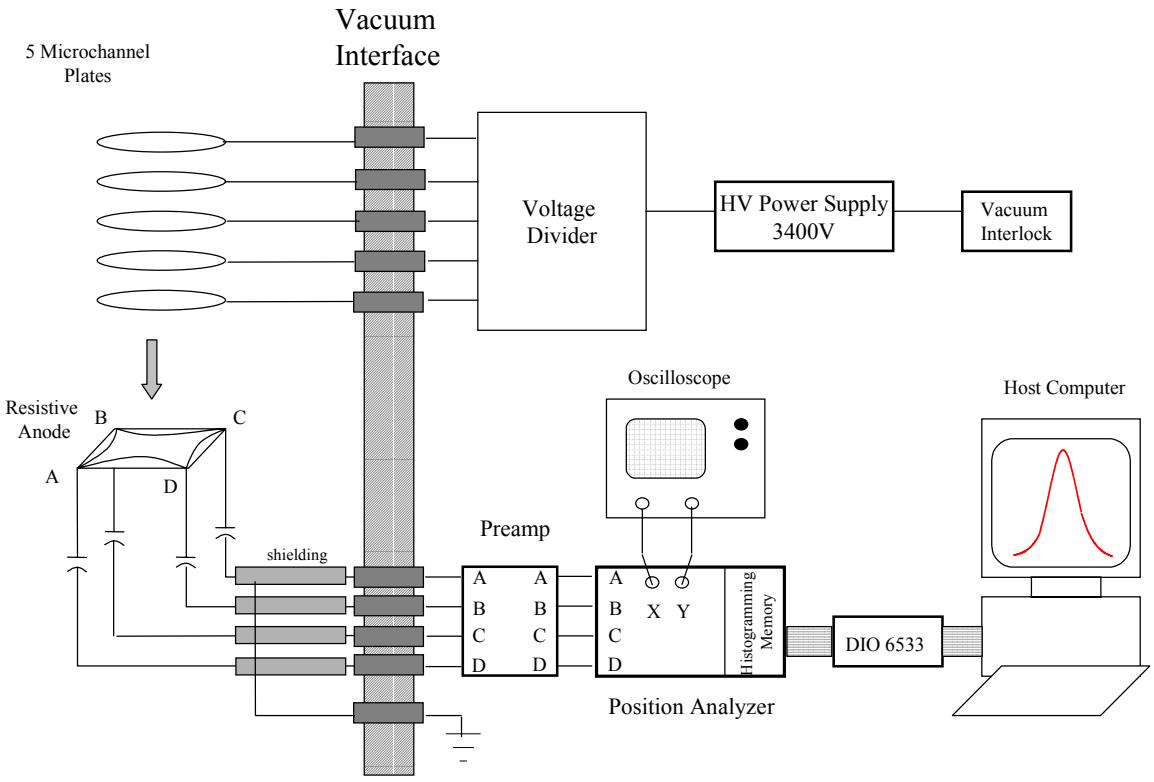

Position sensitive detector and supporting electronics

Figure 2.9. Diagram of the primary elements involved in the photoelectron position sensitive detector and associated electronics.

electrons multiply in a cascading effect: an incident electron hits an electrode in the channel, secondary electrons are produced and collide with the electrode on the opposite side, etc., until they exit the MCP. The incident electrons must hit the first MCP with enough energy to initiate the cascade process, thus the need for photoelectron acceleration in the output lens stack to 300 eV. Each of the MCPs is biased at successively higher voltages so as to propagate the avalanche of electrons through the MCPs. As the electron avalanche proceeds through 5 MCPs the cloud expands and overflows into neighboring microchannels due to space-charge repulsion. However, the channels are small enough such that the final electron cloud produced is resolved as a single localized event when it hits the resistive anode. A Bertan 205B-05R high voltage power supply operating at 3400 V connects to a voltage divider network that supplies the five leads into the chamber. Multiplication through 5 MCPs provides 5 x 10^7 gain in signal, up a factor of 10 from the previous detector with only 2 MCPs.

Once the electrons exit the MCPs, they collide with a resistive anode (see Figure 2.9). This is a metal plate in a "warped" rectangular shape with a circular effective detection area. Electronic leads are connected to each of the four corners (A, B, C, and D). When the electron cloud hits the anode in a specific position, a current is measured at each of the leads that is proportional to the center of gravity of the electron charge pulse. After signal processing in the position analyzer, the X and Y outputs are calculated as

$$X = \frac{B+C}{A+B+C+D},\ Y = \frac{A+B}{A+B+C+D} \tag{2.7}$$

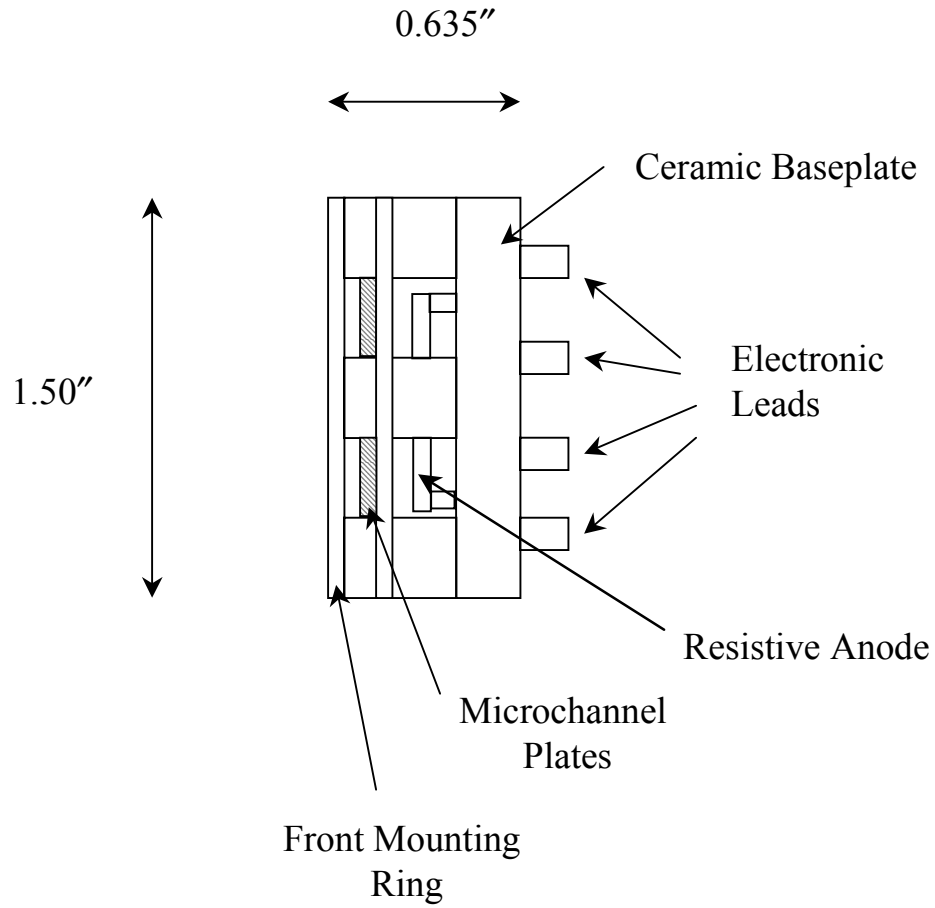

MCP/RAE assembly, side view

Figure 2.10. Multichannel plate/resistive anode encoder assembly, which comprises the position sensitive detector. The detector consists of five multichannel plates placed directly before a resistive anode encoder. The current incident on the plates is amplified and the position information regarding where the emerging electron cloud collides with the resistive anode is passed to signal processing electronics.

The detector yields a FWHM for each resolvable pulse as 1/400 of the sensor diameter. Furthermore, the output is given in a 10-bit digitized form in both X and Y axes.

The MCP/RAE components are held in place on a spring-loaded assembly that is screwed into a 1.5″ diameter ceramic baseplate containing all electrical leads (see Figure 2.10). The 001/SE extra electrically-isolated front ring allows for mounting the assembly from the front as opposed to the rear baseplate. This housing is placed at the very end of the output lens stack such that the first MCP is flush with the end of the output lens stack. The sensor leads are capacitively decoupled and shielded, which is necessary to prevent arcing due to the high voltages applied. The four leads exit the chamber and enter a preamp that amplifies the signals and converts the low-level pulses to high-level shaped bipolar pulses that can be digested by the position analyzer.

The position analyzer accepts the output from the preamp module and converts this into both analog and digital forms of position information as well as other signal event information described below. The position analyzer outputs analog X and Y position. These signals connect directly into an oscilloscope for real-time monitoring of electron flux. Dials on the front panel of the position analyzer allow one to mask out a section of the detector. This is useful to avoid processing "hot spots" into the data, or spots on the detector that produce false events. Hot spots are created when the plates are permanently damaged by arcing to a localized position on the detector. Given the high voltages at which the microchannel plates are biased,

the MCP power supply is interlocked to cut the power in the event that the pressure goes above a certain level if, say, an ion pump shuts off.

The analyzer also outputs various digital pulses related to an electron detection event. When no histogramming memory is installed in the analyzer, these outputs may be connected directly to a computer for the purposes of handshaking and data transfer. The X and Y positions are output in digital format on a 50-pin Amphenol ribbon-type connector on the rear of the position analyzer box. Pins 1-10 output the 10 bits of Y axis position information while pins 11-20 output the available 10 bits of X axis position information. Pin 21 of the connector outputs a digital STROBE pulse while pin 22 outputs digital RATE information. The digital STROBE pulse is a TTL high-to-low edge produced upon the completion of analog to digital conversion of a single detection event. This pulse communicates with an external computer to signal that position information is available to be read ("read-me" signal). The digital RATE pulse is a TTL low-to-high edge produced for every event incoming to the analyzer box with the only criterion being that the event is time-separated from a previous event by 400 nsec. Thus some of the events counted as a RATE pulse may be rejected by the analyzer electronics for not meeting various digital pulse criteria. While a STROBE pulse indicates an event that has met these criteria and thus has been fully processed by the analyzer electronics, the RATE pulse indicates an incoming event to the analyzer. A comparison of the two pulses can determine the ratio of input to output events from the analyzer. The RATE signal may be observed on the front panel meter.

Incorporated inside the position analyzer box is a 2412A Histogramming Buffer Memory card. This serves as an alternative method of interfacing the accumulated data with a computer. Instead of transferring every detected event directly to the computer as it is processed in the analyzer, the events are accumulated within the data buffer and then transferred all at once to the computer. This significantly decreases and simplifies the amount of handshaking and interaction with the host computer, freeing it for other activities.

The output of the position analyzer is read directly into the histogramming memory (HM). Once the HM receives a strobe pulse from the analyzer, it reads the 10-bit X axis information and the 10-bit Y axis information. In other words, each single processed event correlates to a 20-bit word of position information. 10 bits of X axis information means that the X axis is interpreted as having $2^{10} = 1024$ divisions to it. The 10 bits are binary, read from right to left as most significant bit (MSB) to least significant bit (LSB). This corresponds to position information in the following way. The first bit, the MSB, divides the axis in two equal sections. A '1' value for the MSB corresponds to residing in the right half of that division, say, whereas a '0' value corresponds to a location in the left half. The next most significant bit divides the total axis into four equal sections, thus dividing the right half into two. A '1' for this second bit indicates a location in the right half of that division, i.e. the right-most quarter. This is repeated into finer and finer divisions for the full 10 bits. For example, 3 bits divides an axis into $2^3 = 8$ divisions. The word 001 indicates a position anywhere within the 5^{th} division from the left. Obviously, better position resolution requires more bits of information.

While the detector and position analyzer divide the X and Y axes into 10-bits of position information each, the 2412B Histogramming Memory can only process 12 bits total. The user has discretion to appropriate those bits in any manner deemed desirable (i.e., 12 bits in X and 0 bits in Y, or 4 bits in X and 8 bits in Y). In photoelectron spectroscopy, the X axis is the energy dispersion axis and the Y axis is simply a spatial representation of where the electron hits the detector. In the end, we will sum over all y positions to obtain the number of events versus x position (related to electron kinetic energy). Therefore, much more resolution is necessary in the X axis than the Y axis and so 8 bits are assigned to the X axis and the remaining 4 are assigned to the Y axis. This is an improvement over the 7-bit resolution in the energy axis available from the previous detector.

The HM divides the effective detector area into a grid of $2^8 = 256$ divisions in X and $2^4=16$ divisions in Y, or $2^{12}=4096$ boxes total. As each event arrives from the position analyzer, the HM increments a tally of the number of hits for the appropriate square of the grid. At the end of the accumulation time interval designated by the host computer, the HM outputs the integrated number of hits for each grid division. This occurs as a succession of $2^{12}=4096$ digital numbers (one for each grid element) of the HM digital output: each read is a digital number corresponding to the total number of hits recorded within a grid division during the time interval.

The HM buffer space is divided into two "pages". The HM switches back and forth between the two for writing and reading data. For example, the HM will write data to page 1, transfer the data to page 2 and read from page two, write to page 1,

etc. To avoid writing over data, every read is destructive. In other words, reading the data out to the computer simultaneously erases the buffer page.

When taking a spectrum, timing is crucial. All the timing functions are controlled from a LabVIEW 6i program entitled PESDAT running on a MS Windows NT platform on a Gateway 2000.

Data is sampled over the desired spectrum energy range in small overlapping divisions, called segments. For example, a single spectrum may be divided into 100 segments. A segment is defined by its center electron kinetic energy (eKE). Once the center eKEs are calculated by PESDAT for each segment, the necessary V3 voltages are calculated from the optimized V3 voltages determined from the tungsten calibration. PESDAT then sends a timer value, the time interval over which to accumulate data for each segment. This is set to 0.5 seconds. When the data taking begins, PESDAT sends the eKE and V3 voltage for the first segment, which is processed by a voltage controller box to determine the necessary voltages for the input lens stack, and these voltages are applied. Then PESDAT sends a signal to the HM to start data accumulation. When the 0.5 seconds are completed as determined by a timer within the HM, the data is read. Then a new center eKE and V3 value is sent and a start accumulation is sent again for the next segment. This is repeated for each of the number of segments per scan, the data is unpacked, processed, and displayed in PESDAT, and the data accumulation restarts at the first segment.

The model 2412B HM interfaces with a host computer hardware interface that follows HP 98622A GPIO protocol. In this protocol, there is a 16-bit Data In line, 16 bits of Data Out, and I/O, PCTL, and PFLG data transfer control lines. Each of these

digital lines travels over a 50-wire ribbon connector between the HM (in the Position Analyzer box) and the host computer hardware interface. 12 of the 16 bits of the Data In line are used to transfer HM data from the HM to the computer. 16-bit command words are sent from the computer to the HM via the Data Out line. The I/O line is either TTL high or low depending on whether the commands are coming from the host computer to the HM on the Data Out line (high) or if data is coming from the HM to the computer (low). The PCTL line indicates the moment when data transfer in either direction may begin. The computer initiates a transfer by sending a TTL high-to-low edge on the PCTL line. The line stays low until the HM acknowledges the command by sending back a high-to-low edge on the PFLG line. At this point the computer resets the PCTL back to a high level. Thus the PFLG line is used as ready/busy line where if the line is low the HM is busy and not able to accept a command.

In order to set the HM timer, the computer sends a 16-bit word to the HM on the Data Out line. This word will have a 0 in the 15^{th} bit (LSB) and specify the time interval in milliseconds using the remaining 15 bits (0-14). To start the data accumulation and signal the beginning of the preset time interval, a start accumulation command is sent. This is a 16-bit word with both LSB and MSB set to 1. When a start accumulation command is sent, the HM buffer pages are automatically switched.

Thus data are accumulated and transferred to the computer during a scan. The standard PC hardware is not set up for the digital data transfer and handshaking necessary for this operation. Therefore, the HM interfaces with a National

Instruments DIO 6533 (PCI-DIO-32HS) DAQ card. This is a 32-bit parallel digital I/O interface for use with a PC computer for digital input and output, pattern generation, and handshaking. It connects to the computer via a standard ribbon cable. The card translates all the commands and information sent from the computer to HM and reverse. The DIO 6533 device is directly compatible with the LabVIEW software program.

2.8 Data processing

In addition to initiating data transfer and dialogue with the HM and electron detector devices, the PESDAT program also provides a user interface for data acquisition, display, and writing and reading data from files. Unprocessed data is stored in text files with a .SEG extension. In this raw format, the first line of the file is the center eKE at which the data was taken, and the following 256 lines have a single integer each representing the number of accumulated counts at that energy channel position in the detector. Line number 256+2=258 is the center eKE for the second segment followed by 256 lines of integers, etc., all the way through the full number of segments in the scan.

For analysis, the data have to be converted into an absolute energy-calibrated form of eKE vs. counts across the spectrum limits. To begin with, it is necessary to know by how much the segments overlap so they can be combined. The energy spacing between the centers of each segment is known by taking the difference in center eKEs of adjacent segments. What is then needed is the energy width that each

detector channel represents. This is calculated as a quantity called the magnification, or meV/channel. Once the magnification is determined, the segments may be overlapped correctly and combined. Then the absolute energy scale must be fixed. Both these tasks are accomplished by taking a calibration photoelectron spectrum on a daily basis. Usually the calibration anion is O^- for several reasons. It is an atom and therefore has no vibrational or rotational structure and may be accurately fit to a gaussian curve; it is relatively easy to make and detach; and its *EA* is known to much better accuracy than can be resolved on our instrument. The O^- scan determines the magnification, and it measures the position of the *EA* peak, which then can be compared to the true position to calculate the necessary energy scale shift.

A second calibration is performed every time a new argon laser tube is installed. This will slightly change the laser alignment and thus the exact spot of intersection between the laser and ion beams, affecting the angle at which the photoelectrons enter the kinetic energy analyzer. This calibration is done using the photoelectron spectrum of tungsten anion, W^-. The PES of W^- contains 12 energy accessible transitions spread over a majority of the 3.4 eV available eKE range of the instrument. The W^- calibration has two purposes. The first is that for each of these peaks, photoelectron intensity is recorded over a range of V3 voltages and an optimal voltage is chosen. A table of optimal V3 voltage versus eKE is created from which optimal V3 voltages for any center eKE can be interpolated. The second purpose is for an energy compression measurement. The energy scale becomes compressed by a small amount (about 0.5%) at lower eKEs. This may be measured by recording the

absolute position of all the W^- peaks and then comparing to the true line positions as tabulated by Charlotte Moore (*7*). This line determines the compression factor γ.

The last correction to account for is a conversion of energy from the lab frame to the center of mass of the anion frame. Because the reaction $AB^- + h\nu \rightarrow AB + e^-$ happens in the center of mass (CM) frame of the anions AB^-, and the photoelectron kinetic energies (eKE) are measured in the laboratory frame, the kinetic energies must be converted into the CM frame. This is explained in detail elsewhere (*1*). In brief, the final electron kinetic energy is calculated by the following relation

$$eKE = h\nu - \left\{ EA_{ref} + \gamma(\Omega_{ref} - \Omega_{lab}) + Wm_e\left(\frac{1}{M_{ref}} - \frac{1}{M}\right)\right\}, \qquad (2.8)$$

where EA_{ref} is the electron affinity of the reference ion (usually O^-), γ is the energy compression factor, Ω_{ref} is the measured eKE of the reference ion, Ω_{lab} is the measured eKE of the molecule of interest in the lab frame, W is the ion beam energy (38 eV), m_e is the mass of the electron, M_{ref} is the mass of the reference ion, and M is the mass of the molecule of interest. The true eKE is calculated with respect to the eKE of the reference ion multiplied by the compression factor (the second term in the brackets above); this is then corrected into the center of mass frame of the molecules by the third term in the brackets above.

Bibliography

1. J. Ho, Doctoral dissertation, University of Colorado, 1991.

2. J. T. Verdeyen, "Laser Electronics", 3rd. ed. Prentice Hall, Englewood Cliffs, NJ, 1995.

3. A. E. Siegman, "Lasers." University Science Books, Mill Valley, CA, 1986.

4. J. Cooper and R. N. Zare, *J. Chem. Phys.* **48,** 942 (1968).

5. J. H. Moore, C. C. Davis, and M. A. Coplan, "Building Scientific Apparatus", 2nd ed. Addison-Wesley, Redwood City, CA, 1989.

6. C. S. Feigerle, Doctoral dissertation, University of Colorado, 1983.

7. C. E. Moore, "Atomic Energy Levels." Nat. Bur. Stand., U. S. Government Printing Office, Washington DC, 1958.

Chapter 3

Photoelectron spectroscopy of alkyl peroxides ROO^- (R = H, D, CH_3, CD_3, and CH_3CH_2)

3.1 Introduction

Alkyl peroxyl radicals (ROO) are generally the first oxidation products of saturated hydrocarbons in the troposphere (*1-3*). Atmospheric hydrocarbons react with strong oxidizers such as OH, O_3, or NO_3. The OH radical reacts with saturated hydrocarbons by H atom abstraction (*2*). The nascent alkyl radical, R, combines rapidly with atmospheric O_2 in a three-body reaction to produce the corresponding alkyl peroxyl radical (*1*).

$$RH + OH \rightarrow R + H_2O \quad (3.1)$$

$$R + O_2 + M \rightarrow ROO + M \quad (3.2)$$

Atmospheric peroxyl radicals react quickly with NO to generate NO_2, which is photodissociated by sunlight to produce NO and O (^3P). The latter is primarily responsible for the formation of tropospheric ozone (reactions 3.3-3.5) (*4,5*). Given that NO and hydrocarbons are both by-products of combustion, reactions 3.1-3.5 form a crucial part of the chemistry responsible for the formation of photochemical smog in industrialized areas.

$$ROO + NO \rightarrow RO + NO_2 \quad (3.3)$$

$$NO_2 + \text{sunlight} \rightarrow NO + O(^3P) \quad (3.4)$$

$$O_2 + O(^3P) + M \rightarrow O_3 + M \qquad (3.5)$$

Alkyl peroxides are also known to play an important role in the chemistry of combustion (*6*). Under some conditions, particularly at low combustion temperatures (< 700 K) hydrocarbon fuels can undergo a series of facile radical reactions involving the intermediacy of alkyl peroxyl radicals. In an internal combustion engine such chemistry may result in accelerated ignition and indeed premature ignition. This phenomenon is referred to as auto-ignition or "engine knock" and has practical ramifications for engine wear and efficiency (*7*).

This chapter describes the measurement of the negative ion photoelectron spectra of ROO^- anions (R=H, D, CH_3, CD_3, and CH_3CH_2).

$$ROO^- + \hbar\omega_{364nm} \rightarrow ROO + e^-(KE) \qquad (3.6)$$

Analysis of the kinetic energy of the scattered photoelectrons (KE) enables determination of the electron affinity (*EA*) of the corresponding peroxyl radical, *EA*(ROO) as well as molecular vibrational frequencies and anharmonicities and angular distributions.

There have been numerous studies of electronic properties of alkyl peroxyl radicals (*1,3,8,9*). We can use generalized valence bond (GVB) diagrams (*9-11*) in Figure 3.1 to represent the peroxide anions, ROO^-, the peroxyl radicals, ROO, and the peroxyl cations, ROO^+.

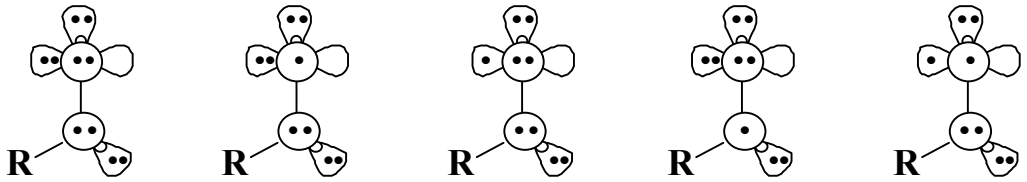

ROO^- ROO ROO^* ROO^* ROO^+

$\tilde{X}\,^1A' \cong -1$ eV $\tilde{X}\,^2A'' \cong 0$ eV $\tilde{A}\,^2A' \cong 1$ eV $\tilde{B}\,^2A'' \cong 5$ eV $\tilde{X}\,^3A'' \cong 11$ eV

Figure 3.1. Generalized valence bond (GVB) diagrams of peroxide anions, ROO^-, the peroxyl radicals, ROO, and the peroxyl cation, ROO^+.

The ground electronic state of alkyl peroxyl radicals is ROO $\tilde{X}\,^2A''$. These radicals display two characteristic electronic excited states: a low-lying ROO $\tilde{A}\,^2A'$ state is present at about 1 eV and there is a high-lying, dissociative state ROO $\tilde{B}\,^2A''$ at a term value of roughly 5 eV. The binding energy (*9*) of the alkyl peroxide anions, ROO^- $\tilde{X}\,^1A'$, is about 1 eV; ionization energies (*12*) of peroxyl radicals are high (*IP*(ROO) ≅ 11 eV).

The photoelectron spectra of ROO^- molecules are in general the most straightforward presented in this thesis. This is true for several reasons. The basic physical picture is fairly intuitive as it is well-represented by the GVB diagrams presented in Fig. 3.1, which depict the highest occupied molecular orbital (HOMO) and HOMO-1 of ROO^- to be localized on the terminal oxygen. Detachment of electrons from these orbitals is expected to excite RO-O stretching modes in forming both the ground state and first excited states of the neutral, as will be shown below. Furthermore, the spectra of the triatomic molecules HOO^- and DOO^- may be considered prototypical photoelectron spectra. In this case, the hydrogen atom

provides a minimum amount of interaction with an OO^- diatomic, and the photophysics involves primarily the two oxygens. Furthermore, many of the photoelectron spectrum features of HOO^- are quite similar to those of OO^- (*13,14*), as will be seen below. The spectra exhibit typical Franck-Condon behavior. All these reasons yield a straightforward spectrum with an uncomplicated analysis. It is therefore important to be able to understand the spectra of HOO^- and DOO^- for the purpose of comparison to the ROO^- molecules with larger alkyl groups (CH_3, CH_3CH_2…) where the interaction between R and OO would be expected to increase.

3.2 Experiment

DOO^- anions were created in a microwave discharge source by introducing the vapor above a mixture of HOOH and D_2SO_4 in D_2O. Enough HOOH remained in the solution to enable the generation of HOO^- anions using the same sample. This simple procedure was not adequate to create the larger ROO^- anions ($R \neq H, D$). Instead, these were created through the reaction of the parent hydroperoxide, ROOH, with hydroxide ions as described in the previous chapter.

Electronic structure calculations were carried out using the GAUSSIAN98 program package (*15*) to aid in interpretation of the photoelectron spectra. The Becke 3LYP hybrid density functional method (*16*) was employed in conjunction with a correlation consistent Dunning basis set of double ζ quality (aug-cc-pVDZ) (*17*) to calculate optimized molecular structures and harmonic frequencies for the anion and

the ground and first excited states of the neutral. The results of these calculations are compared to the measured values in the discussion below.

3.3 HOO^- and DOO^-

The magic angle photoelectron spectrum of HOO^- taken at 200 K sample temperature is shown in Figure 3.2. Comparison between 300 K (not shown) and 200 K spectra confirms that there are no hot bands in this spectrum. The peak marked with a star does not originate from HOO^-, but rather is contamination from OO^- resulting from incomplete rejection of m/z = 32.

The spectrum clearly shows two different Franck-Condon envelopes suggesting transitions into two different electronic states of the neutral molecule. Peaks a1 through a7 have an interpeak spacing of about 1100 cm^{-1}, peaks b1 through b7 have an approximate 900 cm^{-1} separation, while the spacing between peaks a7 and b1 is about 740 cm^{-1}. Because of this, peak b1 is determined to be the 0_0^0 of the $\tilde{X}$ HOO^- to $\tilde{A}$ HOO transition at 1.951 ± 0.004 eV. It is not immediately obvious which peak should be assigned the electron affinity peak. Because the Franck-Condon profile has a shape that is symmetric about peak a4, the *EA* may have too small an intensity to detect, falling to the lower binding energy side of peak a1. However, the term energy of the $\tilde{A}$ state is known to great precision (7029 cm^{-1}) (*18*), which is the spacing between peaks a1 and b1 (7025 cm^{-1}). Therefore, the electron affinity may be assigned with confidence as peak a1, yielding *EA*(HOO) =

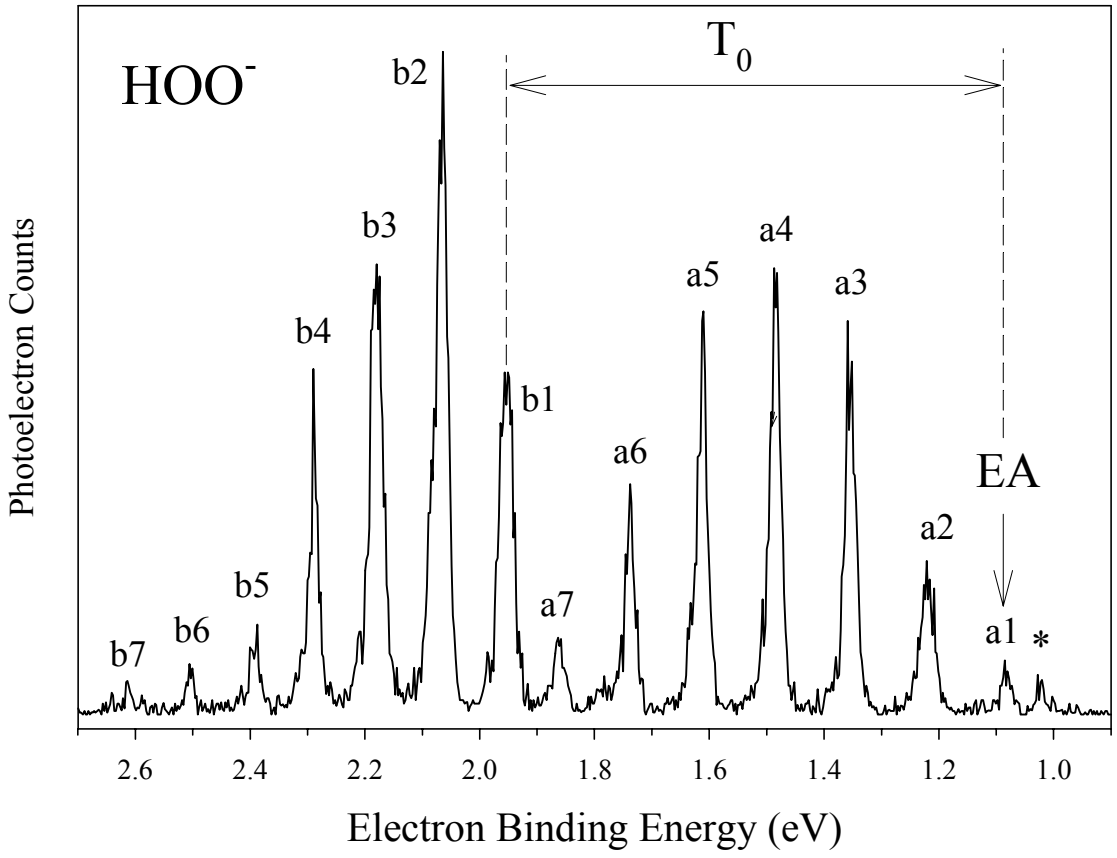

Figure 3.2. 364 nm photoelectron spectrum of HOO^- taken at 200 K and magic angle laser polarization.

Table 3.1. Data extracted from the 364 nm photoelectron spectra (Figures 3.2-3.3) of HOO^- and DOO^-. The data treatments utilized to extract these values and their associated uncertainties (given in parentheses) are discussed in the text.

	EA (eV)	T_0 (eV)	β	$\omega_{O\text{-}O}$ (cm^{-1})	$x_{O\text{-}O}$ (cm^{-1})	$\nu_{O\text{-}O}$ (cm^{-1})
HOO $\tilde{X}\ ^2A''$	1.078(6)		-0.7(1)	1125(6)	11(1)	1102(10)
HOO $\tilde{A}\ ^2A'$		0.872(7)	-0.5(1)	921(4)	5(1)	910(7)
DOO $\tilde{X}\ ^2A''$	1.077(5)			1138(4)	13(1)	1112(7)
DOO $\tilde{A}\ ^2A'$		0.874(7)		955(6)	13(2)	929(10)

1.078 ± 0.006 eV and a term energy of $T_0(\tilde{X}\,HOO - \tilde{A}\,HOO) = 0.872 \pm 0.007$ eV (see Table 3.1). This *EA* agrees precisely with the photoelectron spectroscopy value given in Oakes *et al.* of 1.078 ± 0.017 eV (*19*), although it significantly improves the error bars. The photoelectron spectrum of HOO^- has been reported recently by Clifford *et al.* with an *EA* of 1.089 ± 0.006 eV (*9*) although an addition error was made in the rotational correction to the raw *EA* value. The value reported here is the most current and most accurate measurement available.

Peaks a1 through a7 represent transitions into six quanta of a single vibrational mode in the $\tilde{X}$ state of HOO which will be labeled mode **a**. Likewise, peaks b2 through b7 represent a single progression of six quanta of vibrational excitation in the $\tilde{A}$ state of a mode labeled **b**. Because of the number of well-resolved peaks in this spectrum, the measured energy spacings between all these peaks with respect to the appropriate 0_0^0 peak (a2-a1, a3-a1, a4-a1, etc.), (G(v) –

G(0)) where v = 1-6, of modes **a** and **b** were fitted to Eq. 3.7 (*20*) using a weighted least squares approach:

$$G(v) - G(0) = \omega(v + 1/2) - x(v + 1/2)^2 - 1/2\omega + 1/4x. \qquad (3.7)$$

Fitting the data to Eq. 3.7 gives the harmonic frequency of mode **a**, $\omega_a = 1125 \pm 6$ cm^{-1} and an anharmonicity term, $x_a = 11 \pm 1$ cm^{-1}. Using these parameters we can extract an accurate value for the $1 \leftarrow 0$ vibrational transition of mode **a**, $\nu_a = 1102 \pm 10$ cm^{-1}. Doing the same for mode **b** yields $\omega_b = 921 \pm 4$ cm^{-1}, $x_b = 5 \pm 1$ cm^{-1}, and $\nu_b = 910 \pm 7$ cm^{-1}.

The 90° laser polarization angle spectrum of DOO^- taken at 200 K sample temperature is shown in Figure 3.3. Inspection of the spectrum shows no obvious difference from that of HOO^-. The same analysis discussed above is applied to DOO^-. The electron affinity and term energy are EA(DOO) = 1.077 ± 0.005 eV and $T_0(\tilde{X}$ DOO - $\tilde{A}$ DOO) = 0.874 ± 0.007 eV (see Table 3.1), respectively, which are the same, within error, as for HOO. This is what would be expected since deuteration of the molecule does not affect its electronic structure. However, it does affect its mass and thus some vibrational frequencies. If a normal mode includes motion of a hydrogen atom, its frequency would decrease upon substitution of H for D. Again, using Eq. 3.7 for DOO, the frequency measurements for mode **a** are $\omega_a = 1138 \pm 4$ cm^{-1}, $x_a = 13 \pm 1$ cm^{-1}, and $\nu_a = 1112 \pm 7$ cm^{-1} and for mode **b** are $\omega_b = 955 \pm 6$ cm^{-1}, $x_b = 13 \pm 2$ cm^{-1}, and $\nu_b = 929 \pm 10$ cm^{-1}. The frequencies and anharmonicities for both states in HOO and DOO are reported in Table 3.1. What is important to note is

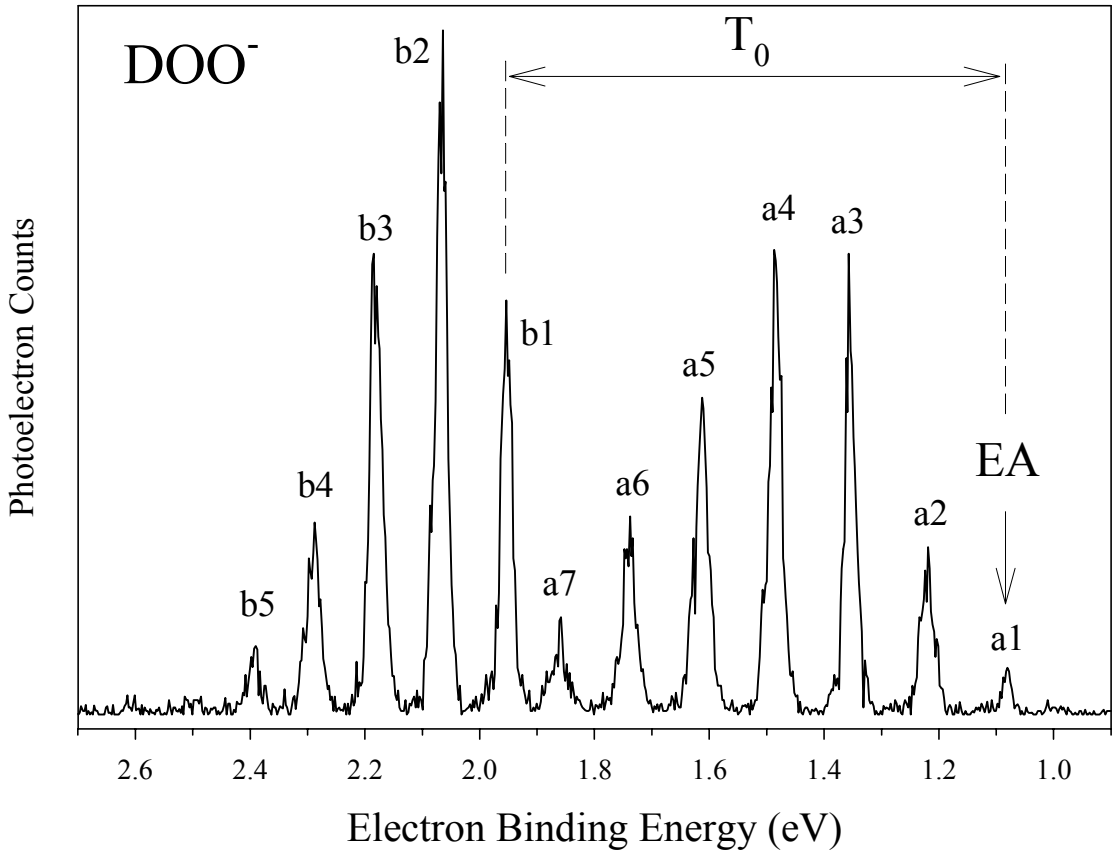

Figure 3.3. 364 nm photoelectron spectrum of DOO^- taken at 200 K and magic angle laser polarization.

that the normal mode fundamentals in both electronic states do not change significantly upon deuteration, as would be expected from the representation given in Fig. 3.1. Thus deuterating the HOO molecule and comparing the spectra of the two isotopomers allows confirmation that the vibrational activity in the photoelectron spectra of HOO^- and DOO^- does not involve hydrogen motion. The only possible vibrational mode candidate then is ν_3, the O-O stretching mode. There is little evidence from the photoelectron spectra of any significant mixing of the O-O stretch and the HOO bend, as has been previously suggested (*21*).

The value of ν_3 (1102 ± 10 cm^{-1}) for $\tilde{X}$ HOO agrees nicely with the IR spectroscopic value of 1097.6 cm^{-1} (*22*), in addition to other more longstanding values (*21,23,24*). It also agrees well with the fundamental frequency found for OO^- (*25*), 1073 ± 50 cm^{-1}. Furthermore, the ν_3 value for the $\tilde{A}$ state (910 ± 7 cm^{-1}) is in agreement with prior findings of Holstein *et al.* (926.5 ± 2.0 cm^{-1}) (*26*). The 929 ± 10 cm^{-1} value of ν_3 in the $\tilde{A}$ state of DOO matches the 930 cm^{-1} frequency reported in the photoelectron spectroscopy study of Oakes *et al.* (*19*). However, their measurement of the DOO^- ν_3 does not agree with the value of the ground state ν_3 mode of DOO^- presented here. It does agree with McKellar (1120.22 (13) cm^{-1}) (*27*) and Smith and Andrews (1123.2 cm^{-1}) (*23*), and it is likely to be a more reliable measurement than the earlier measurement of Oakes *et al.* (*19*) due to a cooler ion source and improved resolution.

An important feature to notice about the spectra in Figures 3.2 and 3.3 is how extended the vibrational progressions are in both ground and excited states of the

neutral molecule. This is a direct indication of a relatively large change in molecular geometry incurred upon detaching an anion electron. The amount that the molecular geometry changes is a direct consequence of the degree to which the detached electrons participate in bonding with other atoms in the molecule. If the detached electron came from a non-bonding orbital, for example, no change in geometry would occur and therefore no vibrational activity would be expected. In the case of HOO, the *ab initio* electronic structure calculations tabulated in Table 3.2 show an O-O

Table 3.2. Molecular geometries for ^{1}A′ HOO^- and $\tilde{X}\,^2$A″ and $\tilde{A}\,^2$A′ states of the neutral HOO radical, resulting from a B3LYP/aug-cc-pVDZ DFT calculation.

	$\tilde{X}\,^1$A′ HOO^-	$\tilde{X}\,^2$A″ HOO	$\tilde{A}\,^2$A′ HOO
r_{OH} (Å)	0.965	0.980	0.976
r_{OO} (Å)	1.513	1.328	1.389
∠HOO	99.3°	105.4°	103.6°

bond length shortening of 0.185 Å between the anion ground state and the neutral ground state and an increase in the HOO bond angle by 6º. This is a relatively substantial change. However, in the case of the O-H bond, the change is only 0.01 Å. This supports the observation that in the spectrum of HOO^- there are six quanta of vibrational excitation in the ground state assigned to pure oxygen stretching along with the finding of no hydrogen participation in the vibrational activity in the spectrum. All the evidence points to the fact that the detached electron does not significantly participate in bonding with the hydrogen, while it plays a large role in

the O-O bond. The change in geometry is somewhat less pronounced in the $\tilde{A} \leftarrow \tilde{X}$ transition than the $\tilde{X} \leftarrow \tilde{X}$ transition ($\Delta r_{O\text{-}O} = 0.124$ Å versus 0.185 Å and $\Delta\angle$HOO of approximately 4º versus 6º). This agrees with the observed structure in that the $\tilde{X}$ state has a slightly more extended profile than the $\tilde{A}$ state.

As was concluded above, the photoelectron detachment is a process fairly localized to an orbital on the terminal oxygen. In the case of OO^-, the orbital would be a pure π orbital. Detachment of this electron produces an angular distribution of approximately –1 (*14*). The value for peaks a1 through a7 in the HOO^- spectrum is -0.7 ± 0.1. This supports the idea that the HOMO orbital in the anion is not severely perturbed by the hydrogen presence. The average value for the peaks involved in the transition into the $\tilde{A}$ state of HOO is slightly lower, -0.5 ± 0.1. It is the HOMO-1 a' orbital which is primarily involved in the bonding with the hydrogen and therefore retains σ character which is absent from the HOMO a" orbital. It is this addition of σ character to the primarily π character found in the $\tilde{X} \leftarrow \tilde{X}$ peaks which lowers the average β value from -0.7 to -0.5 in the $\tilde{X} \leftarrow \tilde{A}$ peaks.

In summary, because of the observation of the O-O stretch, lack of observation of hydrogen activity, and measurement of approximately the same β value, we conclude that electron detachment from HOO^- is similar to detachment from OO^-. This supports the assertion that, in HOO^-, the hydrogen atom may be considered a small perturbation to the OO^- system.

3.4 CH_3OO^-

The 200 K magic angle photoelectron spectrum of CH_3OO^- is presented in Figure 3.4 and the critical data extracted from this spectrum (and those of CD_3OO^- and $CH_3CH_2OO^-$) are listed in Table 3.3. Like the photoelectron spectra of HOO^-

Table 3.3. Data extracted from the 364 nm photoelectron spectra (Figures 3.4-3.6) of CH_3OO^-, CD_3OO^-, and $CH_3CH_2OO^-$. The data treatments utilized to extract these values and their associated uncertainties (given in parentheses) are discussed in the text. The fundamental frequencies (ν) are listed without mode assignments. These are also discussed in the text.

	EA (eV)	T_0 (eV)	β	ω (cm^{-1})	x (cm^{-1})	ν (cm^{-1})	ν (cm^{-1})
$CH_3OO\ \tilde{X}\ ^2A''$	1.161(5)		-0.7(2)	1147(3)	12(1)	1124(5)	482(9)
$CH_3OO\ \tilde{A}\ ^2A'$		0.914(5)	-0.2(2)			1005(10)	910(10)
$CD_3OO\ \tilde{X}\ ^2A''$	1.154(4)			1142(5)	9(1)	1123(7)	440(7)
$CD_3OO\ \tilde{A}\ ^2A'$		0.913(4)				975(10)	840(10)
$CH_3CH_2OO\ \tilde{X}\ ^2A''$	1.186(4)		-0.2(2)	1096(10)	4(2)	1089(16)	234(9)
$CH_3CH_2OO\ \tilde{A}\ ^2A'$		0.938(4)	-0.2(2)			900(15)	178(10)

and DOO^- discussed above, there are two peak profiles present in the spectrum, indicative of transitions to two electronic states of the peroxyl radical. The first band at lower electron binding energy represents a transition to the ground state of the neutral radical, $CH_3OO\ \tilde{X}\ ^2$A", while the second band at higher eBE represents a

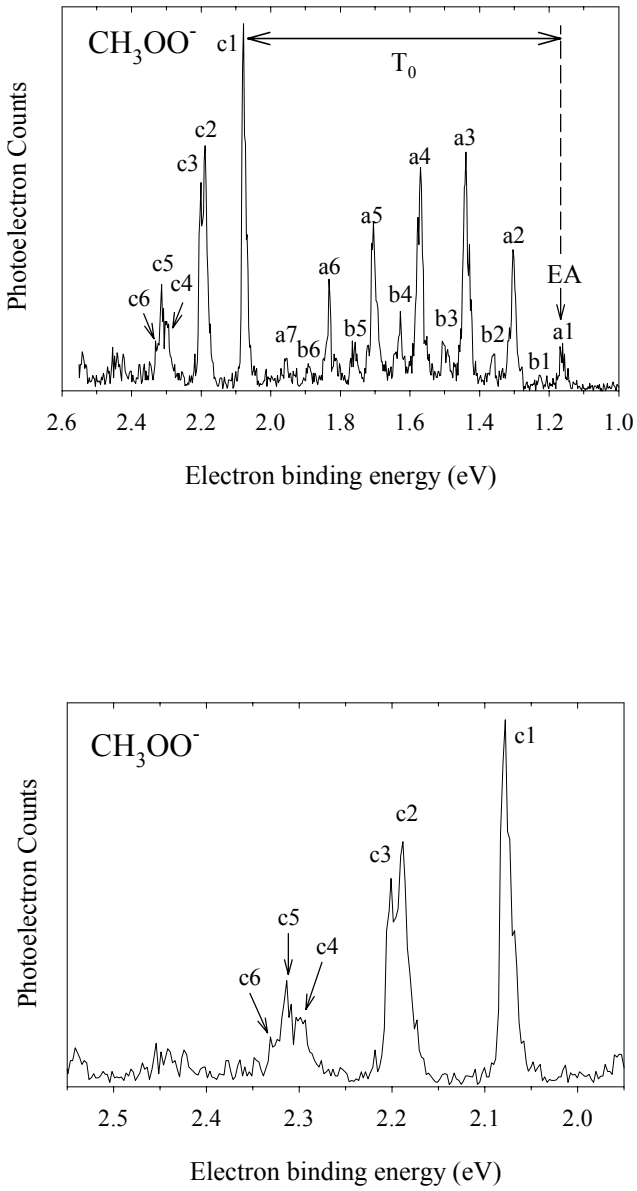

Figure 3.4. 364 nm photoelectron spectrum of CH_3OO^- taken at 200 K and magic angle laser polarization. **(a)** Bottom panel, an expansion of the $\tilde{A} \leftarrow \tilde{X}$ transition spectral profile.

transition to the first excited state of the neutral radical, CH_3OO $\tilde{A}\,^2A'$. Peak c1 (Figure 3.4) can be unambiguously assigned as the 0_0^0 of the $\tilde{A}$ $CH_3OO \leftarrow \tilde{X}$ CH_3OO^- transition. If feature a1 is assigned as the electron affinity, this yields an $EA(CH_3OO)$ = 1.161 ± 0.005 eV and a term energy $T_0(\tilde{X}\,CH_3OO - \tilde{A}\,CH_3OO)$ of 0.914 ± 0.005 eV (or 7370 ± 40 cm^{-1}). The values are slightly larger than for HOO; however to first order, both molecules have the same *EA* and T_0. This measurement of the term energy $T_0(CH_3OO)$ is in excellent agreement with the recent cavity ring-down measurement of Pushkarsky *et al*. (*28*) of 7382.8 ± 0.5 cm^{-1} as well as the longstanding value of Hunziker and Wendt (*29*) of 7375 ± 6 cm^{-1}.

As was seen in HOO, the extended progression of peaks corresponding to the CH_3OO $\tilde{X} \leftarrow$ CH_3OO^- $\tilde{X}$ state transition indicates a significant geometrical change between the ground state anion and neutral structures. By contrast, the second Franck-Condon envelope of peaks corresponding to the $\tilde{A} \leftarrow \tilde{X}$ transition has a narrower profile, with the 0_0^0 (c1) peak being the most intense and subsequent peaks rapidly decreasing in intensity. This indicates a smaller relative change between the $\tilde{X}\,CH_3OO^-$ and $\tilde{A}\,CH_3OO$ geometries than that observed in the $\tilde{X}\,CH_3OO \leftarrow \tilde{X}$ CH_3OO^- transition. This is a somewhat larger contrast than observed in HOO, where both neutral states exhibited comparable and large changes in geometry. The anion and neutral structures predicted by both the qualitative GVB expression (Fig. 3.1) and B3LYP/aug-cc-pVDZ *ab initio* calculations (Table 3.4) support this explanation. In the $\tilde{X} \leftarrow \tilde{X}$ transition the O-O bond length is calculated to change by about 0.16 Å and

Table 3.4. The molecular geometries and harmonic vibrational frequencies (cm^{-1}) for $^1A'$ CH_3OO^- and $\tilde{X}\,^2A''$ and $\tilde{A}\,^2A'$ states of the neutral CH_3OO radicals, calculated at the B3LYP/aug-cc-pVDZ level of theory. Vibrational frequencies given in parentheses represent the values for the d_3-isotopomers. All vibrational frequencies are unscaled.

	CH_3OO^-	CH_3OO	CH_3OO
Molecular Geometries (Å, º)			
	C_S ($\tilde{X}$,$^1A'$)	C_S ($\tilde{X}$,$^2A''$)	C_S ($\tilde{A}$,$^2A'$)
r_e(H_3C-OO)	1.387	1.452	1.440
r_e(H_3CO-O)	1.476	1.317	1.385
∠(H_3C-O-O)	106.2	111.2	107.6
Vibrational Frequencies (cm^{-1})			
a′ modes			
ω_1	2938	3166	3157
	(2176)	(2353)	(2342)
ω_2	2874	3052	3025
	(2057)	(2182)	(2164)
ω_3	1463	1451	1475
	(1147)	(1203)	(1087)
ω_4	1390	1414	1419
	(1053)	(1070)	(1069)
ω_5	1188	1211	1157
	(1012)	(1045)	(1007)
ω_6	1074	1149	1015
	(945)	(985)	(950)
ω_7	806	910	917
	(764)	(825)	(836)
ω_8	428	491	370
	(387)	(444)	(343)
a″ modes			
ω_9	2885	3152	3104
	(2139)	(2342)	(2306)
ω_{10}	1394	1440	1432
	(1015)	(1040)	(1037)
ω_{11}	1145	1111	1150
	(886)	(853)	(884)
ω_{12}	271	129	247
	(207)	(101)	(192)

the C-O-O bond angle by 5^{o}. These are the same geometry changes as found in the HOO molecule. In contrast, as was also the case in HOO, the $\tilde{A} \leftarrow \tilde{X}$ transition calculations predict a smaller change in both the O-O bond length of roughly 0.1 Å and in the C-O-O bond angle of about 2^{o}.

In the Franck-Condon profile for detachment to the ground state, CH_3OO $\tilde{X}$ ^{2}A", there are two vibrational progressions. The most prominent progression is denoted by peaks a1-a7 in Figure 3.4. The peak a1 is assigned as the 0_0^0 transition, while peaks a2-a7 correspond to a progression of six quanta (v_p = 1-6) of an active mode which we label **p**. The measured energy spacings (Table 3.5) between the peaks in this progression are fit to Eq. 3.7 as described above. This gives $\omega_p = 1147 \pm 3$ cm^{-1} and an anharmonicity $x_p = 12 \pm 1$ cm^{-1}, which yields $\nu_p = 1124 \pm 5$ cm^{-1} (see Table 3.3).

In contrast to the spectrum of HOO^-, in addition to the primary progression a less intense although clearly resolved second progression is identified in peaks b1-b6. These peaks appear to the higher binding energy side of the **a** peaks and may be identified as a combination band with this series. We assign b1-b6 as a combination of the progression due to mode **p**, discussed above, plus one quantum of a mode we have labeled **q**. Taking a weighted average of these energy spacings (Table 3.5) we obtain the fundamental of mode **q** to be $\nu_q = 482 \pm 9$ cm^{-1}.

The fundamental of the primary progression, $\nu_p = 1124 \pm 5$ cm^{-1}, correlates well with other fundamental O-O vibrational transitions in peroxyl radicals: (i) for

Table 3.5. Negative ion photoelectron peak positions for CH_3OO^- and CD_3OO^-, uncertainties are given in parentheses. Peak positions are given in wavenumbers (cm^{-1}) relative to 0_0^0 transitions (peaks a1 and c1). Assignments are given for the most prominent transitions labeled as indicated in Figures 3.4 and 3.5.

For CH_3OO the fundamentals are:	$\nu_p = 1124(5)$ cm^{-1} (O-O stretch), $\nu_q = 482(9)$ cm^{-1} (C-O-O bend), $\nu_s = 910(10)$ cm^{-1} (see text), $\nu_t = 1005(10)$ cm^{-1} (see text)
For CD_3OO the fundamentals are:	$\nu_p = 1123(7)$ cm^{-1} (O-O stretch), $\nu_q = 440(7)$ cm^{-1} (C-O-O bend), $\nu_s = 840(10)$ cm^{-1} (see text), $\nu_t = 975(10)$ cm^{-1} (see text)

			CH_3OO	CD_3OO
$\tilde{X}\,^2A''$	a1	0_0^0	0	0
	b1	q_0^1	515(15)	470(15)
	a2	p_0^1	1125(15)	1130(10)
	b2	$p_0^1 q_0^1$	1600(15)	1565(10)
	a3	p_0^2	2225(15)	2235(10)
	b3	$p_0^2 q_0^1$	2700(20)	2660(10)
	a4	p_0^3	3290(15)	3310(10)
	b4	$p_0^3 q_0^1$	3750(15)	3750(10)
	a5	p_0^4	4365(15)	4380(10)
	b5	$p_0^4 q_0^1$	4810(20)	4820(15)
	a6	p_0^5	5390(15)	5425(10)
	b6	$p_0^5 q_0^1$	5870(15)	5850(20)
	a7	p_0^6	6390(15)	6490(25)
$\tilde{A}\,^2A'$	c1	0_0^0	0	0
	c2	s_0^1	910(10)	840(10)
	c3	t_0^1	1005(10)	975(10)
	c4	s_0^2	1790(10)	1690(15)
	c5	$s_0^1 t_0^1$	1910(10)	1800(10)
	c6	t_0^2	2040(15)	1950(10)

HOO, 1102 ± 10 cm^{-1}, as measured in the photoelectron spectrum discussed above, (ii) the ν_3 = 1097.63 cm^{-1} value measured by Tuckett and co-workers (*18,30*), (iii) for matrix isolated CH_3OO, ν_6 = 1109 cm^{-1} measured by Nandi *et al.*(*31*) and, (iv) for CH_3OO the *ab initio* harmonic frequency, ω_6 = 1149 cm^{-1}, calculated at the B3LYP/aug-cc-pVDZ level of theory (Table 3.4). From both the GVB diagrams (Fig. 3.1) and the *ab initio* geometries (Table 3.4), one anticipates strong activity in the RO-O stretching mode upon detachment of the peroxide anion, ROO^-, to the $\tilde{X}$ state of the neutral. Based on these considerations and the good agreement between fundamental frequencies, we assign mode **p** to the CH_3O-O stretching mode ν_6. Similarly, the fundamental frequency ν_q = 482 ± 9 cm^{-1} correlates well with both the CH_3-O-O bending fundamental ν_8 = 492 cm^{-1} measured by Nandi *et al.*(*31*) for matrix isolated CH_3OO and the harmonic frequency, ω_8 = 491 cm^{-1}, calculated at the B3LYP/aug-cc-pVDZ level of theory which corresponds to a H_3C-O-O bending mode (Table 3.4). Theoretical geometries (Table 3.4) predict activity in the H_3C-O-O bending mode upon detachment of the peroxide anion, CH_3OO^-, to the $\tilde{X}$ state of the neutral radical. These considerations lead us to assign mode **q** to the H_3C-O-O bending mode ν_8. This assignment is further supported by the spectrum of CD_3OO^- (which will be further discussed in the subsequent section), where both ν_q and ω_q are shifted to lower frequency.

Examination of the Franck-Condon envelope for the CH_3OO $\tilde{A} \leftarrow CH_3OO^-$ $\tilde{X}$ transition (see expansion Figure 3.4a) reveals a progression of two active modes of similar intensity. Peak c1 is assigned to the 0_0^0 transition, while the peaks c2 and c4

correspond to one and two quanta, respectively, of the mode which we designate **s**. The positions of peaks c1 and c2, given in Table 3.5, fix the fundamental of mode **s** to be $\nu_s = 910 \pm 10$ cm^{-1}. The second progression in the excited state is represented by the peaks c3 and c6, which correspond to one and two quanta, respectively, of the mode that we have assigned as **t**. The positions of peaks c1 and c2, given in Table 3.5, fix the fundamental of mode **t** to be $\nu_t = 1005 \pm 10$ cm^{-1}. The peak c5 in Figure 3.4 represents a combination band of one quantum of **s** and one quantum of **t**.

The $\tilde{A} \leftarrow \tilde{X}$ transition peaks show activity in two modes (**s** and **t)** of similar intensity and frequency (910 and 1005 cm^{-1}). The fundamental frequency $\nu_s = 910 \pm 10$ cm^{-1} is comparable to the frequencies: (i) the O-O stretch fundamental, 910 ± 7 cm^{-1}, measured in the photoelectron spectrum of HOO discussed above, (ii) $\nu_3 = 929.068$ cm^{-1}, which is the fundamental of the O-O stretching mode of the $\tilde{A}$ state of HOO measured by Tuckett and co-workers (*18,30*), and (iii) the vibrational transition at 896 ± 9 cm^{-1} measured for the $\tilde{A}$ state of CH_3OO by Hunziker and Wendt (*29*). The B3LYP/aug-cc-pVDZ calculated harmonic mode $\omega_7 = 917$ cm^{-1} (Table 3.4) is similar in magnitude to ν_s and corresponds to a "symmetric" C-O-O stretching mode. However, the magnitude of $\nu_t = 1005$ cm^{-1} is not significantly different from that of ν_s (910 cm^{-1}). The former frequency is close in magnitude to the calculated harmonic frequency $\omega_6 = 1015$ cm^{-1} which corresponds to a C-O-O "anti-symmetric" stretching mode. The GVB diagrams (Fig 3.1) and *ab initio* calculations both predict some activity in the CH_3O-O stretching vibration for the $\tilde{A} \leftarrow \tilde{X}$ transition. For this reason it is not clear which of these two frequencies, if either, could be strictly assigned to an

O-O stretch. Furthermore, the *ab initio* calculations suggest that the $\tilde{A}$ state vibrations in CH_3OO are unlike the local modes observed for the ground state in that the normal modes involve a significant amount of mixing of local modes. Examination of the CD_3OO^- spectrum should clarify these issues.

The asymmetry parameters β for both electronic transitions in CH_3OO^- (as well as $CD_3OO^-$and $CH_3CH_2OO^-$) are reported in Table 3.3. The $\tilde{X} \leftarrow \tilde{X}$ transition carries an average β of -0.7 ± 0.2 while the $\tilde{A} \leftarrow \tilde{X}$ transition has a β of -0.2 ± 0.2. These values are similar to the corresponding β values observed for HOO and the same conclusions may be made for CH_3OO. Both β values are negative, suggesting detachment from a π-like orbital. The detachment into the $\tilde{X}$ state is close to a β of -1, which (at a electron kinetic energy of roughly 1 eV) implies that the detected electrons are ejected from an essentially pure π orbital. Detachment into the $\tilde{A}$ state yields a β closer to 0, indicating that the orbital from which the electrons are detached possess some of the σ character of the O-C bond.

3.5 CD_3OO^-

The 200 K magic angle photoelectron spectrum of CD_3OO^- is shown in Figure 3.5. An initial comparison does not show any great difference from that of

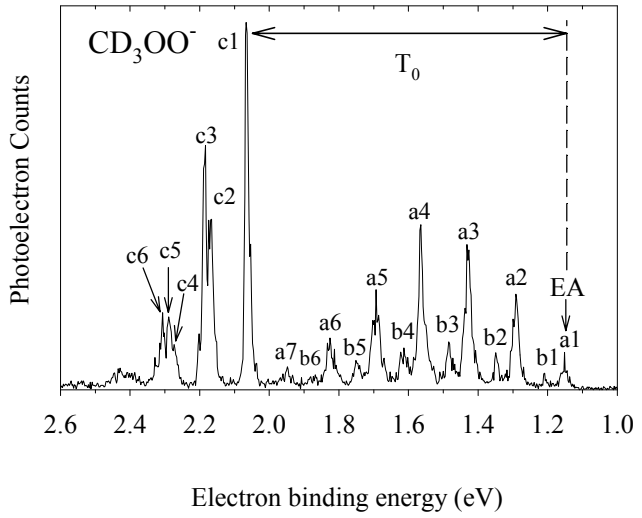

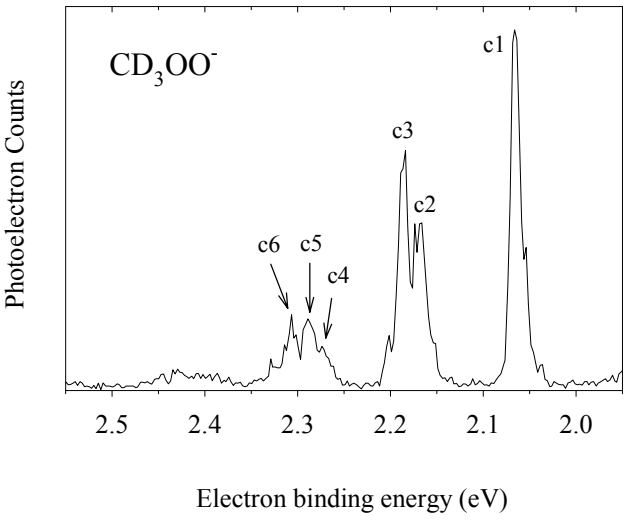

Figure 3.5. 364 nm photoelectron spectrum of CD_3OO^- taken at 200 K and magic angle laser polarization. **(a)** Bottom panel, an expansion of the $\tilde{A} \leftarrow \tilde{X}$ transition spectral profile.

CH_3OO^- in Figure 3.4. Transitions from the anion to both CD_3OO $\tilde{X}\,^2A''$ and $\tilde{A}\,^2A'$ states are observed, with peak c1 assigned as the $\tilde{A}\ 0_0^0$ transition. Feature a1 again corresponds to the electron affinity, with $EA(CD_3OO)$ = 1.154 ± 0.004 eV, slightly less than CH_3OO. This yields a term energy, T_0 = 0.913 ± 0.004 eV (7365 ± 30 cm^{-1}), which agrees with values of Pushkarsky *et al.* (7372.6 ± 0.5 cm^{-1}) (*28*) and Hunziker and Wendt (*29*).

The same two progressions observed in the neutral $\tilde{X}$ state of CH_3OO also appear in CD_3OO. As before, the positions of the **a** peaks (Table 3.5) allow us to determine a harmonic frequency, ω_p = 1142 ± 5 cm^{-1}, and an anharmonicity, x_p = 9 ± 1 cm^{-1}. Using these parameters we can precisely extract a value for the fundamental of mode **p**, ν_p = 1123 ± 7 cm^{-1}. The **b** series of peaks is again a combination of the progression due to mode **p** plus one quantum of mode **q**. Taking a weighted average of these energy spacings (Table 3.5) we obtain the fundamental of mode **q** to be ν_q = 440 ± 7 cm^{-1}.

The harmonic (ω_p) and fundamental (ν_p) frequencies of mode **p** extracted from the CD_3OO^- spectrum are very similar to those obtained from the CH_3OO^- spectrum and both isotopomers also have similar anharmonicity in this mode. The magnitude of this value is also similar to that observed in the DOO^- photoelectron spectrum. The fact that ω_p and fundamental ν_p do not change appreciably upon deuteration confirms the assignment of this mode to a localized O-O stretch because a mode that involves hydrogen motion would have been expected to shift to a lower

frequency upon deuteration. This rationale is also consistent with the matrix work of Nandi *et al.* (*31*) where the fundamental of the O-O stretch mode does not decrease upon deuteration, shifting from 1109 ± 12 cm^{-1} to 1144 ± 12 cm^{-1} in CH_3OO and CD_3OO. In contrast, here the frequency ν_q is shifted 42 cm^{-1} lower upon deuteration, from 482 cm^{-1} to 440 cm^{-1}, which is nearly a 10% shift. This implies that mode **q** does involve hydrogen motion and supports the assignment of mode **q** to the C-O-O bend. Although the hydrogen atoms in this mode may not be moving with respect to the carbon, bending the carbon toward oxygen requires hydrogen motion. Therefore one would anticipate such a shift to lower frequency. This shift is analogous to that observed in the matrix experiments (*31*).

In the $\tilde{A} \leftarrow \tilde{X}$ transition (see Figure 3.5a) there are two active modes close in frequency and intensity, as was also observed in the photoelectron spectrum of CH_3OO^-. One quantum of the first mode is observed at the peak c2 that appears 840 cm^{-1} from the 0_0^0 transition (c1), with a second quantum at 1690 cm^{-1} (c4). The second active mode appears at 975 cm^{-1} (c3), with a second quantum at 1950 cm^{-1} (c6). The peak c5 at 1800 cm^{-1} corresponds to a combination band of one quantum of each of these modes. By analogy with the CH_3OO^- spectrum, we assign these two modes as **s** and **t** with fundamentals, ν_s = 840 ± 10 cm^{-1} and ν_t = 975 ± 10 cm^{-1}. The value of ν_s is red-shifted by about 70 cm^{-1} compared with the corresponding frequency for CH_3OO. This indicates a significant hydrogen contribution to the motion of mode **s,** and therefore this mode cannot be assigned as a pure O-O stretch. By analogy to the $\tilde{X} \leftarrow \tilde{X}$ transition assignments, and by comparison with the *ab initio*

frequency motions discussed for CH_3OO, there is likely some C-O-O bend involved in the motion. The fundamental frequency ν_t has also shifted upon deuteration (30 cm^{-1}) although somewhat less than in the case of ν_s. This suggests that H/D motion is a small component of mode **t** and thus it should be closer to a localized O-O stretch than mode **s**. Thus, in contrast to the $\tilde{X} \leftarrow \tilde{X}$ state, there is evidence for mixing between local modes in the two normal modes observed in the $\tilde{A} \leftarrow \tilde{X}$ transition. Based on their intensity, both modes likely have a large component of O-O stretch with contributions from motion involving the hydrogen atoms, likely the C-O-O bend.

3.6 $CH_3CH_2OO^-$

The 200 K magic angle photoelectron spectrum of $CH_3CH_2OO^-$ is displayed in Figure 3.6. The spectrum is more congested than that of HOO^- or CH_3OO^-, as would be expected for a larger molecule with a greater number of modes. However, the overall structure remains remarkably similar. One sees the same Franck-Condon peak intensity envelopes representing transitions into two electronic states of the neutral. The peak c1 is assigned to the 0_0^0 feature of the $\tilde{A} \leftarrow \tilde{X}$ transition. Peak a1 is the origin of the $\tilde{X} \leftarrow \tilde{X}$ transition and thus gives the electron affinity, $EA(CH_3CH_2OO)$ = 1.186 ± 0.004 eV and the term energy T_0 = 0.938 ± 0.004 eV

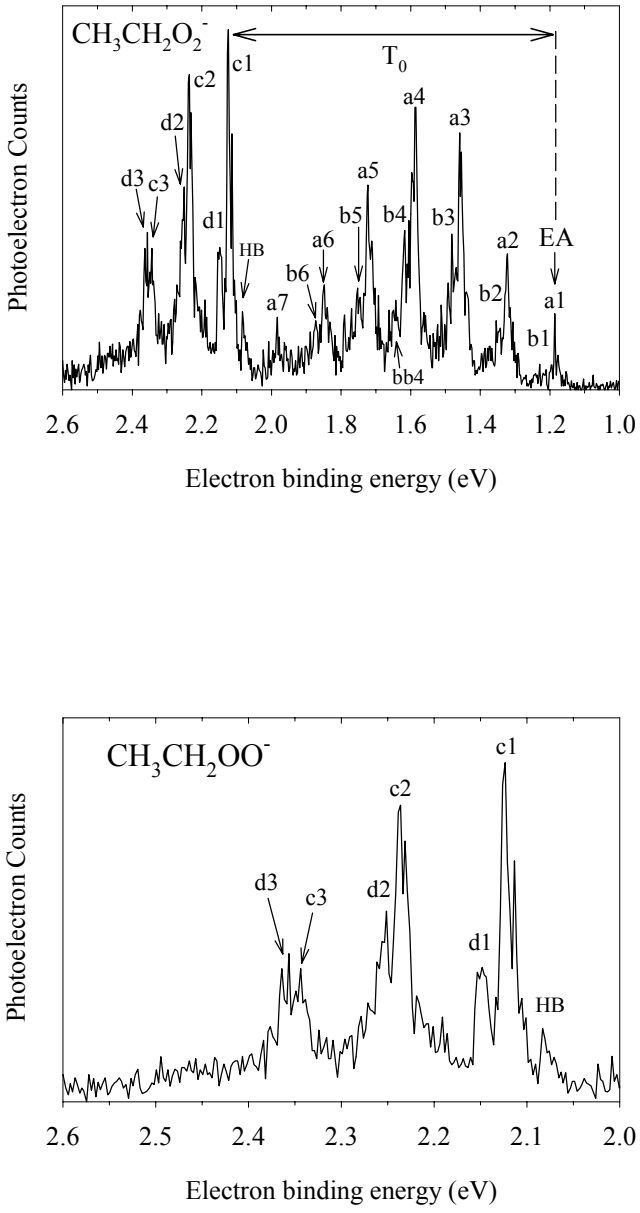

Figure 3.6. 364 nm photoelectron spectrum of $CH_3CH_2OO^-$ taken at 200 K and magic angle laser polarization. **(a)** Bottom panel, an expansion of the $\widetilde{A} \leftarrow \widetilde{X}$ transition spectral profile.

Table 3.6. Negative ion photoelectron peak positions for $CH_3CH_2OO^-$. Peak positions are given in wavenumbers (cm^{-1}) relative to 0_0^0 transitions (peaks a1 and c1). Assignments are given for the most prominent transitions labeled as indicated in Figure 3.6.

For CH_3CH_2OO the fundamentals are:	ν_p = 1089(16) cm^{-1} (O-O stretch), ν_u = 234(9) cm^{-1} (bend). ν_s = 900(15) cm^{-1} (O-O stretch), ν_v = 178(10) cm^{-1} (bend).		
$\widetilde{X}\,^2A''$	a1	0_0^0	0
	b1	u_0^1	240(15)
	a2	p_0^1	1100(10)
	b2	$p_0^1u_0^1$	1305(15)
	a3	p_0^2	2180(15)
	b3	$p_0^2u_0^1$	2315(15)
	a4	p_0^3	3245(15)
	b4	$p_0^3u_0^1$	3490(10)
	bb4	$p_0^3u_0^2$	3695(10)
	a5	p_0^4	4305(15)
	b5	$p_0^4u_0^1$	4545(15)
	a6	p_0^5	5330(15)
	b6	$p_0^5u_0^1$	5540(10)
	a7	p_0^6	6435(10)
$\widetilde{A}\,^2A'$	HB	See text for details	-345(15)
	c1	0_0^0	0
	d1	v_0^1	190(10)
	c2	s_0^1	900(15)
	d2	$s_0^1v_0^1$	1050(15)
	c3	s_0^2	1785(15)
	d3	$s_0^2v_0^1$	1910(25)

(7565 ± 30 cm^{-1}), in agreement with the earlier findings of Hunziker and Wendt (7593 ± 6 cm^{-1}) (*29*). Again, these values are essentially the same as for HOO and CH_3OO. The same primary ground state progression observed in HOO^- and CH_3OO^- appears in peaks a1-a5, and we assign the active mode responsible as **p**. Fitting the energy spacings (Table 3.6) to Eq. 3.7 as previously described gives the harmonic frequency, ω_p = 1096 ± 10 cm^{-1}, and a small anharmonicity, x_p = 4 ± 2 cm^{-1}. Using these parameters we can extract the fundamental frequency of mode **p** to be ν_p = 1089 ± 16 cm^{-1}. A second progression, b1-b6, is assigned as a combination of the progression due to mode **p** plus one quantum of a mode we have labeled **u**. Taking a weighted average of these energy spacings (Table 3.6) we obtain the fundamental of mode **u** to be ν_u = 234 ± 9 cm^{-1}. This frequency is small enough such that one would expect to observe a combination band involving two quanta of mode **u** on top of the **p** progression. This is supported by the observation of peak bb4; however, any other members of such a progression are obscured by noise in the data.

The similarity of ω_p and ν_p between HOO, DOO, CH_3OO, CD_3OO, and CH_3CH_2OO is evidence that this frequency corresponds to a local O-O stretching mode, as increasing the mass of the alkyl substituent has a minimal effect on the measured frequency. The fundamental frequency ν_p = 1089 ± 10 cm^{-1} for CH_3CH_2OO also correlates well with the O-O stretching frequencies: (i) the 1102 ± 10 cm^{-1} HOO value measured above, (ii) ν_3 = 1097.63 cm^{-1} measured (*18,30*) for HOO, (iii) ν_{15} = 1112 cm^{-1} measured (*32*) for matrix isolated CH_3CH_2OO, and (iv) ω_8 = 1199 cm^{-1}, the calculated harmonic frequency that corresponds to a localized O-O

Table 3.7. The molecular geometries and harmonic vibrational frequencies (cm^{-1}) for $^1A'$ $CH_3CH_2OO^-$ and $\tilde{X}\,^2A''$ and $\tilde{A}\,^2A'$ states of the neutral CH_3CH_2OO radicals, calculated at the B3LYP/aug-cc-pVDZ level of theory. All vibrational frequencies are unscaled.

	$CH_3CH_2OO^-$	CH_3CH_2OO	CH_3CH_2OO
Molecular Geometries (Å, º)			
	C_S ($\tilde{X}$,$^1A'$)	C_S ($\tilde{X}$,$^2A''$)	C_S ($\tilde{A}$,$^2A'$)
$r_e(CH_3H_2C\text{-}OO)$	1.388	1.467	1.453
$r_e(CH_3H_2CO\text{-}O)$	1.477	1.316	1.383
$r_e(H_3C\text{-}CH_2OO)$	1.532	1.515	1.517
$\angle(CH_3H_2C\text{-}O\text{-}O)$	106.9	111.6	108.1
Vibrational Frequencies (cm^{-1})			
a′ modes			
ω_1	3065	3122	3123
ω_2	3002	3067	3048
ω_3	2878	3047	3032
ω_4	1485	1479	1500
ω_5	1464	1469	1474
ω_6	1354	1396	1391
ω_7	1325	1354	1361
ω_8	1181	1199	1111
ω_9	1045	1125	1018
ω_{10}	908	1016	999
ω_{11}	816	831	841
ω_{12}	465	501	427
ω_{13}	291	305	279
a″ modes			
ω_{14}	3075	3137	3136
ω_{15}	2872	3116	3079
ω_{16}	1441	1456	1452
ω_{17}	1220	1259	1259
ω_{18}	1163	1134	1167
ω_{19}	789	794	825
ω_{20}	220	215	225
ω_{21}	122	71	120

stretching mode (Table 3.7). Based on these considerations, we assign mode **p** to the CH_3CH_2O-O stretching mode ν_8.

The assignment of mode **u** is not assisted by matrix frequency data, as such low frequencies are not observable in that experiment. However, analogy with the CH_3OO and CD_3OO radicals would identify **u** as a bending mode. Furthermore, the downward shift in the fundamental frequency of 248 cm^{-1} from $\nu_q = 482 \pm 9$ cm^{-1} for CH_3OO to $\nu_q = 234 \pm 9$ cm^{-1} for CH_3CH_2OO supports this assignment. Moving the carbon towards the oxygen would involve movement of more atoms for CH_3CH_2OO than for CH_3OO. Calculations of the harmonic frequencies predict two a′ modes in this region: $\omega_{12} = 501$ cm^{-1} which corresponds to the C-O-O bending mode (*cf.* CH_3OO), and $\omega_{13} = 305$ cm^{-1} which corresponds to a C-C-O bending mode. Thus the active mode **u** may be assigned as a bending mode, although precisely which atoms are involved remains undetermined.

In the $\tilde{A} \leftarrow \tilde{X}$ transition, the largest progression is an active mode denoted by the series of peaks c1-c3. Peak c1 is assigned to the 0_0^0 transition, while the peaks c2 and c3 correspond to one and two quanta, respectively, of the mode which we designate **s**. The energy spacing of the peaks c1 and c2 gives the fundamental frequency of this progression, $\nu_s = 900 \pm 15$ cm^{-1}. In addition, there is evidence of a second active mode in the less intense **d** series of peaks. These features appear to the higher binding energy side of the **s** progression and are thus are assigned as the **s** progression plus one quantum of mode **v**. A weighted average of these energy spacings gives the fundamental of mode **v** as $\nu_v = 178 \pm 10$ cm^{-1}. Finally, the peak

labeled 'HB' (Figure 3.6) to the lower binding energy side of peak c1 is assigned as a vibrational hot band, as its intensity significantly decreases when the sample is cooled from 300 K to 200 K.

By analogy with HOO and CH_3OO, and from examination of the GVB diagrams (Fig. 3.1), activity in the O-O stretch is expected for detachment to the $^2A'$ electronic state. Thus mode **s** is assigned as the O-O stretch. The fundamental frequency, $\nu_s = 900 \pm 15$ cm^{-1}, is comparable to the $\tilde{A}$ state vibrational transition for CH_3CH_2OO measured to be 918 ± 9 cm^{-1} by Hunziker and Wendt (*29*), as well as the HOO photoelectron spectrum measurement (Table 3.1). In contrast to the $\tilde{A} \leftarrow \tilde{X}$ transition of CH_3OO and CD_3OO, the second series of peaks corresponds to a less intense active mode with a small fundamental frequency, $\nu_v = 178 \pm 10$ cm^{-1}. Thus mode **v** is not expected to involve any significant O-O stretching character. The low frequency is more consistent with a bending motion. The lowest calculated harmonic frequency of a′ symmetry (Table 3.7) is $\omega_{13} = 279$ cm^{-1} that corresponds to a C-O-O bending mode.

The β parameters for the two $CH_3CH_2OO^-$ electronic transitions are given in Table 3.3. The $\tilde{X} \leftarrow \tilde{X}$ and the $\tilde{A} \leftarrow \tilde{X}$ transitions have the same asymmetry, with a negative value of -0.2 ± 0.2. This finding is consistent with the other peroxide systems studied where negative β parameters are also observed for both transitions (*9*). However, the lower β value in the $\tilde{X}$ state compared with HOO and CH_3OO

implies that the HOMO orbital is no longer essentially a pure π orbital and character from σ bonds is mixed in, lowering the magnitude of β from about –1 to –0.2.

3.7 Revised thermochemistry of HOO and HOOH

The electron affinity (*EA*) of HOO has another importance, as it provides the means to calculate important thermochemical quantities. Specifically, it can be used in a thermochemical cycle along with the ionization potential of hydrogen, *IP*(H), to determine the gas phase acidity of HOO-H, $\Delta_{acid}H_0$(HOO-H), provided the bond dissociation energy of HOO-H, D_0(HOO-H), has been measured*:

$$\Delta_{acid}H_0(\text{HOO-H}) = D_0(\text{HOO-H}) - EA(\text{HOO}) + IP(\text{H}). \qquad (3.8)$$

D_0(HOO-H) may be in turn determined from the heats of formation of HOO, H, and HOOH:

$$D_0(\text{HOO-H}) = \Delta_f H_0(\text{HOO}) + \Delta_f H_0(\text{H}) - \Delta_f H_0(\text{HOOH}) \qquad (3.9)$$

Because both $\Delta_f H_0$(H) and $\Delta_f H_0$(HOOH) are known precisely, measurement of $\Delta_f H_0$(HOO) gives both D_0(HOO-H) and $\Delta_{acid}H_0$(HOO-H) from equations 3.9 and 3.8, respectively.

The value of $\Delta_f H_0$(HOO) has been essentially unchallenged for the past 20 years. Two different papers have measured $\Delta_f H_0$(HOO), one by Howard in 1980 (*33*)

* The value of D_0(HOO-H) is not directly measured, but is obtained by applying a thermal correction to the measured value $D_{298.15}$(HOO-H).

and one by Hills and Howard in 1984 (*34*). In the first paper, the rate constants for both forward and reverse reactions of

$$HOO + NO \rightarrow OH + NO_2 \quad (3.10)$$

are measured to determine the heat of reaction, ΔH_{rxn}. Then $\Delta_f H_{298}(HOO)$ is determined by

$$\Delta_f H_{298}(HOO) = \Delta_f H_{298}(OH) + \Delta_f H_{298}(NO_2) - \Delta_f H_{298}(NO) - \Delta H_{rxn} \quad (3.11)$$

where $\Delta_f H_{298}(NO_2)$ and $\Delta_f H_{298}(NO)$ are known precisely and $\Delta_f H_{298}(OH)$ has been last determined in 1969 (*35*). In this paper, $\Delta_f H_{298}(HOO) = 2.5 \pm 0.6$ kcal mol^{-1}. The second determination of $\Delta_f H_{298}(HOO)$ studied the reaction

$$OH + ClO \rightarrow HOO + Cl\,. \quad (3.12)$$

Using the heat of reaction, $\Delta_f H_{298}(HOO)$ is determined by

$$\Delta_f H_{298}(HOO) = \Delta_f H_{298}(OH) + \Delta_f H_{298}(ClO) - \Delta_f H_{298}(Cl) + \Delta H_{rxn}. \quad (3.13)$$

Because $\Delta_f H_{298}(ClO)$ and $\Delta_f H_{298}(Cl)$ are known precisely, again we see that $\Delta_f H_{298}(HOO)$ is truly anchored in the value of $\Delta_f H_{298}(OH)$. In this paper, $\Delta_f H_{298}(HOO) = 3.0 \pm 0.4$ kcal mol^{-1}. The value that was chosen for "Chemical Kinetics and Photochemical Data for Use in Stratospheric Modeling" tables (*36*) was 2.8 ± 0.5 kcal mol^{-1}. Therefore, there is some confusion as to the origin of the tabulated value in addition to the issues involved in measuring $\Delta_f H_T(OH)$.

The accepted measurement of $\Delta_f H_{298}$(OH) comes from a spectroscopic method of Carlone and Dalby from 1969 (*35*). They determined D_0(OH $\tilde{X}$) from the relation

$$D_0(\text{OH } \tilde{X}\ ^2\Pi) = \text{P1(1)}(\tilde{A} \leftarrow \tilde{X}\ \text{OH}) + D_0(\tilde{A}\ ^2\Sigma^+\text{OH}) - \text{T}_0\ (^3\text{P} \leftarrow {}^1\text{D O}). \quad (3.14)$$

The first and last terms are known to great precision, while the value of D_0(OH $\tilde{A}$ $^2\Sigma^+$) depends on using a Birge-Sponer extrapolation for $\tilde{A}\ ^2\Sigma^+$ OH, which can be complex. However, the alternative positive ion cycle method has been considered more suspect. In this method, the appearance potential of OH^+ from HOH, AE(HO^+/H_2O), is measured, which is acknowledged as a difficult number to extract. Its value and

$$D_0(\text{HO-H}) = \text{AE}(HO^+/H_2O) - IP(\text{HO}) \quad (3.15)$$

give $\Delta_f H_0$(OH) if *IP*(HO) is known. Recent ZEKE measurements of *IP*(OH) are unambiguous, *IP*(OH) = 104 989 ± 2 cm^{-1} or 13.016 98 ± 0.000 25 eV (*37*). However, recently Ruscic *et al*. (*38*) have precisely re-measured AE(HO^+/H_2O) and recovered the same number from the original measurement. Furthermore, Ruscic *et al*. have done a careful analysis of their data and have appealed to the highest levels of electronic structure theory to calculate the energetics of $OH(^2\Pi) \rightarrow O(^3P_2) + H(^2S_0)$. These calculations clearly favor the recent AE(HO^+/H_2O) measurements of Ruscic *et al*. over the spectroscopic method.

As a result, the heat of formation of OH has been *revised downward* from $\Delta_f H_0$(OH) = 9.3 ± 0.1 kcal mol^{-1} and $\Delta_f H_{298}$(OH) = 9.4 ± 0.1 kcal mol^{-1} to $\Delta_f H_0$(OH) =

8.86 ± 0.07 kcal mol^{-1} and $\Delta_f H_{298}$(OH) = 8.92 ± 0.07 kcal mol^{-1}. This significant shift of 0.5 kcal mol^{-1} in $\Delta_f H_T$(OH), which is outside of the original error bars, places the thermochemistry of HOO at risk. The implications of this are far-reaching. The OH and HOO radicals are key combustion intermediates in the oxidation of all fuels. Equally important, four of the most potent oxidizers in the troposphere are O_3, NO_3, OH, and HO_2. Essentially all volatile organic compounds (VOC's) are oxidized by one of these species. The OH and HOO radicals oxidize literally thousands of VOC's in the atmosphere. Large numbers of rate constants, such as k_1(OH + VOC $\rightarrow$ products), have been measured. It is common to estimate k_{-1}(OH + VOC $\rightarrow$ products) from the thermochemistry. If $\Delta_f H_{298}$(OH) moves, then large numbers of rate constants have to be revised and all models for VOC oxidation have to be re-considered. This implies that the values of $\Delta_f H_0$(OH) and $\Delta_f H_0$(HOO) are of *crucial* importance.

We use the data reported in both Howard and Hills and Howard and thermochemical values from the tables of Gurvich *et al.* (*39*), which represent the most accurate and current thermochemical tables, to compute $\Delta_f H_T$(HOO). Then we repeat the calculation but instead using the most current values of $\Delta_f H_T$(HOO) to date (*40*) (see Tables 3.8 and 3.9). As can be seen from the tables, the values with and without the most recent $\Delta_f H_T$(OH) (*40*) are consistently lower by 0.5 kcal mol^{-1}, as would be expected. The values in Tables 3.8 and 3.9 are used in Eq. 3.9 to determine D_T(HOO-H) (Table 3.10). Finally, the newly revised value of *EA*(HOO) reported here is used in Eq. 3.8 to subsequently determine $\Delta_{acid} H_T$(HOO-H) (Table 3.11). The details of how they were computed are presented in the Appendix.

Table 3.8. Recalculation of $\Delta_f H_T$(HOO) using data measured from the reaction HOO + NO NOO + OH from Howard (*33*) and thermochemical quantities from the tables of Gurvich *et al*. (*39*) using both the $\Delta_f H_T$(OH) from Ref. (*39*) and from Ref. (*40*). All values are in kcal mol^{-1}. Details of the calculations are given in the Appendix.

T (K)	Old value of $\Delta_f H_T$(OH)	New value of $\Delta_f H_T$(OH)[a]
0	3.15 ± 0.43	2.66 ± 0.44
298.15	2.45 ± 0.43	1.96 ± 0.44
400	2.25 ± 0.43	1.76 ± 0.44
500	2.09 ± 0.43	1.60 ± 0.44
700	1.85 ± 0.43	1.36 ± 0.44
1000	1.62 ± 0.43	1.13 ± 0.44

[a] Ref. (*40*)

Table 3.9. Recalculation of $\Delta_f H_T$(HOO) using data measured from the HOO + Cl ClO + OH reaction from Hills and Howard (*34*) and thermochemical quantities from the tables of Gurvich *et al.* (*39*) using both the $\Delta_f H_T$(OH) from Ref. (*39*) and from Ref. (*40*). All values are in kcal mol^{-1}. Details of the calculations are given in the Appendix.

T (K)	Old value of $\Delta_f H_T$(OH)	New value of $\Delta_f H_T$(OH)[a]
0	4.06 ± 0.15	3.58 ± 0.16
298.15	3.36 ± 0.15	2.88 ± 0.16
400	3.17 ± 0.15	2.68 ± 0.16
500	3.01 ± 0.15	2.52 ± 0.16
700	2.77 ± 0.15	2.28 ± 0.16
1000	2.54 ± 0.15	2.05 ± 0.16

[a] Ref. (*40*)

Table 3.10. Calculation of D_T(HOO-H) and $\Delta_{acid}H_T$(HOO-H) using data measured from the reaction HOO + NO NOO + OH from Howard (*33*) and thermochemical quantities from the tables of Gurvich *et al*. (*39*) using both the Δ_fH_T(OH) from Ref. (*39*) and from Ref. (*38*). All values are in kcal mol^{-1}. Details of the calculations are given in the Appendix.

D_T(HOO-H)		
T (K)	Old value of Δ_fH_T(OH)	New value of Δ_fH_T(OH)[a]
0	85.82 ± 0.43	85.33 ± 0.44
298.15	87.03 ± 0.43	86.54 ± 0.44
$\Delta_{acid}H_T$(HOO-H)		
0	374.55 ± 0.45	374.06 ± 0.46
298.15	375.76 ± 0.45	375.27 ± 0.46

[a] Ref. (*38*)

Table 3.11. Calculation of D_T(HOO-H) and $\Delta_{acid}H_T$(HOO-H) using data measured from the HOO + Cl ClO + OH reaction from Hills and Howard (*34*) and thermochemical quantities from the tables of Gurvich *et al.* (*39*) using both the Δ_fH_T(OH) from Ref. (*39*) and from Ref. (*38*). All values are in kcal mol^{-1}. Details of the calculations are given in the Appendix.

D_T(HOO-H)		
T (K)	Old value of Δ_fH_T(OH)	New value of Δ_fH_T(OH)[a]
0	86.73 ± 0.16	86.25 ± 0.17
298.15	87.94 ± 0.16	87.46 ± 0.17
$\Delta_{acid}H_T$(HOO-H)		
0	375.46 ± 0.21	374.98 ± 0.22
298.15	376.67 ± 0.21	376.19 ± 0.22

[a] Ref. (*38*)

One method for checking the $\Delta_f H_T$(HOO) values newly computed above is to measure the heat of reaction for

$$HOO^- + HCCH \rightarrow HOOH + HCC^- . \quad (3.16)$$

This is a similar approach to what was done in Eqs. 3.12 and 3.10 but this reaction does not involve OH. Instead, the measured heat of reaction yields

$$\Delta_{rxn}H_{298} = \Delta_{acid}H_{298}(HCCH) - \Delta_{acid}H_{298}(HOO\text{-}H). \quad (3.17)$$

Because $\Delta_{acid}H_{298}$(HCCH) is known precisely, this experiment would determine $\Delta_{acid}H_{298}$(HOOH). Then, using Eqs. 3.8 and 3.9, the value of $\Delta_f H_{298}$(HOO) and then $\Delta_f H_0$(HOO) may be extracted. The error in this value would be determined solely by the experimental error of $\Delta_{rxn}H_{298}$ and avoids the issues of $\Delta_f H_T$(OH) discussed above.

3.8 Conclusion

The 364 nm photoelectron spectra of ROO^- molecules (R=H, D, CH_3, CD_3, and CH_3CH_2) were presented and analyzed. The HOO^- spectrum was found to be similar to that of OO^-. Going from H to CH_3 and CH_3CH_2 results in greater mixing of the R substituent with the OO^-. This is supported by the observation of activity in the ROO bending mode, the mixing of local vibrational modes in the $\tilde{A}$ state of CH_3OO, and the increased mixing of the HOMO and HOMO-1 anion orbitals with σ

character. However, there are similarities in all these photoelectron spectra as well. The energetics are the same: the electron affinities and term energies, to first order, all hover around 1 eV. Furthermore, even in the largest molecule analyzed, CH_3CH_2OO, all the peroxides exhibit similar structure of their photoelectron spectra. The O-O stretching vibration is the most intense feature in the spectra, and the Franck-Condon peak profiles to first order do not change. Finally, the new determination of the electron affinity of HOO, along with improved values of $\Delta_f H_T$(OH) allow for revised thermochemistry of HOO and HOOH.

Bibliography

1. P. D. Lightfoot, R. A. Cox, J. N. Crowley, M. Destriau, G. D. Hayman, M. E. Jenkin, G. K. Moortgat, and F. Zabel, *Atmos. Environ.* **26A,** 1805 (1992).

2. S. Madronich, J. Greenberg, and S. Paulson, *in "Atmospheric Chemistry and Global Change"* (G. P. Brasseur, J. J. Orlando and G. S. Tyndall, Eds.), p. 325. Oxford University Press, New York, 1999.

3. G. Le Bras, *in "Chemical Processes in Atmospheric Oxidation"*, Vol. 3, (G. Le Bras, Ed.), p. 13. Springer, Berlin, 1997.

4. B. J. Finlayson-Pitts and J. N. Pitts Jr., *Science* **276,** 1045 (1997).

5. F. Kirchner and W. R. Stockwell, *J. Geophys. Res.* **101,** 21007 (1996).

6. S. W. Benson, *J. Am. Chem. Soc.* **87,** 972 (1965).

7. C. K. Westbrook, *Chem. Ind. (Lond.)* **100,** 562 (1992).

8. J. C. Rienstra-Kiracofe, W. D. Allen, and H. F. Schaefer III, *J. Phys. Chem.* **104,** 9823 (2000).

9. E. P. Clifford, P. G. Wenthold, R. Gareyev, W. C. Lineberger, C. H. DePuy, V. M. Bierbaum, and G. B. Ellison, *J. Chem. Phys.* **109,** 10293 (1998).

10. W. A. Goddard III and L. B. Harding, *Annu. Rev. Phys. Chem.* **29,** 363 (1978).

11. R. A. Bair and W. A. Goddard III, *J. Am. Chem. Soc.* **104,** 2719 (1982).

12. M. Litorja and B. Ruscic, *J. Electron Spectrosc. Relat. Phenom.* **97,** 131 (1998).

13. M. J. W. Boness and G. J. Schulz, *Phys. Rev. A* **2,** 2182 (1970).

14. R. J. Celotta, R. A. Bennett, J. L. Hall, M. W. Siegel, and J. Levine, *Phys. Rev. A* **6,** 631 (1972).

15. M. J. Frisch, G. W. Trucks, H. B. Schlegel, G. E. Scuseria, M. A. Robb, J. R. Cheeseman, V. G. Zakrzewski, J. A. J. Montgomery, R. E. Stratmann, J. C. Burant, S. Dapprich, J. M. Millam, A. D. Daniels, K. N. Kudin, M. C. Strain, O. Farkas, J. Tomasi, V. Barone, M. Cossi, R. Cammi, B. Mennucci, C. Pomelli, C. Adams, S. Clifford, J. Ochterski, G. A. Petersson, P. Y. Ayala, Q.

Cui, K. Morokuma, D. K. Malick, A. D. Rabuck, K. Raghavachari, J. B. Foresman, J. Cioslowski, J. V. Ortiz, A. G. Baboul, B. B. Stefanov, G. Liu, A. Liashenko, P. Piskorz, I. Komaromi, R. Gomperts, R. L. Martin, D. J. Fox, T. Keith, M. A. Al-Laham, C. Y. Peng, A. Nanayakkara, C. Gonzalez, M. Challacombe, P. M. W. Gill, B. Johnson, W. Chen, M. W. Wong, J. L. Andres, C. Gonzalez, M. Head-Gordon, E. S. Replogle, and J. A. Pople, *Gaussian 98, Revision A.7*, Gaussian, Inc., Pittsburgh PA, 1998.

16. A. D. Becke, *J. Phys. Chem.* **98,** 5648 (1993).

17. T. H. Dunning Jr., *J. Chem. Phys.* **90,** 1007 (1989).

18. R. P. Tuckett, P. A. Freedman, and W. J. Jones, *Mol. Phys.* **37,** 379 (1979).

19. J. M. Oakes, L. B. Harding, and G. B. Ellison, *J. Chem. Phys.* **83,** 5400 (1985).

20. P. F. Bernath, "Spectra of Atoms and Molecules.", 1st ed. Oxford University Press, New York, 1995.

21. M. E. Jacox and D. E. Milligan, *J. Mol. Spec.* **42,** 495 (1972).

22. J. B. Burkholder, P. D. Hammer, C. J. Howard, J. P. Towle, and J. M. Brown, *J. Mol. Spec.* **151,** 493 (1992).

23. D. W. Smith and L. Andrews, *J. Chem. Phys.* **60,** 81 (1974).

24. J. W. C. Johns, A. R. W. McKellar, and M. Riggin, *J. Chem. Phys.* **68,** 3957 (1978).

25. M. J. Travers, D. C. Cowles, and G. B. Ellison, *Chem. Phys. Lett.* **164,** 449. (1989).

26. K. J. Holstein, E. H. Fink, and F. Zabel, *J. Mol. Spec.* **99,** 231 (1983).

27. A. R. W. Mc Kellar, *J. Chem. Phys.* **71,** 81 (1979).

28. M. B. Pushkarsky, S. J. Zalyubovsky, and T. A. Miller, *J. Chem. Phys.* **112,** 10695 (2000).

29. H. E. Hunziker and H. R. Wendt, *J. Chem. Phys.* **64,** 3488 (1976).

30. R. P. Tuckett, P. A. Freedman, and W. J. Jones, *Mol. Phys.* **37,** 403 (1979).

31. S. Nandi, S. J. Blanksby, X. Zhang, M. R. Nimlos, D. C. Dayton, and G. B. Ellison, *J. Phys. Chem. A***,** (in press, 2001).

32. G. Chettur and A. Snelson, *J. Phys. Chem.* **91,** 3483 (1987).

33. C. J. Howard, *J. Am. Chem. Soc.* **102,** 6937-6941 (1980).

34. A. J. Hills and C. J. Howard, *J. Chem. Phys.* **81,** 4458 (1984).

35. C. Carlone and F. W. Dalby, *Can. J. Phys.* **47,** 1945 (1969).

36. W. B. De More, S. P. Sander, D. M. Golden, R. F. Hampson, M. J. Kurylo, C. J. Howard, A. R. Ravishankara, C. E. Kolb, and M. J. Molina, "Chemical Kinetics and Photochemical Data for Use in Stratospheric Modeling, Evaluation Number 12." Jet Propulsion Laboratory, NASA, Pasadena, 1997.

37. R. T. Wiedmann, R. G. Tonkyn, and M. G. White, *J. Chem. Phys.* **97,** 768 (1992).

38. B. Ruscic, D. Feller, D. A. Dixon, K. A. Peterson, L. B. Harding, R. L. Asher, and A. F. Wagner, *J. Phys. Chem. A* **105,** 1-4 (2001).

39. *Thermodynamic Properties of Individual Substances*, Vol. 1, edited by L. V. Gurvich, I. V. Veyts, and C. B. Alcock (Hemisphere Pub. Corp., New York, 1989).

40. B. Ruscic, D. Feller, D. A. Dixon, K. A. Peterson, L. B. Harding, R. L. Asher, and A. F. Wagner, *J. Phys. Chem. A* **105,** 1-4 (2001). The values reported in this citation have since been revised slightly by the authors. The most current values are: $\Delta_f H_0(OH) = 8.86 \pm 0.07$ kcal mol^{-1} and $\Delta_f H_{298}(OH) = 8.92 \pm 0.07$ kcal mol^{-1}.

Chapter 4

Photoelectron spectroscopy of alkoxy radicals RO^- (R = CH_3, CD_3, CH_3CH_2, CD_3CD_2, $(CH_3)_2CH$, and $(CH_3)_3C$)

4.1 Introduction

There is great motivation to understand the structure and properties of alkoxy radicals due to their prevalence in combustion processes, interstellar and atmospheric chemistry, and as intermediaries in hydrocarbon reactions. However, the theoretical challenges posed by their inherent structure also offer great motivation for their investigation.

Methoxy radical in particular is one of the smallest organics, which makes it well-suited to study via both experiment and calculation. Consequently, there has been no shortage of experimental work on this ubiquitous radical. Some of the earlier research involved laser magnetic resonance (LMR) (*1*), microwave studies (*2*) and negative ion photoelectron spectroscopy (*3*), as well as numerous fluorescence spectroscopic examinations of the $\tilde{A}$ to $\tilde{X}$ electronic transitions (*4-9*); however, analysis of much of this data was complicated by the overlap and congestion due to room temperature samples as well as poor resolution. Furthermore, there was no indication of any Jahn-Teller effects that would be expected as a result of both the electronic degeneracy of the ^2E ground state and the high-symmetry C_{3v} configuration. Supersonic expansion of the sample in laser-induced fluorescence

(LIF) experiments significantly clarified the spectral features (*10-14*), permitting the first direct observation of Jahn-Teller activity in methoxy radical (*15*). However, it was only within the past several years that the advent of improved resolution techniques in conjunction with supersonic expansions allowed the biggest step toward understanding the spectroscopy of methoxy radical (*16,17*). Specifically, the rotationally resolved stimulated emission pumping (SEP) studies have allowed assignment of vibronic symmetry to the CH_3O spectroscopic features because the rotational profile of a transition is a signature of the vibronic symmetry of the states involved (*18,19*).

Such information has been a breakthrough for advancing the theoretical understanding of CH_3O and its Jahn-Teller activity. Early theoretical works have computed geometries (*20,21*), and Jahn-Teller stabilization energies and distortions (*22*). It is only recently that full treatments with the ability to predict spectroscopic features have started to appear (*23*). Specificially, in a recent review, Barckholtz and Miller (*24*) presented the first theoretical treatment of the Jahn-Teller problem including a multimode analysis of both linear and quadratic Jahn-Teller coupling as well as spin-orbit coupling. They were able to incorporate Temps' rotationally resolved SEP data into their model, which in turn calculated the Jahn-Teller parameters that fully characterize the Jahn-Teller activity of the radical.

There have been considerably fewer studies involving CH_3CH_2O, $(CH_3)_2CHO$, and $(CH_3)_3CO$. Negative ion photoelectron spectra of the anions have established electron affinities (*EA*s) for these three species, although the resolution of the spectra was not sufficient to yield significant spectral detail (*25,26*). Like CH_3O,

the majority of the investigations of CH_3CH_2O have employed fluorescence spectroscopy (*5,9,10,27-29*). Most recently, LIF of jet-cooled CH_3CH_2O has allowed spectroscopic identification of several vibrational modes (*30*). Various *ab initio* calculations have been performed on CH_3CH_2O (*31,32*) and $CH_3CH_2O^-$ (*20*); however, there appears to be some discrepancy as to the symmetry of the ground electronic state of the radical (*25,27,29*). Fluorescence excitation spectra of $(CH_3)_2CHO$ were recorded to determine rate constants for reaction with various gases (*5,33*). In addition, Foster *et al.* (*10*) obtained rotationally resolved spectra for jet-cooled CH_3O, CH_3CH_2O, as well as $(CH_3)_2CHO$. Based on the rotational structure of the spectra, they assign the ground state of ethoxy radical to be $^2A''$ with a low-lying $^2A'$ state, whereas in iso-propoxy radical, the rotational signature of the fluorescence transitions suggests that the symmetry switches to a $^2A'$ ground state with a $^2A''$ first excited state. Aside from the *EA* determination in the PES study (*25*), our understanding of tert-butoxy extends to a structure calculation of the anion and radical (*6,20*) and measurement of the electron photodetachment cross section of the anion (*6*).

The previous chapter examined the structure of ROO species. In that case, we observed a suite of molecules that increased in complexity with larger R group while retaining much of the same underlying structure seen in the smallest HOO molecule. One might assume that the RO molecules would follow the same behavior; furthermore, because there is one less oxygen involved in bonding, they should yield simpler molecular structure. However, this is not the case due to geometrical considerations. Methoxide is a closed-shell anion with C_{3v} symmetry. The highest

occupied molecular orbitals involve the two nonbonding essentially atomic p orbitals highly localized on the oxygen atom (*11,15,21,22*). The 3.408 eV laser photon can photodetach an electron from either the p_x or the p_y orbital, resulting in two energetically equivalent configurations for the radical. A schematic of these degenerate orbitals is shown in Figure 4.1. The degenerate electronic state coupled

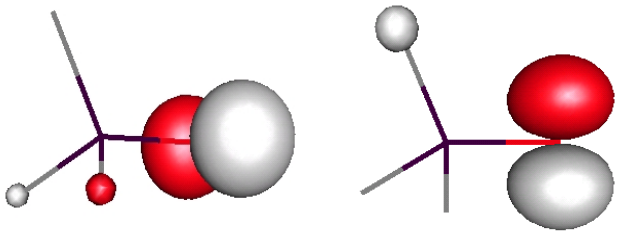

Figure 4.1. Schematic of the two degenerate highest occupied molecular orbitals of $\tilde{X}\ ^1A_1$ CH_3O^-.

with the C_{3v} symmetry of the radical causes a Jahn-Teller effect in CH_3O. Replacing one of the hydrogens in CH_3O with a methyl group to yield CH_3CH_2O breaks the C_{3v} symmetry of CH_3O. This should only be a small perturbation away from the C_{3v} configuration, and thus the resultant splitting in energy of the previously degenerate p-like orbitals is expected to be small. Substituting two hydrogens in CH_3O for methyl groups gives $(CH_3)_2CHO$. This can be thought of as an even larger departure than in CH_3CH_2O away from the methoxy radical C_{3v} structure and thus perturbing

the orbital energies even further. However, if we replace each hydrogen in CH_3O with a methyl group to obtain $(CH_3)_3CO$, we return to the C_{3v} symmetry of CH_3O and accordingly we would expect Jahn-Teller effects to be manifested in this radical. In this paper we attempt to characterize these highest occupied molecular orbitals and their interactions via the $\tilde{X} \leftarrow \tilde{X}$ and $\tilde{A} \leftarrow \tilde{X}$ photelectron spectra as the number of methyl groups substituted for hydrogens increases. We present anion photoelectron spectra of the alkoxides CH_3O^-, $CH_3CH_2O^-$, $(CH_3)_2CHO^-$, and $(CH_3)_3CO^-$, as well as CD_3O^- and $CD_3CD_2O^-$ using a photon energy of 3.408 eV for different laser polarization angles and different sample temperatures. In addition, *ab initio* calculations for ethoxy and iso-propoxy anions and radicals are presented in order to guide the assignment of the spectral peaks.

4.2 Experiment

Details on ion synthesis were discussed in Chapter 2. The CD_3O photoelectron spectrum contains contamination from DOO^- peaks. The flow tube conditions described above also allow for the synthesis of DOO^- through the reaction of CD_3OD with OO^-. Because both DOO^- and CD_3O have m/z = 34, the DOO^- could not be eliminated via mass selection. A separate pure DOO^- photoelectron spectrum was subsequently obtained and was subtracted from the CD_3O^- spectrum.

Ab initio calculations of both CH_3CH_2O and $(CH_3)_2CHO$ anions and radicals were implemented using the GAUSSIAN94 program package (*34*). In CH_3CH_2O, two sets of calculations were employed. The first, referred to as Method 1, used the

density functional theory B3LYP method with a 6-31+G* basis set, while the second, Method 2, used the B3LYP method with an aug-cc-pVDZ basis set. In $(CH_3)_2CHO$, Method 2 was employed for the anion and ground state of the radical, but no potential minimum for the first excited state was found. Therefore a third set of calculations was executed using a HF method with an aug-cc-pVDZ basis set for the anion and ground state of the $(CH_3)_2CHO$ radical, and the CIS method with the aug-cc-pVDZ basis set for the first excited state of $(CH_3)_2CHO$. This is referred to as Method 3. The GAUSSIAN94 calculation output files, which include optimized geometries, normal modes, and vibrational frequencies, were then used in the CDECK suite of programs (*35*). This package calculates Franck-Condon factors for the possible anion to neutral transitions using a harmonic oscillator approximation, and outputs a stick photoelectron spectrum simulation. This stick spectrum is then convoluted with a 10 meV Gaussian function to produce a simulated spectrum that can be directly compared to the data. If the correspondence between theory and experiment is good, the theoretical output may be used as a guide for understanding and assigning the experimental spectral features. The calculated vibrational frequencies are not scaled unless otherwise stated.

A different procedure, referred to as Method A, was used to simulate the photoelectron spectrum of $(CH_3)_3CO^-$. In this case, the anion and neutral potential energy surfaces were assumed to be harmonic. Experimental frequencies were input, assuming the same frequency in the anion and neutral species for each mode. The change in geometry between the anion and neutral was adjusted in order to reproduce the intensities of the peaks in the experimental spectrum. Finally, the simulated peaks

were convoluted with a full-width at half-maximum (FWHM) of 10 meV. No hot bands were simulated.

4.3 CH_3O^-

A detailed theoretical description of Jahn-Teller effects, particularly with respect to CH_3O radical, has recently been given by Barckholtz and Miller (*24*). A brief overview is given here. As mentioned above, the ground electronic state of CH_3O has a two-fold degeneracy in its C_{3v} geometry configuration. This degeneracy leads to a Jahn-Teller phenomenon: in order to minimize energy, the radical will distort, thus breaking the C_{3v} symmetry and lifting the degeneracy. CH_3O has six vibrational modes. Three are symmetric a_1 modes: ν_1 CH stretch, ν_2 umbrella, and ν_3 CO stretch; and three are asymmetric *e* modes: ν_4 CH stretch, ν_5 HCH scissors, and ν_6 methyl rock, which involves movement of the oxygen off the C_{3v} axis toward one of the hydrogens. The symmetric modes by definition do not provide the distortion necessary to remove the degeneracy and lower the energy, and thus only the asymmetric *e* vibrational modes can be Jahn-Teller active. The methoxy radical is known to exhibit a "dynamic" Jahn-Teller effect, where the zero-point energies of the vibrations are much greater than the stabilization energy of the Jahn-Teller distortion (*24*). Therefore the distortion is not large enough to provide a permanent departure from C_{3v} to C_s symmetry and must be treated as a vibronic coupling problem where the asymmetric vibrational *e* modes couple to the degenerate E electronic states.

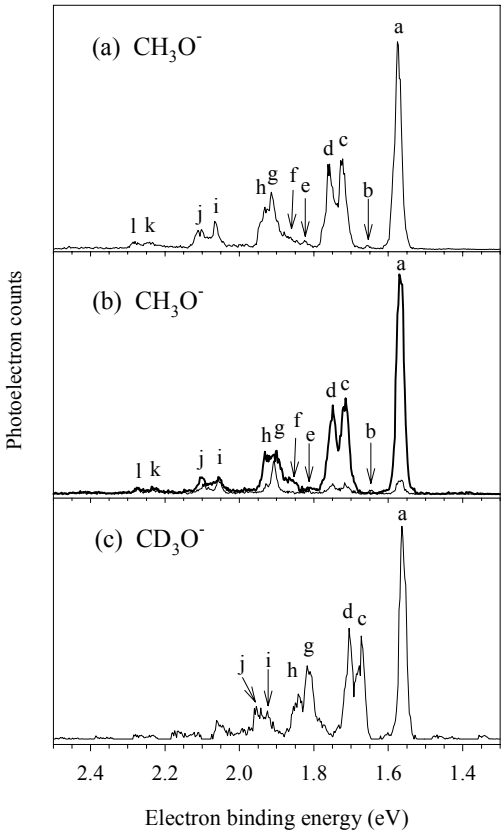

Figure 4.2. a) Magic angle photoelectron spectrum of CH_3O^- taken at 300K sample temperature. (b) 300K photoelectron spectrum of CH_3O^- taken at 90° (heavy line) and 0° (light line) polarization angles with respect to the electron detection axis. (c) Magic angle photoelectron spectrum of CD_3O^- taken at 300K sample temperature, DOO^- subtracted. See text for details.

The room temperature magic angle, and 0° and 90° photoelectron spectra for CH_3O^- are presented in Figure 4.2a and b, respectively. Peak a is assigned as the 0_0^0 transition that gives $EA(CH_3O)$ = 1.572 ± 0.004 eV. The magic angle spectrum shows what appears at first glance to be a regular Franck-Condon progression of doublets in peaks a, c and d, g and h, i and j, and k and l. Closer examination of the spacings, however, reveals that this is not the case. The interpeak spacings of c and d, g and h, i and j, and k and l are 255 cm^{-1}, 155 cm^{-1}, 365 cm^{-1}, and 355 cm^{-1}, respectively. Furthermore, the spacing between peaks a and c, c and g, g and i, and i and k are 1210 cm^{-1}, 1530 cm^{-1}, 1195 cm^{-1}, and 1400 cm^{-1}, respectively. In addition, there are the relatively weak peaks b and e whose photoelectron angular distributions differ markedly from the other peaks in the spectrum. Peaks a, c, d, f, and h show similar behavior in the 90° and 0° polarization scans in that their intensities are heavily weighted in the 90° direction (Figure 4.2b). This is reflected in the asymmetry parameter values (β of about −1) for these peaks listed in Table 4.1. The opposite is true for peaks b and e, whose β values are closer to +1. (These values are taken from closeup spectra of the region, which are not shown). Peaks g, i, j, k, and l display essentially isotropic angular distributions and β is around 0 as given in Table 4.1.

The position and intensity of the magic angle spectrum peaks agree well with a recently published CH_3O^- photoelectron spectrum by Osborn and co-workers (*36*). In contrast to the original photoelectron spectra taken of CH_3O^- under significantly poorer resolution (*3*), none of the major features in the spectra in Figure 4.2a are

Table 4.1. Peak positions, asymmetry β values, and assignments for the photoelectron spectrum of CH_3O^-. Errors on β values are ± 0.1. Assignments are made to SEP peak positions (cm^{-1}) and vibronic symmetries given in Ref. (*19*). See text for details.

Peak	Position (cm^{-1})	β	Assignment
a	0	-0.9	0 0_0^0 (E)
b	630 ± 10	≥ 1.2	652 6_0^1 (A_1)
c	1210 ± 10	-0.9	1198 6_0^1 (E)
d	1465 ± 10	-0.8	1490 5_0^1 (E)
e	2015 ± 30	≥ 1.0	2018 $2_0^1 6_0^1$ (A_1)
f	2450 ± 90	-0.8	2432 $2_0^1 3_0^1$ (E)
			2441 $5_0^1 6_0^1$ (E)
			2488 6_0^3 (E)
g	2740 ± 10	-0.2	2730 5_0^2 (E)
			2750 ?
			2760 $2_0^1 5_0^1$ (A_1)
h	2895 ± 10	-0.7	2862 [5_0^2 / 4_0^1 (E)]
i	3935 ± 10	-0.1	-
j	4300 ± 10	-0.3	-
k	5335 ± 30	-0.1	-
l	5690 ± 15	-0.1	-

spaced such that they could be assigned to any of the three a_1 symmetric vibrational modes: ν_1 = 2869 cm^{-1}, ν_2 = 1375 cm^{-1}, ν_3 = 1062 cm^{-1} (*14*). This leaves only the doubly degenerate *e* vibrational modes ν_4, ν_5, and ν_6; the fact that all the prominent

spectral features can be attributed to asymmetric modes testifies to the presence of significant Jahn-Teller effects in CH_3O.

Due to the dynamic nature of the Jahn-Teller effect in CH_3O, *ab initio* calculations using programs such as GAUSSIAN94 that are based on the Born-Oppenheimer approximation are not feasible as they do not account for the vibronic coupling of electronic and vibrational energy levels. For this reason, and to understand more about the photoelectron spectrum of CH_3O^-, we compare our peak positions with those observed by Temps (*19*) who has catalogued and assigned vibronic symmetry to lines observed in rotationally resolved SEP/LIF studies of CH_3O and CD_3O.

We are able to use the information provided by the β parameters as discussed above, in addition to Temps' results, to make assignments (see Table 4.1). The 0_0^0 transition, peak a, necessarily carries an E vibronic symmetry assignment. This is because the degenerate E symmetry of the electronic state couples with the totally symmetric vibrationless level to give E vibronic symmetry, $E \otimes a1 = E_{vibronic}$. Peaks b, c, and d are assigned to the 6_0^1 (A_1), the 6_0^1 (E), and the 5_0^1 (E) vibronic lines, respectively. Peaks a, c, and d (β of about -1) are all assigned to E vibronic symmetry while peak b ($\beta \geq 1.2$) has A symmetry; this suggests a strong correlation between asymmetry parameters and the vibronic symmetry assignment given to the final state involved in the anion to neutral transition. Furthermore, the A vibronic peak has an intensity significantly smaller than that of its neighboring peaks of E symmetry. With this in mind, peak e is assigned to the $2_0^1 6_0^1$ (A_1) transition at 2018 cm^{-1}, as its β value and relative intensity are similar to that of peak b.

A similar phenomenon was observed (*37*) in the photoelectron spectrum of C_2H^-. In this case, the spectrum was dominated by peaks assigned to Franck-Condon-allowed transitions. However, structure on a scale approximately 50 times smaller than the origin transition was observed, which was attributed to non-Franck-Condon transitions into odd quanta of asymmetric modes in the ground state of the radical. In addition, the non-Franck-Condon peaks displayed asymmetry parameters with opposite sign as the peaks corresponding to activity of symmetric modes of the neutral. These normally forbidden transitions gain intensity via an electronic state mixing between the ground state of the neutral and an excited electronic state. The same mechanism is proposed to explain anomalous intensities in the $\tilde{A}\ ^2A_1 \leftrightarrow \tilde{X}\ ^2E$ excitation spectrum of methoxy radical (*17,38*). In the LIF studies, for peaks involving modes of *e* vibrational symmetry, normally forbidden parallel transitions are observed with intensities of comparable magnitude to the allowed perpendicular transitions. Here the electronic state mixing is suggested to be between the $\tilde{A}$ state and a closely lying excited E electronic state. In the case of the CH_3O^- photoelectron spectrum, the ground E electronic state of the radical may mix with an excited electronic state although the first excited state lies several eV above the ground state.

Peak f, which falls at 2450 cm^{-1}, has the same β value as peaks a, c, and d. It may correspond to either the $2_0^1 3_0^1$ (E) line at 2432 cm^{-1}, the $5_0^1 6_0^1$ (E) line at 2441 cm^{-1}, or the 0_0^0 (E) line at 2488 cm^{-1}. Due to its breadth, peak f may obtain intensity from any or all of these lines. At 2740 cm^{-1} above the origin lies peak g. Its β value is closer to zero than the previous large-intensity peaks mentioned with significant intensity. This suggests that peak g is a mix of peaks with E and peaks with A1

vibronic symmetry. The possibilities are the 5_0^2 (E) line at 2730 cm^{-1}, a line of undetermined symmetry at 2750 cm^{-1}, and the $2_0^1 5_0^1$ (A_1) line at 2760 cm^{-1}. Peak h falls into the same category as peaks a, c, d, and f at 2895 cm^{-1}. Its assignment is either the 2862 cm^{-1} line (this line was given a tentative vibronic label of [$5_0^2 / 4_0^1$ (E)](*19*), which is distinguished by its brackets in Table 4.1), or the 4_0^1 (E) transition at 2889 cm^{-1}. Lines with excitation energies greater than 3000 cm^{-1} are not assigned. The higher the transition lies in the $\tilde{X}\ ^2E$ potential well, the more vibronic mixing there is, rendering it too difficult to determine vibronic symmetry past this energy (*19*).

It should be emphasized that the photoelectron spectrum of CH_3O^- is dominated by the Jahn-Teller-active (asymmetric) vibrational modes and the normally expected features due to vibrations solely of symmetric modes are absent. Peaks e, f, and g carry assignments involving combination bands of symmetric and asymmetric vibrational modes. Thus we do see activity of the symmetric modes in the CH_3O^- photoelectron spectrum, although only when coupled with motion from the asymmetric modes.

The spin-orbit splitting of the ground state of methoxy radical is 61.5 ± 1.0 cm^{-1} (about 7 meV) (*1,39*), which is less than the resolution of our experiment. Nevertheless, the spin-orbit splitting contributes to the widths of the peaks observed. The FWHM of peaks a, c, and d in the cold magic angle spectrum of CH_3O^- are 172, 158, and 102 cm^{-1} respectively. As energy increases, the spin-orbit splitting is quenched, as expected (*22,24*). Both spin-orbit and Jahn-Teller interactions compete for orbital angular momentum and as the Jahn-Teller energy interaction increases at

higher energies in the potential well, the spin-orbit splitting should necessarily decrease.

4.4 CD_3O^-

The room temperature deuterated methoxide spectrum with DOO^- subtracted (see section 4.2) is shown in Figure 4.2c. Peak a, the 0_0^0 transition, falls at an energy of 1.559 ± 0.004 eV.

At first glance, we see the same coarse structure in CD_3O^- as in CH_3O^- in that the intensity pattern and the relative spacings are the same. The peaks appear to have uniformly shifted to smaller binding energy; in fact, if a one-to-one correspondence is assumed between peaks a, c, d, g, h, i, and j in both spectra, which is not intuitively unreasonable, all of these peaks shift their position in an essentially uniform manner relative to peak a by between 21 and 26 %. This agrees with the findings in the recent photoelectron spectrum of CD_3O^- (*36*). A vibrational mode that involves a large amount of hydrogen movement would decrease in frequency upon substituting hydrogen with deuterium and thus a photoelectron peak would shift to lower binding energy. A mode that involves little or no hydrogen movement will not shift. The CO stretch, ν_3, is the only mode of CD_3O that falls into this category. Therefore the evidence indicates that we are not seeing any activity in the symmetric ν_3 mode.

We should be able to use the information provided by the β parameter signature of the peaks to further corroborate the apparent one-to-one correspondence and make assignments. Assignments for CD_3O are made in the same manner as

discussed in CH_3O, i.e., matching our lines to those of Temps LIF/SEP studies of CD_3O (*19*) taking into account both the position and the β parameter/symmetry of the peak as reported in Table 4.2. In the case of peaks a, c, d, and h, the β parameter

Table 4.2. Peak positions, asymmetry (β) values, and assignments for the photoelectron spectrum of CD_3O^-. Errors on β values are ± 0.1. Assignments are made to SEP peak positions (cm^{-1}) and vibronic symmetries given in Ref. (*19*).

Peak	Position (cm^{-1})	β	Assignment
a	0	-0.9	0 0_0^0 (E)
c	920 ± 15	-0.9	885 6_0^1 (E)
d	1160 ± 15	-0.9	1172 5_0^1 (E)
g	2035 ± 15	-0.6	1995 5_0^2 (E)
h	2275 ± 20	-0.8	? [5_0^2 / 4_0^1 (E)]
i	2920 ± 15	-0.4	-
j	3180 ± 20	-	-

values for the peaks in both the CH_3O^- and CD_3O^- spectra are essentially identical; this provides additional confirmation that peaks a, c, d, and h in the CH_3O^- and CD_3O^- spectra can be attributed to the same set of transitions. Peaks c and d are assigned to 6_0^1 (E) and 5_0^1 (E), respectively, as is seen in peaks c and d in CH_3O^-. Peak g, however, has a β of –0.2 in CH_3O^- but a β of –0.6 in CD_3O^-, which is a significant change in asymmetry parameter. It is likely that the three vibronic lines that were assigned to peak g in the CH_3O^- spectrum shifted, but by different amounts. The shifts could happen in such a way that the 5_0^2 (E) line no longer overlaps with an A line, and therefore its β looks more like peaks c and d. Peak g is therefore assigned

to the 5_0^2 (E) line of CD_3O^- at 1995 cm^{-1}. This further supports the assignments for peak g in CH_3O^-.

Peaks h in both spectra have similar asymmetry values, and therefore they are confirmed to be the same peak, either the [5_0^2 / 4_0^1 (E)] line or the 4_0^1 (E) line assigned in CH_3O^-. However, the 4_0^1 (E) assigned position does not match peak h in CD_3O^-, so both peaks h obtain the [5_0^2 / 4_0^1 (E)] assignment. The Temps assignments for CD_3O^- terminate around 2200 cm^{-1} (*19*), so we are not able to confirm the assignment of the CD_3O^- peak h as the [5_0^2 / 4_0^1 (E)] line. Peak i in CD_3O^- has changed its value of β significantly, so it is possible that the peak i in CH_3O^- is composed of several different lines which shift by different amounts upon deuteration, as has been discussed above for peak g.

4.5 $CH_3CH_2O^-$ and $CD_3CD_2O^-$

The 90° and 0° polarization photoelectron spectra at 200 K of $CH_3CH_2O^-$ are shown in Figure 4.3a. No structure in the $CH_3CH_2O^-$ photoelectron spectra could be attributed to hot bands. Peak a is assigned as the *EA* at 1.712 ± 0.004 eV.

Examination of the spectra shows that there are two groups of peaks with contrasting β parameters (see Table 4.3). The first group, which includes peaks a and e possesses a $\beta < 1$, while peaks b-d and f-i have opposite angular distributions, $\beta > 1$. The existence of the two groups of β values indicates that they correspond to different

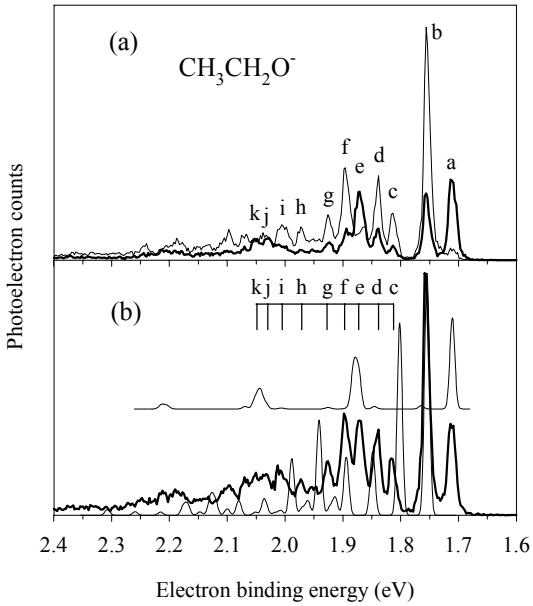

Figure 4.3. a) 200K $CH_3CH_2O^-$ photoelectron spectrum taken at 90° (heavy line) and 0° (light line) polarization angles with respect to the electron detection axis. (b) The 200K $CH_3CH_2O^-$ magic angle photoelectron spectrum is displayed in bold. The thin line at the baseline corresponds to a Method 2 (B3LYP/aug-cc-pVDZ) simulation of the photoelectron transition into the $\tilde{A}$ state of CH_3CH_2O as described in the text. The floated line is the simulation of the photoelectron transition into the $\tilde{X}$ state of CH_3CH_2O.

Table 4.3. Peak positions, asymmetry (β) values, and assignments for the photoelectron spectrum of $CH_3CH_2O^-$ and $CD_3CD_2O^-$. Errors on β values are ± 0.1.

	$CH_3CH_2O^-$			$CD_3CD_2O^-$	
Peak	Position (cm^{-1})	β	Peak	Position (cm^{-1})	β
a	0	-0.8	a	0	-0.7
b	355 ± 10	0.9	b	275 ± 10	0.9
c	830 ± 10	0.9	c	660 ± 20	1.2
d	1040 ± 10	0.7	d	805 ± 10	0.6
e	1295 ± 10	-0.4	e	1090 ± 10	0.2
f	1490 ± 10	0.8	f	1380 ± 15	0.8
g	1730 ± 10	0.7	g	1915 ± 15	0.5
h	2110 ± 15	0.9	h	2135 ± 10	0.1
i	2365 ± 15	0.6	i	2360 ± 15	0.6
j	2575 ± 10	0.1			
k	2740 ± 15	-0.1			

electronic states. This is strong evidence supporting the presence of a low-lying first excited state of ethoxy radical. Peaks a and e correspond to transitions from the ground state of $CH_3CH_2O^-$ anion into the ground state of neutral CH_3CH_2O, while peaks b-d, and f-i represent transitions into the first excited state of the neutral. Therefore, the spacing between peaks a and b, 355 ± 10 cm^{-1}, determines the term energy of the first excited state. To our knowledge, this quantity has never before been directly measured, although there has been a laser fluorescence study of CH_3CH_2O that did not observe any excited states within 300 cm^{-1} of the ground state (*27*). The direct observation of the ground to first excited state spacing in the radical

supports the substitution argument previously mentioned. The substitution of one hydrogen of CH_3O with a methyl group perturbs the C_{3v} geometry and thus slightly lifts the electronic degeneracy present in methoxy radical.

The spacing between peaks a and e is 1295 cm^{-1} and the position of two quanta falls at 2590 cm^{-1}, which is in the vicinity of peaks j and k. The fact that the β values for peaks j and k are the same within error, however, indicates that the second quantum transition is contributing to both these peaks, and therefore they receive the same assignment in the ground state of the radical. The spacings between peaks b and d match that of peaks d and g, about 685 cm^{-1}. Furthermore, the intensity pattern between peaks b, d, and g matches that of a typical Franck-Condon progression and therefore these peaks are assigned as a vibrational progression in the first excited state of the radical. The relationship between the remaining peaks, aside from which electronic state in the radical they belong to, is unclear.

Comparison of the observed spectrum with information provided by *ab initio* calculations of CH_3CH_2O and $CH_3CH_2O^-$ can help clarify and confirm the above observations. Method 2 (B3LYP/aug-cc-pVDZ) calculates the anion to be a 1A' state, while the radical has a ^{2}A" ground state with a ^{2}A' first excited electronic state predicted to lie 360 cm^{-1} higher. This spacing is in good agreement with the observed difference between peaks a and b.

The CDECK simulation of the photoelectron spectrum of $CH_3CH_2O^-$ using the results from Method 2 is presented in Figure 4.3b along with the magic angle photoelectron spectrum taken at 200 K sample temperature. The simulation at the baseline represents the first excited state results while the floated plot represents the

ground state simulation. The positions and intensities of the 0_0^0 peaks in the simulations (peaks a and b) are fixed to match the experimental peaks (in bold).

Method 2 predicts the most active mode in the $\tilde{X}\ ^2A'' \leftarrow \tilde{X}\ ^1A'$ photoelectron spectrum to be ν_9 at 1303 cm^{-1}, a symmetric scissor motion of the non-methyl hydrogens. As is shown in Figure 4.3b, the simulation has excellent agreement for the intensity of peak e with respect to peak a, as well as the intensities of peaks j/k with respect to peak a. These peaks are therefore given the assignment of 9_0^1 and 9_0^2, respectively.

The agreement between the excited state calculation and experiment is not as conclusive, however. For example, the predicted intensity of peak c is highly overestimated. Furthermore, peaks c and d are predicted to form a progression in a single mode, and from examining their intensities in the experimental spectrum, this is not obviously true. This would also conflict with the implication that peaks d and g form a vibrational progression. Peak f lines up well with the simulation peak corresponding to the fundamental of ν_7, the CO stretch predicted at 1118 cm^{-1}. However, it is unclear which simulated peak to match to peak g. For features to higher binding energy of peak g (and including peak g), the agreement with the simulation is ambiguous. In short, the less-than-ideal match between the experimental intensities and spacings and those derived by theoretical means does not help us to assign the remaining peaks. This lack of agreement is not completely unexpected, however. If the ground and first excited states of CH_3CH_2O are separated by only 355 cm^{-1}, the two states should couple together strongly with the effect of perturbing vibrational levels away from a harmonic oscillator

approximation, and the intensities of the transitions may be affected as well. Therefore, peaks d and g are tentatively assigned as the first and second quanta in a vibrational progression in the $\tilde{A}$ state whose motion is undetermined, while peak f may correspond to the fundamental of ν_7.

The 0° and 90° polarization spectra of $CD_3CD_2O^-$ are shown in Figure 4.4. Peaks a and b have similar relative angular distributions and intensities as peaks a and b in $CH_3CH_2O^-$, and the spacing has decreased to 275 ± 10 cm^{-1} (see Table 4.3). As in $CH_3CH_2O^-$, peaks a and b are assigned to the transitions into the ground and first excited state of the radical, respectively. Peak a is assigned as the *EA* at 1.699 ± 0.004 eV.

In contrast to the $CH_3CH_2O^-$ photoelectron spectrum, there is no peak that may be grouped with peak a as having similar β parameter. The mode assigned in the ground state of the ethoxy radical, ν_9 at 1303 cm^{-1}, is predicted by Method 2 to shift to 965 cm^{-1} upon deuteration. There is no match for such a peak in the $CD_3CD_2O^-$ experimental spectrum. Method 2 also calculates that the mode (7 tentatively assigned to the $CH_3CH_2O^-$ photoelectron spectrum at 1118 cm^{-1} would shift to 987 cm^{-1}. This may correspond to peak e in the $CD_3CD_2O^-$ spectrum.

Comparison of the $CH_3CH_2O^-$ and $CD_3CD_2O^-$ photoelectron spectra suggests that many of the features of the $CH_3CH_2O^-$ spectrum have been crowded together due to the shifting expected upon deuteration. There are fewer features in the $CD_3CD_2O^-$ spectrum, and for peaks to the higher binding energy of peak d, the line shapes are

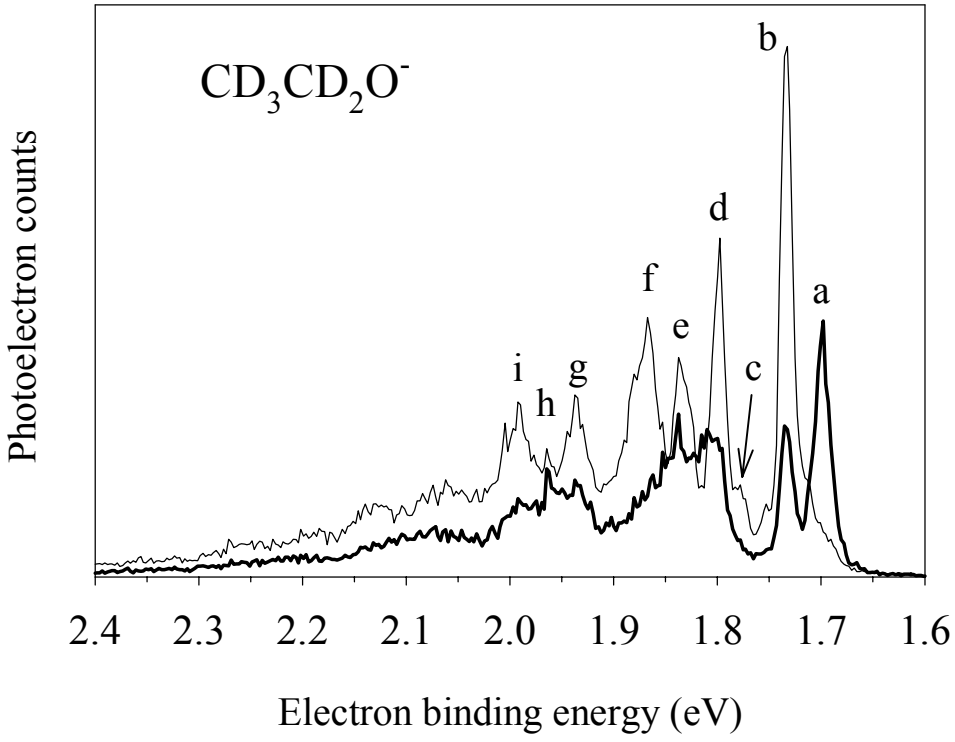

Figure 4.4. 300K $CD_3CD_2O^-$ photoelectron spectrum taken at 90° (heavy line) and 0° (light line) polarization angles with respect to the electron detection axis.

such that they appear to be formed from several peaks. This blending would also affect the intensities of the observed features and their asymmetry parameters. Unlike in the CH_3O^- photoelectron spectrum, we are not able to make a visual correspondence between peaks in the deuterated and non-deuterated spectra. As was the case in $CH_3CH_2O^-$, aside from the few assigned transitions, the simulated spectrum did not accurately reproduce either the relative spacings or the intensities of the spectral features in a consistent manner. Therefore, the congestion observed in the photoelectron spectrum of $CD_3CD_2O^-$ hinders any possible corroboration with structure in the spectrum of $CH_3CH_2O^-$.

In the $CH_3CH_2O^-$ photoelectron spectrum no signature of dissociation of the species is observed. Photodissociation of $CH_3CH_2O^-$ has been observed with a 2.331 eV photon with a low branching ratio of dissociative to stable products (*40*).

4.6 $(CH_3)_2CHO^-$

The magic angle spectrum for $(CH_3)_2CHO^-$ at 200 K sample temperature is displayed in Figure 4.5. The β parameters for all the peaks in the $(CH_3)_2CHO^-$ spectrum are essentially identical, spreading over a small range between 0.1 and 0.5. For this reason the polarization spectra are not shown.

The observed peaks and their positions in the $(CH_3)_2CHO^-$ photoelectron spectrum are given in Table 4.4. The electron affinity for $(CH_3)_2CHO$, corresponding to the position of peak a, is 1.847 ± 0.004 eV. The Method 1 calculation predicts an anion with a $^1A'$ ground state and C_s symmetry. The neutral ground state is calculated

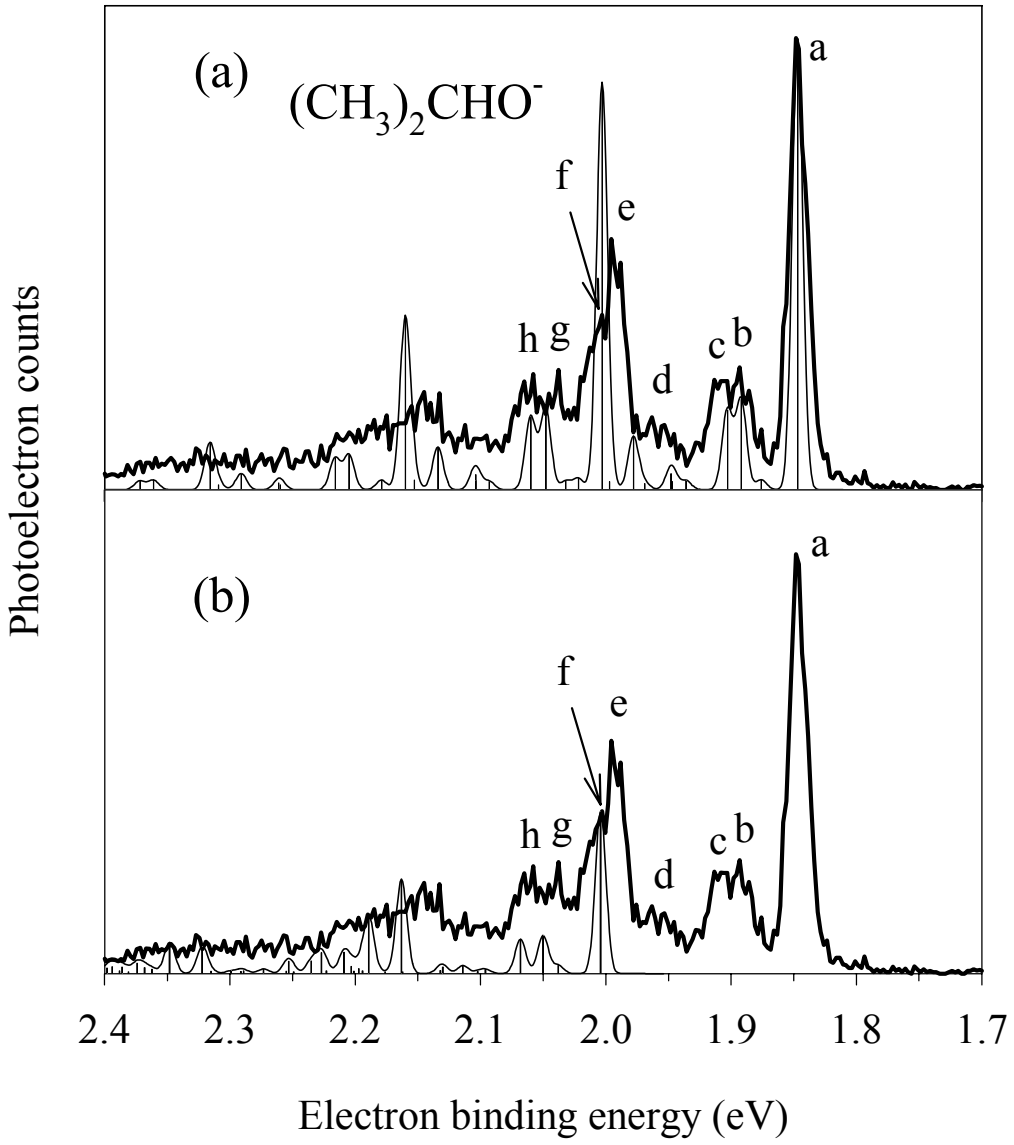

Figure 4.5. a) The 200 K magic angle photoelectron spectrum of $(CH_3)_2CHO^-$ is displayed in bold. The thin line corresponds to a theoretical simulation using Method 1 (B3LYP/6-31+G*) of the photoelectron transition into the $\tilde{X}$ state of $(CH_3)_2CHO$. (b) The 200K magic angle photoelectron spectrum of $(CH_3)_2CHO^-$ is displayed in bold. The thin line corresponds to a theoretical simulation using Method 3 (CIS/aug-cc-pVDZ) of the photoelectron transition into the $\tilde{A}$ state of $(CH_3)_2CHO$.

Table 4.4. Peak positions and assignments for the photoelectron spectrum of $(CH_3)_2CHO^-$.

Peak	Position (cm^{-1})	Assignment
hot band	-330 ± 25	$3'^0_1$
a	0	0^0_0 $\tilde{X}\ ^2A' \leftarrow \tilde{X}\ ^1A'$
b	375 ± 25	3^1_0
c	500 ± 15	5^1_0
d	925 ± 50	See text.
e	1175 ± 15	0^0_0 $\tilde{A}\ ^2A'' \leftarrow \tilde{X}\ ^1A'$ or 14^1_0
f	1270 ± 20	0^0_0 $\tilde{A}\ ^2A'' \leftarrow \tilde{X}\ ^1A'$ or 14^1_0
g	1545 ± 15	$\tilde{X} \leftarrow \tilde{X}\ 3^1_0 14^1_0$ + $\tilde{A} \leftarrow \tilde{X}\ 4^1_0$
h	1740 ± 40	$\tilde{X} \leftarrow \tilde{X}\ 5^1_0 14^1_0$ + $\tilde{A} \leftarrow \tilde{X}\ 5^1_0$

as a $^2A'$ state with C_s geometry. A peak measured from the room temperature photoelectron spectrum (not shown) is assigned as the hot band transition $3'^0_1$, where ν'_3 is the CCC bend predicted at 360 cm^{-1} in the anion. The CDECK simulation of the photoelectron transition into the ground state radical using results from Method 1 is displayed in Figure 4.5a. The spectrum simulation reproduces both the spacing and intensity of many of the spectral features relatively well. Peak b corresponds to one quantum of vibration in ν_3, predicted at 360 cm^{-1}, which is the CCC bending motion in the radical. Peak c is assigned to one quantum of ν_5, a CCCO symmetric bending mode, which Method 1 calculates at 452 cm^{-1}. Peak d is the result of several transitions. The one with the greatest intensity is the fundamental of ν_{10}, a rocking motion of all hydrogens, predicted to fall at 1054 cm^{-1}. In addition there is a smaller

peak to lower binding energy that is primarily composed of overtones and combination bands of ν_3 and ν_5.

The simulation predicts the most active vibration to be ν_{14}, the CO stretch, to lie at 1262 cm^{-1} above the 0_0^0 transition. This is a better match with the position of peak f (1270 cm^{-1}) than peak e (1175 cm^{-1}). However, because peak e is the most intense peak in the spectrum after peak a, the simulated peak may also be assigned to peak e. Therefore it is not clear if it is peak e or peak f that corresponds to 14_0^1. The observation of the CO stretch is expected because detaching an electron localized on the oxygen should affect the CO bond and thus activate the CO stretch, parallel to the O-O stretch activity observed in the ROO molecules. However, unlike the $CH_3CH_2O^-$ spectrum, we are not able to use peaks with contrasting β values to distinguish between different electronic states. What is clear, however, is that the peak that is not assigned to 14_0^1 is absent from the photoelectron spectrum simulation of the transition into the ground state of $(CH_3)_2CHO$. Thus either peak e or f is the 0_0^0 transition from the ground state anion into the first excited state of the neutral. The term energy of the $\tilde{A}$ state is therefore assigned as the average of the positions of peak e and f, 1225 ± 65 cm^{-1}. This spacing is believable in light of the substitution argument applied above. Specifically, replacing two of the hydrogens in CH_3O with methyl groups can be considered a perturbation that lifts the degeneracy of the CH_3O $\tilde{X}$ ^2E state to a greater degree than in CH_3CH_2O.

The assignment of transitions into the first excited state of $(CH_3)_2CHO$ can be further supported by *ab initio* calculations. Method 3 (HF/CIS/aug-cc-pVDZ) predicts that the anion has a $^1A'$ ground state with C_s geometry and that the neutral

has a ^{2}A' ground state with C_s geometry, in agreement with Method 1. The CIS calculation additionally predicts that the first excited state is a ^{2}A" state with C_s geometry, 2011 cm^{-1} above the $\tilde{X}$ ^{2}A' state. This agrees fairly well with our measurement of the term energy of the excited state. The CDECK simulation of the photoelectron spectrum using the results from the Method 3 calculation is displayed in Figure 4.5b. In this figure, the intensity and position of the 0_0^0 simulation peak are fixed to match peak f, although choosing between peaks e and f is arbitrary, as discussed above. It is clear that both peaks g and h are composed of transitions into both the $\tilde{X}$ and $\tilde{A}$ electronic states of the radical. Peak g is assigned to the overtone combination $3_0^1 14_0^1$ in the ground state radical plus 4_0^1 in the first excited state, the CCC bend, predicted to fall 371 cm^{-1} above the 0_0^0 $\tilde{A} \leftarrow \tilde{X}$ transition. Similarly, peak h results from the overtone of $5_0^1 14_0^1$ ground state modes plus 5_0^1 in the $\tilde{A}$ state, the CCCO symmetric bend, predicted at 516 cm^{-1}. Beyond peak h the convolution of features from transitions into both ground state and first excited states in the radical is too complex to make unambiguous assignments.

It is interesting that our calculations predict a ^{2}A" ground state with a ^{2}A' first excited state in ethoxy radical, while in iso-propoxy radical, the two states are reversed. This is in agreement with the rotational spectroscopy of Foster *et al.* (*10*). They postulate that this is because in CH_3CH_2O, the non-bonding a' orbital that lies in the C_s plane is closer to the methyl group; in $(CH_3)_2CHO$, the a' orbital is closest to the non-methyl hydrogen and it is the out-of-plane a" orbital that has the maximum opportunity for interaction with the two methyl groups. The ordering of the states

observed here implies that the proximity of a lone-pair orbital to a methyl group serves to lower its energy relative to the other lone-pair orbital.

4.7 $(CH_3)_3CO^-$

The magic angle photoelectron spectrum of $(CH_3)_3CO^-$ at 200 K is displayed in Figure 4.6. As was the case for $(CH_3)_2CHO^-$, there is essentially no variation in β parameter over the span of the spectrum, as it ranges between 0.1 and -0.3.

Peak b is measured at 435 cm^{-1} above the 0_0^0 transition. This is the same spacing between peaks b and c, peaks d and e, and peaks e and f. This suggests that peaks b and c form a vibrational progression in one mode, and peaks e and f form the same vibrational progression in combination with peak d. Peak d falls at 1205 cm^{-1} above peak a, and peak g lies at twice that amount, implying that peaks d and g form a second vibrational progression.

Because $(CH_3)_3CO$ is expected to exhibit Jahn-Teller effects due to its C_{3v} geometry and concomitant degenerate $\tilde{X}\ ^2E$ electronic ground state (*6*), we were unable to carry out our own calculations on $(CH_3)_3CO$ using *ab initio* methods based on the Born-Oppenheimer approximation. However, recently Barckholtz and Miller have outlined a method for *ab initio* calculations that includes coupling between electronic and vibrational wave functions and is therefore able to compute spectroscopically observable parameters of Jahn-Teller species (*41*). A calculation for $(CH_3)_3CO$ using this above method (*42*) corroborates the assignments proposed above (see Table 4.5). It predicts the symmetric a_1 CCC umbrella mode ν_6 at 389

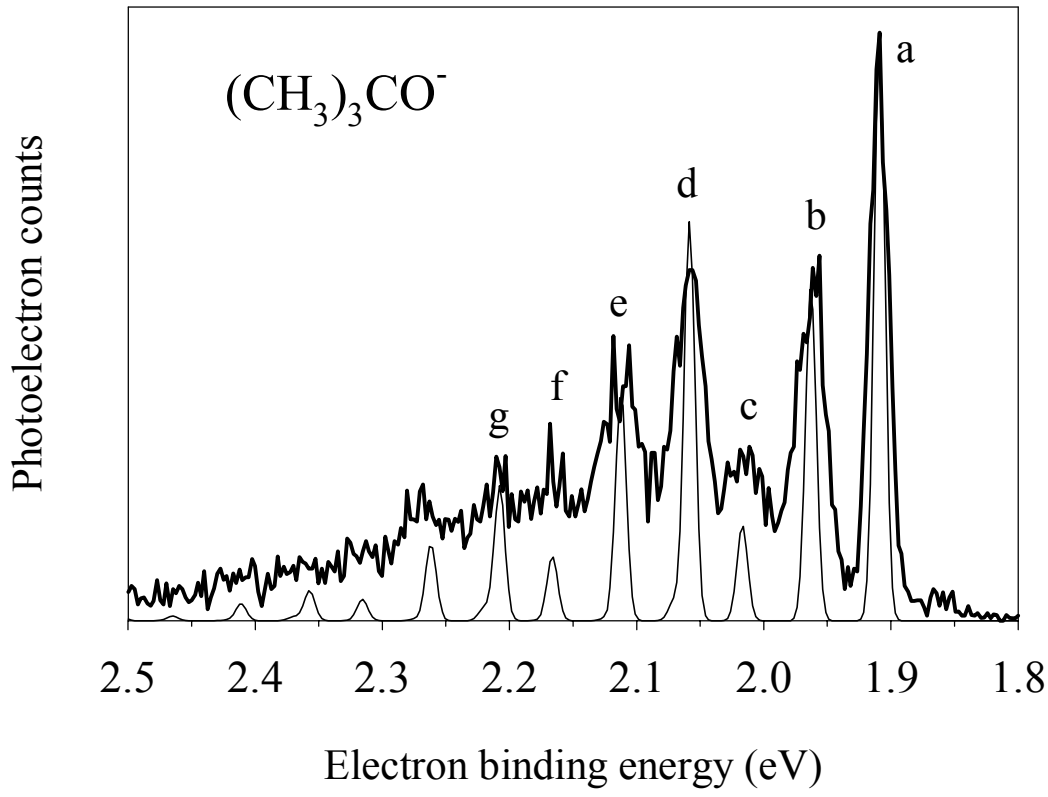

Figure 4.6. Magic angle photoelectron spectrum of $(CH_3)_3CO^-$ taken at 200K sample temperature in bold. The thin line corresponds to a Franck-Condon simulation of the photoelectron spectrum in a simple harmonic oscillator approximation using experimental frequencies (Method A). See text for details.

Table 4.5. Peak positions and assignments for the photoelectron spectrum of $(CH_3)_3CO^-$.

Peak	Position (cm^{-1})	Assignment
hot band	-440 ± 25	$6''^0_1$
a	0	0^0_0
b	435 ± 15	6^1_0
c	855 ± 25	6^2_0
d	1205 ± 15	18^1_0
e	1625 ± 45	$18^1_0\ 6^1_0$
f	2080 ± 30	$18^1_0\ 6^2_0$
g	2410 ± 30	18^2_0

cm^{-1} and the a_1 mode ν_{18} at 1234 cm^{-1} which is the CO stretching motion. In the anion, mode ν'_6 corresponds to the same CCC umbrella motion as the radical mode ν_6, and is predicted at the slightly lower frequency of 381 cm^{-1}. A peak was measured from the room temperature photoelectron spectrum (not shown) at 440 cm^{-1}, which we assign as a hot band resulting from excitation from $6''^0_1$. The observation of the CO stretch is expected for the same reason discussed in $(CH_3)_2CHO$.

Figure 4.6 displays a spectral simulation created using Method A. The experimental frequencies of 435 and 1205 cm^{-1} are input to produce the displayed curve. The agreement is surprisingly accurate considering the relative crudeness of the simulation for such a theoretically complicated species. This point will be discussed further below.

4.8 Vibronic coupling and Jahn-Teller effects

As was stated above in the discussion of ethoxy radical, the majority of the vibrational features in the $CH_3CH_2O^-$ photoelectron spectrum exhibit irregular frequency and intensity patterns that the reasonably high-level calculations and simulations fail to accurately reproduce. This has been attributed to the vibronic coupling between the ground and first excited states in the radical, separated by only 355 cm^{-1}. In the photoelectron spectrum of $(CH_3)_2CHO^-$, however, regularly spaced series of peaks are observed that, with the help of theoretical simulations, can be explained and assigned. In $(CH_3)_2CHO$, the excitation to the first excited state (1225 cm^{-1}) is approximately three times greater than in CH_3CH_2O; therefore the degree of coupling between the $\tilde{X}$ and $\tilde{A}$ states of $(CH_3)_2CHO$ would be expected to be smaller. In addition, however, one must consider the magnitude of the frequencies involved with respect to the energy splitting between the interacting electronic states. In $(CH_3)_2CHO$, the majority of the assigned peaks--b, c, d, and possibly e--fall at energies less than the energy where the $\tilde{A}$ state begins. Therefore, vibronic coupling effects would be expected only for peaks at greater binding energies than peaks e or f. In ethoxy radical this is not the case. The splitting between the electronic states of the neutral is small enough that all of the observed features are subject to vibronic coupling effects.

The existence of the signature of vibronic coupling upon the frequency and spacings of the photoelectron features can be explained, and this may be the reason for the variation of β in the $CH_3CH_2O^-$ spectrum and not in $(CH_3)_2CHO^-$.

The relative ordering of the a' and a" orbital energy is switched between CH_3CH_2O and $(CH_3)_2CHO$, but both orbitals show the same pπ character. Therefore there is no reason to first order why transitions to the ground and first excited states, corresponding to detaching electrons from the a' and a" orbitals, would exhibit different angular distributions, which is the case for $(CH_3)_2CHO$, but not for CH_3CH_2O. Thus the different angular distribution behavior for the two species must be originating from another source. In the CH_3O^- photoelectron spectrum, electronic state coupling is proposed to explain intensity in peaks that have different angular distributions than the other peaks in the spectrum. It is possible that the same kind of mixing can explain the angular distribution variation for peaks in the $CH_3CH_2O^-$ spectrum through coupling either between the $\tilde{X}$ and $\tilde{A}$ states of the radical, or between either of these states and a third electronic state.

The relationship of $(CH_3)_3CO$ to CH_3O with respect to the prominence of Jahn-Teller effects in the photoelectron spectra is similar to that between CH_3CH_2O and $(CH_3)_2CHO$ with respect to vibronic coupling effects. The CH_3O^- photoelectron spectrum is dominated by activity in the *e* asymmetric modes falling at positions determined by the Jahn-Teller coupling parameters of the radical. In $(CH_3)_3CO$, however, the major structure is assigned to harmonic progressions in symmetric a_1 vibrational modes. Furthermore, the method used for simulation of the spectrum in Figure 4.6 only allows for optimization of a limited number of free parameters strictly

within the Born-Oppenheimer approximation and nevertheless provides a surprisingly accurate simulation of the photoelectron spectrum. This does not mean, however, that there is no Jahn-Teller activity in the $(CH_3)_3CO$ radical. A simulation of the Jahn-Teller active modes in the $(CH_3)_3CO$ spectrum indicates that the most prominent Jahn-Teller transitions have an intensity of about 10 % of the origin transition (*42*). Although $(CH_3)_3CO$ is expected to be Jahn-Teller-active, the activity is predicted to be small, which is what we observe in our spectrum. The greater amount of vibrational activity in the larger $(CH_3)_3CO$ radical, as well as the resolution of our experiment, produces a baseline of intensity under which any Jahn-Teller transitions may lie. This may include transitions into pure *e* vibrational modes as well as any combinations of symmetric and asymmetric modes. The fact that the gross structure of the $(CH_3)_3CO^-$ photoelectron spectrum may be assigned to regularly-spaced transitions into symmetric vibrational modes characterizes this species more closely with $(CH_3)_2CHO$ than CH_3O. Furthermore, the asymmetry parameter behavior of $(CH_3)_2CHO$ and $(CH_3)_3CO$ is similar because β is constant across the spectrum. In light of these parallels, it may prove more fruitful to think of $(CH_3)_2CHO$ as a geometrical perturbation away from the $(CH_3)_3CO$ structure, where one methyl group has been substituted by a hydrogen.

4.9 Thermochemistry

The *EA*s for each neutral in this study are reported in Table 4.6. The *EA*s have been rotationally corrected and the error bars account for energy compression,

rotational broadening, and measurement fitting error. The table lists previous photoelectron spectrum determinations of the *EA* for comparison. In each case, agreement with the prior studies is good and the error bars have improved. In the

Table 4.6. Electron Affinities (*EA*) in eV. Values have been rotationally corrected. See text for details.

Species	*EA*(eV)	Literature Value	Reference
CH_3O	1.572 ± 0.004	1.568 ± 0.005	(*36*)
CD_3O	1.559 ± 0.004	1.551 ± 0.005	(*36*)
CH_3CH_2O	1.712 ± 0.004	1.715 ± 0.007	(*26*)
CD_3CD_2O	1.699 ± 0.004	1.703 ± 0.007	(*26*)
$(CH_3)_2CHO$	1.847 ± 0.004	1.839 ± 0.029	(*25*)
$(CH_3)_3CO$	1.909 ± 0.004	$1.912\ ^{+0.029}_{-0.054}$	(*25*)

case of $(CH_3)_2CHO$ and $(CH_3)_3CO$, the error bars have been improved dramatically, by a factor of at least seven.

As was outlined in Chapter 3 and Eq. 3.9, the RO *EA*s from this work may be used together with literature values of the gas-phase acidity (GPA) of ROH (*26,43-49*) and the ionization potential of the hydrogen atom in a thermochemical cycle to determine the bond dissociation energy, D_{300}(RO-H) (*50*), where R = CH_3, CD_3, CH_3CH_2, CD_3CD_2, $(CH_3)_2CH$, and $(CH_3)_3C$. Because the ionization potential of the hydrogen atom and the RO *EA*s were measured at 0 K, and the GPAs of ROH were measured at 300 K, a thermal correction to the bond dissociation energy was incorporated into the values calculated in Table 4.7 (*50*) (This correction has been illustrated in the Appendix). The GPAs chosen were the directly determined

experimental values with the best error bars, where available, and those used for R = CH_3, $(CH_3)_2CH$, and $(CH_3)_3C$ are not significantly different than those measured in

Table 4.7. Derived thermochemical data. Values were computed with literature values for $\Delta_{acid}H_{300}$(ROH) and electron affinities from this work as outlined in Ref. (*50*). Numbers in parentheses are offered as alternative values originating from independent determinations. All values are in kJ/mol.

R	$\Delta_{acid}H_{300}$(ROH)	D_{300}(RO-H)	Δ_fH_{300}(RO)	$\Delta_fH_{300}(RO^-)$	$\Delta_fH_{300}(RO^+)$
CH_3	1600 ± 2[a]	440 ± 3	21 ± 4	-138 ± 2	1060 ± 10
CD_3	1597 ± 8[b]	436 ± 9	-	-	-
CH_3CH_2	1586 ± 5[c]	441 ± 6	-12 ± 7	-185 ± 5	980 ± 15
CD_3CD_2	1582 ± 9[d]	436 ± 10	-	-	-
$(CH_3)_2CH$	1578 ± 3[e] (1576 ± 4[c])	445 ± 4	-46 ± 5	-231 ± 4	840 ± 10
$(CH_3)_3C$	1575 ± 3[e] (1573 ± 3[c])	447 ± 4	-83 ± 5	-274 ± 4	810 ± 10

[a] Ref. (*43*)
[b] Ref. (*44*)
[c] Ref. (*48*)
[d] Ref. (*26*)
[e] Ref. (*45-47,49*)

DeTuri *et al*. (*48*). The calculated bond dissociation energy values (see Table 4.7) agree well with those of DeTuri *et al.* (*48*), who have used the *EA*s reported in this work with their GPAs to calculate bond dissociation energies. We find that within the given error bars, the energy needed for the reaction ROH → RO + H is relatively independent of R, where R is an aliphatic hydrocarbon.

In addition, literature values for Δ_fH_{300}(H) and $\Delta_fH_{300}(H^+)$ (*51*), Δ_fH_{300}(ROH) (*52*), and IP_0(RO)(*53-55*) allow calculation of the heats of formation for the undeuterated RO, RO^-, and RO^+ species according to the methods outlined in Ref. (*50*) and in Eq. 3.9. The Δ_fH_{300} (RO) and $\Delta_fH_{300}(RO^-)$ values show a stabilization

effect with an increase in the size of R. This effect is greater in the anion than in the radical, a result of inductive effects in the anion. The differences in the amount of stabilization in the anion with respect to the neutral may be examined most precisely by looking at the differences in the *EA*s. The *EA* changes by the same amount when going from CH_3O to CH_3CH_2O as when going from CH_3CH_2O to $(CH_3)_2CHO$, but the difference between the *EA*s of $(CH_3)_2CHO$ and $(CH_3)_3CO$ is only half that amount. This indicates that the degree of perturbation of the system decreases when substituting the last H in CH_3O for a methyl group.

It is also interesting to note that the same decrease in *EA*, 0.013 eV, is observed upon deuteration for both CH_3O and CH_3CH_2O. This implies that deuteration decreases the zero point energy by a greater amount in the radical than in the anion.

The heat of formation of the cation also displays a stabilization effect with increasing size of R. It should be noted that $\Delta_f H_{300}(RO^+)$ is highly dependent on the value of IP_0(RO), and in the case of $(CH_3)_2CHO$ and $(CH_3)_3CO$, the IP_0 values used are the only available measurements and have not been confirmed recently.

4.10 Conclusion

Photoelectron spectra of alkoxides were presented and analyzed. Jahn-Teller effects dominate the CH_3O^- and CD_3O spectra, with peaks of contrasting β value carrying different vibronic symmetry assignments. The splitting between the ground $\tilde{X}\ ^2$A" and first excited $\tilde{A}\ ^2$A' states of CH_3CH_2O is observed directly at 355 ± 10

cm^{-1}. This close spacing causes vibronic coupling between the two states that perturbs vibrational levels; as a result, the ability of theoretical calculations to effectively explain the vibrational structure of CH_3CH_2O is hindered. Both the $(CH_3)_2CHO^-$ and $(CH_3)_3CO^-$ spectra show good agreement with theoretical predictions. The splitting between the ground $\tilde{X}\ ^2A'$ and first excited $\tilde{A}\ ^2A''$ states of $(CH_3)_2CHO$ is determined to be $1225 \pm 65\ cm^{-1}$. No vibronic coupling is observed directly for $(CH_3)_2CHO$, as is true for Jahn-Teller activity in $(CH_3)_3CO$. There is no evidence of photodissociation of the species in any of the spectra. Finally, the electron affinities of all six neutrals (RO) were measured, showing good agreement with previous measurements, and in some cases to much greater accuracy. Values of D_{300}(RO-H), as well as the heat of formation for the alkoxide neutrals, anions, and cations are tabulated. We also see that although the ROO peroxides are larger molecules than the alkoxy RO radicals, it is the RO spectra that are more difficult to analyze and understand. This is due to the inherently bent ROO shape that avoids any of the Jahn-Teller degeneracy issues associated with a high symmetry C_{3v} geometrical configuration. The final chapter examines the spectra of diatomic metal oxides, which are the smallest molecules considered in this thesis, although they have also proven the most challenging to understand, and metal dioxides.

Bibliography

1. D. K. Russell and H. E. Radford, *J. Chem. Phys.* **72,** 2750 (1980).

2. Y. Endo, S. Saito, and E. Hirota, *J. Chem. Phys.* **81,** 122 (1984).

3. P. C. Engelking, G. B. Ellison, and W. C. Lineberger, *J. Chem. Phys.* **69,** 1826-1832 (1978).

4. H. R. Wendt and H. E. Hunziker, *J. Chem. Phys.* **71,** 5202-5205 (1979).

5. K. Ohbayashi, H. Akimoto, and I. Tanaka, *J. Phys. Chem.* **81,** 798-802 (1977).

6. B. K. Janousek, A. H. Zimmerman, K. J. Reed, and J. I. Brauman, *J. Am. Chem. Soc.* **100,** 6142-6148 (1978).

7. G. Inoue, H. Akimoto, and M. Okuda, *J. Chem. Phys.* **72,** 1769-1775 (1980).

8. G. Inoue, H. Akimoto, and M. Okuda, *Chem. Phys. Lett.* **63,** 213-216 (1979).

9. T. Ebata, H. Yanagishita, K. Obi, and I. Tanaka, *Chem. Phys.* **69,** 27-33 (1982).

10. S. C. Foster, Y. C. Hsu, C. P. Damo, X. M. Liu, C. Y. Kung, and T. A. Miller, *Journal of Physical Chemistry* **90,** 6766-6769 (1986).

11. S. C. Foster, P. Misra, T. Y. D. Lin, C. P. Damo, C. C. Carter, and T. A. Miller, *J. Phys. Chem.* **92,** 5914-5921 (1988).

12. K. Fuke, K. Ozawa, and K. Kaya, *Chem. Phys. Lett.* **126,** 119-123 (1986).

13. X. M. Liu, C. P. Damo, T. Y. D. Lin, S. C. Foster, P. Misra, L. Yu, and T. A. Miller, *J. Phys. Chem.* **93,** 2266-2275 (1989).

14. P. Misra, X. M. Zhu, C. Y. Hsueh, and J. B. Halpern, *Chem. Phys.* **178,** 377-385 (1993).

15. S. D. Brossard, P. G. Carrick, E. L. Chappell, S. C. Hulegaard, and P. C. Engelking, *J. Chem. Phys.* **84,** 2459-2465 (1986).

16. Y. Y. Lee, G. H. Wann, and Y. P. Lee, *J. Chem. Phys.* **99,** 9465-9471 (1993).

17. D. E. Powers, M. B. Pushkarsky, and T. A. Miller, *J. Chem. Phys.* **106,** 6863-6877 (1997).

18. A. Geers, J. Kappert, F. Temps, and T. J. Sears, *J. Chem. Phys.* **98,** 4297-4300 (1993).

19. F. Temps, personal communication.

20. K. B. Wiberg, *J. Am. Chem. Soc.* **112,** 3379 (1990).

21. D. R. Yarkony, H. F. Schaefer III, and S. Rothenberg, *J. Am. Chem. Soc.* **96,** 656-659 (1974).

22. G. D. Bent, G. F. Adams, R. H. Bartram, G. D. Purvis, and R. J. Bartlett, *J. Chem. Phys.* **76,** 4144-4156 (1982).

23. H. Koppel, *Z. Phys. Chem.* **200,** 3-10 (1997).

24. T. A. Barckholtz and T. A. Miller, *Int. Rev. Phys. Chem.* **17,** 435-524 (1998).

25. G. B. Ellison, P. C. Engelking, and W. C. Lineberger, *J. Phys. Chem.* **86,** 4873-4878 (1982).

26. T. T. Dang, E. L. Motell, M. J. Travers, E. P. Clifford, G. B. Ellison, C. H. DePuy, and V. M. Bierbaum, *Int. J. Mass Spectrom. Ion Process.* **123,** 171-185 (1993).

27. S. C. Foster and T. A. Miller, *J. Phys. Chem.* **93,** 5986-5999 (1989).

28. G. Inoue, M. Okuda, and H. Akimoto, *J. Chem. Phys.* **75,** 2060-2065 (1981).

29. X. Q. Tan, J. M. Williamson, S. C. Foster, and T. A. Miller, *J. Phys. Chem.* **97,** 9311-9316 (1993).

30. X. Zhu, M. M. Kamal, and P. Misra, *Pure Appl. Opt.* **5,** 1021 (1996).

31. L. A. Curtiss, D. J. Lucas, and J. A. Pople, *J. Chem. Phys.* **102,** 3292-3300 (1995).

32. C. Sosa and H. B. Schlegel, *J. Am. Chem. Soc.* **109,** 7007-7015 (1987).

33. R. J. Balla, H. H. Nelson, and J. R. Mcdonald, *Chem. Phys.* **99,** 323-335 (1985).

34. M. J. Frisch, G. W. Trucks, H. B. Schlegal, P. M. W. Gill, B. G. Johnson, M. A. Robb, J. R. Cheeseman, T. Kieth, G. A. Petersson, J. A. Montgomery, K. Raghavachari, M. A. Al-Laham, V. G. Zakrewski, J. V. Ortiz, J. B. Foresman, J. Cioslowski, B. B. Stefanov, A. Nanayakkara, M. Challacombe, C. Y. Peng, P. Y. Ayala, W. Chen, M. W. Wong, J. L. Andres, E. S. Replogle, R. Gomperts, R. L. Martin, D. J. Fox, J. S. Binkley, D. J. Defrees, J. Baker, J. J. P. Stewart, M. Head-Gordon, C. Gonzalez, and J. A. Pople, *Gaussian94*, Gaussian, Inc., 1994.

35. We wish to thank Peter Chen and Cameron Logan for providing a copy of their CDECK program.

36. D. L. Osborn, D. J. Leahy, E. H. Kim, E. De Beer, and D. M. Neumark, *Chem. Phys. Lett.* **292,** 651-655 (1998).

37. K. M. Ervin and W. C. Lineberger, *Journal of Physical Chemistry* **95,** 1167-1177 (1991).

38. F. Temps, "Molecular Dynamics and Spectroscopy by Stimulated Emission Pumping." World Scientific, Singapore, 1995.

39. P. G. Carrick, S. D. Brossard, and P. C. Engelking, *J. Chem. Phys.* **83,** 1995-1996 (1985).

40. L. S. Alconcel, J. A. Davies, H. J. Deyerl, and R. E. Continetti, personal communication.

41. T. A. Barckholtz and T. A. Miller, *J. Phys. Chem. A* **103,** 2321-2336 (1999).

42. T. A. Barckholtz, personal communication.

43. D. L. Osborn, D. J. Leahy, E. M. Ross, and D. M. Neumark, *Chem. Phys. Lett.* **235,** 484-489 (1995).

44. M. J. Haas and A. G. Harrison, *Int. J. Mass Spectrom. Ion Process.* **124,** 115-124 (1993).

45. S. G. Lias, J. E. Bartmess, J. F. Liebman, J. L. Holmes, R. D. Levin, and W. G. Mallard**,** J. Phys. Chem. Ref. Data **17,** Suppl. No. 1 (1988).

46. K. M. Ervin, S. Gronert, S. E. Barlow, M. K. Gilles, A. G. Harrison, V. M. Bierbaum, C. H. DePuy, W. C. Lineberger, and G. B. Ellison, *J. Am. Chem. Soc.* **112,** 5750-5759 (1990).

47. D. H. Mordaunt and M. N. R. Ashfold, *J. Chem. Phys.* **101,** 2630 (1994).

48. V. F. De Turi and K. M. Ervin, *J. Phys. Chem.* **103,** 6911 (1999).

49. V. F. De Turi, M. A. Su, and K. M. Ervin, *J. Phys. Chem.* **103,** 1468 (1999).

50. G. B. Ellison, G. E. Davico, V. M. Bierbaum, and C. H. DePuy, *Int. J. Mass Spectrom. Ion Process.* **156,** 109-131 (1996).

51. C. E. Moore, "Atomic Energy Levels." National Bureau of Standards, Washington, 1971.

52. J. B. Pedley, R. D. Naylor, and S. P. Kirby, "Thermochemical Data of Organic Compounds." Chapman and Hall, New York, 1986.

53. B. Ruscic and J. Berkowitz, *J. Chem. Phys.* **95,** 4033-4039 (1991).

54. B. Ruscic and J. Berkowitz, *J. Chem. Phys.* **101,** 10936-10946 (1994).

55. J. M. Williams and W. H. Hamill, *J. Chem. Phys.* **49,** 4467 (1968).

Chapter 5

Photoelectron spectroscopy of Group VIII transition metal oxides XO^-, OXO^- (X = Ni, Pd, and Pt)

5.1 Introduction

Metal oxides play a central role in a variety of fields including high temperature materials, catalysis, semiconductors, and electrode materials (*1-8*). Thus, understanding their properties has both technological and fundamental importance. Despite this importance, it is remarkable how relatively little information exists about the basic structure and properties of Ni, Pd, and Pt metal oxides, with the majority of the literature concentrating on the lighter metal oxides. The open d, p, and s shells give rise to an enormous complexity in the energy level structure that provides a daunting challenge to theorists and experimentalists alike.

For NiO, several experimental spectroscopic studies (*9-16*) have identified a $^3\Sigma^-$ ground state, measured the vibrational frequency, and measured the electron affinity (*15,16*), among other observations. An essentially Ni^+O^- ionic picture of the NiO ground state has emerged (*11,17*). This ionic framework is desirable because it allows the electronic properties of the molecule to be treated, to first order, as those of the atomic oxygen, which is well-understood. The experimental work has been supported by various theoretical studies of NiO ground and excited electronic states (*17-23*).

Much less is known for PdO and PdO^-. Several theoretical investigations (*17,24-29*) have concluded that either the $^3\Sigma^-$ or the $^3\Pi$ is the PdO ground state, both lying close in energy. Theoretical studies have found relativistic effects less important for PdO than PtO (*26,29*). PdO is calculated to be quite ionic (*17*), although covalent bonds are formed. The photoelectron spectrum of PdO^- was reported recently (*30*) where the negative ion was created in a laser ablation source.

For PtO, more spectroscopic data are available than for PdO although there are no anion photoelectron spectra. The electronic ground state of PtO was reported to be $^1\Sigma^+$ in early spectroscopic studies (*31-33*). Later, it became clear that the ground state is a $^3\Sigma^-$ state with a low-lying, related state only 936 cm^{-1} above the ground state (*34*). Scullman and co-workers (*35,36*) reported transitions to several uv-vis states of gaseous PtO, but have no information on the states lying 0-2 eV above the ground state. Theoretical efforts have primarily focused on the consequences of relativistic effects on the molecular geometry and other physical properties (*26,37*).

Information on the metal dioxide species ONiO, OPdO, and OPtO is scarce. Experimental data exist for ONiO and OPtO (*14,15,38*), and a few theoretical studies have calculated molecular structures and electronic properties (*28,39,40*). Several photoelectron spectroscopic studies have been carried out on similar metal molecules, such as CuO^- (*41,42*), RhO^- (*43*), PdC_2H^- and PdC_2HN^- (*44*), $PdCO^-$ and $PdCN^-$ (*45*).

One of the main difficulties associated with analysis of these metal oxide species lies in their inherent electronic structure (*46*). The valence configurations of the metal atoms include many open-shell d orbitals, which are spaced closely spaced

in energy and also close in energy to the valence s orbitals. Upon bonding with oxygen, the result is a molecule with a high density of valence energy levels, often rendering electronic spectra quite crowded and thus difficult to sort out. Furthermore, the proximity of energy states leads to mixing of the orbital characters, which results in spectroscopic properties that bear little resemblance to a simple zero-order picture. All these reasons render theoretical calculations difficult, even without the additional complication of relativistic effects. These include radial contraction of the s and p electrons along with the radial expansion of the outer d electrons, as well as spin-orbit splitting (*47*). The magnitude of these effects varies as Z^2, and therefore becomes dominant by the 6^{th} row metal oxides.

The 364 nm photoelectron spectra of XO^- and OXO^- molecules are presented (X=Ni, Pd, and Pt). The electron affinities (*EA*s) for all six molecules are identified, as well as vibrational frequencies and bond length changes. Several low-lying electronic states of the neutral and anion XO molecules are assigned, which allow for measurements of anion and neutral spin-orbit splittings. While the assignments reported here differ from some of the earlier photoelectron findings, the differences arise primarily from the better energy resolution available in the present apparatus. Vibrational frequencies for the OXO molecules are measured, as is the bond length change of $OPtO^-$ upon electron detachment. The measurements obtained here provide a much improved although still incomplete description of the low-lying states of these metal oxide molecules.

5.2 Experiment

As was discussed in detail in Chapter 2, the metal oxide anions were produced in the sputter source connected to the flowing afterglow. Metal oxide ions are produced downstream from the sputter source by adding a small amount of oxygen into the flow tube. Platinum is the easiest metal to sputter, producing ion currents of about 80 pA for PtO^-. NiO^- was by far the most difficult to obtain, with our best efforts producing < 10 pA. Typical metal dioxide currents, however, were roughly 100 pA. The hot anions produced in the sputter source undergo collisional relaxation with the He buffer gas in the flow tube. However, spectra were also collected with the flow tube cooled by liquid nitrogen, which substantially lowers the anion vibrational temperature. In this way, spectra were collected at both 300 K (no cooling) and 200 K (liquid nitrogen-cooled) flow tube temperatures.

To assist in the interpretation of the spectra, we carried out *ab initio* calculations for the electronic ground states of the OPtO anion and neutral species. The calculations employed the hybrid density functional theory (DFT) method B3LYP, and the SDD effective core potential/basis set was used for Pt while the aug-cc-pVTZ basis set was used for oxygen, as implemented in the GAUSSIAN 98 suite of programs (*48*). In addition, a harmonic-oscillator Franck-Condon program was used to simulate the vibrational progressions in the photoelectron spectra (*49*). Vibrational frequencies, origin peak position, and geometry differences between anion and neutral are directly determined from this simulation, without recourse to *ab initio* calculations.

5.3 Analysis of NiO, PdO, and PtO

5.3.1 NiO

An orbital diagram of the ground state of NiO is presented in Fig. 5.1. Although this is oversimplified and cannot be interpreted too literally (*46*), it can serve as a zero-order picture of the molecular orbitals to aid in analysis of the NiO^- photoelectron spectrum. The orbitals are formed from the $3d^8$ and $4s^2$ orbitals of Ni with the $2p^4$ orbitals of O. The result is bonding $\sigma^2\pi^4$ orbitals, nonbonding δ^4 orbitals, and weakly antibonding $d\sigma^2$ and π^2 orbitals. There are also nonbonding $4s\sigma^2$ orbitals formed from the valence 4s orbitals of Ni. There is a consensus in the literature that the ground state of NiO is a $\sigma^2\pi^4\delta^4\pi^2\sigma^2\ ^3\Sigma^-$ state (*9-11,17-20,50*) with substantial ionic character. To form the anion NiO^-, the extra electron fills one of the antibonding π orbitals to make a $^2\Pi_{3/2}$ state. In the 3.408 eV photoelectron spectrum of NiO^-, we expect to observe several low-lying neutral NiO states through detachment of any one of the $\delta^4\pi^3\sigma^2$ electrons. In general, detachment of $s\sigma$ electrons is expected to produce intense photoelectron peaks due to the fact that their diffuse spatial distributions yield a large cross-section for detachment. However, because the $d\sigma$ and $s\sigma$ orbitals are expected to be close in energy, they can mix and it is not unreasonable in these molecules to expect a large intensity from $d\sigma$ electron detachment as well.

The 364 nm photoelectron spectrum of NiO^- taken under 200 K flow tube conditions and 0° polarization direction is displayed in Fig. 5.2. The spectrum shows

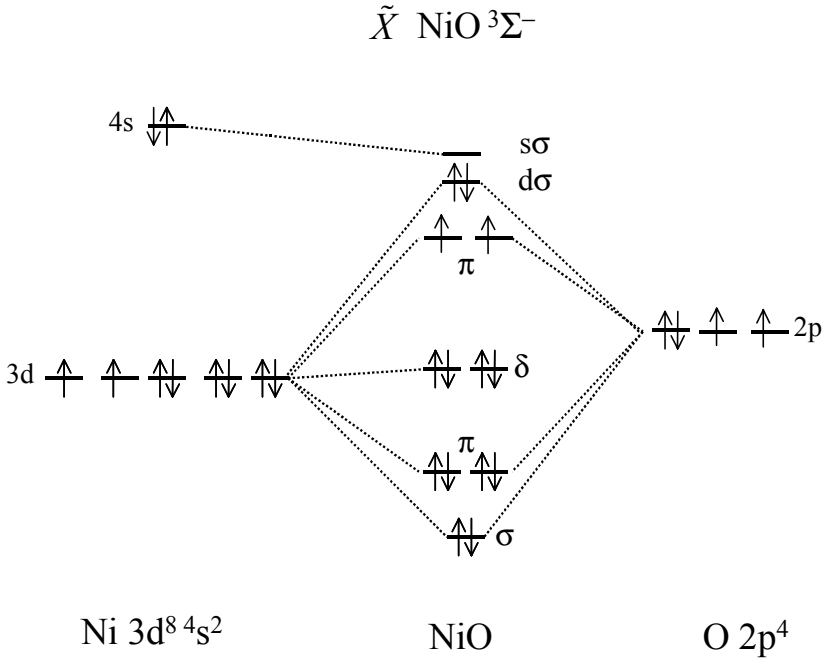

Figure 5.1. Molecular orbital diagram of the $^3\Sigma^-$ ground state of NiO showing the mixing of atomic O and Ni orbitals.

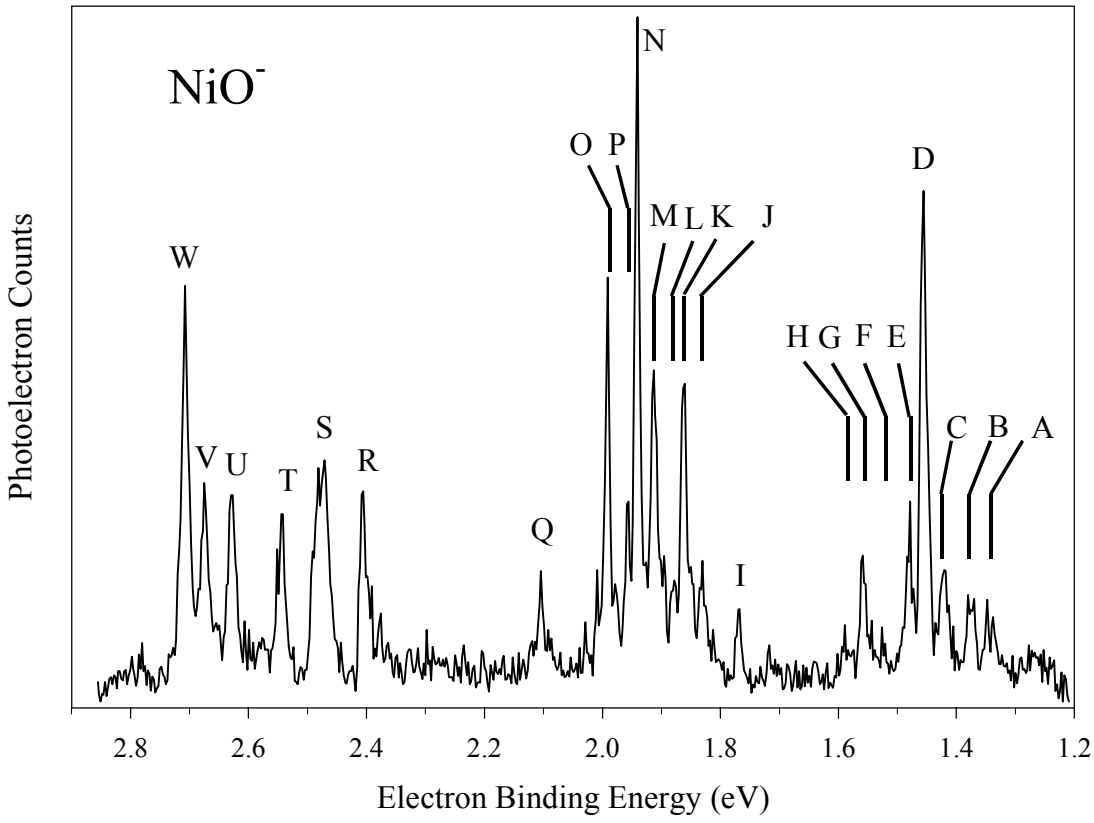

Figure 5.2. 364 nm photoelectron spectrum of NiO^- taken at 0° laser polarization angle and 200 K flow tube temperature.

many sharply resolved features, labeled A through W, with a large variation in intensity. There is a high density of peaks within about 1.5 eV, indicating transitions into several low-lying electronic states in neutral NiO. The β parameters were measured for every peak in the spectrum. With two exceptions, all the peaks in the spectrum yield β values of > 1. The exceptions are peaks I and Q, which both have an isotropic angular distribution, i.e., $\beta = 0$.

There have been two recent photoelectron spectroscopy studies of NiO^-, one by Wu and Wang (*15*) and one by Moravec and Jarrold (*16*). Both studies employ pulsed laser ablation ion sources coupled with time-of-flight electron kinetic energy analysis. The energy resolution is not constant over the spectrum energy range, but varies between roughly 10 and 50 meV. For metal oxides, NiO in particular with such a great density of peaks, the resolution results in blending several peaks together, eliminating many of the features observed here or changing their appearance or relative intensities. The result is that a full assignment of the spectrum can be very difficult. The spectra reported here are generally consistent with the earlier data (*15,16*), but the higher resolution permits observation of many new features that necessitate alternative interpretations. The differences in assignments are discussed below.

Peak N is the most intense peak in the spectrum and is located 0.485 eV above peak D. Peak P falls nearby at 0.536 eV above peak D. As was stated above, σ electron-detachment is expected to yield the highest intensity peaks. In this case, σ electron detachment from $\delta^4\sigma^2\pi^3$ NiO^- gives a $^3\Pi$ state. In a fluorescence detection experiment, Friedman-Hill and Field (*11*) measure the $^3\Pi_2$ state falling at 0.484 eV

Table 5.1. Absolute and relative positions, and assignments for peaks in the photoelectron spectrum of NiO^-.

Peak	Position (eV)	Relative Position (cm^{-1})	Assignment
A		-910 ± 15	$\tilde{X}\ ^3\Sigma^- \leftarrow \tilde{A}'$
B		-650 ± 10	$\tilde{X}\ ^3\Sigma^- \leftarrow \tilde{A}$
C		-275 ± 10	$\tilde{X}\ ^3\Sigma^- \leftarrow \tilde{X}'\ ^2\Pi_{1/2}$
D	1.455 ± 0.004		
E		190 ± 10	$\tilde{X}\ ^3\Sigma^-$ (v=1) $\leftarrow \tilde{A}$
F		550 ± 20	$\tilde{X}\ ^3\Sigma^-$ (v=1) $\leftarrow \tilde{X}'\ ^2\Pi_{1/2}$
G		825 ± 10	$\tilde{X}\ ^3\Sigma^-$ (v=1) $\leftarrow \tilde{X}\ ^2\Pi_{3/2}$
H		1055 ± 20	$\tilde{X}\ ^3\Sigma^-$ (v=2) $\leftarrow \tilde{A}$
I	1.768 ± 0.004	–	–
J		-885 ± 10	$^3\Pi_2 \leftarrow \tilde{A}'$
K		-635 ± 10	$^3\Pi_2 \leftarrow \tilde{A}$
L		-500 ± 10	$^3\Pi_1 \leftarrow \tilde{A}'$
M		-230 ± 10	$^3\Pi_1 \leftarrow \tilde{A}$ and $^3\Pi_2 \leftarrow \tilde{X}'\ ^2\Pi_{1/2}$ [a]
N	1.940 ± 0.004	0	$^3\Pi_2 \leftarrow \tilde{X}\ ^2\Pi_{3/2}$
O		125 ± 10	$^3\Pi_1 \leftarrow \tilde{X}'\ ^2\Pi_{1/2}$
P	1.991 ± 0.004	405 ± 10	$^3\Pi_1 \leftarrow \tilde{X}\ ^2\Pi_{3/2}$
Q	2.103 ± 0.004	–	–
R	2.404 ± 0.004	0	$^3\Phi_4$, $^3\Delta_3$, or $^3\Pi_2 \leftarrow \tilde{X}\ ^2\Pi_{3/2}$ [a]
S		575 ± 10	$^3\Phi_3$, $^3\Delta_2$, or $^3\Pi_1 \leftarrow \tilde{X}\ ^2\Pi_{3/2}$ [a]
T		1130 ± 10	$^3\Phi_2$, $^3\Delta_1$, or $^3\Pi_0 \leftarrow \tilde{X}\ ^2\Pi_{3/2}$ [a]
U		-640 ± 10	$^1\Pi \leftarrow \tilde{A}\ ^2\Pi_{3/2}$
V		-265 ± 10	$^1\Pi \leftarrow \tilde{X}'\ ^2\Pi_{1/2}$
W	2.706 ± 0.004	0	$^1\Pi \leftarrow \tilde{X}\ ^2\Pi_{3/2}$

[a] See text for details.

Table 5.2. Summary of assignments for NiO and NiO^-. All values are from this paper unless otherwise stated.

		Relative Energy(eV)	T_e (eV)	$\nu(cm^{-1})$	r_e (Å)
NiO^-	$\tilde{X}\ ^2\Pi_{3/2}$	-1.455(4) -1.470(3)[a] -1.46(2)[b]	0		1.67(1)
	$\tilde{X}'\ ^2\Pi_{1/2}$		0.034		
	$\tilde{A}$		0.081		
	$\tilde{A}'$		0.113		
NiO	$^3\Sigma^-$	0	0	825 840[a] 800[b] 839.69[c*] 825.74[d] 825.7[e]	1.627[g]
	?		0.313		1.67(1)
	$^3\Pi_2$		0.485 0.484[c]		1.67(1)
	$^3\Pi_1$		0.536 0.533[c] 0.532[a]		1.67(1)
	?		0.648		1.67(1)
	$^3\Phi_4$, $^3\Delta_3$, or $^3\Pi_2$[f]		0.949		1.67(1)
	$^3\Phi_3$, $^3\Delta_2$, or $^3\Pi_1$[f]		1.020		1.67(1)
	$^3\Phi_2$, $^3\Delta_1$, or $^3\Pi_0$[f]		1.089		1.67(1)
	$^1\Pi$		1.251		1.67(1)

[a] Ref. (*16*) (Anion photoelectron spectroscopy).
[b] Ref. (*15*) (Anion photoelectron spectroscopy).
[c] Ref. (*11*) (LIF).
[d] Ref. (*9*) (Matrix IR).
[e] Ref. (*14*) (Matrix IR).
[f] See text for details.
[g] Refs. (*10,12,13*).
* ω_e

excitation energy above the ground state. Likewise, they measure the $^3\Pi_1$ state at 0.533 eV. Both these measurements coincide with the spacing between peaks N and

P and peak D and securely fix the assignment of the $^3\Pi_2$ and $^3\Pi_1$ and $^3\Sigma^-$ states, respectively (see Tables 5.1 and 5.2). Therefore, peak D is assigned as the electron affinity transition, with *EA*(NiO) = 1.455 ± 0.004 eV. This agrees with the value of Wu and Wang (*15*) at 1.46(2) eV and qualitatively agrees with that of Moravec and Jarrold (*16*) at 1.470(3) eV. Moravec and Jarrold also find the $^3\Pi_1$ electronic state at 0.532 eV excitation energy, in agreement with our assignment. Wu and Wang assign this band to the $^3\Pi$ NiO electronic state. However, they put the $^3\Pi_1$ state at 0.49 eV excitation energy and the $^3\Pi_0$ state at 0.55 eV excitation energy, in conflict with the Friedman-Hill and Field (*11*) measurement cited above. This results in assigning their peak at 0.43 eV excitation energy as the $^3\Pi_2$ state, as opposed to the anion excited state assignment offered below. The spacing between the $^3\Pi_2$ and $^3\Pi_1$ peaks, 405 ± 10 cm^{-1}, gives the neutral NiO spin-orbit splitting (see Table 5.7). We do not observe the $^3\Pi_0 \leftarrow {}^2\Pi_{3/2}$ transition, which could be attributed to the spin-orbit value changing by more than ½.

Peak G, at a third of the intensity of the electron affinity peak, is 825 cm^{-1} to the higher binding energy side of peak D (Table 5.1). This value coincides with the vibrational frequency values measured in Argon matrix-isolated NiO (ν = 825.74 cm^{-1} from Ref. (*9*) and 825.7 cm^{-1} from Ref. (*14*)) and ω = 839.69 cm^{-1} measured in Ref. (*11*), and the photoelectron spectrum measurements of ν = 840 cm^{-1} (*16*) and ν = 800 cm^{-1} (*15*). Peak G, therefore, is assigned as the first quantum of the NiO stretch. Using a Franck-Condon fitting routine (*49*), a 0.04 ± 0.01 Å change in bond length is fit to the v=0 and v=1 peaks assuming a 1.627 Å measured neutral bond length (*10,12,13*). Because the detached electron comes from an antibonding orbital, the

anion bond length is expected to be larger than the neutral bond length. This results in a Ni-O^- separation of 1.67 ± 0.01 Å. As will be discussed below, peak G is the only manifestation of vibrational activity in the NiO^- spectrum. Therefore, the remaining peaks in the spectrum must be assigned to individual electronic states of NiO where the neutral bond length is nearly equal to the anion bond length of 1.67 Å (see Table 5.2).

The intensity of the (v=1) $^3\Sigma^- \leftarrow$ (v′=0) $^2\Pi_{3/2}$ peak (G) relative to the origin peak is determined by the magnitude of the $\langle 1|0\rangle^2$ Franck-Condon factor as explained in Eq. 1.5,

$$\frac{I(1,0)}{I(0,0)} = \langle 1|0\rangle^2 . \qquad (5.1)$$

Assuming a harmonic-oscillator approximation means that $\langle 1|0\rangle^2 = \langle 0|1\rangle^2$. The intensity of the (v=0) $^3\Sigma^- \leftarrow$ (v′=1) $^2\Pi_{3/2}$ peak relative to the origin peak depends on both the $\langle 0|1\rangle^2$ factor as well as the relative populations of the anion v=0 and v=1 states:

$$\frac{I(0,1)}{I(0,0)} = \frac{N(v=1)}{N(v=0)}\langle 1|0\rangle^2 . \qquad (5.2)$$

Given the fact that the intensity of peaks A-C is comparable to that of peak G, this means that if peaks A-C originate from vibrational hot bands, then

$$\frac{I(1,0)}{I(0,0)} \approx \frac{I(0,1)}{I(0,0)} . \qquad (5.3)$$

Equating Eqs. 5.1 and 5.2 implies that the population needed in the anion v′=1 state would have to be on the same order as that in the v=0 state, which is not at all likely in our ion source. Thus the intensity of peaks A-C is much too great to suggest they

originate from vibrational hot bands, as was assigned in Refs. (*15*) and (*16*). These peaks must result from transitions from electronically excited NiO^-. Furthermore, Peak C is 275 cm^{-1} from the *EA* peak, which is simply too small a frequency to be a NiO^- vibration. NiO has considerable ionic character and therefore the anion may be considered $Ni–O^-$ (*11*). Therefore the spin-orbit splitting would be expected to be on the order of the O^- spin-orbit splitting, which is about 180 cm^{-1} (*51*) as opposed to the Ni^- spin-orbit splitting, which is around 1500 cm^{-1} (*52*). The 275 cm^{-1} splitting observed here (Table 5.7) is in the range of what would be expected for the $^2\Pi_{3/2} - {}^2\Pi_{1/2}$ energy spacing of NiO^-. Thus peak C is assigned as the $^3\Sigma^- \leftarrow \tilde{X}' \, ^2\Pi_{1/2}$ transition.

Peaks A and B, therefore, must result from transitions originating in another anion excited electronic state. Peak B is 650 cm^{-1} from the electron affinity peak (Table 5.1) and is assigned as an unspecified $\tilde{A}$ state in the anion. Peak A is 260 cm^{-1} to the lower binding energy side of the $^3\Sigma^- \leftarrow \tilde{A}$ transition, which is similar to the anion $^2\Pi_{3/2}–{}^2\Pi_{1/2}$ spacing. Thus it is possible that peak A is the spin-orbit excited counterpart of this $^3\Sigma^- \leftarrow \tilde{A}$ peak. Peak A is assigned as an unspecified $\tilde{A}'$ state in the anion. One possible orbital configuration of this anion excited electronic state $\tilde{A}$ is (Fig. 5.1) the excitation of two $d\sigma^2$ electrons to $s\sigma^2$ electrons, which would produce a $^2\Pi_{3/2}$ state with a $\delta^4\pi^3 s\sigma^2$ configuration. This excited electronic state should have a $^2\Pi_{3/2} - {}^2\Pi_{1/2}$ energy spacing on the same order as that of the anion ground state splitting, as is what we observe here. Other possibilities include the spin-orbit

components of $d\sigma^1\ s\sigma^1\ ^{2,4}\Pi$ states. With the information available to us, a definite assignment is not possible.

Peak E is 190 cm^{-1} from the *EA* peak, which is too small to be the vibrational frequency of NiO. Instead, it is assigned to $^3\Sigma^-$ (v=1) $\leftarrow \tilde{A}$ (Table 5.1). Peak F is 825 cm^{-1} from peak C, which is the fundamental of the NiO vibration assigned above, and thus is attributed to the $\tilde{X}\ ^3\Sigma^-$ (v=1) $\leftarrow \tilde{X}'\ ^2\Pi_{1/2}$ transition. Peak H is 1055 cm^{-1} from peak D. This is most likely the $\tilde{X}\ ^3\Sigma^-$ (v=2) $\leftarrow \tilde{A}$ transition (825 x 2- 650 = 1000), although because peak H is somewhat ragged, there is some room for error in the interpretation.

Peak I, at a 0.313 eV term energy (Table 5.1), has an isotropic angular distribution ($\beta = 0$), in contrast to peaks A-H and J-P ($\beta > 1$). Thus it must constitute a separate electronic state. The relatively low intensity suggests detachment from a δ orbital. Walch and Goddard (*18*) calculate a $^1\Delta$ as the first excited state, although later calculations (*53*) place this state at much higher energies. Our data do not permit assignment of this state.

Peak K is 635 cm^{-1} to the lower binding energy side of the NiO $^3\Pi_2$ peak (N). This is the $NiO^-\ ^2\Pi_{3/2} - \tilde{A}$ spacing. Peak K is about half the intensity of peak N and, along the same line of reasoning outlined above, is too great to originate from a vibrational hot band and so it must come from an excited electronic state. Peak K is assigned as the $^3\Pi_2 \leftarrow \tilde{A}$ transition. Peak J falls 250 cm^{-1} to the lower binding energy side of peak K, which is the anion $\tilde{A} - \tilde{A}'$ spacing. Peak J is assigned as the $^3\Pi_2 \leftarrow \tilde{A}'$ transition (Table 5.1).

Peak M is 635 cm^{-1} from the NiO $^3\Pi_1$ peak (P). Because this is the $NiO^- \, ^2\Pi_{3/2} - \tilde{A}$ spacing, peak M receives the assignment $^3\Pi_1 \leftarrow \tilde{A}$. However, peak M is about ¾ the intensity of the NiO $^3\Pi_1$ peak, compared with the relative $^3\Pi_2 \leftarrow \tilde{A}$ and $^3\Pi_2 \leftarrow ^2\Pi_{3/2}$ intensities. Peak M also sits 230 cm^{-1} to the lower binding energy side of the $^3\Pi_2$ peak (N) and there is a shoulder to the right of peak M. This shoulder is the $^3\Pi_2 \leftarrow \tilde{X}' \, ^2\Pi_{1/2}$ transition. The two lines are close enough that their intensities both add into peak M, accounting for its additional intensity. Peak L falls 270 cm^{-1} from peak M ($^3\Pi_1 \leftarrow \tilde{A}$) and 905 cm^{-1} from peak P ($^3\Pi_1 \leftarrow \tilde{X} \, ^2\Pi_{3/2}$). Peak L receives the assignment $^3\Pi_1 \leftarrow \tilde{A}'$. Peak O is 280 cm^{-1} from the $^3\Pi_1 \leftarrow \tilde{X} \, ^2\Pi_{3/2}$ peak and thus is assigned as $^3\Pi_1 \leftarrow \tilde{X}' \, ^2\Pi_{1/2}$ (Table 5.1).

Peak Q appears 0.648 eV above the *EA* transition. This peak has a contrasting isotropic ($\beta = 0$) angular distribution from peaks J through P, and thus arises from a different electronic state. Furthermore, the intensity is much less than peaks in the $^3\Pi$ state, ruling out detachment of a σ electron to form this peak. As was the case for peak I, the relatively small intensity suggests detachment from a δ orbital. A possible assignment is the $^3\Phi$ state that Bauschlicher *et al.* (*17*) calculate at 0.720 eV, produced from detaching a non-bonding δ electron. The fact that the detached electron would be non-bonding correlates with the lack of vibrational structure observed. Moravec and Jarrold (*16*) assign this peak as the $^3\Phi_3$ state, and they find a second peak at 0.77 eV excitation energy that they ascribe to the $^3\Phi_2$ state. This latter peak is absent in our spectrum, and casts doubt on the $^3\Phi$ assignment. The $^1\Delta$ state seems more likely, but without further theoretical comparison, peak Q is unassigned.

Peak R is measured at 0.949 eV excitation energy, with peak S at 1.020 eV and T at 1.089 eV. Both Moravec and Jarrold (*16*) and Wu and Wang (*15*) observe this group of peaks, and assign them as a vibrational progression in a $^1\Delta$ NiO state. Although they are equally spaced, these three peaks are not likely to be a vibrational progression, however. Such an extended vibrational progression would necessitate a substantial change in bond length (> 0.1 Å). Even though a relative lack of vibrational activity is observed in the rest of the spectrum (only the ground state has any, with only a single quantum of excitation observed), this would not be impossible. However, such a bond length change would be expected to result in possibly another peak between peaks T and U, and would produce significant hot band excitation, neither of which we observe. These peaks are therefore assigned as transitions into a triplet NiO state.

The intensity of peaks R-T is smaller than most of the other peaks in the spectrum, which rules out σ electron detachment for the formation of these peaks. Bauschlicher *et al.* (*17*) calculate a $^3\Delta$ state at 1.02 eV excitation energy that would arise from π electron detachment. Another possibility is the $^3\Phi$ state created by detaching a δ electron. Bauschlicher *et al.* (*17*) predict this to lie at 0.720 eV above the $^3\Sigma^-$ state, and Bridgeman (*23*) calculates this state at 0.768 eV excitation energy. Finally, Walch and Goddard (*18*) predict a $^3\Pi$ state arising from a $\delta^3\pi^3\sigma^2$ configuration to lie approximately 1 eV above the ground state. Because more data are needed to choose between these potential assignments, peaks R, S, and T may be assigned to any of these three triplet states (Tables 5.1 and 5.2).

Peaks U, V, and W are a fairly intense ensemble of peaks with peak W 1.251 eV above the electron affinity peak (Table 5.1). One might expect that these peaks come from a neutral triplet state, like the $\delta^3\pi^3\sigma^2\ ^3\Pi$ assignment in Moravec and Jarrold (*16*) or the $\delta^3\pi^3\sigma^2\ ^3\Phi$ assignment by Wu and Wang (*15*). However, this is not the case. The intensity of peak W with respect to others in this spectrum suggests that it arises from detachment of a σ electron, not a δ electron whose cross section for detachment should be relatively small. Peaks V and U are spaced just as the hot bands seen for peaks D and N. Specifically, peak V is 265 cm^{-1} from peak W, which is the same anion $^2\Pi_{3/2}$–$^2\Pi_{1/2}$ splitting previously assigned, and peak U is 640 cm^{-1} from peak W, which is the anion $^2\Pi_{3/2}$– $\tilde{A}$ energy difference (see Table 5.1). The 265 cm^{-1} and 640 cm^{-1} energy spacing is repeated in several places in the NiO^- photoelectron spectrum presented here. However, the associated assignment of electronic (not vibrational) hot bands is truly anchored in peaks U and V, where only simple inspection of their intensities is needed to rule out a vibrational assignment. Therefore we assign peak W as the $^1\Pi \leftarrow\ ^2\Pi_{3/2}$ transition formed from detaching a σ electron. No spin-orbit splitting in the neutral state is observed, consistent with the singlet assignment. Peak W is assigned as the $^1\Pi \leftarrow\ ^2\Pi_{1/2}$ state while peak V corresponds to the $^1\Pi \leftarrow\ \tilde{A}$ transition.

A summary of results for the photoelectron spectrum of NiO^- is given in Table 5.2. In this spectrum we have identified transitions from four electronic states of the anion, the ground $\tilde{X}\ ^2\Pi_{3/2}$ state and its spin-orbit excited $\tilde{X}'\ ^2\Pi_{1/2}$ state at 275 cm^{-1} (Table 5.7), plus two additional unspecified $\tilde{A}$ and $\tilde{A}'$ electronic states at higher

excitation energies. In neutral NiO, the ground $^3\Sigma^-$ is observed and the electron affinity is 1.455 eV. The $^3\Pi$ and $^1\Pi$ states are assigned as well as another triplet state, either a $^3\Phi_{4,3,2}$, a $^3\Delta_{3,2,1}$, or a $^3\Pi_{2,1,0}$ state. The $^3\Pi_2$ and $^3\Pi_1$ spin-orbit spacing is 405 cm^{-1} (Table 5.7). A vibrational frequency of 825 cm^{-1} was found for the NiO ground state, as well as a bond length change of 0.04 Å, yielding an anion bond length of 1.67 Å.

5.3.2 PdO

The 364 nm photoelectron spectrum of PdO^- recorded at 200 K flow tube temperature and magic angle polarization is shown in Fig. 5.3. This is an expanded spectrum focusing on the lower binding energy range of the spectrum, although a full scan was also taken at 200 K flow tube temperature (not shown). There are several peaks of various intensities within a relatively small energy range, as was the case for NiO^-, although the density of peaks is considerably less than for NiO^-.

The orbital configuration for PdO^- may be treated as similar to that of NiO^- (see Fig. 5.1), with a $\sigma^2\ \pi^4\ \delta^4\ \pi^3\ \sigma^2\ \ ^2\Pi_{3/2}$ ground state. Those calculating PdO electronic states agree that the $\delta^4\ \pi^2\ \sigma^2\ ^3\Sigma^-$ and $\delta^4\ \pi^3\ \sigma^1\ ^3\Pi$ states lie close in energy (*17,24-28*), but are inconclusive as to which is the ground state. Peak A is small compared to others in the spectrum so it does not originate from the σ electron detachment that would produce the $^3\Pi$ state. Rather, the peak is produced from π electron detachment, resulting in the $^3\Sigma^-$ state. Thus the $^3\Sigma^- \leftarrow {}^2\Pi_{3/2}$ transition is

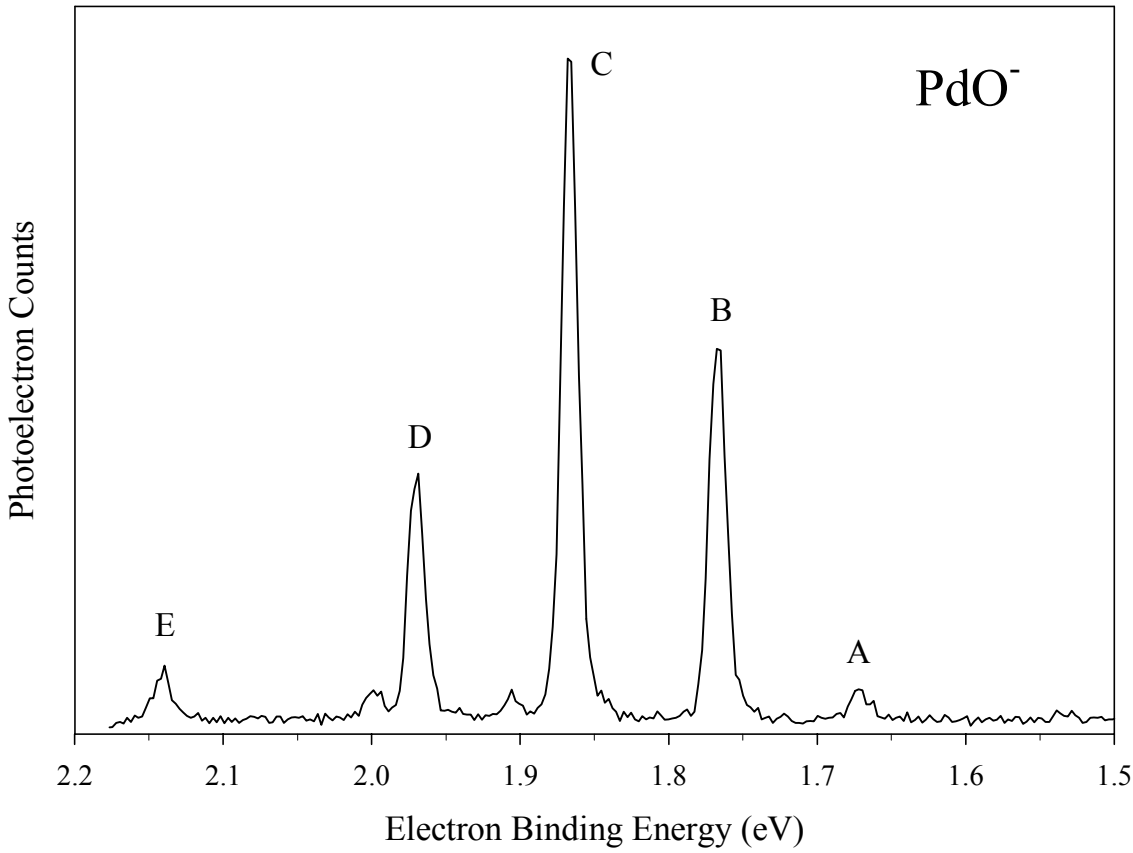

Figure 5.3. 364 nm photoelectron spectrum of the onset region of PdO^- taken at magic angle polarization and 200 K flow tube temperature.

assigned to peak A (see Tables 5.3 and 5.4) and corresponds to the electron affinity, *EA*(PdO) = 1.672 ± 0.004 eV. Klopcic *et al.* (*30*) have recently reported a photoelectron spectrum of PdO^- using a laser ablation ion source and a time of flight electron energy analyzer with roughly 5-50 meV energy resolution. The peaks in their photoelectron spectrum qualitatively match ours with one exception. They observe a peak at 1.570 eV binding energy that they take to be the electron affinity. This peak is absent in our spectrum (see Fig. 5.3) and for reasons outlined below, we differ in our assignment of the *EA*.

Peak B is located 0.095 eV above the *EA* transition (Table 5.3). It has a β of 0.8, which contrasts with that of peak A (0.4), and confirms that peaks A and B represent two different PdO electronic states. Peak B, therefore, is assigned as $^3\Pi \leftarrow {}^2\Pi_{3/2}$. The approximate 100 meV energy difference between the $^3\Pi$ and $^3\Sigma^-$ states in neutral PdO is consistent with calculations (*17,24-28*) that predict the two states to be close in energy. Furthermore, peak B is the second most-intense peak in the spectrum; thus it is expected to result from the σ electron detachment necessary to produce a $^3\Pi$ state in PdO.

Peaks B, C, and D form a trio of intense peaks. They all have similar angular distributions (β around 1) and are evenly spaced (about 0.1 eV between B and C and C and D). They do not constitute a vibrational progression, however, for several reasons. First, peaks B-D would make a relatively extensive vibrational progression. If this were the case, we would expect to see vibrational hot bands in the spectrum and we do not. Second, and more importantly, efforts to simulate these peaks as a vibrational progression using a Franck-Condon fitting routine (*49*) failed. The bond

Table 5.3. Absolute and relative positions, anisotropy parameters (β), and assignments for peaks in the photoelectron spectrum of PdO^-.

Peak	Position (eV)	Relative Position (cm^{-1})	β	Assignment
A′		-335 ± 20		$^3\Sigma^- \leftarrow \tilde{X}'\ ^2\Pi_{1/2}$
A	1.672 ± 0.004	0	0.4 (2)	$^3\Sigma^- \leftarrow \tilde{X}\ ^2\Pi_{3/2}$
B′		-340 ± 15		$^3\Pi_2 \leftarrow \tilde{X}'\ ^2\Pi_{1/2}$
B	1.767 ± 0.004	0	0.8 (1)	$^3\Pi_2 \leftarrow \tilde{X}\ ^2\Pi_{3/2}$
C′		-330 ± 10		$^3\Pi_1 \leftarrow \tilde{X}'\ ^2\Pi_{1/2}$
C	1.867 ± 0.004	0	1.5 (1)	$^3\Pi_1 \leftarrow \tilde{X}\ ^2\Pi_{3/2}$
D′		-345 ± 30		$^3\Pi_0 \leftarrow \tilde{X}'\ ^2\Pi_{1/2}$
D	1.970 ± 0.004	0	1.1 (1)	$^3\Pi_0 \leftarrow \tilde{X}\ ^2\Pi_{3/2}$
E′		-390 ± 30		$^1\Delta$, $^1\Sigma$, or $^3\Phi \leftarrow \tilde{X}\ ^2\Pi_{1/2}$ [a]
E	2.141 ± 0.004	0	1.1 (1)	$^1\Delta$, $^1\Sigma$, or $^3\Phi \leftarrow \tilde{X}\ ^2\Pi_{3/2}$ [a]
F′		-350 ± 15		$^1\Pi \leftarrow \tilde{X}'\ ^2\Pi_{1/2}$
F	2.236 ± 0.004	0	1.2 (1)	$^1\Pi \leftarrow \tilde{X}\ ^2\Pi_{3/2}$
G′		-350 ± 20		$^3\Phi$ or $^3\Pi \leftarrow \tilde{X}\ ^2\Pi_{1/2}$ [a]
G	2.454 ± 0.004	0	-0.2 (2)	$^3\Phi$ or $^3\Pi \leftarrow \tilde{X}\ ^2\Pi_{3/2}$ [a]

[a] See text for details.

Table 5.4. Summary of assignments for PdO and PdO^-.

		Relative Energy (eV)	T_e (eV)
PdO^-	$^2\Pi_{3/2}$	-1.672(4)	0
	$^2\Pi_{1/2}$		0.041
PdO	$^3\Sigma^-$	0	0
	$^3\Pi_2$		0.095
	$^3\Pi_1$		0.195
	$^3\Pi_0$		0.298
	$^1\Delta$, $^1\Sigma$, or $^3\Phi$		0.469
	$^1\Pi$		0.564
	$^3\Phi$ or $^3\Pi$		0.782

length change necessary to approach simulating the height of peak C results in a large v=3 peak that should appear between peaks D and E; no such peak appears in our spectrum (see Fig. 5.3). So, while the approximately 100 meV separation between peaks B, C, and D could equally well have represented either the PdO vibrational frequency or the spin-orbit splitting, the modeling rules out the former. Thus B, C, and D are assigned to the $^3\Pi_{2,1,0} \leftarrow {}^2\Pi_{3/2}$, respectively (Table 5.3). The neutral PdO $^3\Pi_2$–$^3\Pi_1$ spin-orbit splitting is measured to be 805 ± 10 cm^{-1} (Table 5.7).

Peak E is located at 0.469 eV excitation energy (Table 5.3). Its intensity eliminates an assignment as the $^1\Pi$ state, which would result from detaching a σ electron and would have a relatively large cross-section for detachment. A possible assignment is the $^3\Phi$ or $^1\Delta$ states formed by detaching a δ electron. Alternatively, Schwerdtfeger *et al.* (*24*) predict a $^1\Sigma^+$ state at 0.48 eV excitation energy. The data do not allow a selection between any of these possibilities. The small peaks to the higher binding energy side of peaks C and D are left unassigned.

Peaks F and G are the last two peaks visible in the full scan of the photoelectron spectrum of PdO^- at 200 K flow tube temperature (not shown), although they are out of the range of the close-up scan displayed in Fig. 5.3. They are, however, visible in the 300 K flow tube spectrum in Fig. 5.4, discussed below. Peak F, at 0.564 eV above the $^3\Sigma^- \leftarrow {}^2\Pi_{3/2}$ (Table 5.3), has a comparable intensity to the $^3\Pi_{2,1,0} \leftarrow {}^2\Pi_{3/2}$ peaks and a similar β (approximately 1). The height of the peak as well as its angular distribution points to σ electron detachment in its formation. Therefore peak F is assigned to the $^1\Pi \leftarrow {}^2\Pi_{3/2}$ transition.

Peak G at 0.782 eV excitation energy has an essentially isotropic angular distribution and is a relatively small feature in the spectrum. This suggests δ electron detachment and possible final states include $^3\Phi$ and $^1\Phi$ or a $^3\Pi$ or $^1\Pi$, depending on which δ electron is detached. Hund's rules would suggest that the triplet states would lie lower in energy than the singlet states, and therefore a $^3\Phi$ or $^3\Pi$ state is expected for the assignment for peak G. However, without additional *ab initio* investigation, the identity of this peak cannot be further specified.

The 364 nm photoelectron spectrum of PdO^- taken at 300 K flow tube temperature and magic angle polarization is displayed in Fig. 5.4. A comparison of Figs. 5.3 and 5.4 shows that every feature A-E in the 200 K flow tube spectrum doubles at a position of lower binding energy and at lower intensity. Comparing Fig. 5.4 and the full scan spectrum taken at 200 K flow tube temperature (not shown) reveals the same for peaks F and G. These "new" peaks are labeled A′-G′ in Fig. 5.4. They are obviously temperature dependent and must result from an anion excited state. The intensities of peaks A′-G′ are too great with respect to their unprimed counterparts to result from a vibrationally excited anion state especially due to the complete lack of transitions into vibrationally excited neutral PdO. Furthermore, the spacing between primed and unprimed peaks is 330 ± 10 cm^{-1} (choosing the spacing between peaks C and C′ with the smallest error—see Table 5.3), which is too small for the stretching vibration. Thus the primed peaks originate from an electronically excited anion state, either the $^2\Pi_{1/2}$ spin-orbit excited state or another low-lying excited electronic state.

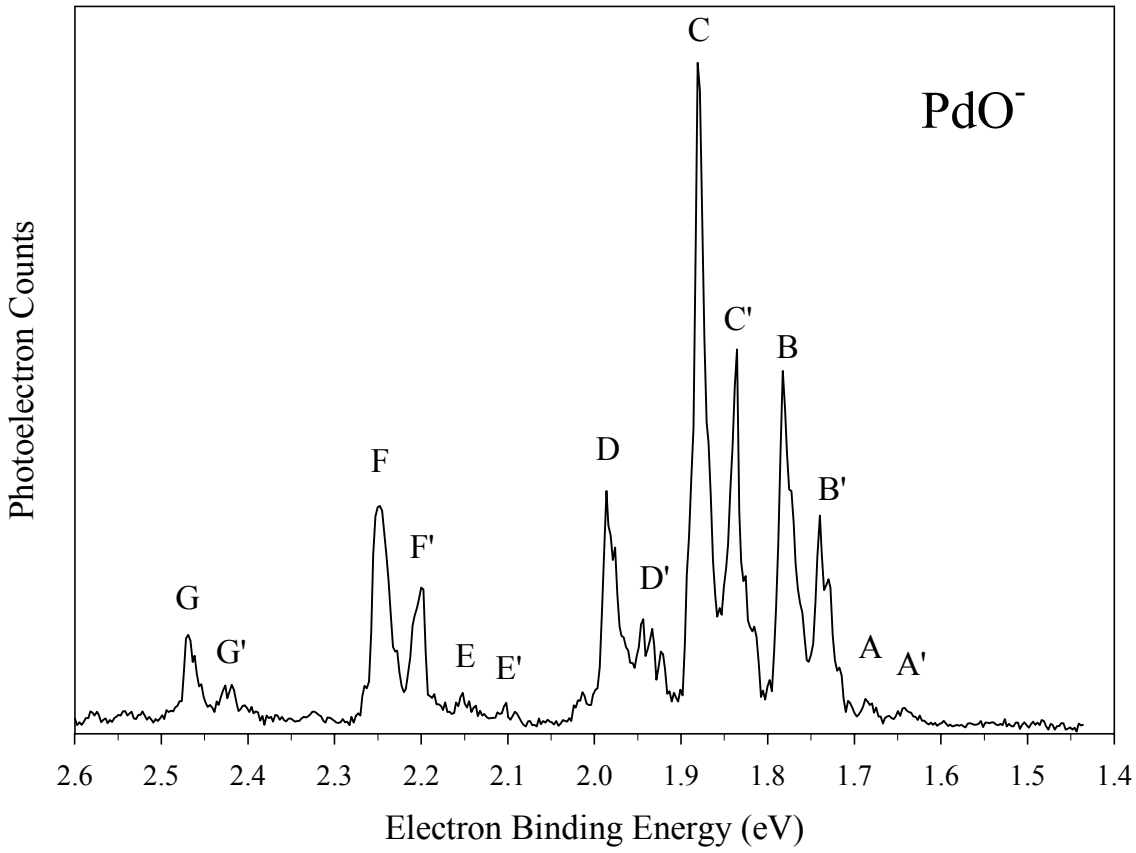

Figure 5.4. 364 nm magic angle photoelectron spectrum of PdO^- taken at 300 K flow tube temperature.

The spin-orbit excited state is the most likely explanation. The ionic nature of the Ni–O bond allowed a first-order estimate for the anion spin-orbit splitting (close to the splitting of O^-). That line of reasoning is not guaranteed to be applicable to PdO. However, a different argument is proposed for why the 330 cm^{-1} spacing between primed and unprimed peaks is expected as a spin-orbit splitting in PdO^-. The electron affinity of Pd^- is around 0.5 eV. This is relatively low, testifying to the low electronegativity of Pd. Thus in the PdO^- molecule, the extra electron would be expected to be more localized on the oxygen atom and so the spin-orbit splitting of PdO^- would be closer to the value of atomic O^- (approximately 200 cm^{-1}) than the Pd^- value (around 3000 cm^{-1} (*52*)). The primed peaks are therefore assigned as transitions from the anion spin-orbit excited $^2\Pi_{1/2}$ state.

In the photoelectron spectra of both NiO^- and PdO^- we identify anion $^2\Pi_{3/2}$ and $^2\Pi_{1/2}$ transitions into both $^3\Pi$ and $^1\Pi$ neutral states. The neutral spin-orbit splittings, about 400 cm^{-1} for NiO and around 800 cm^{-1} for PdO (Table 5.7), correlate well with the trends found for CuO (279 cm^{-1}) (*41*) and AgO (269 cm^{-1}) (*54,55*) for two reasons. First, the CuO and AgO splittings are closer to the atomic oxygen spin-orbit splitting (hundreds of cm^{-1}) than that of the metal atom (thousands of cm^{-1}), as is the case for NiO and PdO. Second, there is not a significant difference in the magnitude of the splitting going from CuO to AgO; in NiO and PdO, although the neutral spin-orbit splitting does double, the values still are closer to the O^- splitting than those of the metal anion.

The assignments extracted from the photoelectron spectrum of PdO are summarized in Table 5.4. Both the $^2\Pi_{3/2}$ and $^2\Pi_{1/2}$ PdO^- states as well as PdO $^3\Pi$

and $^1\Pi$ states are identified. The ground state of PdO was found to be $^3\Sigma^-$, as in NiO, and *EA*(PdO) = 1.672 eV. Two other excited PdO states were observed, one being either a $^1\Delta$, $^1\Sigma$, or $^3\Phi$ state and one being either a $^3\Pi$ or $^3\Phi$ state. No vibrational activity was observed in the spectrum, unlike in the NiO^- spectrum. The anion $^2\Pi_{3/2}$ – $^2\Pi_{1/2}$ splitting is 330 cm^{-1} while the neutral $^3\Pi_2$ - $^3\Pi_1$ splitting is 805 cm^{-1} (see Table 5.7).

5.3.3 PtO

The 200 K flow tube temperature photoelectron spectrum of $\delta^4\pi^3\sigma^2$ PtO^- recorded at magic angle laser polarization is displayed in Fig. 5.5. The spectrum shows two intense peaks surrounded by multiple smaller features. As was the reasoning in the photoelectron spectra of NiO^- and PdO^-, detaching a σ electron is expected to have a large cross section and therefore yield an intense photoelectron peak. As the orbital configuration for PtO may be treated as parallel to that of NiO and PdO (Fig. 5.1), this corresponds to production of a PtO Π state. Thus peaks F and K are transitions into Π electronic states. In analogy to the assignment in NiO^- and PdO^-, peak F is assigned as the transition into the $\delta^4\pi^3\sigma^1$ $^3\Pi_2$ state.

It is natural to suppose that peaks G and H are transitions into the $^3\Pi_1$ and $^3\Pi_0$ neutral states; however, this is not the case. Instead, peaks E, F, G, H, and I correspond to vibrational levels of the $^3\Pi_2 \leftarrow {}^2\Pi_{3/2}$ transition. Because peak E, which is 770 cm^{-1} from peak F, has an intensity that varies with the anion temperature, it is

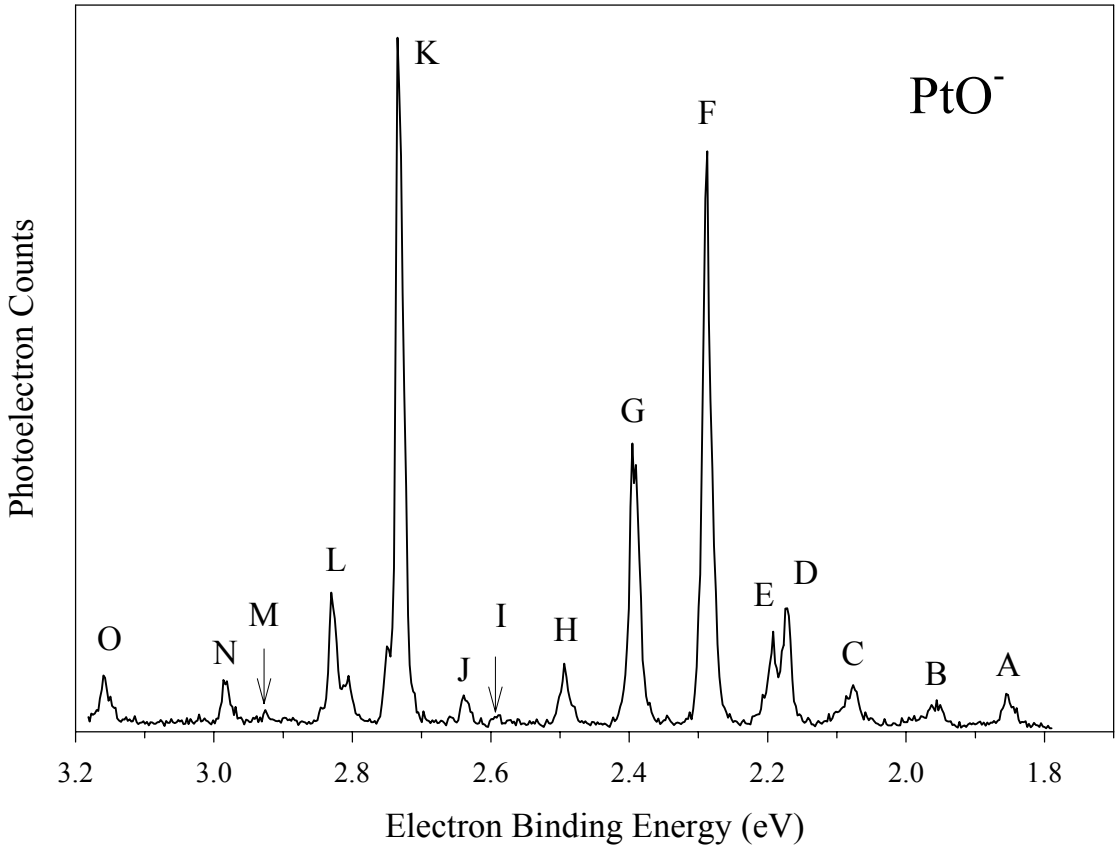

Figure 5.5. 364 nm magic angle photoelectron spectrum of PtO^- taken at 200 K flow tube temperature.

Table 5.5. Absolute and relative positions, anisotropy parameters (β), and assignments for the photoelectron spectrum of PtO^-.

Peak	Absolute Position (eV)	Relative Position (cm^{-1})	Position Relative to Peak F (cm^{-1})	β	Assignment [a]
A	1.851 (4)	0	-3510 (10)	0.4 (2)	$^3\Pi_2 \leftarrow {}^2\Pi_{1/2}$
B		855 (15)	-2655 (10)	0.3 (2)	$(v=1)\,^3\Pi_2 \leftarrow {}^2\Pi_{1/2}$
C		-770 (15)	-1695 (10)	0.0 (2)	$^3\Sigma_{0^+}^- \leftarrow (v=1)\,^2\Pi_{3/2}$
D	2.172 (4)	0	-930(10)	0.0 (1)	$^3\Sigma_{0^+}^- \leftarrow {}^2\Pi_{3/2}$
E		-770 (10)	-770(10)	0.9 (1)	$^3\Pi_2 \leftarrow (v=1)\,^2\Pi_{3/2}$
F	2.287 (4)	0	0	0.9 (1)	$^3\Pi_2$ and $^3\Sigma_1^- \leftarrow {}^2\Pi_{3/2}$
G		845 (10)	845 (10)	1.1 (1)	$(v=1)\,^3\Pi_2 \leftarrow {}^2\Pi_{3/2}$
H		1655 (10)	1655 (10)	1.1 (1)	$(v=2)\,^3\Pi_2 \leftarrow {}^2\Pi_{3/2}$
I		2450 (10)	2450 (10)	–	$(v=3)\,^3\Pi_2 \leftarrow {}^2\Pi_{3/2}$
J		-765 (10)	2815 (10)	0.4 (2)	$^3\Pi_1 \leftarrow (v=1)\,^2\Pi_{3/2}$
K	2.731 (4)	0	3580 (10)	1.1 (1)	$^3\Pi_1 \leftarrow {}^2\Pi_{3/2}$
L		780 (10)	4360 (10)	1.2 (1)	$(v=1)\,^3\Pi_1 \leftarrow {}^2\Pi_{3/2}$
M		1565 (10)	5145 (10)	–	$(v=2)\,^3\Pi_1 \leftarrow {}^2\Pi_{3/2}$
N	2.982 (4)			1.0 (2)	–
O	3.157 (4)			0.2 (2)	–

[a] All states are v=0 unless otherwise specified.

Table 5.6. Summary of assignments for PtO and PtO^-.

		Relative Energy(eV)	T_e (eV)	$\nu(cm^{-1})$	r_e(Å)
PtO^-	$^2\Pi_{3/2}$	-2.172	0	770	r_{PtO-}
	$^2\Pi_{1/2}$		0.321		
PtO	$^3\Sigma^-_{0^+}$	0	0		
	$^3\Pi_2$ and $^3\Sigma^-_1$		0.115	845	$r_{PtO-} - 0.05(1)^b$
			0.116[a]		
	$^3\Pi_1$		0.559	780	$r_{PtO-} - 0.035(10)^b$
	?		0.810		
	?		0.985		

[a] Measurement of $^3\Sigma^-_{0^+} - {}^3\Sigma^-_1$ splitting from Refs. (*34*) and (*35*).

[b] See text for details.

assigned to the v′=1 transition from the anion (see Tables 5.5 and 5.6). Peaks G, H, and I are transitions into the v=1,2, and 3 levels in $^3\Pi_2$ PtO, respectively. This conclusion is verified in several ways. First, the angular distributions for peaks E-H are equal (β around 1.0), indicating they all arise from detachment out of the same orbital. Second, the angular distributions of peaks A through D have contrasting values (β < 1) and thus are not assigned with peaks E-I. In addition, if peaks G and H were actually $^3\Pi_1$ and $^3\Pi_0$ states rather than the v=1 and v=2 of the $^3\Pi_2$ state, then there is no observed vibrational excitation of PtO, rendering the $\langle 2|0\rangle^2$ and $\langle 1|0\rangle^2$ Franck-Condon factors both < 0.01. The intensity of the (0,1) hot band relative to the (0,0) origin is given by

$$\frac{I(0,1)}{I(0,0)} = \frac{N(v=1)}{N(v=0)}\langle 1|0\rangle^2 \le 0.01\frac{N(v=1)}{N(v=0)}. \qquad (5.4)$$

As the observed intensity ratio between peaks E and F is about 0.1, this implies

$$\frac{N(v=1)}{N(v=0)} > 10 \ , \qquad (5.5)$$

which is an unreasonable population in the excited state. Thus we are forced to conclude that peaks F-I form a vibrational progression in $^3\Pi_2$ PtO.

To further support this conclusion, the intensities and positions of peaks E-I are well reproduced using a harmonic oscillator-approximation Franck-Condon fitting routine (*49*). The anion has a 770 cm^{-1} fundamental frequency, and the neutral fundamental frequency is 845 cm^{-1} (Table 5.5). These values are used in the simulation to determine a Pt—O bond length shortening of 0.05 ± 0.01 Å upon electron detachment from PtO^-, which is larger than the Δr_e measured in NiO. The detached electron is expected to be in an antibonding orbital (see Fig. 5.1), as is supported by the fact that the anion frequency is smaller than the neutral frequency. Therefore the removal of the electron shortens the PtO bond length.

Because in the photoelectron spectra of NiO^- and PdO^- we observe transitions into both the neutral $^3\Pi_2$ and $^3\Pi_1$ electronic states, we expect the same for PtO^-. Peaks J, K, L, and M are therefore attributed to $^3\Pi_1 \leftarrow {}^2\Pi_{3/2}$ transitions. Like the $^3\Pi_2 \leftarrow (v'=1)\ {}^2\Pi_{3/2}$ peak, peak J has an intensity dependent on the source temperature and thus is assigned as the v′=1 transition from the anion. Peaks L and M represent transitions into the v=1 and 2 levels in the neutral, respectively. Peaks K and L both have angular distributions of approximately 1.1. Like peaks E-I, both the intensities and positions of peaks J-M are quite accurately reproduced using a Franck-Condon fitting routine. In this case, the anion fundamental frequency is 765 cm^{-1} (identical to that measured in the $^3\Pi_2 \leftarrow {}^2\Pi_{3/2}$ transition) while the neutral fundamental is 780 cm^{-1}

(Table 5.5). Upon electron detachment the bond length shortens by an amount fit to be 0.035 ± 0.010 Å. Again, the anion frequency is smaller than the neutral frequency, although there is a smaller change (15 cm^{-1}) than in the $^3\Pi_2 \leftarrow {}^2\Pi_{3/2}$ case (75 cm^{-1}). This agrees with the smaller bond length change found, as well as the fact that the observed vibrational progression is less extensive than in the $^3\Pi_2 \leftarrow {}^2\Pi_{3/2}$ case. The PtO $^3\Pi_2$–$^3\Pi_1$ spacing, 3580 ± 10 cm^{-1}, gives the neutral spin-orbit splitting (see Table 5.7).

Table 5.7. Anion $^2\Pi_{3/2}$–$^2\Pi_{1/2}$ spin-orbit splittings and neutral $^3\Pi_2$–$^3\Pi_1$ spin-orbit splittings for the NiO, PdO, and PtO molecules.

	$^2\Pi_{3/2}$–$^2\Pi_{1/2}$	$^3\Pi_2$–$^3\Pi_1$
NiO	275 ± 10 cm^{-1}	405 ± 10 cm^{-1}
PdO	330 ± 10 cm^{-1}	805 ± 10 cm^{-1}
PtO	3510 ± 10 cm^{-1}	3580 ± 10 cm^{-1}

As was the case for the PdO^- photoelectron spectrum, there are peaks to the lower binding energy side of the $^3\Pi_2 \leftarrow {}^2\Pi_{3/2}$ peak with significantly smaller intensity and contrasting angular distribution (< 1). Peak D is sharp and well-defined, while peaks A-C are broad and less intense. The identity of the PtO $^3\Sigma^-_{0^+}$ ground state is well established (*26,33-36*), which is the same $^3\Sigma^-$ ground state of NiO and PdO. The first excited state $^3\Sigma^-_1$ of PtO was observed 936 cm^{-1} above the ground state (*34,35*). These two PtO states are related to each other. The lower energy one is the $\mathbf{0}^+$ state while the other is the **1** state in Hund's coupling case *c* (*56*), which together correspond to the $^3\Sigma^-$ ground state of PtO (*35,36*). Peak D is located 930 ± 10 cm^{-1} to the lower binding energy side of the $^3\Pi_2 \leftarrow {}^2\Pi_{3/2}$ peak (Table 5.5), which matches

the observed $^3\Sigma_1^- - ^3\Sigma_{0^+}^-$ splitting. Peak F therefore is coincident with the second half of the ground state, the $^3\Sigma_1^-$ peak. Peak D is assigned as the electron affinity, EA(PtO) = 2.172 ± 0.004 eV.

The intensity of peaks A-C relative to the $^3\Pi_2 \leftarrow {}^2\Pi_{3/2}$ peak varies with the source temperature. These peaks originate from excited states in the anion. Peak C is located 770 cm^{-1} to the lower binding energy side of the $^3\Sigma_{0^+}^- \leftarrow {}^2\Pi_{3/2}$ peak (Table 5.5), which is the anion $^2\Pi_{3/2}$ fundamental frequency. It also shares the same isotropic angular distribution as the electron affinity peak. Peak C therefore is assigned as the transition from the v=1 anion level to the $^3\Sigma_{0^+}^-$ PtO state. Peak A is located 3510 ± 10 cm^{-1} from the $^3\Pi_2 \leftarrow {}^2\Pi_{3/2}$ peak, and peak B is the same distance from the (v=1) $^3\Pi_2 \leftarrow {}^2\Pi_{3/2}$ peak. Peaks A and B, therefore, are assigned as transitions from the anion spin-orbit excited $^2\Pi_{1/2}$ states into the v = 0 and 1 levels of neutral $^3\Pi_2$ PtO, respectively. By analogy, one would expect to see the (v=2) $^3\Pi_2 \leftarrow {}^2\Pi_{1/2}$ transition and at first glance peak C would be the candidate. This is not completely the case, however. The (v=2) $^3\Pi_2 \leftarrow {}^2\Pi_{1/2}$ transition would be expected to have a smaller intensity than peaks A and B, which is not true for peak C. Also, the spacing between peak C and H is 3350 cm^{-1}, 160 cm^{-1} short of the required spacing. However, there is a small shoulder to the lower binding energy side of peak C that fulfills the required interpeak spacings and is of the expected intensity. Regardless, the (v=2) $^3\Pi_2 \leftarrow {}^2\Pi_{1/2}$ transition should have a small enough intensity (in analogy to the relative intensities of the v = 0, 1, and 2 $^3\Pi_2 \leftarrow {}^2\Pi_{3/2}$ peaks) that it blends into the structure of peak C.

Frum and co-workers (*36*) observed a $^3\Pi$ state with a $\delta^3\pi^3\sigma^2$ configuration. They measured a $^3\Pi_2 - {}^3\Sigma_{0^+}^-$ splitting of 8935 cm^{-1} (1.108 eV). Therefore a peak corresponding to this $^3\Pi_2$ state (when peak D is the *EA*) should be at 1.108 + 2.172 = 3.28 eV. In addition, a weaker transition to the $^3\Pi_0$ level might appear at 3.19 eV. However, the sensitivity of the electron kinetic energy analyzer drops off for binding energies greater than about 3.2 eV. The fact that we do not see either of these transitions is a consequence of the instrument cutoff and therefore remains consistent with the electron affinity $^3\Sigma_{0^+}^-$ assignment to peak D at 2.172 eV.

The electron affinity assignment given here is the one that allows for the most consistent analysis of the peaks based on literature values. We agree with the 936 cm^{-1} experimental $^3\Sigma_1^- - {}^3\Sigma_{0^+}^-$ splitting of Sassenberg and Scullman (*34,35*) with the spacing between peaks D and F, and observe a repetition of that spacing between peaks E and C. Furthermore, we are consistent with the measurements of Frum *et al.* (*36*) discussed above. If peaks A, B, or C were assigned as the electron affinity, we would disagree with either Frum *et al.* or Sassenberg and Scullman by substantial amounts (> 100 cm^{-1}). In addition, with peak A assigned as the $^3\Pi_2 \leftarrow {}^2\Pi_{1/2}$ hot band transition, the anion spin-orbit splitting of 3510 cm^{-1} is of comparable magnitude as the spin-orbit splitting in the neutral PtO, as measured between peaks F and K, 3580 cm^{-1}, which would be expected. Finally, the 0.115 eV splitting between the $^3\Sigma^-$ and $^3\Pi_2$ states in PtO is nearly equal to that in PdO (0.095 eV). The relative intensities

of the $^3\Sigma^- \leftarrow {}^2\Pi_{3/2}$ and $^3\Pi_2 \leftarrow {}^2\Pi_{3/2}$ transitions are also the same between the spectra of PtO^- and PdO^- as are the relative angular distributions.

Peak N, at 0.810 eV excitation energy (Table 5.5), remains unassigned. Peak O sits at 0.985 eV excitation energy and has an isotropic angular distribution. This is similar to peak G in the photoelectron spectrum of PdO^- (Fig. 5.4) because both peaks are around 1 eV above the ground state and both show isotropic angular distributions. Consequently, both should receive the same assignment, although it is not clear what that assignment should be.

As summarized in Table 5.6, like the spectra of NiO^- and PdO^-, the photoelectron spectrum of PtO^- shows transitions from both the anion $^2\Pi_{3/2}$ and $^2\Pi_{1/2}$ states, and a $^3\Sigma^-$ neutral ground state. PtO $^3\Pi_2$ and $^3\Pi_1$ states were also identified, and *EA*(PtO) = 2.172 eV. An anion vibrational frequency of 770 cm^{-1} was measured, as well as a neutral PtO stretch of 845 cm^{-1} in the $^3\Pi_2$ state and 780 cm^{-1} in the $^3\Pi_1$ state. The bond length is measured to shorten by 0.05 Å for the $^3\Pi_2 \leftarrow {}^2\Pi_{3/2}$ transition while it shortens by 0.035 Å for the $^3\Pi_1 \leftarrow {}^2\Pi_{3/2}$ transition. The anion $^2\Pi_{3/2}$ - $^2\Pi_{1/2}$ splitting is 3510 cm^{-1} while the neutral $^3\Pi_2$ - $^3\Pi_1$ splitting is 3580 cm^{-1} (Table 5.7).

5.4 Discussion of NiO, PdO, and PtO

Spectroscopic studies of NiO by Friedman-Hill and Field (*11*) show that the ground state of NiO is strongly ionic and imply that the anion is formed by adding an

essentially nonbonding electron to Ni, giving a zero-order Ni – O^- structure. For both PdO and NiO, the observed spin orbit splittings in both the $\pi^3\sigma\ ^3\Pi_2$ neutral and the $\pi^3\sigma^2\ ^2\Pi$ anion are closer to the O^- splitting than the metal spin orbit splitting (see Table 5.7). This observation makes a very strong case that both NiO and PdO are strongly ionic, with PdO somewhat less ionic than NiO, based upon its larger spin-orbit splitting. However, the PtO^- spin-orbit splitting of around 3500 cm^{-1} is more accurately described as roughly halfway between the atomic anion spin-orbit splittings of O^- (180 cm^{-1} (*51*)) and Pt^- (around 9500 cm^{-1} (*57*)). Thus the PtO bond possesses a significantly higher covalent character than either NiO or PdO.

A single peak in the photoelectron spectrum of NiO^- is assigned as vibrational excitation in the neutral ground state. Transitions into the several remaining NiO electronic states display no vibrational excitation and thus originate from detaching essentially nonbonding electrons. For electron detachment from PdO^-, no vibrational excitation is observed indicating detachment of only nonbonding electrons. In contrast, in the spectrum of PtO^-, not only are two extended vibrational progressions observed, but one of those originates from a larger Δr_e than in the NiO^- case. These observations are a direct indication of the important relativistic effects on the valence orbitals of PtO. The antibonding orbitals from which the anion electrons are detached have become more antibonding than in NiO and PdO. Furthermore, the relativistic contraction of the metal atom s orbitals is expected to have two important effects. One is that the reduction in size allows better mixing with the oxygen p orbitals, rendering the $s\sigma^2$ orbitals no longer non-bonding. Second, the relativistic expansion of the metal d orbitals in conjunction with this contraction of the metal s orbitals

allows for better mixing of the characters of the $s\sigma^2$ and the HOMO $d\sigma^2$ orbitals. The shift of the metal 4s contribution from non-bonding to anti-bonding $s\sigma^2$ orbitals and the mixing of the $s\sigma^2$ and $d\sigma^2$ orbitals implies an increased influence of the metal on the HOMO electron properties, testifying to the significant increase in covalent character of the PtO bond with respect to the NiO and PdO bonds.

As explained above, the covalent nature of the PtO bond means that the spin orbit splitting in both the anion $\pi^3\sigma^2$ states and the neutral $\pi^3\sigma$ states should approach the mean of the splittings for the individual atoms. It is for this reason that the $^3\Pi_2 - {}^3\Pi_1$ splitting increases from 405 cm^{-1} in NiO, to 805 cm^{-1} in PdO, and to 3580 cm^{-1} in PtO (see Table 5.7). Thus, peak K must correspond to the transition to the $^3\Pi_2$ state of PtO, rather than the $^1\Pi$ state. The photoelectron spectra of NiO^- and PdO^- exhibit strong transitions to the $\pi^3\sigma$ $^3\Pi_2$ and $^3\Pi_1$ electronic states. If peak K were assigned as the $^1\Pi$ state, it would leave unanswered the question of where is the $^3\Pi_1$ state, which must be both intense and accessible with 3.408 eV photons. These observations are supported by previous theoretical findings. Chung *et al.* (*26*) performed gradient-corrected density functional calculations incorporating relativistic effects on NiO, PdO, and PtO. They find a change in bonding mechanism going from NiO to PtO molecules. Despite the fact that PtO has many more protons, neutrons, and electrons than PdO, the strong relativistic contraction in PtO results in a bond length calculated to be shorter than that of PdO due to an enhanced covalence of the Pt—O bond.

5.5 Analysis of ONiO, OPdO, and OPtO

5.5.1 ONiO

The 364 nm magic angle photoelectron spectrum of $ONiO^-$ at 300 K flow tube temperature is show in Fig. 5.6. The spectrum shows relatively few features within 3.408 eV of available photon energy, resulting from the dropoff of energy analyzer sensitivity for electron kinetic energies less than about 0.2 electron kinetic energy (eKE) (electron binding energies greater than approximately 3.2 eV). Peaks A and C appear to be part of a Franck-Condon progression of peaks, with the much more intense peak (A) being the origin. It is therefore assigned as the electron affinity at 3.043 ± 0.004 eV (see Table 5.8). Recently, Wu and Wang (*15*) reported the photoelectron spectra of both NiO_2^- and $ONiO^-$. Our result agrees nicely with their measurement of *EA*(ONiO) = 3.05(1) eV. Furthermore, Gutsev *et al.* (*40*) calculate an electron affinity of *EA*(ONiO) = 3.25 eV, agreeing with the measurement presented here.

Peak C is separated from the electron affinity peak by 745 cm^{-1}. This agrees with Wang *et al.* (*15*), who measure a vibrational frequency of 750 cm^{-1}. Peak C is assigned as the fundamental in the symmetric stretch frequency of ONiO.

Peaks B and D are small features, each located to the higher binding energy side of the $\tilde{X}$ v=0 and 1 peaks by 250 cm^{-1} each. Peaks B and D retain the same

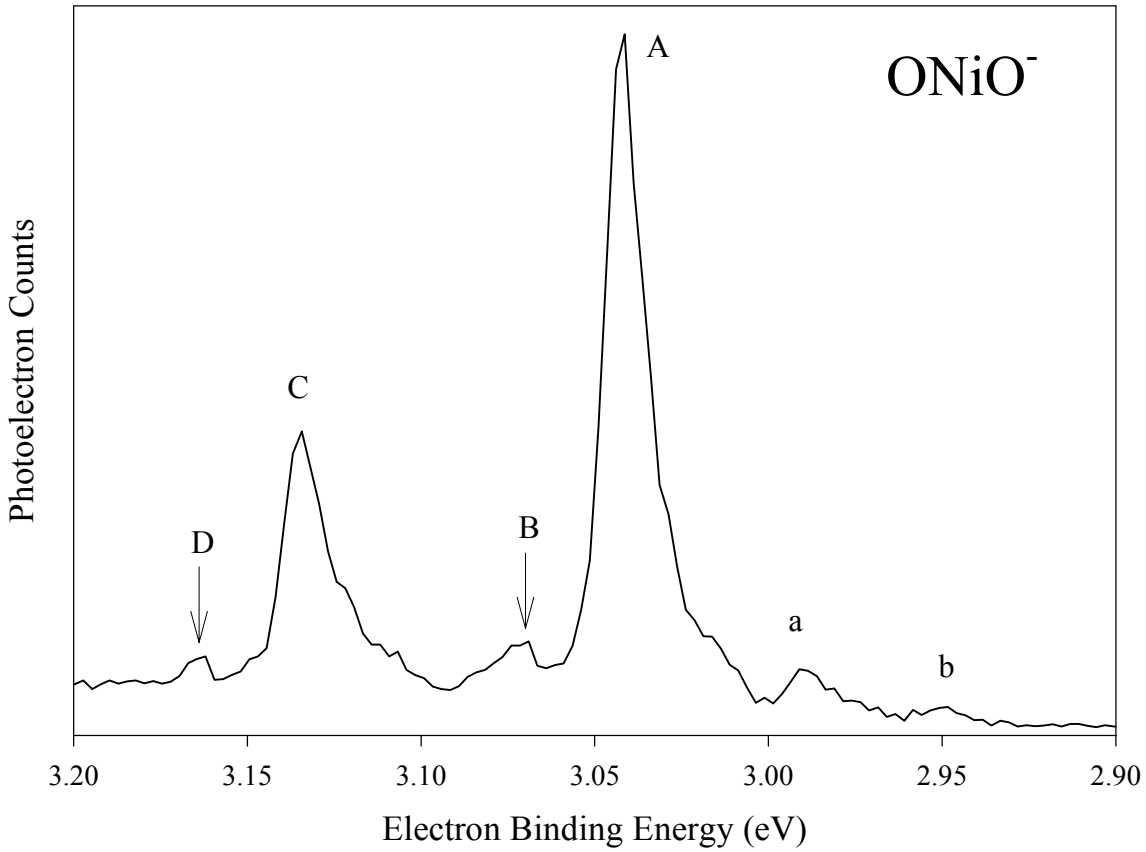

Figure 5.6. 364 nm magic angle photoelectron spectrum of $ONiO^-$ at 300 K flow tube temperature.

Table 5.8. Electron affinity and vibrational frequency measurements and literature values for the OXO $^1\Sigma_g^+ \leftarrow {}^2A_2$ OXO^- (X=Ni, Pd, Pt) photoelectron spectra.

OXO	*EA* (OXO) (eV)[a]	Literature (eV)	Symmetric Stretch ν(cm^{-1})	Literature (cm^{-1})	r_{X-O} (Å)
$ONiO^-$			715 ± 15		
ONiO	3.043 ± 0.004	3.05 ± 0.01[b] 3.25[c]	745 ± 10	750 ± 30[b] 819[c]	
OPdO	3.086 ± 0.004		680 ± 10	730[d]	
$OPtO^-$			760 ± 15	870[f]	r_{Pt-O-}
OPtO	2.677 ± 0.004	2.72 ± 0.20[e]	895 ± 10	980[f]	$r_{Pt-O-} - 0.07(1)$

[a] This work.
[b] Photoelectron spectrum measurement: Ref (*15*).
[c] DFT calculation: Ref. (*40*).
[d] B3LYP calculation: Ref. (*28*).
[e] Thermodynamic cycle determination: Ref. (*38*).
[f] B3LYP calculation, unscaled, this paper.

relative intensities in the cool sample ONiO photoelectron spectrum (not shown), ruling out vibrational hot bands as a possible assignment. Peaks a and b to the lower binding energy side of peak A vanish upon cooling the sample and are assigned as hot bands. Peak b is 715 cm^{-1} from peak A, which is similar to the 750 cm^{-1} stretch frequency assigned to the neutral. Peak b, therefore, is assigned as the symmetric stretch $v'=1$ transition from the anion. Peak a, at 425 cm^{-1} from peak A, could be an excitation of an anion bending mode, or alternatively may be an excitation from the anion spin-orbit excited state. Without further data to choose between these possibilities, peak a remains unassigned.

It is expected that ONiO has a linear structure (*58*). Gutsev *et al.* (*40*) calculate a linear $^1\Sigma_g^+$ ground state of ONiO with an 819 cm^{-1} symmetric stretch

frequency, which confirms our vibrational assignment (see Table 5.8). They also calculate a slightly bent $^2A_2$ anion ground state with a 170° ONiO bond angle. Thus the calculations find both ONiO and $ONiO^-$ are essentially linear molecules, and it is reasonable to assume the same geometry for OPdO and OPtO molecules and their anions. It is possible that peaks B and D therefore originate from transitions into two quanta of a neutral low-frequency antisymmetric bending mode, which would be Franck-Condon-allowed but not intense. Alternatively, Gutsev *et al.* (*40*) calculate a low-lying $^3A_2$ ONiO state at only 560 cm^{-1} excitation energy. It is possible that peaks B and D may be attributed to this state.

5.5.2 OPdO

The 200 K flow tube temperature 364 nm magic angle photoelectron spectrum of $OPdO^-$ is shown in Fig. 5.7. The spectrum is remarkably similar to that of $ONiO^-$ in Fig. 5.6. Peak A is assigned as the electron affinity at 3.086 ± 0.004 eV. Peak B is 680 cm^{-1} from the electron affinity peak, and is assigned as one quantum in the symmetric stretch vibration. There are no known experimental data with which to compare these values. As stated above, Gutsev *et al.* (*40*) calculates a linear $^1\Sigma_g^+$ ground state for ONiO and this is assumed to be true for OPdO and OPtO (*28,39*). Bare *et al.* (*28*) calculate a linear OPdO $^1\Sigma_g$ state with 730 cm^{-1} symmetric stretch frequency, which agrees with the value reported here.

Peak a falls at 340 cm^{-1} to the lower binding energy side of the electron affinity. This peak retains the same relative intensity in both the 300 K (not shown)

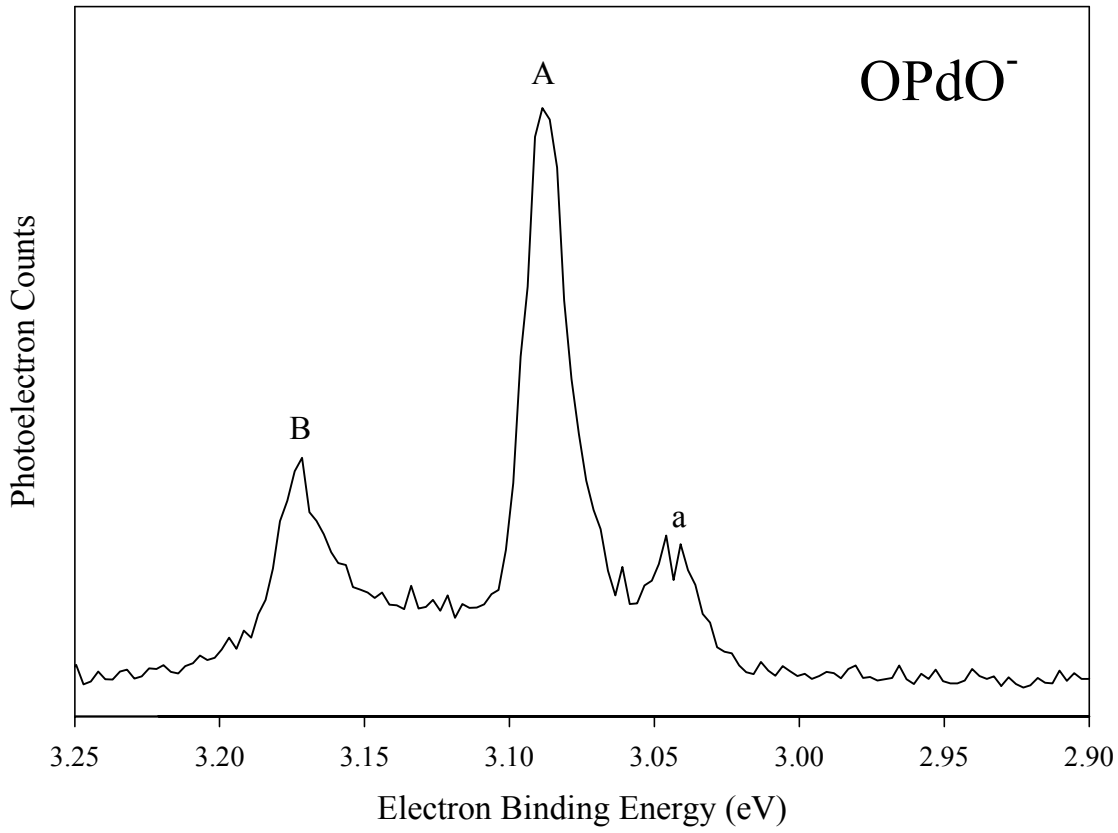

Figure 5.7. 364 nm photoelectron spectrum of $OPdO^-$ taken at magic angle polarization angle and 200 K flow tube temperature.

and 200 K flow tube temperature spectra, thus it cannot be a vibrational hot band. This suggests that peak a originates from a spin-orbit excited state in the anion.

5.5.3 OPtO

The magic angle, 200 K flow tube temperature 364 nm photoelectron spectrum of $OPtO^-$ is displayed in Fig. 5.8. Peaks a, b, and c display temperature dependence whereas peak A, which has a much stronger intensity than peaks a-c, does not. Peak A is assigned as the 0-0 transition from the anion, yielding *EA*(OPtO) = 2.677 ± 0.004 eV. The photoelectron spectrum of $OPtO^-$ contrasts with that of $ONiO^-$ and $OPdO^-$ in that the lower electron affinity of OPtO (2.7 eV versus 3.1 eV—see Table 5.8) allows for a larger number of accessible features within the 3.408 eV photon energy. The *EA* is in agreement with the value reported by Rudnyi and co-workers (2.72 ± 0.20 eV) (*38*), although the error bars are improved by almost 2 orders of magnitude. Peaks A through E represent transitions into four quanta of a single vibrational mode in the ground electronic state of OPtO with the fundamental frequency of this symmetric stretching mode measured to be 895 cm^{-1}.

As stated above, peaks a, b, and c are clear evidence of the presence of hot bands. From the position of peak a (v′=1) and b (v′=2) with respect to the electron affinity the vibrational frequency of $OPtO^-$ is obtained, 760 cm^{-1}. However, the separation between peaks b and c is larger than the one between a and b by greater

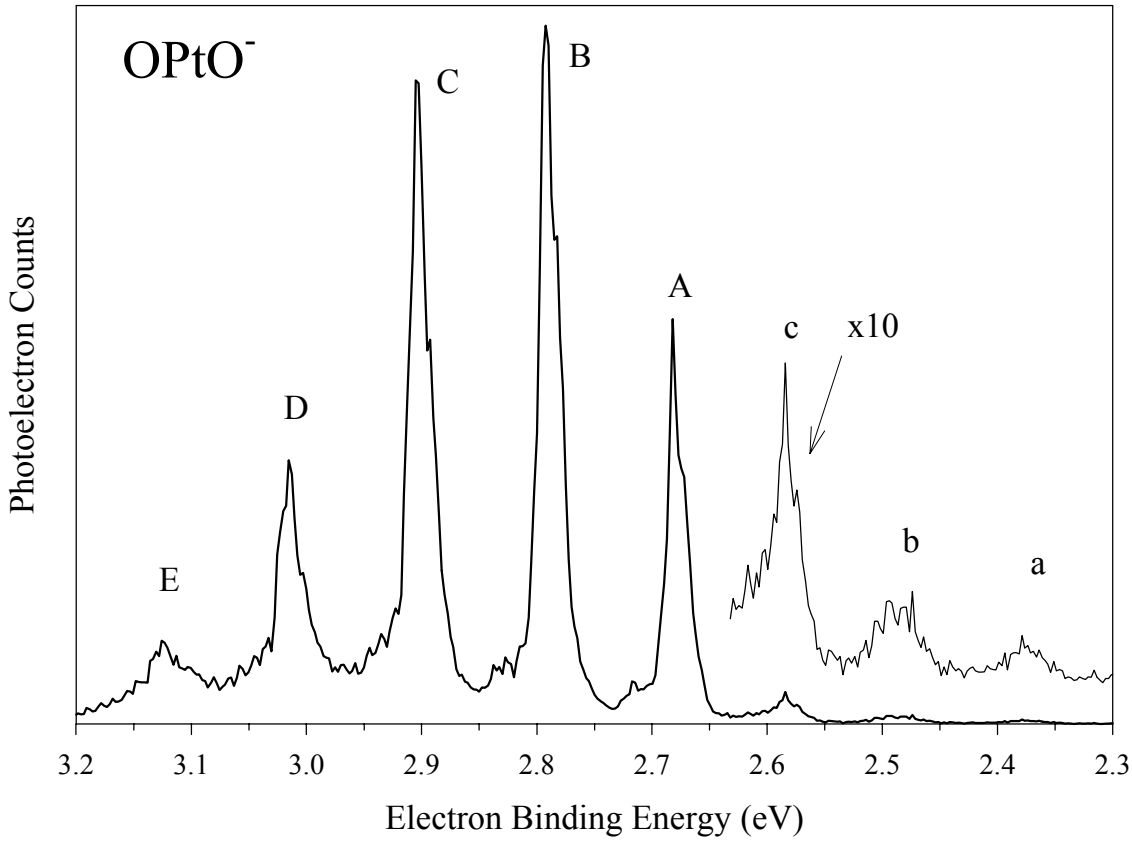

Figure 5.8. 364 nm photoelectron spectrum of OPtO– taken at magic angle polarization angle and 200 K flow tube temperature.

than 100 cm^{-1}. Peak c is broad enough to suggest that it is likely composed of both the v′=3 transition from the anion as well as the spin-orbit excited state of the anion.

Because the OPtO photoelectron spectrum consists of an extended vibrational progression with several resolved peaks, it was simulated using a Franck-Condon empirical fitting routine (*49*). In this way we were able to fit the change in molecular geometry to the spectrum features. Assuming a linear molecule symmetric about the Pt atom, the Pt—O bond length was found to change by 0.07 ± 0.01 Å when transitioning from anion to neutral OPtO. This is a substantial bond length change, which agrees with the broad Franck-Condon profile observed in this photoelectron spectrum.

Ab initio frequencies and molecular geometries were also calculated for OPtO and $OPtO^-$. The Pt—O bond length in the anion was found to be 1.778 Å while that of the neutral was shorter at 1.707 Å. This yields a bond contraction of 0.071 Å, in excellent agreement with the empirical finding described above. Furthermore, a shorter bond in neutral OPtO indicates that the detached electron originated from an antibonding HOMO in the anion. Table 5.8 shows the calculated frequency values that agree very well with the experimental values, when scaled by an empirical 0.93 factor. In agreement with previous calculations (*28*), the molecular geometry of both $OPtO^-$ and OPtO ground states is predicted to be linear. Consequently, only one totally symmetric mode (the symmetric stretching mode) could be active within the Franck-Condon approximation in the $^1\Sigma_g$ ground state of OPtO, in agreement with the experimental results.

5.6 Discussion of ONiO, OPdO, and OPtO

The spectra of $ONiO^-$ and $OPdO^-$ display quickly decaying peak profiles. Extrapolating from the ratio of heights of the electron affinity peak to the neutral v=1 symmetric stretch vibration in Figs. 5.6 and 5.7, even with greater laser photon energy, one would expect to see essentially one more peak in the vibrational progression. This contrasts with the extended profile observed in $OPtO^-$, where the origin peak is not the most intense. As was the case for PtO discussed above with respect to NiO and PdO, we have evidence for significantly greater vibrational activity in OPtO with respect to ONiO and OPdO. In the OPtO case, detaching the anion electron produces a greater bond length change than in ONiO or OPdO due to a HOMO electron that is more antibonding. This is a result of an increased covalent nature of the O—Pt bond as was discussed for PtO.

Spectra were also taken at different polarization angles (not shown) for all three OXO molecules. A value of 0.6 was obtained for the anisotropy parameter (β) across the different peaks of the spectra of both $OPtO^-$ and $OPdO^-$. This value is consistent with electron detachment from a molecular orbital of π symmetry and agrees with values obtained for similar systems where a π electron is detached, as in the case of WO_2^- (*59*). The calculations agree with this picture indicating that the extra electron in the anion is occupying a π^* molecular orbital. This result also agrees with the fact that the anion shows a smaller stretching frequency that the neutral, suggesting that the extra electron in the anion is occupying an antibonding orbital. In

contrast, however, the spectrum of $ONiO^-$ yields a β value of –0.2, which may be considered an isotropic angular distribution.

5.7 Conclusion

The 364 nm photoelectron spectra of XO^- and OXO^- anions (X=Ni, Pd, and Pt) were recorded and analyzed. Electron affinities ($^3\Sigma^- \leftarrow {}^2\Pi_{3/2}$) were identified for all three XO^- spectra. Anion $^2\Pi_{3/2}$–$^2\Pi_{3/2}$ spin-orbit splittings were identified as well as neutral $^3\Pi_2$–$^3\Pi_1$ spin-orbit splittings for NiO, PdO, and PtO. Several of the assignments for NiO and PdO were corrected from existing literature values. A small amount of vibrational activity was observed in the spectra of NiO^- and significantly more was observed in PtO^-, and bond length changes were deduced. Molecular spin-orbit splittings attest to the large covalent character of the PtO bond with respect to the NiO and PdO bonds. Electron affinities and symmetric stretch vibrational frequencies were extracted from the spectra of the OXO^- molecules, as well as an O-X bond length change in OPtO.

Bibliography

1. H. Y. H. Chan, S. Zou, and M. J. Weaver, *J. Phys. Chem. B* **103,** 11141-11151 (1999).

2. T. Sasaki, N. Koshizaki, and K. M. Beck, *Appl. Phys. A: Mater. Sci. Process.* **69,** S771-S774 (1999).

3. L. Maya, L. Riester, T. Thundat, and C. S. Yust, *J. Appl. Phys.* **84,** 6382-6386 (1998).

4. O. L. Shcheka, N. V. Dobrodey, and T. B. Emelina, *Int. J. Quantum Chem.* **50,** 181-188 (1994).

5. G. Boschloo and A. Hagfeldt, *J. Phys. Chem. B* **105,** 3039-3044 (2001).

6. S. C. Su, J. N. Carstens, and A. T. Bell, *J. Catal.* **176,** 125-135 (1998).

7. V. Biju and M. A. Khadar, *Mat. Sci. Eng. A-Struct.* **304,** 814-817 (2001).

8. J. R. Mc Bride, G. W. Graham, C. R. Peters, and W. H. Weber, *J. Appl. Phys.* **69,** 1596-1604 (1991).

9. D. W. Green, G. T. Reedy, and J. G. Kay, *J. Mol. Spectrosc.* **78,** 257-266 (1979).

10. V. I. Srdanov and D. O. Harris, *J. Chem. Phys.* **89,** 2748-2753 (1988).

11. E. J. Friedman-Hill and R. W. Field, *J. Mol. Spectrosc.* **155,** 259-276 (1992).

12. R. S. Ram and P. F. Bernath, *J. Mol. Spectrosc.* **155,** 315-325 (1992).

13. K.-I. Namiki and S. Saito, *Chem. Phys. Lett.* **252,** 343-347 (1996).

14. A. Citra, G. V. Chertihin, L. Andrews, and M. Neurock, *J. Phys. Chem. A* **101,** 3109-3118 (1997).

15. H. Wu and L.-S. Wang, *J. Chem. Phys.* **107,** 16-21 (1997).

16. V. D. Moravec and C. C. Jarrold, *J. Chem. Phys.* **108,** 1804-1810 (1998).

17. C. W. Bauschlicher, Jr. , C. J. Nelin, and P. S. Bagus, *J. Chem. Phys.* **82,** 3265-3276 (1985).

18. S. P. Walch and W. A. Goddard III, *J. Am. Chem. Soc.* **100,** 1338-1348 (1978).

19. C. W. Bauschlicher, Jr., *Chem. Phys.* **93,** 399-404 (1985).

20. M. Dolg, U. Wedig, H. Stoll, and H. Preuss, *J. Chem. Phys.* **86,** 2123-2131 (1987).

21. E. G. Bakalbassis, M.-A. D. Stiakaki, A. C. Tsipis, and C. A. Tsipis, *Chem. Phys.* **205,** 389-399 (1996).

22. E. Lorda, F. Illas, and P. S. Bagus, *Chem. Phys. Lett.* **256,** 377-382 (1996).

23. A. J. Bridgeman, *J. Chem. Soc. Dalton. Trans.***,** 4555-4562 (1996).

24. P. Schwerdtfeger, J. S. Mc Featers, J. J. Moore, D. M. Mc Pherson, R. P. Cooney, G. A. Bowmaker, M. Dolg, and D. Andrae, *Langmuir* **7,** 116-125 (1991).

25. P. E. M. Siegbahn, *Chem. Phys. Lett.* **201,** 15-23 (1993).

26. S.-C. Chung, S. Kruger, G. Pacchioni, and N. Rosch, *J. Chem. Phys.* **102,** 3695-3702 (1995).

27. E. Broclawik, R. Yamauchi, A. Endou, M. Kubo, and A. Miyamoto, *J. Chem. Phys.* **104,** 4098-4104 (1996).

28. W. D. Bare, A. Citra, G. V. Chertihin, and L. Andrews, *J. Phys. Chem. A* **103,** 5456-5462 (1999).

29. A. Dedieu, *Chem. Rev.* **100,** 543-600 (2000).

30. S. A. Klopcic, V. D. Moravec, and C. C. Jarrold, *J. Chem. Phys.* **110,** 10216-10217 (1999).

31. C. Nilsson, R. Scullman, and N. Mehendale, *J. Mol. Spectrosc.* **35,** 172-189 (1970).

32. R. Scullman, U. Sassenberg, and C. Nilsson, *Can. J. Phys.* **53,** 1991-1999 (1975).

33. K. Jansson and R. Scullman, *J. Mol. Spectrosc.* **61,** 299-312 (1976).

34. U. Sassenberg and R. Scullman, *J. Mol. Spectrosc.* **68,** 331-332 (1977).

35. U. Sassenberg and R. Scullman, *Phys. Scr.* **28,** 139-149 (1983).

36. C. I. Frum, R. Engleman, Jr. , and P. F. Bernath, *J. Mol. Spectrosc.* **150,** 566-575 (1991).

37. E. J. J. Kirchner, E. J. Baerends, U. Van Slooten, and A. W. Kleyn, *J. Chem. Phys.* **97,** 3821-3830 (1992).

38. E. B. Rudnyi, O. V. Kuznetsova, E. A. Kaibicheva, and L. N. Sidorov, *Temperatur* **28,** 864-870 (1991).

39. P. E. M. Siegbahn, *J. Phys. Chem.* **97,** 9096-9102 (1993).

40. G. L. Gutsev, B. K. Rao, and P. Jena, *J. Phys. Chem. A* **104,** 11961-11971 (2000).

41. M. L. Polak, M. K. Gilles, J. Ho, and W. C. Lineberger, *J. Phys. Chem.* **95,** 3460-3462 (1991).

42. H. Wu, S. R. Desai, and L.-S. Wang, *J. Phys. Chem. A* **101,** 2103-2111 (1997).

43. X. Li and L.-S. Wang, *J. Chem. Phys.* **109,** 5264-5268 (1998).

44. V. D. Moravec and C. C. Jarrold, *J. Chem. Phys.* **112,** 792-798 (2000).

45. S. A. Klopcic, V. D. Moravec, and C. C. Jarrold, *J. Chem. Phys.* **110,** 8986-8991 (1999).

46. A. J. Merer, *Annu. Rev. Phys. Chem.* **40,** 407-38 (1989).

47. P. Pyykko, *Chem. Rev.* **88,** 563-594 (1988).

48. M. J. Frisch, G. W. Trucks, H. B. Schlegel, G. E. Scuseria, M. A. Robb, J. R. Cheeseman, V. G. Zakrzewski, J. A. Montgomery, R. E. Stratmann, J. C. Burant, S. Dapprich, J. M. Millam, A. D. Daniels, K. N. Kudin, M. C. Strain, O. Farkas, J. Tomasi, V. Barone, M. Cossi, R. Cammi, B. Mennucci, C. Pomelli, C. Adamo, S. Clifford, J. Ochterski, G. A. Petersson, P. Y. Ayala, Q. Cui, K. Morokuma, D. K. Malick, A. D. Rabuck, K. Raghavachari, J. V. Foresman, J. Cioslowski, J. V. Ortiz, A. G. Baboul, B. B. Stefanov, G. Liu, A. Liashenko, P. Piskorz, I. Komaromi, R. Gomperts, R. L. Martin, D. J. Fox, T. Keith, M. A. Al-Laham, C. Y. Peng, A. Nanayakkara, C. Gonzales, M. Challacombe, P. M. W. Gill, B. Johnson, W. Chen, M. W. Wong, J. L. Andres, M. Head-Gordon, E. S. Replogle, and J. A. Pople, *Gaussian 98*, Gaussian, Inc., 1998.

49. K. M. Ervin, *PESCAL99*, 1999.

50. C. W. Bauschlicher, Jr. and P. Maitre, *Theor. Chim. Acta* **90,** 189-203 (1995).

51. D. M. Neumark, K. R. Lykke, T. Andersen, and W. C. Lineberger, *Phys. Rev. A* **32,** 1890-1892 (1985).

52. M. Scheer, C. A. Brodie, R. C. Bilodeau, and H. K. Haugen, *Phys. Rev. A* **58,** 2051-2062 (1998).

53. C. W. Bauschlicher, Jr. , S. R. Langhoff, H. Partridge, and M. Sodupe, *J. Phys. Chem.* **97,** 856-859 (1993).

54. T. C. Steimle, K. Y. Jung, and B.-Z. Li, *J. Chem. Phys.* **103,** 1767-1772 (1995).

55. L. C. O' Brien, S. J. Wall, and M. K. Sieber, *J. Mol. Spectrosc.* **183,** 57-60 (1997).

56. P. F. Bernath, "Spectra of Atoms and Molecules." Oxford University Press, New York, NY, 1995.

57. J. Thøgersen, M. Scheer, L. D. Steele, and H. K. Haugen, *Phys. Rev. Lett.* **76,** 2870-2873 (1996).

58. R. J. Van Zee, Y. M. Hamrick, S. Li, and W. Weltner, Jr., *J. Phys. Chem.* **96,** 7247-7251 (1992).

59. G. E. Davico, R. L. Schwartz, T. M. Ramond, and W. C. Lineberger, *J. Phys. Chem. A* **103,** 6167-6172 (1999).

Comprehensive bibliography

1. L. S. Alconcel, J. A. Davies, H. J. Deyerl, and R. E. Continetti, personal communication.

2. P. W. Atkins, "Physical Chemistry.", 2nd ed. W. H. Freeman and Company, San Francisco, 1978.

3. R. A. Bair and W. A. Goddard, III, *J. Am. Chem. Soc.* **104,** 2719 (1982).

4. E. G. Bakalbassis, M.-A. D. Stiakaki, A. C. Tsipis, and C. A. Tsipis, *Chem. Phys.* **205,** 389-399 (1996).

5. R. J. Balla, H. H. Nelson, and J. R. Mcdonald, *Chem. Phys.* **99,** 323-335 (1985).

6. T. A. Barckholtz, personal communication.

7. T. A. Barckholtz and T. A. Miller, *Int. Rev. Phys. Chem.* **17,** 435-524 (1998).

8. T. A. Barckholtz and T. A. Miller, *J. Phys. Chem. A* **103,** 2321-2336 (1999).

9. W. D. Bare, A. Citra, G. V. Chertihin, and L. Andrews, *J. Phys. Chem. A* **103,** 5456-5462 (1999).

10. C. W. Bauschlicher, Jr., *Chem. Phys.* **93,** 399-404 (1985).

11. C. W. Bauschlicher, Jr. , S. R. Langhoff, H. Partridge, and M. Sodupe, *J. Phys. Chem.* **97,** 856-859 (1993).

12. C. W. Bauschlicher, Jr. and P. Maitre, *Theor. Chim. Acta* **90,** 189-203 (1995).

13. C. W. Bauschlicher, Jr. , C. J. Nelin, and P. S. Bagus, *J. Chem. Phys.* **82,** 3265-3276 (1985).

14. A. D. Becke, *J. Phys. Chem.* **98,** 5648 (1993).

15. A. A. Bengali, S. M. Casey, C.-L. Cheng, J. P. Dick, P. T. Fenn, P. W. Villalta, and D. G. Leopold, *J. Am. Chem. Soc.* **114,** 5257-5268 (1992).

16. S. W. Benson, *J. Am. Chem. Soc.* **87,** 972 (1965).

17. G. D. Bent, G. F. Adams, R. H. Bartram, G. D. Purvis, and R. J. Bartlett, *J. Chem. Phys.* **76,** 4144-4156 (1982).

18. P. F. Bernath, "Spectra of Atoms and Molecules." Oxford University Press, New York, NY, 1995.

19. V. Biju and M. A. Khadar, *Mat. Sci. Eng. A-Struct.* **304,** 814-817 (2001).

20. M. J. W. Boness and G. J. Schulz, *Phys. Rev. A* **2,** 2182 (1970).

21. G. Boschloo and A. Hagfeldt, *J. Phys. Chem. B* **105,** 3039-3044 (2001).

22. L. M. Branscomb and S. J. Smith, *Phys. Rev.* **98,** 1028 (1955).

23. A. J. Bridgeman, *J. Chem. Soc. Dalton. Trans.***,** 4555-4562 (1996).

24. E. Broclawik, R. Yamauchi, A. Endou, M. Kubo, and A. Miyamoto, *J. Chem. Phys.* **104,** 4098-4104 (1996).

25. S. D. Brossard, P. G. Carrick, E. L. Chappell, S. C. Hulegaard, and P. C. Engelking, *J. Chem. Phys.* **84,** 2459-2465 (1986).

26. J. B. Burkholder, P. D. Hammer, C. J. Howard, J. P. Towle, and J. M. Brown, *J. Mol. Spec.* **151,** 493 (1992).

27. C. Carlone and F. W. Dalby, *Can. J. Phys.* **47,** 1945 (1969).

28. P. G. Carrick, S. D. Brossard, and P. C. Engelking, *J. Chem. Phys.* **83,** 1995-1996 (1985).

29. R. J. Celotta, R. A. Bennett, J. L. Hall, M. W. Siegel, and J. Levine, *Phys. Rev. A* **6,** 631 (1972).

30. H. Y. H. Chan, S. Zou, and M. J. Weaver, *J. Phys. Chem. B* **103,** 11141-11151 (1999).

31. G. Chettur and A. Snelson, *J. Phys. Chem.* **91,** 3483 (1987).

32. S.-C. Chung, S. Kruger, G. Pacchioni, and N. Rosch, *J. Chem. Phys.* **102,** 3695-3702 (1995).

33. A. Citra, G. V. Chertihin, L. Andrews, and M. Neurock, *J. Phys. Chem. A* **101,** 3109-3118 (1997).

34. E. P. Clifford, P. G. Wenthold, R. Gareyev, W. C. Lineberger, C. H. De Puy, V. M. Bierbaum, and G. B. Ellison, *J. Chem. Phys.* **109,** 10293 (1998).

35. J. V. Coe, J. T. Snodgrass, C. B. Freidhoff, K. M. Mc Hugh, and K. H. Bowen, *J. Chem. Phys.* **84,** 618 (1986).

36. J. Cooper and R. N. Zare, *J. Chem. Phys.* **48,** 942 (1968).

37. L. A. Curtiss, D. J. Lucas, and J. A. Pople, *J. Chem. Phys.* **102,** 3292-3300 (1995).

38. T. T. Dang, E. L. Motell, M. J. Travers, E. P. Clifford, G. B. Ellison, C. H. De Puy, and V. M. Bierbaum, *Int. J. Mass Spectrom. Ion Process.* **123,** 171-185 (1993).

39. G. E. Davico, T. M. Ramond, and W. C. Lineberger, *J. Chem. Phys.* **113,** 8852-8853 (2000).

40. G. E. Davico, R. L. Schwartz, T. M. Ramond, and W. C. Lineberger, *J. Phys. Chem. A* **103,** 6167-6172 (1999).

41. G. E. Davico, R. L. Schwartz, T. M. Ramond, and W. C. Lineberger, *J. Am. Chem. Soc.* **121,** 6047-6054 (1999).

42. W. B. De More, S. P. Sander, D. M. Golden, R. F. Hampson, M. J. Kurylo, C. J. Howard, A. R. Ravishankara, C. E. Kolb, and M. J. Molina, "Chemical Kinetics and Photochemical Data for Use in Stratospheric Modeling, Evaluation Number 12." Jet Propulsion Laboratory, NASA, Pasadena, 1997.

43. V. F. De Turi and K. M. Ervin, *J. Phys. Chem.* **103,** 6911 (1999).

44. V. F. De Turi, M. A. Su, and K. M. Ervin, *J. Phys. Chem.* **103,** 1468 (1999).

45. A. Dedieu, *Chem, Rev,* **100,** 543-600 (2000).

46. M. Dolg, U. Wedig, H. Stoll, and H. Preuss, *J. Chem. Phys.* **86,** 2123-2131 (1987).

47. T. H. Dunning Jr., *J. Chem. Phys.* **90,** 1007 (1989).

48. T. Ebata, H. Yanagishita, K. Obi, and I. Tanaka, *Chem. Phys.* **69,** 27-33 (1982).

49. G. B. Ellison, G. E. Davico, V. M. Bierbaum, and C. H. De Puy, *Int. J. Mass Spectrom. Ion Process.* **156,** 109-131 (1996).

50. G. B. Ellison, P. C. Engelking, and W. C. Lineberger, *J. Phys. Chem.* **86,** 4873-4878 (1982).

51. Y. Endo, S. Saito, and E. Hirota, *J. Chem. Phys.* **81,** 122 (1984).

52. P. C. Engelking, G. B. Ellison, and W. C. Lineberger, *J. Chem. Phys.* **69,** 1826-1832 (1978).

53. K. M. Ervin, *PESCAL99*, 1999.

54. K. M. Ervin, S. Gronert, S. E. Barlow, M. K. Gilles, A. G. Harrison, V. M. Bierbaum, C. H. De Puy, W. C. Lineberger, and G. B. Ellison, *J. Am. Chem. Soc.* **112,** 5750-5759 (1990).

55. K. M. Ervin and W. C. Lineberger, *Journal of Physical Chemistry* **95,** 1167-1177 (1991).

56. K. M. Ervin and W. C. Lineberger, *in* "*Advances in Gas Phase Ion Chemistry"*, Vol. 1, (N. G. Adams and L. M. Babcock, Eds.), JAI Press, Greenwich, 1992.

57. C. S. Feigerle, Doctoral dissertation, University of Colorado, 1983.

58. B. J. Finlayson-Pitts and J. N. Pitts Jr., *Science* **276,** 1045 (1997).

59. S. C. Foster, Y. C. Hsu, C. P. Damo, X. M. Liu, C. Y. Kung, and T. A. Miller, *J. Phys. Chem.* **90,** 6766-6769 (1986).

60. S. C. Foster and T. A. Miller, *J. Phys. Chem.* **93,** 5986-5999 (1989).

61. S. C. Foster, P. Misra, T. Y. D. Lin, C. P. Damo, C. C. Carter, and T. A. Miller, *J. Phys. Chem.* **92,** 5914-5921 (1988).

62. E. J. Friedman-Hill and R. W. Field, *J. Mol. Spectrosc.* **155,** 259-276 (1992).

63. M. J. Frisch, G. W. Trucks, H. B. Schlegal, P. M. W. Gill, B. G. Johnson, M. A. Robb, J. R. Cheeseman, T. Kieth, G. A. Petersson, J. A. Montgomery, K. Raghavachari, M. A. Al-Laham, V. G. Zakrewski, J. V. Ortiz, J. B. Foresman, J. Cioslowski, B. B. Stefanov, A. Nanayakkara, M. Challacombe, C. Y. Peng, P. Y. Ayala, W. Chen, M. W. Wong, J. L. Andres, E. S. Replogle, R. Gomperts, R. L. Martin, D. J. Fox, J. S. Binkley, D. J. Defrees, J. Baker, J. J. P. Stewart, M. Head-Gordon, C. Gonzalez, and J. A. Pople, *Gaussian94*, Gaussian, Inc., 1994.

64. M. J. Frisch, G. W. Trucks, H. B. Schlegel, G. E. Scuseria, M. A. Robb, J. R. Cheeseman, V. G. Zakrzewski, J. A. J. Montgomery, R. E. Stratmann, J. C. Burant, S. Dapprich, J. M. Millam, A. D. Daniels, K. N. Kudin, M. C. Strain, O. Farkas, J. Tomasi, V. Barone, M. Cossi, R. Cammi, B. Mennucci, C. Pomelli, C. Adams, S. Clifford, J. Ochterski, G. A. Petersson, P. Y. Ayala, Q. Cui, K. Morokuma, D. K. Malick, A. D. Rabuck, K. Raghavachari, J. B. Foresman, J. Cioslowski, J. V. Ortiz, A. G. Baboul, B. B. Stefanov, G. Liu, A. Liashenko, P. Piskorz, I. Komaromi, R. Gomperts, R. L. Martin, D. J. Fox, T. Keith, M. A. Al-Laham, C. Y. Peng, A. Nanayakkara, C. Gonzalez, M. Challacombe, P. M. W. Gill, B. Johnson, W. Chen, M. W. Wong, J. L. Andres, C. Gonzalez, M. Head-Gordon, E. S. Replogle, and J. A. Pople, *Gaussian 98, Revision A.7*, Gaussian, Inc., Pittsburgh PA, 1998.

65. C. I. Frum, R. Engleman, Jr. , and P. F. Bernath, *J. Mol. Spectrosc.* **150,** 566-575 (1991).

66. K. Fuke, K. Ozawa, and K. Kaya, *Chem. Phys. Lett.* **126,** 119-123 (1986).

67. M. Gausa, G. Gantefor, H. O. Lutz, and K. H. Meiwes-Broer, *Int. J. Mass Spectrom.* **102,** 227-237 (1990).

68. M. Gausa, R. Kaschner, G. Seifert, J. H. Faehrmann, H. O. Lutz, and K. H. Meiwes-Broer, *J. Chem. Phys.* **104,** 9719-9728. (1996).

69. A. Geers, J. Kappert, F. Temps, and T. J. Sears, *J. Chem. Phys.* **98,** 4297-4300 (1993).

70. W. A. Goddard, III and L. B. Harding, *Annu. Rev. Phys. Chem.* **29,** 363 (1978).

71. D. W. Green, G. T. Reedy, and J. G. Kay, *J. Mol. Spectrosc.* **78,** 257-266 (1979).

72. *Thermodynamic Properties of Individual Substances*, Vol. 1, edited by L. V. Gurvich, I. V. Veyts, and C. B. Alcock (Hemisphere Pub. Corp., New York, 1989).

73. G. L. Gutsev, B. K. Rao, and P. Jena, *J. Phys. Chem. A* **104,** 11961-11971 (2000).

74. M. J. Haas and A. G. Harrison, *Int. J. Mass Spectrom. Ion Process.* **124,** 115-124 (1993).

75. K. A. Hanold, C. R. Sherwood, M. C. Garner, and R. E. Continetti, *Rev. Sci. Instrum.* **66,** 5507 (1995).

76. D. C. Harris and M. D. Bertolucci, "Symmetry and Spectroscopy." Dover Publications, New York, 1989.

77. A. J. Hills and C. J. Howard, *J. Chem. Phys.* **81,** 4458 (1984).

78. J. Ho, Doctoral dissertation, University of Colorado, 1991.

79. K. J. Holstein, E. H. Fink, and F. Zabel, *Journal of Molecular Spectroscopy* **99,** 231 (1983).

80. C. J. Howard, *J. Am. Chem. Soc.* **102,** 6937-6941 (1980).

81. H. E. Hunziker and H. R. Wendt, *J. Chem. Phys.* **64,** 3488 (1976).

82. G. Inoue, H. Akimoto, and M. Okuda, *Chem. Phys. Lett.* **63,** 213-216 (1979).

83. G. Inoue, H. Akimoto, and M. Okuda, *J. Chem. Phys.* **72,** 1769-1775 (1980).

84. G. Inoue, M. Okuda, and H. Akimoto, *J. Chem. Phys.* **75,** 2060-2065 (1981).

85. M. E. Jacox and D. E. Milligan, *J. Mol. Spectrosc.* **42,** 495 (1972).

86. B. K. Janousek, A. H. Zimmerman, K. J. Reed, and J. I. Brauman, *J. Am. Chem. Soc.* **100,** 6142-6148 (1978).

87. K. Jansson and R. Scullman, *J. Mol. Spectrosc.* **61,** 299-312 (1976).

88. J. W. C. Johns, A. R. W. Mc Kellar, and M. Riggin, *J. Chem. Phys.* **68,** 3957 (1978).

89. E. J. J. Kirchner, E. J. Baerends, U. Van Slooten, and A. W. Kleyn, *J. Chem. Phys.* **97,** 3821-3830 (1992).

90. F. Kirchner and W. R. Stockwell, *J. Geophys. Res.* **101,** 21007 (1996).

91. S. A. Klopcic, V. D. Moravec, and C. C. Jarrold, *J. Chem. Phys.* **110,** 10216-10217 (1999).

92. S. A. Klopcic, V. D. Moravec, and C. C. Jarrold, *J. Chem. Phys.* **110,** 8986-8991 (1999).

93. H. Koppel, *Z. Phys. Chemie-Int. J. Res. Phys. Chem. Chem. Phys.* **200,** 3-10 (1997).

94. G. Le Bras, *in* "*Chemical Processes in Atmospheric Oxidation"*, Vol. 3, (G. Le Bras, Ed.) p. 13. Springer, Berlin, 1997.

95. Y. Y. Lee, G. H. Wann, and Y. P. Lee, *J. Chem. Phys.* **99,** 9465-9471 (1993).

96. X. Li and L.-S. Wang, *J. Chem. Phys.* **109,** 5264-5268 (1998).

97. S. G. Lias, J. E. Bartmess, J. F. Liebman, J. L. Holmes, R. D. Levin, and W. G. Mallard**,** J. Phys. Chem. Ref. Data **17,** Suppl. No. 1 (1988).

98. P. D. Lightfoot, R. A. Cox, J. N. Crowley, M. Destriau, G. D. Hayman, M. E. Jenkin, G. K. Moortgat, and F. Zabel, *Atmos. Environ.* **26A,** 1805 (1992).

99. M. Litorja and B. Ruscic, *J. Electron Spectrosc. Relat. Phenom.* **97,** 131 (1998).

100. X. M. Liu, C. P. Damo, T. Y. D. Lin, S. C. Foster, P. Misra, L. Yu, and T. A. Miller, *J. Phys. Chem.* **93,** 2266-2275 (1989).

101. E. Lorda, F. Illas, and P. S. Bagus, *Chem. Phys. Lett.* **256,** 377-382 (1996).

102. C. Luder and K. H. Meiwes-Broer, *Chem. Phys. Lett.* **294,** 391-396 (1998).

103. S. Madronich, J. Greenberg, and S. Paulson, *in* "*Atmospheric Chemistry and Global Change"*, (G. P. Brasseur, J. J. Orlando and G. S. Tyndall, Eds.), p. 325. Oxford University Press, New York, 1999.

104. L. Maya, L. Riester, T. Thundat, and C. S. Yust, *J. Appl. Phys.* **84,** 6382-6386 (1998).

105. J. R. Mc Bride, G. W. Graham, C. R. Peters, and W. H. Weber, *J. Appl. Phys.* **69,** 1596-1604 (1991).

106. A. R. W. Mc Kellar, *J. Chem. Phys.* **71,** 81 (1979).

107. A. J. Merer, *Annu. Rev. Phys. Chem.* **40,** 407-38 (1989).

108. R. B. Metz, A. Weaver, S. E. Bradforth, T. N. Kitsopoulos, and D. M. Neumark, *J. Phys. Chem.* **94,** 1377-1388. (1990).

109. P. Misra, X. M. Zhu, C. Y. Hsueh, and J. B. Halpern, *Chem. Phys.* **178,** 377-385 (1993).

110. C. E. Moore, "Atomic Energy Levels." National Bureau of Standards, Washington, 1971.

111. J. H. Moore, C. C. Davis, and M. A. Coplan, "Building Scientific Apparatus.", 2nd ed. Addison-Wesley, Redwood City, CA, 1989.

112. V. D. Moravec and C. C. Jarrold, *J. Chem. Phys.* **108,** 1804 (1998).

113. V. D. Moravec and C. C. Jarrold, *J. Chem. Phys.* **112,** 792-798 (2000).

114. D. H. Mordaunt and M. N. R. Ashfold, *J. Chem. Phys.* **101,** 2630 (1994).

115. A. Nakajima, T. Taguwa, K. Hoshino, T. Sugioka, T. Naganuma, F. Ono, K. Watanabe, K. Nakao, Y. Konishi, R. Kishi, and K. Kaya, *Chem. Phys. Lett.* **214,** 22-26 (1993).

116. K.-I. Namiki and S. Saito, *Chem. Phys. Lett.* **252,** 343-347 (1996).

117. S. Nandi, S. J. Blanksby, X. Zhang, M. R. Nimlos, D. C. Dayton, and G. B. Ellison, *J. Phys. Chem. A***,** (in press, 2001).

118. Y. Negishi, T. Yasuike, F. Hayakawa, M. Kizawa, S. Yabushita, and A. Nakajima, *J. Chem. Phys.* **113,** 1725-1731 (2000).

119. D. M. Neumark, K. R. Lykke, T. Andersen, and W. C. Lineberger, *Phys. Rev. A* **32,** 1890-1892 (1985).

120. C. Nilsson, R. Scullman, and N. Mehendale, *J. Mol. Spectrosc.* **35,** 172-189 (1970).

121. L. C. O' Brien, S. J. Wall, and M. K. Sieber, *J. Mol. Spectrosc.* **183,** 57-60 (1997).

122. J. M. Oakes, L. B. Harding, and G. B. Ellison, *J. Chem. Phys.* **83,** 5400 (1985).

123. K. Ohbayashi, H. Akimoto, and I. Tanaka, *J. Phys. Chem.* **81,** 798-802 (1977).

124. D. L. Osborn, D. J. Leahy, D. R. Cyr, and D. M. Neumark, *J. Phys. Chem.* **104,** 5026 (1996).

125. D. L. Osborn, D. J. Leahy, E. H. Kim, E. De Beer, and D. M. Neumark, *Chem. Phys. Lett.* **292,** 651-655 (1998).

126. D. L. Osborn, D. J. Leahy, E. M. Ross, and D. M. Neumark, *Chem. Phys. Lett.* **235,** 484-489 (1995).

127. J. B. Pedley, R. D. Naylor, and S. P. Kirby, "Thermochemical Data of Organic Compounds." Chapman and Hall, New York, 1986.

128. M. L. Polak, M. K. Gilles, J. Ho, and W. C. Lineberger, *J. Phys. Chem.* **95,** 3460-3462 (1991).

129. L. A. Posey, M. J. Deluca, and M. A. Johnson, *Chem. Phys. Lett.* **131,** 170-174 (1986).

130. D. E. Powers, M. B. Pushkarsky, and T. A. Miller, *J. Chem. Phys.* **106,** 6863-6877 (1997).

131. M. B. Pushkarsky, S. J. Zalyubovsky, and T. A. Miller, *J. Chem. Phys.* **112,** 10695 (2000).

132. P. Pyykko, *Chem. Rev.* **88,** 563-594 (1988).

133. R. S. Ram and P. F. Bernath, *J. Mol. Spectrosc.* **155,** 315-325 (1992).

134. T. M. Ramond, G. E. Davico, R. L. Schwartz, and W. C. Lineberger, *J. Chem. Phys.* **112,** 1158-1169 (2000).

135. J. C. Rienstra-Kiracofe, W. D. Allen, and H. F. Schaefer III, *J. Phys. Chem.* **104,** 9823 (2000).

136. J. C. Rienstra-Kiracofe, G. S. Tschumper, H. F. Schaefer III, S. Nandi, and G. B. Ellison, *Chem. Revs.***,** (2001, in press).

137. E. B. Rudnyi, O. V. Kuznetsova, E. A. Kaibicheva, and L. N. Sidorov, *Temperatur* **28,** 864-870 (1991).

138. B. Ruscic and J. Berkowitz, *J. Chem. Phys.* **95,** 4033-4039 (1991).

139. B. Ruscic and J. Berkowitz, *J. Chem. Phys.* **101,** 10936-10946 (1994).

140. B. Ruscic, D. Feller, D. A. Dixon, K. A. Peterson, L. B. Harding, R. L. Asher, and A. F. Wagner, *J. Phys. Chem. A* **105,** 1-4 (2001).

141. D. K. Russell and H. E. Radford, *J. Chem. Phys.* **72,** 2750 (1980).

142. T. Sasaki, N. Koshizaki, and K. M. Beck, *Appl. Phys. A: Mater. Sci. Process.* **69,** S771-S774 (1999).

143. U. Sassenberg and R. Scullman, *J. Mol. Spectrosc.* **68,** 331-332 (1977).

144. U. Sassenberg and R. Scullman, *Phys. Scr.* **28,** 139-149 (1983).

145. M. Scheer, C. A. Brodie, R. C. Bilodeau, and H. K. Haugen, *Phys. Rev. A* **58,** 2051-2062 (1998).

146. R. L. Schwartz, G. E. Davico, T. M. Ramond, and W. C. Lineberger, *J. Phys. Chem. A* **103,** 8213-8221 (1999).

147. P. Schwerdtfeger, J. S. Mc Featers, J. J. Moore, D. M. Mc Pherson, R. P. Cooney, G. A. Bowmaker, M. Dolg, and D. Andrae, *Langmuir* **7,** 116-125 (1991).

148. R. Scullman, U. Sassenberg, and C. Nilsson, *Can. J. Phys.* **53,** 1991-1999 (1975).

149. O. L. Shcheka, N. V. Dobrodey, and T. B. Emelina, *Int. J. Quantum Chem.* **50,** 181-188 (1994).

150. P. E. M. Siegbahn, *Chem. Phys. Lett.* **201,** 15-23 (1993).

151. P. E. M. Siegbahn, *J. Phys. Chem.* **97,** 9096-9102 (1993).

152. A. E. Siegman, "Lasers." University Science Books, Mill Valley, CA, 1986.

153. H. R. Siekmann, E. Holub-Krappe, B. Wrenger, C. Pettenkofer, and K. H. Meiwes-Broer, *Z. Phys. B* **90,** 201-206 (1993).

154. H. R. Siekmann, C. Luder, J. Faehrmann, H. O. Lutz, and K. H. Meiwes-Broer, *Z. Phys. D* **20,** 417-420 (1991).

155. D. W. Smith and L. Andrews, *J. Chem. Phys.* **60,** 81 (1974).

156. C. Sosa and H. B. Schlegel, *J. Am. Chem. Soc.* **109,** 7007-7015 (1987).

157. V. I. Srdanov and D. O. Harris, *J. Chem. Phys.* **89,** 2748-2753 (1988).

158. T. Steimle, M. Tanimoto, K. Namiki, and S. Saito, *J. Chem. Phys.* **108,** 7616-7622 (1998).

159. T. C. Steimle, K. Y. Jung, and B.-Z. Li, *J. Chem. Phys.* **103,** 1767-1772 (1995).

160. S. C. Su, J. N. Carstens, and A. T. Bell, *J. Catal.* **176,** 125-135 (1998).

161. X. Q. Tan, J. M. Williamson, S. C. Foster, and T. A. Miller, *J. Phys. Chem.* **97,** 9311-9316 (1993).

162. F. Temps, personal communication.

163. F. Temps, "Molecular Dynamics and Spectroscopy by Stimulated Emission Pumping." World Scientific, Singapore, 1995.

164. J. Thøgersen, M. Scheer, L. D. Steele, and H. K. Haugen, *Phys. Rev. Lett.* **76,** 2870-2873 (1996).

165. M. J. Travers, D. C. Cowles, and G. B. Ellison, *Chem. Phys. Lett.* **164,** 449. (1989).

166. R. P. Tuckett, P. A. Freedman, and W. J. Jones, *Mol. Phys.* **37,** 379 (1979).

167. R. P. Tuckett, P. A. Freedman, and W. J. Jones, *Mol. Phys.* **37,** 403 (1979).

168. R. J. Van Zee, Y. M. Hamrick, S. Li, and W. Weltner, Jr., *J. Phys. Chem.* **96,** 7247-7251 (1992).

169. J. T. Verdeyen, "Laser Electronics.", 3rd. ed. Prentice Hall, Englewood Cliffs, NJ, 1995.

170. S. P. Walch and W. A. Goddard III, *J. Am. Chem. Soc.* **100,** 1338-1348 (1978).

171. L.-S. Wang, H.-S. Cheng, and J. Fan, *J. Chem. Phys.* **102,** 9480 (1995).

172. H. R. Wendt and H. E. Hunziker, *J. Chem. Phys.* **71,** 5202-5205 (1979).

173. C. K. Westbrook, *Chem. Ind. (Lond.)* **100,** 562 (1992).

174. K. B. Wiberg, *J. Am. Chem. Soc.* **112,** 3379 (1990).

175. R. T. Wiedmann, R. G. Tonkyn, and M. G. White, *J. Chem. Phys.* **97,** 768 (1992).

176. J. M. Williams and W. H. Hamill, *J. Chem. Phys.* **49,** 4467 (1968).

177. H. Wu, S. R. Desai, and L.-S. Wang, *J. Phys. Chem. A* **101,** 2103-2111 (1997).

178. H. Wu and L.-S. Wang, *J. Chem. Phys.* **107,** 16-21 (1997).

179. C. Xu, G. R. Burton, T. R. Taylor, and D. M. Neumark, *J. Chem. Phys.* **107,** 3428 (1997).

180. D. R. Yarkony, H. F. Schaefer III, and S. Rothenberg, *J. Am. Chem. Soc.* **96,** 656-659 (1974).

181. V. Zengin, B. J. Persson, K. M. Strong, and R. E. Continetti, *J. Chem. Phys.* **105,** 9740 (1996).

182. X. Zhu, M. M. Kamal, and P. Misra, *Pure Appl. Opt.* **5,** 1021 (1996).

Appendix

A.1 Howard recalculation

This appendix illustrates precisely how the quantities in Tables 3.8-3.11 were calculated. Table 3.8 shows the results of recalculation of $\Delta_f H_T$(HOO) using data from Howard (*1*) and thermochemical quantities from the tables of Gurvich *et al*. (*2*) using both the $\Delta_f H$(OH) from Ref. (*2*) and from Ref. (*3*). In the Howard paper, the rate constants for the forward and reverse reaction of

$$HO_2 + NO \rightleftharpoons OH + NO_2 \qquad (A.1)$$

Were measured to yield a temperature-dependent equilibrium constant $K_{equi} = (0.116 \pm 0.026)\exp\{(7145 \pm 255)/RT\}$ (*1*). If R = 1.9864776 cal/mol K and T = 700K, RT = 1.9864776 * 700 = 1390.5343 cal/mol, since the experiment took place at 700K. (Note: I keep an arbitrary number of digits in all numbers until the final values, at which point I round) Then $K_{equi} = 0.116 * \exp(7145/1390.5343) = 19.769643$.

To determine the error in K_{equi}, ΔK_{equi} :

1. First, determine uncertainty in $\exp\{(7145 \pm 255)/RT\}$

   Let $y = \exp \alpha/RT$, where $\alpha = 7145$

   $\Delta y = |dy/d\alpha| \, \delta\alpha$

   $= (1/RT) * (\exp \alpha/RT) * 255$

   $= (255/1390.5343) * \exp 7145/ 1390.5343$

   $= 31.2535$

so exp{(7145 ± 255)/RT} evaluated at T=700 becomes

170.428 ± 31.2535 (not rounding yet)

2. Multiply this with 0.116 ± 0.026

(0.116 ± 0.026)* (170.428 ± 31.2535)

= 19.769643 ± 19.769643 *$\{(0.026/0.116)^2 + (31.2535/170.428)^2)\}^{1/2}$

= 19.769643 ± 19.769643 * 0.289598

= 19.769643 ± 5.725

3. K_{equi} = 20 ± 6 (or 19.8 ± 5.7)

I want to determine the value of $\Delta_{rxn}H_{700}$,

$$\Delta_{rxn}H_{700} = -RT \ln K_{equi} + T \Delta_{rxn}S. \quad (A.2)$$

First, calculate -RT ln K_{equi}, then the error ΔRT ln K_{equi}.

-RT ln K_{equi} = - 1390.5343 cal/mol * ln (19.769643) = -4149.5596 cal/mol

= - 17361.757 J/mol

Δ ln K_{equi} = |d ln K_{equi} / d K_{equi} | δK_{equi}

= 1/ K_{equi} * δK_{equi}

= 1/19.769643 * 5.725

= 0.289585

ΔRT ln K_{equi} = 1390.5343 cal/mol * 0.289585

= 402.6778 cal/mol

= 1684.80423 J/mol

-RT ln K_{equi} = -17361.757 ± 1684.804 J/mol

Now calculate T $\Delta_{rxn}S$:

$$\Delta_{rxn}S_{700} = S_{700}(OH) + S_{700}(NO_2) - S_{700}(HO_2) - S_{700}(NO) \qquad (A.3)$$

From the Gurvich thermochemical tables (*2*):

S_{700} (OH) = 209.002 J/K mol

S_{700} (NO_2) = 276.471 J/K mol

S_{700} (HO_2) = 262.271 J/K mol

S_{700} (NO) = 236.755 J/K mol

Here I am neglecting any error in the entropy as it will be small. (Speaking of entropy, if anyone reads this far into the thesis, let me know and I'll buy you a case of beer!)

$\Delta_{rxn}S_{700}$ = 209.002 + 276.471 - 262.271 - 236.755 = -13.553 J/K mol

T $\Delta_{rxn}S_{700}$ = -13.553 J/K mol * 700K = -9487.1 J/mol

Now I can calculate $\Delta_{rxn}H_{700}$:

$\Delta_{rxn}H_{700}$ = (- 17361.757 ± 1684.804 J/mol) + -9487.1 J/mol

= - 26.848857 ± 1.684804 kJ/mol

= - 26.85 ± 1.68 kJ/mol

= - 6.417 ± 0.4027 kcal/mol

The next step is to determine the heat of formation of HOO:

$$\Delta_f H_{700}(HO_2) = \Delta_f H_{700}(OH) + \Delta_f H_{700}(NO_2) - \Delta_{rxn}H_{700} - \Delta_f H_{700}(NO) \qquad (A.4)$$

From the Gurvich tables (*2*):

$\Delta_f H_0(NO_2) = 37.000 \pm 0.5$ kJ/mol

$\Delta_f H_0(NO) = 90.773 \pm 0.43$ kJ/mol

$\Delta_f H_0(OH) = 39.110 \pm 0.21$ kJ/mol

Here I am assuming that the uncertainty will not change with temperature. To use these values in Eq. A.4, they must be converted from 0 to 700 K. The value of $\Delta_f H_{700}(NO_2)$ can be calculated using the following:

$$\Delta_f H_{700}(NO_2) = \Delta_f H_0(NO_2) + \int_0^{700} dT \{C_p(NO_2) - C_p(O_2) - \tfrac{1}{2} C_p(N_2)\} \qquad (A.5)$$

$H°(700) - H°(0)\ (NO_2) = 27.635$ kJ/mol

$H°(700) - H°(0)\ (O_2) = 21.180$ kJ/mol

$H°(700) - H°(0)\ (N_2) = 20.607$ kJ/mol

so that $\Delta_f H_{700}(NO_2) = 37.000 + 27.635 - 21.180 - 0.5 * 20.607$

$= 33.152 \pm 0.5$ kJ/mol

Repeat to find $\Delta_f H_{700}(NO)$:

$\Delta_f H_{700}(NO) = \Delta_f H_0(NO) + \int dT \{C_p(NO) - 0.5\ C_p(O_2) - 0.5\ C_p(N_2)\}$

$H°(700) - H°(0)\ (NO) = 21.489$ kJ/mol

$H°(700) - H°(0)\ (O_2) = 21.180$ kJ/mol

$H°(700) - H°(0)\ (N_2) = 20.607$ kJ/mol

so that $\Delta_f H_{700}(NO) = 90.773 + 21.489 - 0.5 * 21.180 - 0.5 * 20.607$

$= 91.369 \pm 0.43$ kJ/mol

Repeat once more to find $\Delta_f H_{700}(OH)$:

$$\Delta_f H_{700}(OH) = \Delta_f H_0(OH) + \int dT \{C_p(OH) - 0.5\ C_p(O_2) - 0.5\ C_p(H_2)\}$$

$$H°(700) - H°(0)\ (OH) = 20.701 \text{ kJ/mol}$$

$$H°(700) - H°(0)\ (O_2) = 21.180 \text{ kJ/mol}$$

$$H°(700) - H°(0)\ (H_2) = 20.216 \text{ kJ/mol}$$

so that $\Delta_f H_{700}(OH) = 39.110 + 20.701 - 0.5 * 21.180 - 0.5 * 20.216$

$$= 39.113 \pm 0.21 \text{ kJ/mol (9.35 kcal/mol)}$$

$$\Delta_f H_{700}(HO_2) = \Delta_f H_{700}(OH) + \Delta_f H_{700}(NO_2) - \Delta_{rxn} H_{700} - \Delta_f H_{700}(NO) \qquad (A.4)$$

This makes $\Delta_f H_{700}(HO_2) = 39.113 \text{ kJ/mol} + 33.152 \text{ kJ/mol} - (-26.849 \text{ kJ/mol}) - 91.369 \text{ kJ/mol}$

$$= 7.745 \text{ kJ/mol} \pm \{(0.21)^2 + (0.5)^2 + (1.68)^2 + (0.43)^2\}^{1/2}$$

$$= 7.745 \pm 1.817 \text{ kJ/mol}$$

$\Delta_f H_{700}(HO_2) = 1.85 \pm 0.43$ kcal/mol

Now I want to convert $\Delta_f H_{700}(HO_2)$ to other temperatures aside from 700K. This is done through heat capacity corrections:

$$\Delta_f H_{298.15}(HO_2) = \Delta_f H_{700}(HO_2) - \int_0^{700} dT \{C_p(HO_2) - C_p(O_2) - 0.5\ C_p(H_2)\}$$

$$+ \int_0^{298} dT \{C_p(HO_2) - C_p(O_2) - 0.5\ C_p(H_2)\} \qquad (A.6)$$

The integral of the heat capacity is tabulated in Ref. (*2*):

$H°(700) - H°(0)\ (HO_2) = 25.873$ kJ/mol

$H°(700) - H°(0)\ (O_2) = 21.180$ kJ/mol

$H°(700) - H°(0)\ (H_2) = 20.216$ kJ/mol

$H°(298) - H°(0)\ (HO_2) = 10.003$ kJ/mol

$H°(298) - H°(0)\ (O_2) = 8.680$ kJ/mol

$H°(298) - H°(0)\ (H_2) = 8.468$ kJ/mol

$$\Delta_f H_{298.15}(HO_2) = 7.745 - \{25.873 - 21.180 - \tfrac{1}{2}\ 20.216\} + \{10.003 - 8.680 - \tfrac{1}{2}\ 8.468\}$$

$$= 7.745 - \{-5.415\} + \{-2.911\}$$

$$= 10.249 \pm 1.817 \text{ kJ/mol}$$

$\Delta_f H_{298.15}(HO_2) = 2.45 \pm 0.43$ kcal/mol

$$\Delta_f H_0(HO_2) = \Delta_f H_{700}(HO_2) - \int_0^{700} dT\ \{C_p(HO_2) - C_p(O_2) - 0.5\ C_p(H_2)\} \quad (A.7)$$

$H°(700) - H°(0)\ (HO_2) = 25.873$ kJ/mol

$H°(700) - H°(0)\ (O_2) = 21.180$ kJ/mol

$H°(700) - H°(0)\ (H_2) = 20.216$ kJ/mol

$$\Delta_f H_0(HO_2) = 7.745 - \{25.873 - 21.180 - \tfrac{1}{2}\ 20.216\}$$

$$= 7.745 - \{-5.415\}$$

$$= 13.160 \pm 1.817 \text{ kJ/mol}$$

$\Delta_f H_0(HO_2) = 3.15 \pm 0.43$ kcal/mol

$$\Delta_f H_{400}(HO_2) = \Delta_f H_{700}(HO_2) - \int_0^{700} dT \{C_p(HO_2) - C_p(O_2) - 0.5\, C_p(H_2)\}$$

$$+ \int_0^{400} dT \{C_p(HO_2) - C_p(O_2) - 0.5\, C_p(H_2)\} \quad (A.8)$$

$H°(700) - H°(0)\ (HO_2) = 25.873$ kJ/mol

$H°(700) - H°(0)\ (O_2) = 21.180$ kJ/mol

$H°(700) - H°(0)\ (H_2) = 20.216$ kJ/mol

$H°(400) - H°(0)\ (HO_2) = 13.676$ kJ/mol

$H°(400) - H°(0)\ (O_2) = 11.706$ kJ/mol

$H°(400) - H°(0)\ (H_2) = 11.426$ kJ/mol

$\Delta_f H_{400}(HO_2) = 7.745 - \{25.873 - 21.180 - ½\ 20.216\} + \{13.676 - 11.706 - ½\ 11.426\}$

$= 7.745 - \{5.415\} + \{-3.743\}$

$= 9.417 \pm 1.817$ kJ/mol

$\Delta_f H_{400}(HO_2) = 2.25 \pm 0.43$ kcal/mol

$$\Delta_f H_{500}(HO_2) = \Delta_f H_{700}(HO_2) - \int_0^{700} dT \{C_p(HO_2) - C_p(O_2) - 0.5\, C_p(H_2)\}$$

$$+ \int_0^{500} dT \{C_p(HO_2) - C_p(O_2) - 0.5\, C_p(H_2)\} \quad (A.9)$$

$H°(700) - H°(0)\ (HO_2) = 25.873$ kJ/mol

$H°(700) - H°(0)\ (O_2) = 21.180$ kJ/mol

$H°(700) - H°(0)\ (H_2) = 20.216$ kJ/mol

$H°(500) - H°(0)\ (HO_2) = 17.527$ kJ/mol

$H°(500) - H°(0)\ (O_2) = 14.765$ kJ/mol

$H°(500) - H°(0)\ (H_2) = 14.350$ kJ/mol

$\Delta_f H_{500}(HO_2) = 7.745 - \{25.873 - 21.180 - ½\ 20.216\} + \{(17.527 - 14.765 - ½\ 14.350\}$

$= 7.745 - \{-5.415\} + \{-4.413\}$

$= 8.747 \pm 1.817$ kJ/mol

$\Delta_f H_{500}(HO_2) = 2.09 \pm 0.43$ kcal/mol

$$\Delta_f H_{1000}(HO_2) = \Delta_f H_{700}(HO_2) - \int_0^{700} dT\ \{C_p(HO_2) - C_p(O_2) - 0.5\ C_p(H_2)\}$$

$$+ \int_0^{1000} dT\ \{C_p(HO_2) - C_p(O_2) - 0.5\ C_p(H_2)\} \qquad (A.10)$$

$H°(700) - H°(0)\ (HO_2) = 25.873$ kJ/mol

$H°(700) - H°(0)\ (O_2) = 21.180$ kJ/mol

$H°(700) - H°(0)\ (H_2) = 20.216$ kJ/mol

$H°(1000) - H°(0)\ (HO_2) = 39.585$ kJ/mol

$H°(1000) - H°(0)\ (O_2) = 31.387$ kJ/mol

$H°(1000) - H°(0)\ (H_2) = 29.147$ kJ/mol

$\Delta_f H_{1000}(HO_2) = 7.745 - \{25.873 - 21.180 - ½\ 20.216\} + \{39.585 - 31.387 - ½\ 29.147\}$

$= 7.745 - \{-5.415\} + \{-6.3755\}$

$= 6.785 \pm 1.817$ kJ/mol

$\Delta_f H_{1000}(HO_2) = 1.62 \pm 0.43$ kcal/mol

Now that I have calculated values of $\Delta_f H_T(HO_2)$ for T = 0, 298, 400, 500, 700, and 1000K, using thermochemical tables (*2*) and the K_{equi} of Ref. (*1*) as the only source of information, I want to repeat the process, but using newly measured $\Delta_f H_0(OH)$ supplied by B. Ruscic (*3*). This value is

$\Delta_f H_0(OH) = 8.86 \pm 0.07$ kcal/mol $= 37.07 \pm 0.29$ kJ/mol

which must be converted to 700 K to be used in Eq. A.4.

$$\Delta_f H_{700}(OH) = \Delta_f H_0(OH) + \int_0^{700} dT\ \{C_p(OH) - 0.5\ C_p\ (O_2) - 0.5\ C_p\ (H_2)\} \quad (A.11)$$

$H°(700) - H°(0)\ (OH) = 20.701$ kJ/mol

$H°(700) - H°(0)\ (O_2) = 21.180$ kJ/mol

$H°(700) - H°(0)\ (H_2) = 20.216$ kJ/mol

so that $\Delta_f H_{700}(OH) = 37.07 + 20.701 - 0.5 * 21.180 - 0.5 * 20.216$

$= 37.073 \pm 0.29$ kJ/mol (8.86 kcal/mol)

Using Eq. A.4, this makes $\Delta_f H_{700}(HO_2) = 37.073$ kJ/mol + 33.152 kJ/mol – (-26.849 kJ/mol) – 91.369 kJ/mol

$= 5.705$ kJ/mol $\pm \{(0.29)^2 + (0.5)^2 + (1.68)^2 + (0.43)^2\}^{1/2}$

$= 5.705 \pm 1.828$ kJ/mol

$\Delta_f H_{700}(HO_2) = 1.36 \pm 0.44$ kcal/mol

Now I repeat Eqs. A.6-A.10 but using this different value of $\Delta_f H_{700}(HO_2)$ to convert to different temperatures.

$$\Delta_f H_{298.15}(HO_2) = \Delta_f H_{700}(HO_2) - \int_0^{700} dT\ \{C_p(HO_2) - C_p(O_2) - 0.5\ C_p(H_2)\}$$

$$+ \int_0^{298.15} dT\ \{C_p(HO_2) - C_p(O_2) - 0.5\ C_p(H_2)\} \qquad \text{(A.12)}$$

$H°(700) - H°(0)\ (HO_2) = 25.873$ kJ/mol

$H°(700) - H°(0)\ (O_2) = 21.180$ kJ/mol

$H°(700) - H°(0)\ (H_2) = 20.216$ kJ/mol

$H°(298) - H°(0)\ (HO_2) = 10.003$ kJ/mol

$H°(298) - H°(0)\ (O_2) = 8.680$ kJ/mol

$H°(298) - H°(0)\ (H_2) = 8.468$ kJ/mol

$\Delta_f H_{298.15}(HO_2) = 5.705 – (25.873 – 21.180 – ½\ 20.216) + (10.003 – 8.680 – ½\ 8.468)$

$= 5.705 – (-5.415) + (-2.911)$

$= 8.209 \pm 1.828$ kJ/mol

$\Delta_f H_{298.15}(HO_2) = 1.96 \pm 0.44$ kcal/mol

$$\Delta_f H_0(HO_2) = \Delta_f H_{700}(HO_2) - \int_0^{700} dT\ \{C_p(HO_2) - C_p(O_2) - 0.5\ C_p(H_2)\} \quad (A.13)$$

$H°(700) - H°(0)\ (HO_2) = 25.873$ kJ/mol

$H°(700) - H°(0)\ (O_2) = 21.180$ kJ/mol

$H°(700) - H°(0)\ (H_2) = 20.216$ kJ/mol

$\Delta_f H_0(HO_2) = 5.705 – \{25.873 – 21.180 – ½\ 20.216\}$

$= 5.705 – \{-5.415\}$

$= 11.12 \pm 1.828$ kJ/mol

$\Delta_f H_0(HO_2) = 2.66 \pm 0.44$ kcal/mol

$$\Delta_f H_{400}(HO_2) = \Delta_f H_{700}(HO_2) - \int_0^{700} dT\ \{C_p(HO_2) - C_p(O_2) - 0.5\ C_p(H_2)\}$$

$$+ \int_0^{400} dT\ \{C_p(HO_2) - C_p(O_2) - 0.5\ C_p(H_2)\} \quad (A.14)$$

$H°(700) - H°(0)\ (HO_2) = 25.873$ kJ/mol

$H°(700) - H°(0)\ (O_2) = 21.180$ kJ/mol

$H°(700) - H°(0)\ (H_2) = 20.216$ kJ/mol

$H°(400) - H°(0)\ (HO_2) = 13.676$ kJ/mol

$H°(400) - H°(0)\ (O_2) = 11.706$ kJ/mol

$H°(400) - H°(0)\ (H_2) = 11.426$ kJ/mol

$$\Delta_f H_{400}(HO_2) = 5.705 - (25.873 - 21.180 - \tfrac{1}{2}\ 20.216) + (13.676 - 11.706 - \tfrac{1}{2}\ 11.426)$$

$$= 5.705 - (-5.415) + (-3.743)$$

$$= 7.377 \pm 1.828 \text{ kJ/mol}$$

$\Delta_f H_{400}(HO_2) = 1.76 \pm 0.44$ kcal/mol

$$\Delta_f H_{500}(HO_2) = \Delta_f H_{700}(HO_2) - \int_0^{700} dT\ \{C_p(HO_2) - C_p(O_2) - 0.5\ C_p(H_2)\}$$

$$+ \int_0^{500} dT\ \{C_p(HO_2) - C_p(O_2) - 0.5\ C_p(H_2)\} \qquad \text{(A.15)}$$

$H°(700) - H°(0)\ (HO_2) = 25.873$ kJ/mol

$H°(700) - H°(0)\ (O_2) = 21.180$ kJ/mol

$H°(700) - H°(0)\ (H_2) = 20.216$ kJ/mol

$H°(500) - H°(0)\ (HO_2) = 17.527$ kJ/mol

$H°(500) - H°(0)\ (O_2) = 14.765$ kJ/mol

$H°(500) - H°(0)\ (H_2) = 14.350$ kJ/mol

$\Delta_f H_{500}(HO_2) = 5.705 – (25.873 – 21.180 – ½\ 20.216) + (17.527 – 14.765 – ½\ 14.350)$

$= 5.705 – (-5.415) + (-4.413)$

$= 6.707 \pm 1.828$ kJ/mol

$\Delta_f H_{500}(HO_2) = 1.60 \pm 0.44$ kcal/mol

$$\Delta_f H_{1000}(HO_2) = \Delta_f H_{700}(HO_2) - \int_0^{700} dT\ \{C_p(HO_2) - C_p(O_2) - 0.5\ C_p(H_2)\} + \int_0^{1000} dT\ \{C_p(HO_2) - C_p(O_2) - 0.5\ C_p(H_2)\} \quad \text{(A.16)}$$

$H°(700) - H°(0)\ (HO_2) = 25.873$ kJ/mol

$H°(700) - H°(0)\ (O_2) = 21.180$ kJ/mol

$H°(700) - H°(0)\ (H_2) = 20.216$ kJ/mol

$H°(1000) - H°(0)\ (HO_2) = 39.585$ kJ/mol

$H°(1000) - H°(0)\ (O_2) = 31.387$ kJ/mol

$H°(1000) - H°(0)\ (H_2) = 29.147$ kJ/mol

$\Delta_f H_{1000}(HO_2) = 5.705 – (25.873 – 21.180 – ½\ 20.216) + (39.585 – 31.387 – ½\ 29.147)$

$= 5.705 – (-5.415) + (-6.3755)$

$= 4.745 \pm 1.828$ kJ/mol

$\Delta_f H_{1000}(HO_2) = 1.13 \pm 0.44$ kcal/mol

Now I can determine D_0(HOO-H) and $D_{298.15}$(HOO-H)through the equation

$$D_0(\text{HOO-H}) = \Delta_f H_0(\text{HOO}) + \Delta_f H_0(\text{H}) - \Delta_f H_0(\text{HOOH}) \qquad \text{(A.17)}$$

From the thermochemical tables(*2*):

$\Delta_f H_0(\text{H}) = 216.035 \pm 0.006$ kJ/mol $= 51.634 \pm 0.001$ kcal/mol

$\Delta_f H_{298.15}(\text{H}) = 217.998 \pm 0.006$ kJ/mol $= 52.103 \pm 0.001$ kcal/mol

$\Delta_f H_0(\text{HOOH}) = -129.89 \pm 0.22$ kJ/mol $= -31.04 \pm 0.05$ kcal/mol

$\Delta_f H_{298.15}(\text{HOOH}) = -135.88 \pm 0.22$ kJ/mol $= -32.48 \pm 0.05$ kcal/mol

so with the value of $\Delta_f H_0$(OH) from the tables(*2*),

D_0(HOO-H) = 3.15 + 51.634 – (-31.04)

$= 85.82$ kcal/mol $\pm ((0.43)^2+(0.001)^2+(0.05)^2)^{1/2}$

$= 85.82 \pm 0.43$ kcal/mol

$D_{298.15}$(HOO-H) = 2.45 + 52.103 – (-32.48)

$= 87.03$ kcal/mol $\pm ((0.43)^2+(0.001)^2+(0.05)^2)^{1/2}$

$= 87.03 \pm 0.43$ kcal/mol

And with the new value of $\Delta_f H_0$(OH) (*3*),

D_0(HOO-H) = 2.66 + 51.634 – (-31.04)

$= 85.33$ kcal/mol $\pm ((0.44)^2+(0.001)^2+(0.05)^2)^{1/2}$

$= 85.33 \pm 0.44$ kcal/mol

$D_{298.15}$(HOO-H) = 1.96 + 52.103 – (-32.48)

$= 86.54$ kcal/mol $\pm ((0.44)^2+(0.001)^2+(0.05)^2)^{1/2}$

$= 86.54 \pm 0.44$ kcal/mol

Finally, now I can determine $\Delta_{acid}H_0$(HOO-H) and $\Delta_{acid}H_{298.15}$(HOO-H).

$$\Delta_{acid}H_0(\text{HOO-H}) = D_0(\text{HOO-H}) - EA(\text{HOO}) + IP\ (\text{H}) \quad \text{(A.18)}$$

$\Delta_{acid}H_{298.15}$(HOO-H) = $D_{298.15}$(HOO-H) – *EA*(HOO) + *IP*(H)- thermal correction (A.19)

The thermal correction occurs because the *EA* and *IP* are both measured at 0 K.

thermal correction =

$$\int_{0}^{298.15} dT \{C_p(HO_2) - C_p(HO_2^-) + C_p(H) - C_p(H^+)\} \quad (A.20)$$

From the thermochemical tables (*2*):

$H°(298.15) - H°(0)\ (HO_2) = 10.003$ kJ/mol

$H°(298.15) - H°(0)\ (HO_2^-) = 10.017$ kJ/mol

$H°(298.15) - H°(0)\ (H) = 6.197$ kJ/mol

$H°(298.15) - H°(0)\ (H^+) = 6.197$ kJ/mol

thermal correction = 10.003 - 10.017 + 6.197 - 6.197 kJ/mol

= -0.014 kJ/mol

= -0.00335 kcal/mol

From Table 3.1,

EA(HOO) = 1.078 ± 0.006 eV = 24.8593 ± 0.13836 kcal/mol

IP(H) = 313.587 kcal/mol

so with the value of $\Delta_f H_0$(OH) from the tables (*2*),

$\Delta_{acid} H_0$(HOO-H) = 85.82 - 24.8593 + 313.587

$= 374.548 \text{ kcal/mol} \pm ((0.43)^2+(0.13836)^2+(0.0)^2)^{1/2}$

$= 374.55 \pm 0.45$ kcal/mol

$\Delta_{acid}H_{298.15}$(HOO-H) = 87.03 - 24.8593 + 313.587 – (-0.00335)

$= 375.761 \text{ kcal/mol} \pm ((0.43)^2+(0.13836)^2+(0.0)^2)^{1/2}$

$= 375.76 \pm 0.45$ kcal/mol

And with the new value of $\Delta_f H_0$(OH) (*3*),

$\Delta_{acid}H_0$(HOO-H) = 85.33 - 24.8593 + 313.587

$= 374.058 \text{ kcal/mol} \pm ((0.44)^2+(0.13836)^2+(0.0)^2)^{1/2}$

$= 374.06 \pm 0.46$ kcal/mol

$\Delta_{acid}H_{298.15}$(HOO-H) = 86.54 - 24.8593 + 313.587 – (-0.00335)

$= 375.271 \text{ kcal/mol} \pm ((0.44)^2+(0.13836)^2+(0.0)^2)^{1/2}$

$= 375.27 \pm 0.46$ kcal/mol

A.2 Hills and Howard recalculation

Table 3.9 shows the results of recalculation of $\Delta_f H_T$(HOO) using data from Hills and Howard (*4*) and thermochemical quantities from the tables of Gurvich *et al*. (*2*) using both the $\Delta_f H$(OH) from Ref. (*2*) and from Ref. (*3*). Here I repeat all of the above calculations but instead starting from reaction rates from Hills and Howard

instead. In the Hills and Howard paper, the rate constants for the forward and reverse reaction of OH + ClO.

$K_{equi} = k_{1a}/k_{22}$

$k_{1a} = 0.86\ k_1 = 0.86 * (8.0 \pm 1.4) \times 10^{-12} \exp\{(235 \pm 46/T)\}\ cm^3\ molecule^{-1}\ s^{-1}$

$= 6.88 \pm 1.2 \times 10^{-12} \exp\{(235 \pm 46/T)\}\ cm^3\ molecule^{-1}\ s^{-1}$

$k_{1a}\ (298.15) = 6.88 \pm 1.2 \times 10^{-12} \exp\{0.7882 \pm 0.1543\}\ cm^3\ molecule^{-1}\ s^{-1}$

$= 15.1321 \times 10^{-12}\ cm^3\ molecule^{-1}\ s^{-1}$

compute the error Δ in k_{1a} (298.15)

$(6.88 \pm 1.2 \times 10^{-12}) * \exp\{0.7882 \pm 0.1543\}$

$= (6.88 \pm 1.2 \times 10^{-12})\ \{\exp(0.7882) \pm \exp(0.7882) * 0.1543\}$

$= (6.88 \pm 1.2 \times 10^{-12})\ (2.19943 \pm 0.33937)$

$= 15.1321 \times 10^{-12} \pm 15.1321 \times 10^{-12} * \{ (1.2/6.88)^2 + (0.33937/2.19943)^2 \}^{1/2}$

$= 15.1321 \pm 3.524 \times 10^{-12}\ cm^3\ molecule^{-1}\ s^{-1}$

$k_{22} = 9.1 \times 10^{-12}\ cm^3\ molecule^{-1}\ s^{-1}$

K_{equi} (298.15) = 15.1321 ± 3.524/9.1 = 1.6629 ± 0.387 (1.66 ± 0.39)

Again I want to calculate

$$\Delta_{rxn}H_{298.15} = -RT \ln K_{equi} + T\,\Delta_{rxn}S \qquad (A.20)$$

Using Gurvich data (*2*):

$S_{298}(OH) = 183.737$ J/mol K

$S_{298}(ClO) = 225.101$ J/mol K

$S_{298}(HO_2) = 229.102$ J/mol K

$S_{298}(Cl) = 165.189$ J/mol K

$\Delta_f H_{298}(OH) = 39.349 \pm 0.21$ kJ/mol

$\Delta_f H_{298}(ClO) = 101.627 \pm 0.11$ kJ/mol

$\Delta_f H_{298}(Cl) = 121.302 \pm 0.008$ kJ/mol

$$\Delta_{rxn} S_{298} = S_{298}(HO_2) + S_{298}(Cl) - S_{298}(OH) - S_{298}(ClO) \quad \text{(A.21)}$$

$= 229.102 + 165.189 - 183.737 - 225.101$ J/mol K

$= -14.547$ J/mol K

$T \Delta_{rxn} S_{298} = -4.337$ kJ/mol

$R = 1.9864776$ cal/mol K $= 8.3114223$ J/mol K

and $T = 298.15$ K

$RT = 2.478$ kJ/mol

Determining the error in ln K_{equi}

$\Delta \ln K_{equi} = |d \ln K_{equi} / d K_{equi} | \delta K_{equi}$

$= 1/ K_{equi} * \delta K_{equi}$

$= 1/1.6629 * 0.387$

$= 0.23273$

$-RT \ln K = - 2.478 \text{ kJ/mol} * \ln 1.6629$

$= - 1.26022 \text{ kJ/mol}$

$\Delta RT \ln K_{equi} = 2.478 \text{ kJ/mol} * 0.23273$

$= 0.5767 \text{ kJ/mol}$

$-RT \ln K_{equi} = -1.26022 \pm 0.5767 \text{ kJ/mol}$

Plugging into Eq. A.20 gives

$\Delta_{rxn}H_{298} = -RT \ln K + T\, S_{298rxn}$

$= (-1.26022 \pm 0.5767) + (- 4.337)$

$= - 5.59722 \pm 0.5767 \text{ kJ/mol}$

Then $\Delta_{rxn}H_{298}$ yields $\Delta_f H_{298}(HO_2)$

$\Delta_f H_{298}(HO_2) = \Delta_f H_{298}(OH) + \Delta_{rxn}H_{298} - \Delta_f H_{298}(Cl) + \Delta_f H_{298}(ClO)$ (A.22)

$= 39.349 + (- 5.59722) – 121.302 + 101.627 \pm \{(0.21)^2 + (0.5767)^2 + (0.008)^2 + (0.11)^2\}^{1/2}$

$= 14.0768 \pm 0.624 \text{ kJ/mol}$

$\Delta_f H_{298}(HO_2) = 3.36 \pm 0.15$ kcal/mol

Again I want to convert this value to various different temperatures (0, 400, 500, 700, and 1000 K) through heat capacity corrections.

$$\Delta_f H_0(HO_2) = \Delta_f H_{298}(HO_2) - \int_0^{298} dT \{C_p(HO_2) - C_p(O_2) - 0.5\, C_p(H_2)\} \quad (A.23)$$

$H°(298) - H°(0)\ (HO_2) = 10.003$ kJ/mol

$H°(298) - H°(0)\ (O_2) = 8.680$ kJ/mol

$H°(298) - H°(0)\ (H_2) = 8.468$ kJ/mol

$\Delta_f H_0(HO_2) = 14.0768 - (10.003 - 8.680 - ½\ 8.468)$

$= 14.0768 - (-2.911)$

$= 16.988 \pm 0.624$ kJ/mol

$\Delta_f H_0(HO_2) = 4.06 \pm 0.15$ kcal/mol

$$\Delta_f H_{400}(HO_2) = \Delta_f H_{298}(HO_2) - \int_0^{298} dT \{C_p(HO_2) - C_p(O_2) - 0.5\, C_p(H_2)\}$$

$$+ \int_0^{400} dT \{C_p(HO_2) - C_p(O_2) - 0.5\, C_p(H_2)\} \quad (A.24)$$

$H°(298) - H°(0)\ (HO_2) = 10.003$ kJ/mol

$H°(298) - H°(0)\ (O_2) = 8.680$ kJ/mol

$H°(298) - H°(0)\ (H_2) = 8.468$ kJ/mol

$H°(400) - H°(0)\ (HO_2) = 13.676$ kJ/mol

$H°(400) - H°(0)\ (O_2) = 11.706$ kJ/mol

$H°(400) - H°(0)\ (H_2) = 11.426$ kJ/mol

$$\Delta_f H_{400}(HO_2) = 14.0768 - (10.003 - 8.680 - \tfrac{1}{2}\ 8.468) + (13.676 - 11.706 - \tfrac{1}{2}\ 11.426)$$

$$= 14.0768 - (-2.911) + (-3.743)$$

$$= 13.245 \pm 0.624 \text{ kJ/mol}$$

$\Delta_f H_{400}(HO_2) = 3.17 \pm 0.15$ kcal/mol

$$\Delta_f H_{500}(HO_2) = \Delta_f H_{298}(HO_2) - \int_0^{298} dT\ \{C_p(HO_2) - C_p(O_2) - 0.5\ C_p(H_2)\}]$$

$$+ \int_0^{500} dT\ \{C_p(HO_2) - C_p(O_2) - 0.5\ C_p(H_2)\} \qquad \text{(A.25)}$$

$H°(298) - H°(0)\ (HO_2) = 10.003$ kJ/mol

$H°(298) - H°(0)\ (O_2) = 8.680$ kJ/mol

$H°(298) - H°(0)\ (H_2) = 8.468$ kJ/mol

$H°(500) - H°(0)\ (HO_2) = 17.527$ kJ/mol

$H°(500) - H°(0)\ (O_2) = 14.765$ kJ/mol

$H°(500) - H°(0)\ (H_2) = 14.350$ kJ/mol

$$\Delta_f H_{500}(HO_2) = 14.0768 - (10.003 - 8.680 - \tfrac{1}{2}\ 8.468) + (17.527 - 14.765 - \tfrac{1}{2}\ 14.350)$$

$= 14.0768 - (-2.911) + (-4.413)$

$= 12.575 \pm 0.624$ kJ/mol

$\Delta_f H_{500}(HO_2) = 3.01 \pm 0.15$ kcal/mol

$$\Delta_f H_{700}(HO_2) = \Delta_f H_{298}(HO_2) - \int_0^{298} dT \{C_p(HO_2) - C_p(O_2) - 0.5\, C_p(H_2)\} + \int_0^{700} dT \{C_p(HO_2) - C_p(O_2) - 0.5\, C_p(H_2)\} \quad \text{(A.26)}$$

$H°(298) - H°(0)\ (HO_2) = 10.003$ kJ/mol

$H°(298) - H°(0)\ (O_2) = 8.680$ kJ/mol

$H°(298) - H°(0)\ (H_2) = 8.468$ kJ/mol

$H°(700) - H°(0)\ (HO_2) = 25.873$ kJ/mol

$H°(700) - H°(0)\ (O_2) = 21.180$ kJ/mol

$H°(700) - H°(0)\ (H_2) = 20.216$ kJ/mol

$\Delta_f H_{700}(HO_2) = 14.0768 - (10.003 - 8.680 - \frac{1}{2}\, 8.468) + (25.873 - 21.180 - \frac{1}{2}\, 20.216)$

$= 14.0768 - (-2.911) + (-5.415)$

$= 11.573 \pm 0.624$ kJ/mol

$\Delta_f H_{700}(HO_2) = 2.77 \pm 0.15$ kcal/mol

$$\Delta_f H_{1000}(HO_2) = \Delta_f H_{298}(HO_2) - \int_0^{298} dT \{C_p(HO_2) - C_p(O_2) - 0.5\, C_p(H_2)\}$$

$$+ \int_0^{1000} dT \{C_p(HO_2) - C_p(O_2) - 0.5\, C_p(H_2)\} \qquad (A.27)$$

$H°(298) - H°(0)\ (HO_2) = 10.003$ kJ/mol

$H°(298) - H°(0)\ (O_2) = 8.680$ kJ/mol

$H°(298) - H°(0)\ (H_2) = 8.468$ kJ/mol

$H°(1000) - H°(0)\ (HO_2) = 39.585$ kJ/mol

$H°(1000) - H°(0)\ (O_2) = 31.387$ kJ/mol

$H°(1000) - H°(0)\ (H_2) = 29.147$ kJ/mol

$\Delta_f H_{1000}(HO_2) = 14.0768 - (10.003 - 8.680 - ½\ 8.468) + (39.585 - 31.387 - ½\ 29.147)$

$= 14.0768 - (-2.911) + (-6.3755)$

$= 10.612 \pm 0.624$ kJ/mol

$\Delta_f H_{1000}(HO_2) = 2.54 \pm 0.15$ kcal/mol

Now I want to repeat the calculation of $\Delta_f H_T(HO_2)$ using the newly measured $\Delta_f H_{298}(OH)$ supplied by B. Ruscic (*3*). This value is

$\Delta_f H_{298}(OH) = 8.92 \pm 0.07$ kcal/mol

$= 37.32 \pm 0.29$ kJ/mol

Recompute $\Delta_f H_{298}(HO_2)$

$\Delta_f H_{298}(HO_2) = \Delta_f H_{298}(OH) + \Delta_{rxn} H_{298} - \Delta_f H_{298}(Cl) + \Delta_f H_{298}(ClO)$

$= 37.32 + (- 5.59722) - 121.302 + 101.627 \pm \{(0.29)^2 + (0.5767)^2 + (0.008)^2 + (0.11)^2\}^{1/2}$

$= 12.0478 \pm 0.655$ kJ/mol

$\Delta_f H_{298}(HO_2) = 2.88 \pm 0.16$ kcal/mol

Now once more I convert $\Delta_f H_{298}(HO_2)$ to other temperatures

$$\Delta_f H_0(HO_2) = \Delta_f H_{298}(HO_2) - \int_0^{298} dT \{C_p(HO_2) - C_p(O_2) - 0.5\, C_p(H_2)\} \quad (A.28)$$

$H°(298) - H°(0)\ (HO_2) = 10.003$ kJ/mol

$H°(298) - H°(0)\ (O_2) = 8.680$ kJ/mol

$H°(298) - H°(0)\ (H_2) = 8.468$ kJ/mol

$\Delta_f H_0(HO_2) = 12.0478 - (10.003 - 8.680 - ½\ 8.468)$

$= 12.0478 - (-2.911)$

$= 14.959 \pm 0.655$ kJ/mol

$\Delta_f H_0(HO_2) = 3.58 \pm 0.16$ kcal/mol

$$\Delta_f H_{400}(HO_2) = \Delta_f H_{298}(HO_2) - \int_0^{298} dT \{C_p(HO_2) - C_p(O_2) - 0.5\, C_p(H_2)\}$$

$$+ \int_0^{400} dT \{C_p(HO_2) - C_p(O_2) - 0.5\, C_p(H_2)\} \qquad \text{(A.29)}$$

$H°(298) - H°(0)\ (HO_2) = 10.003$ kJ/mol

$H°(298) - H°(0)\ (O_2) = 8.680$ kJ/mol

$H°(298) - H°(0)\ (H_2) = 8.468$ kJ/mol

$H°(400) - H°(0)\ (HO_2) = 13.676$ kJ/mol

$H°(400) - H°(0)\ (O_2) = 11.706$ kJ/mol

$H°(400) - H°(0)\ (H_2) = 11.426$ kJ/mol

$\Delta_f H_{400}(HO_2) = 12.0478 - (10.003 - 8.680 - ½\ 8.468) + (13.676 - 11.706 - ½\ 11.426)$

$= 12.0478 - (-2.911) + (-3.743)$

$= 11.216 \pm 0.655$ kJ/mol

$\Delta_f H_{400}(HO_2) = 2.68 \pm 0.16$ kcal/mol

$$\Delta_f H_{500}(HO_2) = \Delta_f H_{298}(HO_2) - \int_0^{298} dT \{C_p(HO_2) - C_p(O_2) - 0.5\, C_p(H_2)\}$$

$$+ \int_0^{500} dT \{C_p(HO_2) - C_p(O_2) - 0.5\, C_p(H_2)\} \qquad \text{(A.30)}$$

$H°(298) - H°(0)\ (HO_2) = 10.003$ kJ/mol

$H°(298) - H°(0)\ (O_2) = 8.680$ kJ/mol

$H°(298) - H°(0)\ (H_2) = 8.468$ kJ/mol

$H°(500) - H°(0)\ (HO_2) = 17.527$ kJ/mol

$H°(500) - H°(0)\ (O_2) = 14.765$ kJ/mol

$H°(500) - H°(0)\ (H_2) = 14.350$ kJ/mol

$$\Delta_f H_{500}(HO_2) = 12.0478 - (10.003 - 8.680 - \tfrac{1}{2}\, 8.468) + (17.527 - 14.765 - \tfrac{1}{2}\, 14.350)$$

$$= 12.0478 - (-2.911) + (-4.413)$$

$$= 10.546 \pm 0.655 \text{ kJ/mol}$$

$\Delta_f H_{500}(HO_2) = 2.52 \pm 0.16$ kcal/mol

$$\Delta_f H_{700}(HO_2) = \Delta_f H_{298}(HO_2) - \int_0^{298} dT \{C_p(HO_2) - C_p(O_2) - 0.5\, C_p(H_2)\}$$

$$+ \int_0^{700} dT \{C_p(HO_2) - C_p(O_2) - 0.5\, C_p(H_2)\} \qquad \text{(A.31)}$$

$H°(298) - H°(0)\ (HO_2) = 10.003$ kJ/mol

$H°(298) - H°(0)\ (O_2) = 8.680$ kJ/mol

$H°(298) - H°(0)\ (H_2) = 8.468$ kJ/mol

$H°(700) - H°(0)\ (HO_2) = 25.873$ kJ/mol

$H°(700) - H°(0)\ (O_2) = 21.180$ kJ/mol

$H°(700) - H°(0)\ (H_2) = 20.216$ kJ/mol

$$\Delta_f H_{700}(HO_2) = 12.0478 - (10.003 - 8.680 - \tfrac{1}{2}\ 8.468) + (25.873 - 21.180 - \tfrac{1}{2}\ 20.216)$$

$$= 12.0478 - (-2.911) + (-5.415)$$

$$= 9.544 \pm 0.655 \text{ kJ/mol}$$

$\Delta_f H_{700}(HO_2) = 2.28 \pm 0.16$ kcal/mol

$$\Delta_f H_{1000}(HO_2) = \Delta_f H_{298}(HO_2) - \int_0^{298} dT\ \{C_p(HO_2) - C_p(O_2) - 0.5\ C_p(H_2)\}]$$

$$+ \int_0^{1000} dT\ \{C_p(HO_2) - C_p(O_2) - 0.5\ C_p(H_2)\} \qquad \text{(A.32)}$$

$H°(298) - H°(0)\ (HO_2) = 10.003$ kJ/mol

$H°(298) - H°(0)\ (O_2) = 8.680$ kJ/mol

$H°(298) - H°(0)\ (H_2) = 8.468$ kJ/mol

$H°(1000) - H°(0)\ (HO_2) = 39.585$ kJ/mol

$H°(1000) - H°(0)\ (O_2) = 31.387$ kJ/mol

$H°(1000) - H°(0)\ (H_2) = 29.147$ kJ/mol

$\Delta_f H_{1000}(HO_2) = 12.0478 – (10.003 – 8.680 – ½\ 8.468) + (39.585 – 31.387 – ½\ 29.147)$

$= 12.0478 – (-2.911) + (-6.3755)$

$= 8.583 \pm 0.655$ kJ/mol

$\Delta_f H_{1000}(HO_2) = 2.05 \pm 0.16$ kcal/mol

Now I can determine D_0(HOO-H) and D_{298}(HOO-H) through the equation

$$D_0(\text{HOO-H}) = \Delta_f H_0(\text{HOO}) + \Delta_f H_0(\text{H}) – \Delta_f H_0(\text{HOOH}) \qquad \text{(A.33)}$$

From the thermochemical tables (*2*):

$\Delta_f H_0(H) = 216.035 \pm 0.006$ kJ/mol = 51.634 ± 0.001 kcal/mol

$\Delta_f H_{298.15}(H) = 217.998 \pm 0.006$ kJ/mol = 52.103 ± 0.001 kcal/mol

$\Delta_f H_0(HOOH) = -129.89 \pm 0.22$ kJ/mol = -31.04 ± 0.05 kcal/mol

$\Delta_f H_{298.15}(HOOH) = -135.88 \pm 0.22$ kJ/mol = -32.48 ± 0.05 kcal/mol

so using the value of $\Delta_f H_0(OH)$ from these tables,

D_0(HOO-H) = 4.06 + 51.634 – (-31.04)

= 86.734 kcal/mol ± $((0.15)^2+(0.001)^2+(0.05)^2)^{1/2}$

= 86.73 ± 0.16 kcal/mol

$D_{298.15}$(HOO-H) = 3.36 + 52.103 – (-32.48)

= 87.943 kcal/mol ± $((0.15)^2+(0.001)^2+(0.05)^2)^{1/2}$

= 87.94 ± 0.16 kcal/mol

And with the new value of $\Delta_f H_0$(OH) (*3*),

D_0(HOO-H) = 3.58 + 51.634 – (-31.04)

= 86.254 kcal/mol ± $((0.16)^2+(0.001)^2+(0.05)^2)^{1/2}$

= 86.25 ± 0.17 kcal/mol

$D_{298.15}$(HOO-H) = 2.88 + 52.103 – (-32.48)

= 87.463 kcal/mol ± $((0.16)^2+(0.001)^2+(0.05)^2)^{1/2}$

= 87.46 ± 0.17 kcal/mol

And finally, now I can determine $\Delta_{acid}H_0$(HOO-H) and $\Delta_{acid}H_{298}$(HOO-H) using Eqs. A.18-20:

From the thermochemical tables:

$H°(298.15) - H°(0)\ (HO_2) = 10.003$ kJ/mol

$H°(298.15) - H°(0)\ (HO_2^-) = 10.017$ kJ/mol

$H°(298.15) - H°(0)\ (H) = 6.197$ kJ/mol

$H°(298.15) - H°(0)\ (H^+) = 6.197$ kJ/mol

thermal correction = 10.003 - 10.017 + 6.197 - 6.197 kJ/mol

= -0.014 kJ/mol

= -0.00335 kcal/mol

From Table 3.1, EA(HOO) = 1.078 ± 0.006 eV = 24.8593 ± 0.13836 kcal/mol

IP(H) = 313.587 kcal/mol

so using the value of $\Delta_f H_0$(OH) from the tables,

$\Delta_{acid} H_0$(HOO-H) = 86.734 - 24.8593 + 313.587

$= 375.462$ kcal/mol ± $((0.158)^2+(0.13836)^2+(0.0)^2)^{1/2}$

= 375.46 ± 0.21 kcal/mol

$\Delta_{acid} H_{298.15}$(HOO-H) = 87.943 - 24.8593 + 313.587 – (-0.00335)

$= 376.674$ kcal/mol ± $((0.158)^2+(0.13836)^2+(0.0)^2)^{1/2}$

= 376.67 ± 0.21 kcal/mol

And with the new value of $\Delta_f H_0$(OH) (*3*),

$\Delta_{acid} H_0$(HOO-H) = 86.254 - 24.8593 + 313.587

= 374.982 kcal/mol ± $((0.168)^2+(0.13836)^2+(0.0)^2)^{1/2}$

= 374.98 ± 0.22 kcal/mol

$\Delta_{acid} H_{298.15}$(HOO-H) = 87.463 - 24.8593 + 313.587 – (-0.00335)

= 376.194 kcal/mol ± $((0.168)^2+(0.13836)^2+(0.0)^2)^{1/2}$

= 376.19 ± 0.22 kcal/mol

Bibliography

1. C. J. Howard, *J. Am. Chem. Soc.* **102,** 6937-6941 (1980).

2. *Thermodynamic Properties of Individual Substances*, Vol. 1, edited by L. V. Gurvich, I. V. Veyts, and C. B. Alcock (Hemisphere Pub. Corp., New York, 1989).

3. B. Ruscic, D. Feller, D. A. Dixon, K. A. Peterson, L. B. Harding, R. L. Asher, and A. F. Wagner, *J. Phys. Chem. A* **105,** 1-4 (2001). The values reported in this citation have since been revised slightly by the authors. The most current values are: $\Delta_f H_0(OH) = 8.86 \pm 0.07$ kcal mol^{-1} and $\Delta_f H_{298}(OH) = 8.92 \pm 0.07$ kcal mol^{-1}.

4. A. J. Hills and C. J. Howard, *J. Chem. Phys.* **81,** 4458 (1984).